Topological Phases
of Interacting Fermions in Optical Lattices
with Artificial Gauge Fields

Michael Buchhold

Master's Thesis in the Department of Theoretical Physics

at the

Johann Wolfgang Goethe University of Frankfurt

July 2012

Contents

0. Introduction

During the last century since its mathematically correct formulation by Heisenberg, Dirac, Born, Schrödinger, von Neumann and others in the late 1920's , quantum mechanics has branched out into almost every aspect of 20th century physics and into many other disciplines, such as quantum chemistry, quantum electronics, quantum optics, and quantum information science. However, despite the great success of quantum mechanics in explaining the effects of nature in a mathematical rigorous way, there are still many open issues remaining that have not yet been well understood theoretically. These issues are commonly intractable because the physical effects can not be described by a simplified theory such as mean-field or perturbation theory or the size of the system becomes too large for the Hamiltonian to be treated exactly by classical computers. A seminal paper by Richard Feynman [47], argued that a classical computer will always experience an exponential slowdown when it is applied to a quantum mechanical problem and proposed, as an alternative to circumvent this limitation, the concept of a universal quantum simulator. Nowadays, experimentalists have already developed a poor man's version of Feynman's universal quantum simulator, which can be referred to as *purpose-based quantum simulators* [129]. The basic idea of this approach is to engineer the Hamiltonian of the quantum system of interest in a highly controllable environment and to obtain all the desired quantities by simply measuring its properties.

A prominent example for a realization of a quantum simulator is that of ultracold atoms, which constitute remarkably flexible playgrounds for solid state and quantum many-body physics with an impressive degree of control combined with high-fidelity measurements [15, 30, 112, 26, 48]. Among the fascinating experimental achievements of cold gases, is the realization of an atomic Bose-Einstein condensate (BEC) [36, 5], the observation of vortices and superfluidity in a rotating fermionic gas [202] and the observation Anderson localization in a disordered BEC [12, 153]. Adding optical lattices to ultracold atom simulations, experimentalists have been able to realize interacting lattice models for both fermionic and bosonic atoms with a high tunability of the microscopic parameters [15, 60, 14], such as the interparticle interaction strength and the hopping amplitudes of the lattice. With these experiments, many effects known only from solid state physics have been explored in the context of optical lattices, such as the fermionic and bosonic Mott-insulator transition [60, 98, 159] or fermionic non-equilibrium transport [73, 160]. On the other hand, many classes of systems, well known from condensed matter physics, have not yet been addressed within cold-atom experiments. This is mainly because there exist certain difficulties with their realization, which the experimentalists have to overcome, such as very low entropies required of the emergence of magnetic order or the absence of charge for neutral atoms, which makes it very difficult to simulate orbital magnetism. Nowadays, one direction of optical lattice experiments is to implement artificial gauge fields for neutral atoms, which mimic both the presence of an external magnetic field for charged particles, i.e. orbital magnetism, represented by Abelian gauge fields, and intrinsic effects such as Rashba- or Dresselhaus-type spin-orbit coupling, represented by non-Abelian gauge fields. While there are many interesting physical regimes to address in systems with artificial gauge fields, one major goal of

cold-atom experiments is to realize topological phases of matter, such as quantum Hall or quantum spin Hall insulators.

The general interest in topological insulators began in 1980, when an unexpected quantization of the Hall conductance for a sample in a strong magnetic field at very low temperatures was discovered by von Klitzing *et al.* [104], today known as the quantum Hall effect. The quantum Hall effect could be explained theoretically and concisely by Laughlin only one year later [115] and in 1982 Halperin [77] demonstrated the existence of the famous edge states, which are gapless states at the edge of a quantum Hall sample, energetically connecting different bulk bands, and responsible for the quantized Hall conductance. In the same year, an influential paper by Thouless *et al.* was published [182], relating the quantization of the Hall conductance to the topology of the infinite system and therefore proving its extreme robustness against external perturbations. This work was the starting point for the classification of phases of matter by topological invariants. In the following years, there was a persistent interest in topological phases of matter leading, for instance, to the formulation of the bulk-boundary correspondence and in 1988, to the introduction of Haldane's model, which is a theoretical model describing spinless electrons on the honeycomb lattice, which exhibits an intrinsic quantum Hall effect without the need for an external magnetic field [76].

In 2005, Kane and Mele [101] predicted the existence of a so-called quantum spin Hall effect, by considering a time-reversal symmetric combination of two Haldane models for spinful fermions – a model that closely resembles graphene with a strong intrinsic spin-orbit coupling. This model, today known as the Kane-Mele model, does not show a quantized Hall conductance since spin-up and spin-down electrons travel in opposite directions, such that the topological invariant for this model is zero. On the other hand, the spin Hall conductivity is strictly quantized and Kane and Mele argued that there must be an additional topological invariant, which characterizes this so-called quantum spin Hall effect. This topological invariant was determined by Kane and Mele later that year [100] to be a $\mathbb{Z}_2$ invariant, taking only the two values $\nu = 0, 1$, in contrast to the quantum Hall effect, which is characterized by a $\mathbb{Z}$ invariant. Experimentally, the quantum spin Hall effect is very difficult to observe in graphene, since the spin-orbit coupling is usually very weak. Instead Bernevig *et al.* [9] predicted the quantum spin Hall effect would appear in mercury telluride quantum wells as that compound has an unusually strong spin-orbit coupling. Only one year later, in 2007, the quantum spin Hall effect was observed experimentally by König *et al.* [110] in the proposed quantum wells. However, in two dimensions there has not been any other experiment performed that has observed $\mathbb{Z}_2$ topological insulators in any material.

At this point, optical lattice experiments with artificial gauge fields provide the perfect playground for investigating topological insulators. Recently there has been made much progress in implementing artificial Abelian [96, 140, 167, 170, 54, 97] and non-Abelian gauge fields [34, 125, 56, 120], such that the next group that experimentally realizes a quantum spin Hall insulator could come from the cold-atom community. In particular, we would like to mention Ian Spielman's experiments at NIST, where experimentalists are attempting to synthesize a quantum spin Hall insulator with ultracold ^{6}Li on a atom chip [57]. The controlled observation of the extraordinary phenomenology of topological insulators would shed new light on quantum many-body theory. There are still many open issues in the context of interacting topological insulators, which could be clarified by optical lattice experiments and can up to now not be addressed by other solid state experiments because of the accessible parameter regime for these is strongly limited. For instance there have been contradictory results published on the interacting phase diagram of graphene, where some Monte-Carlo calculations predict the presence of a spin-liquid phase for intermediate interactions [130, 197] while others show the absence of this phase for any interaction strength [168], such that experimental evidence is required for a definite answer of this problem. Further questions to address are the robustness of topologically protected edge states against inter-particle interactions and disorder [42, 21], the robustness of the $\mathbb{Z}_2$ classification in general [89] or the transition from chiral to helical edge states in the presence of spin-orbit interaction [56].

In this thesis, we theoretically investigate geometry, disorder, detection methods and interactions in explicit realizations of topological insulators in optical lattices. The effect of the optical lattice geometry, induced by the smooth trapping potentials inherent to cold-atom experiments is a major difference between optical lattices and solid state systems. We investigate the topological invariants of these systems and show that they do not depend on the trapping geometry of the system. We show that sharp boundaries are not required to realize quantum Hall or quantum spin Hall physics in optical lattices and, on the

contrary, that edge states which belong to a smooth confinement exhibit additional interesting properties, such as spatially resolved splitting and merging of bulk bands and the emergence of robust auxiliary states in bulk gaps to preserve the topological quantum numbers. In addition, we numerically validate that these states are robust against disorder and analyze possible detection methods, with a focus on Bragg spectroscopy, to demonstrate that the edge states can be detected and that Bragg spectroscopy can reveal how topological edge states are connected to the different bulk bands. Furthermore, we consider a spinful and time-reversal invariant version of the Hofstadter problem which can be realized in cold atom experiments. Using a combination of real-space dynamical mean-field theory and analytical techniques, we discuss the effect of on-site interactions and determine the corresponding phase diagram. In particular, we investigate the semi-metal to antiferromagnetic insulator transition and the stability of different topological insulator phases in the presence of strong interactions. We also determine the spectral function of the interacting system which allows us to study the edge states of the strongly correlated topological phases.

This thesis is structured as follows:

- In the first section, we give a general introduction to the Hubbard model and introduce real-space dynamical mean-field theory as the numerical model to address the physics of interacting lattice models with artificial gauge fields.

- In the second section, Monte-Carlo methods are introduced on a very general level with a focus on quantum Monte-Carlo methods, namely diagrammatic Monte-Carlo algorithms.

- For the real-space dynamical mean-field theory, an impurity solver is required, which solves a zero-dimensional interacting impurity problem, described by a non-interacting Green's function which is non-local in time. In this thesis we focus on continuous-time quantum Monte-Carlo impurity solvers, which are explained in great detail in the third chapter.

- In the fourth chapter, we give an overview of improvements and extension to the original formulation of the continuous-time Monte-Carlo solvers, which we implemented to treat systems including Abelian and non-Abelian gauge fields.

- The fifth chapter gives a brief overview over optical lattice experiments and the experimental implementation of artificial gauge fields.

- To discuss the realization of $\mathbb{Z}$ topological insulators, such as the quantum Hall effect, we begin the 6th chapter with a brief introduction of the quantum Hall effect, topological invariants and edge states. Then we discuss the realization of topological phases in cold-atom experiments by implementing the optical lattice version of the famous Hofstadter model [87].

- In the 7th chapter, we introduce $\mathbb{Z}_2$ topological insulators, such as the quantum spin Hall effect and investigate the effect of interactions on the topological phase and the edge states as well as the interaction driven phase transition from a semi-metal to a magnetically ordered insulator. Subsequently, we discuss how non-Abelian gauge fields influence the magnetic order in the insulating phase.

- In the last chapter, we provide some conclusions and an outlook of this thesis.

1. The Fermi-Hubbard Model and the DMFT Approximation

In this chapter, we will introduce the paradigmatic Hubbard model, describing interacting Fermions on a lattice and the computational method to analyze its properties, which is the Dynamical Mean-Field Theory (DMFT) as well as its real-space extention, the real-space Dynamical Mean-Field Theory (RDMFT). Dynamical Mean-Field Theory (DMFT) is a method well suited to analyze the local correlations of strongly interacting Fermions in homogenous lattice systems in large dimensions (i.e. $d \geq 3$), and has been succesfully used to describe the interaction driven Metal-insulator transition and to calculate dynamical quantities of the Hubbard model. Our interest lies in the analysis of inhomogenous lattice systems, where the inhomogeneity is caused by artificial gauge fields and/or an additional external trapping potential. We therefore make use of the extended real space version of DMFT, which also is described in the following sections.

1.1   The Fermi Hubbard Model

The fermionic Hubbard model (more commonly referred to as the Hubbard model) is a theoretical model, describing spinful lattice Fermions, typically in the lowest band approximation, that are interacting with each other only locally [91, 93, 92]. This model, with its extensions to more general lattice structures or interactions [187, 18, 134], is one of the most important theoretical models in condensed matter physics, being able to describe the interaction driven metal-Mott insulator transition at half-filling [136, 53], superconductivity in the case of attractive interactions [109, 33], inter- and intra-band magnetism [180, 178, 49] and many more effects, known from solid state experiments.

In this section, we shortly review single-particle physics in a periodic lattice potential, then introduce interactions between particles and, finally, express the corresponding many-particle Hamiltonian in second quantization. At the end of the section, we give a brief overview of the physical properties of the Hubbard model that are most relevant to the work in this thesis.

Non-interacting particles in a periodic lattice potential $V(\mathbf{x})$, of which we consider only square or cubic lattices, are described by the first-quantized Hamiltonian

$$H_0 = \frac{\mathbf{p}^2}{2m} + V(\mathbf{x}). \tag{1.1}$$

Due to Bloch's theorem, the eigenfunctions of this Hamiltonian can be cathegorized by two quantum numbers, namely the band index α, with $\alpha \in \mathbb{N}$, and the quasi-momentum $\mathbf{k}$, with $k_{x,y,z} \in \{\frac{\pi(2l-L)}{La_{x,y,z}}\}$,

where $a_{x,y,z}$ are the lattice constants in the corresponding directions, L is the number of lattice sites and $l = 1, ..., L$ is an integer label. The eigenfunctions of Hamiltonian (1.1) are called Bloch functions $\psi_{\alpha\mathbf{k}}(\mathbf{x})$ and have the periodicity

$$\psi_{\alpha\mathbf{k}}(\mathbf{x} + \mathbf{R}) = e^{i\mathbf{k}\mathbf{R}}\psi_{\alpha\mathbf{k}}(\mathbf{x}), \tag{1.2}$$

where $\mathbf{R}$ is a lattice vector and fulfill the eigenvalue equation

$$H_0\psi_{\alpha,\mathbf{k}}(\mathbf{x}) = \epsilon_\alpha(\mathbf{k})\psi_{\alpha,\mathbf{k}}(\mathbf{x}). \tag{1.3}$$

The values $\epsilon_\alpha(\mathbf{k})$ for fixed α, as a function of $\mathbf{k}$ constitute the dispersion of the band α. In many cases, there exists a band gap $\Delta_{\alpha,\beta}$ between the bands, i.e.

$$\Delta_{\alpha,\beta} := \min_{\mathbf{k},\mathbf{k}'}|\epsilon_\alpha(\mathbf{k}) - \epsilon_\beta(\mathbf{k}')| > \mathbf{0}, \tag{1.4}$$

for $\alpha \neq \beta$. In sufficiently deep lattices, the gap between the first and second band is much larger than the bandwidth Γ of the first band,

$$\Gamma = \max_{\mathbf{k},\mathbf{k}'}|\epsilon_1(\mathbf{k}) - \epsilon_1(\mathbf{k}')|. \tag{1.5}$$

If this is the case and additionally all other relevant energy scales (the typical interaction strength and the temperature k_BT) are also smaller than the first band gap, it is perfectly reasonable to describe low energy physics in a lowest band approximation. The Hamiltonian (1.1) is then reduced to

$$H_0 = \sum_{\alpha,\mathbf{k}}|\alpha,\mathbf{k}\rangle\epsilon_\alpha(\mathbf{k})\langle\alpha,\mathbf{k}| \approx \sum_{\mathbf{k}}|\mathbf{k}\rangle\epsilon(\mathbf{k})\langle\mathbf{k}|, \tag{1.6}$$

where $|\alpha,\mathbf{k}\rangle$ are the Bloch states and we suppress the index $\alpha = 1$ in the last step, considering only the lowest band in the Hamiltonian.

From a given set of Bloch states $\{|\alpha,\mathbf{k}\rangle\}$ it is possible, via unitary transformation, to construct a new set of basis states. Well known in this context are the so-called Wannier states, which are obtained from the Bloch states by a Fourier transformation

$$|\alpha,i\rangle = \frac{1}{L}\sum_{\mathbf{k}}e^{-i\mathbf{k}\mathbf{R}_i}|\alpha,\mathbf{k}\rangle, \tag{1.7}$$

where $\mathbf{R}_i$ is the lattice coordinate of site i. The Wannier states are found to be a very good basis for expressing a general Hamiltonian $H = H_0 + H'$ as soon as H' contains only local or short ranging operators, since the Wannier states combine both localization of the wave function $\langle\mathbf{x}|\alpha,i\rangle = w_i(\mathbf{x})$ on the lattice site i and the separation into different bands α, being well separated by a band gap Δ. Again, we focus only on the lowest band and reexpress the Hamiltonian in the Wannier basis, which leads to

$$H_0 = \sum_{\mathbf{k}}\epsilon(\mathbf{k})|\mathbf{k}\rangle\langle\mathbf{k}| = \sum_{i,j,\mathbf{k}}\frac{e^{i\mathbf{k}(\mathbf{R_i}-\mathbf{R_j})}\epsilon(\mathbf{k})}{L^2}|i\rangle\langle j| = \sum_{ij}t_{ij}|i\rangle\langle j|. \tag{1.8}$$

The matrix elements t_{ij} are called hopping matrix elements or hopping parameters and describe the transfer rate from state $|j\rangle$ to state $|i\rangle$ in a lattice.

Generally, if one is interested in the interplay between a non-local part H_0 and a local (and often many-particle) part H' in a Hamiltonian $H = H_0 + H'$ and not in the exact band structure of realistic materials, it is reasonable to make a further approximation, called the tight-binding approximation. In the tight-binding approximation, the hopping parameters are considered to be non-zero only for nearest neighbours i, j in the lattice. This becomes exact in the limit of very deep, isotropic lattices (sometimes called the atomic limit) and is a reasonable approximation if the lattice is not too shallow, in which case the lowest band approximation would no longer hold true. Within the tight-binding limit, the Hamiltonian H_0 then finally reads

$$H_0 = \sum_{\langle i,j\rangle}t_{ij}|i\rangle\langle j|, \tag{1.9}$$

where $\langle i,j\rangle$ indicates that the sum runs only over nearest neighbours i, j. Throughout this thesis, we will always make use of the tight-binding approximation, first because we are mainly interested in the

competing effects of local interactions and non-local dispersion and, second, because the periodic lattice structures, which are experimentally created in optical lattice experiments, are described perfectly by this approximation (see chapter optical lattices).

Next, we consider the representation of interactions in a lattice system. In general, n-particle interactions can be described by a sum of n-particle operators $\hat{O}_n$. Here, we only consider two-particle interactions, as higher numbers of particles cannot be present on a single lattice site. Usually, the interaction operators are diagonal in real-space, described by an interaction potential $U(\mathbf{x}_1, \mathbf{x}_2)$, between two particles, located at the coordinates $\mathbf{x}_1$ and $\mathbf{x}_2$. As most interaction only depend on the distance $\mathbf{x}_1 - \mathbf{x}_2$ of the corresponding particles, $U(\mathbf{x}_1, \mathbf{x}_2) = U(\mathbf{x}_1 - \mathbf{x}_2)$, which makes the interactions translationally invariant. In the Wannier representation, the interaction operator H' is then given by

$$H' = \sum_{ijlm} U_{ijlm}|ij\rangle\langle lm|, \quad \text{with} \quad U_{ijlm} = \int dx_1 dx_2 U(\mathbf{x}_1 - \mathbf{x}_2)w_i^*(\mathbf{x}_1)w_j^*(\mathbf{x}_2)w_l(\mathbf{x}_1)w_m(\mathbf{x}_2), \quad (1.10)$$

where $|ij\rangle$ is an anti-symmetric two fermion state, i.e. $|ij\rangle = 1/\sqrt{2}(|i\rangle|j\rangle - |j\rangle|i\rangle)$. So far, we have not included the Fermion's spin in this formalism, which was not necessary since we do not consider interaction operators that change the spin. However, the spin is crucial for the Hubbard model, since it has been formulated first for interacting electrons in solid state systems. When adding a fermionic spin $\sigma = \uparrow, \downarrow$ pointing either in positive or negative z-direction the interaction operator reads

$$H' = \frac{1}{2} \sum_{ijlm\sigma\sigma'} U_{ijlm}|i\sigma j\sigma'\rangle\langle l\sigma m\sigma'|, \quad (1.11)$$

where we exploited the fact that the spin is unchanged by the interactions.

Many-particle physics can be conveniently expressed in the framework of second quantization, where the states in (1.9) and (1.11) are represented by fermionic creation and annihilation operators $c_{i\sigma}^\dagger, c_{j\sigma'}$. These operators fulfill fermionic anticommutation relations

$$\{c_\alpha^\dagger, c_{\alpha'}\} = c_\alpha^\dagger c_{\alpha'} + c_{\alpha'} c_\alpha^\dagger = \delta_{\alpha, \alpha'} \quad (1.12)$$

and any anti-symmetrized fermionic N-particle state $|\Psi_N\rangle$ is expressed as

$$|\Psi_N\rangle = |\alpha_1...\alpha_N\rangle = \prod_{i=1}^N c_{\alpha_i}^\dagger|0\rangle. \quad (1.13)$$

Within the second quantization formalism, the Hamiltonian $H = H_0 + H'$, which is a combination of the lattice Hamiltonian H_0 and the interaction operator H', takes on the form

$$H = \sum_{ij\sigma} t_{ij} c_{i\sigma}^\dagger c_{j\sigma} + \frac{1}{2} \sum_{ijlm\sigma\sigma'} U_{ijlm} c_{i\sigma'}^\dagger c_{j\sigma}^\dagger c_{m\sigma} c_{l\sigma'}. \quad (1.14)$$

The interaction matrix elements U_{ijlm} describe the energy associated with a scattering process of two particles in the quantum states l, m, scattering into the states i, j. Very often, only s-wave scattering processes, which are the lowest order scattering processes, are considered, such that the matrix elements contributing to H up to leading order are those with $i = j = l = m$. In solid state systems, this approximation is usually justified by the large screening of the Coulomb interaction, which makes the resulting interaction short ranged. In contrast, in optical lattice experiments, no screening effect is present but the small energy of the system implies that p-wave scattering (and all higher orders) is unaffected by the interaction strength and can therefore be neglected. With the reduction of the interaction to s-wave processes, the final well known Hubbard Hamiltonian is

$$H = \sum_{ij\sigma} t_{ij} c_{i\sigma}^\dagger c_{j\sigma} + \frac{1}{2} \sum_{i\sigma\sigma'} U_{iiii} c_{i\sigma'}^\dagger c_{i\sigma}^\dagger c_{i\sigma} c_{i\sigma'} = \sum_{ij\sigma} t_{ij} c_{i\sigma}^\dagger c_{j\sigma} + \sum_i U n_{i\uparrow} n_{i\downarrow}, \quad (1.15)$$

where $n_{i\sigma} = c_{i\sigma}^\dagger c_{i\sigma}$ is the local number operator for spin σ.

To briefly illustrate the rich physics described by the Hubbard model, we examine the half-filled case for zero temperature in three dimensions. In general, the Hubbard model, as it is described by (1.15), has charge and spin degrees of freedom, which determine the possible physical phases of the system. For weak interactions, the system is in a metallic phase, or Fermi liquid, which is well described by non-interacting fermionic quasiparticles with an effective mass $m^*(\mathbf{k}) = (\nabla_\mathbf{k}^2 \epsilon(\mathbf{k}))$. At a critical interaction, the charge degrees of freedom are frozen out and the system becomes strictly insulating, the called a Mott insulator. The density of states at the Fermi energy vanishes and two separated Hubbard bands are formed, one of which is completely occupied, and the other completely empty. For stronger interactions, the system possesses only spin degrees of freedom.

For very strong interactions, the Hamiltonian (1.15) can be expanded in orders of t/U, which results in the antiferromagnetic Heisenberg model

$$H_{\text{AF}} = \frac{4t^2}{U} \sum_{\langle i,j \rangle} \mathbf{S}_i \mathbf{S}_j + \mathcal{O}\left(\frac{t^3}{U^2}\right), \tag{1.16}$$

favoring antiferromagnetic ordering. In the limit of infinite interactions $U/t \rightarrow \infty$ the ground state of the Hubbard model is the Néel state, which is the ground state of the AF-Heisenberg model. The excitation spectrum of the Hubbard model can be divided into charge and spin excitations. For all regimes of t/U the spin excitations are gapless and the low energy excitations are described in a spin-wave theory framework. In contrast, the charge excitations have a completely different structure on both sides of the critical Mott point. In the metallic phase, the charge excitations are gapless and the low energy physics is well described by non-interacting particles, whereas in the Mott insulating phase, the excitations are gapped and the excitational structure consists of particle- hole excitations.

With this short overview, we finish this section and come to the derivation of the Dynamical Mean-Field Theory, the computational method to investigate the properties of interacting lattice models, such as the Hubbard model. The Hubbard model itself will be investigated further and in more detail in the following chapters of this thesis in the context of topological phases, caused by the addition of gauge fields to the single-particle Hamiltonian (1.9), see chapter 6.

1.2   Dynamical Mean-Field Theory

In this section, we describe Dynamical Mean-Field Theory (DMFT) and present a derivation of the DMFT self-consistency equations based on the cavity method. DMFT is a powerful method, previously used extensively to analyze the Hubbard model (i.e. to determine phase diagrams or to calculate dynamical quantities) in large dimensions $d \geq 3$. The main idea of the DMFT approximation can be formulated within very few words, although the theoretical justification of this approximation and the derivation of the self-consistency equations is very non-trivial. Within DMFT, the self-energy of the lattice is considered to be local, in other words the quasi-momentum dependence of the self-energy is neglected completely,

$$\Sigma(\mathbf{k}, \omega) \longrightarrow \Sigma(\omega). \tag{1.17}$$

As usual in Mean-Field theories, this projects the physical quantities (in our case the single-particle Green's functions) onto a subspace of smaller complexity and henceforth makes these easier to determine. The challenge of this approximation is now to find the best self-energy of the form (1.17), which is done by applying the self-consistency equations later derived in this section.

It was first proven by Metzner and Vollhardt [133], that the self-energy becomes local in the limit of infinite dimensions, i.e. that the DMFT approximation is exact in infinite dimensions. Subsequently, much progress was achieved by establishing the DMFT approximation and justifying this approximation in finite, but large, dimensions. One of the first achievements of the DMFT approach was then the analysis of the interaction driven Metal-Mott insulator transition in the Hubbard model and the determination of the exact phase diagram.

To illustrate the steps towards the derivation of the DMFT self-consistency condition, we start with writing down the action of the Hubbard model. For theoretical calculations, we choose to use a functional

integral formulation in terms of Grassmann variables as it is taught in most theoretical lectures on many-body physics. Here, we denote Grassmann variables by $c_\alpha^\dagger$ and c_α, which is the same notation as we use for fermionic creation and annihilation operators. However, in contrast to operators, the Grassmann variables $c_\alpha^\dagger$ and c_α are different and completely independent variables. Using the same symbols for both Grassmann variables and operators has been well established in the scientific literature and it should always be clear from context, which picture we are working in (i.e. operators or Grassmann fields).

In the functional integral representation, the partition function is given by the expression

$$Z = \int \prod_{i,\sigma} \mathcal{D}[c_{i\sigma}^\dagger, c_{i\sigma}] \, e^{-S}, \tag{1.18}$$

where the grand-canonical action of the Hubbard model takes on the form

$$S = \int_0^\beta d\tau d\tau' \sum_{i,j,\sigma} c_{i\sigma}^\dagger(\tau)(G^0)_{ij,\sigma}^{-1}(\tau - \tau')c_{j\sigma}(\tau') + U \int_0^\beta d\tau \sum_i n_{i\uparrow}(\tau)n_{i\downarrow}(\tau). \tag{1.19}$$

Here, $G_{ij,\sigma}^0(\tau)$ is the non-interacting Green's function, as defined in the literature, the lattice sites are labeled with i, j, respectively, and σ is the spin, $\sigma = \uparrow, \downarrow$, which is good quantum number for the model considered here.

Due to the local self-energy, in the following derivation, we will see that it is sufficient to determine the local interacting Green's functions $G_{ij,\sigma}(\tau)$ to uniquely identify the matrix elements of the self-energy. These Green's functions are determined by the the expression

$$G_{ii\sigma}(\tau) = \frac{1}{Z} \int \prod_{j,\sigma} \mathcal{D}[c_{j\sigma}^\dagger, c_{j\sigma}] \, c_{i\sigma}(\tau)c_{i\sigma}^\dagger \, e^{-S}. \tag{1.20}$$

To simplify this expression, we realize, that the integration over all degrees of freedom, except that of (i, σ) can be done before inserting the creation and annihilation operators in this expression. We define the effective action for the determination of the local Green's functions by

$$\frac{1}{Z_{\text{eff},i}} \, e^{-S_{\text{eff},i}} = \frac{1}{Z} \int \prod_{j \neq i, \sigma'} \mathcal{D}[c_{j\sigma}^\dagger, c_{j\sigma}] e^{-S}, \tag{1.21}$$

such that the Green's function integral reads

$$G_{ii\sigma}(\tau) = \frac{1}{Z_{\text{eff},i}} \int \prod_{\sigma'} \mathcal{D}[c_{i\sigma'}^\dagger, c_{i\sigma'}] \, c_{i\sigma}(\tau)c_{i\sigma}^\dagger \, e^{-S_{\text{eff},i}}. \tag{1.22}$$

Note that the effective action $S_{\text{eff},i\sigma}$ only contains Grassmann variables $c_{i\sigma}^\dagger$ and $c_{i\sigma}$ and therefore, if the effective action is known, the determination of the local Green's functions reduces to a zero-dimensional problem (as it is for instance given by the Anderson impurity model). Due to this, we want to find an approximate expression (again exact in infinite dimensions) for the effective action.

We decompose the total system into the local part, i.e. the lattice site i (setting $i = 0$ without loss of generality) and the cavity system, which is the whole lattice but without site i and perform the same decomposition to the action of the system (1.19). This splits the action into a local action S_0, the cavity action $S^{(0)}$ and the coupling of the local part to the cavity ΔS, where we have defined

$$S_0 = \int_0^\beta d\tau \, S_0(\tau) = \int_0^\beta d\tau \sum_\sigma c_{0\sigma}^\dagger(\tau)(\partial_\tau - \mu)c_{0\sigma}(\tau) + U n_{0\uparrow}(\tau)n_{0\downarrow}(\tau) \tag{1.23}$$

and

$$\Delta S = \int_0^\beta d\tau \, \Delta S(\tau) = -\int_0^\beta d\tau \sum_{j\sigma} t_{j0} c_{j\sigma}^\dagger(\tau)c_{0\sigma}(\tau) + t_{0j} c_{0\sigma}^\dagger(\tau)c_{j\sigma}(\tau). \tag{1.24}$$

With this separation of terms, we can rewrite expression (1.21) such that

$$e^{-S_{\text{eff}}} = \frac{Z_{\text{eff}}}{Z} e^{-S_0} \int \prod_\sigma \mathcal{D}[c_{i\sigma}^\dagger, c_{i\sigma}] e^{-\Delta S} e^{-S^{(0)}} = \frac{Z_{\text{eff}} Z^{(0)}}{Z} e^{-S_0} \langle e^{-\Delta S} \rangle^{(0)}, \tag{1.25}$$

where we have suppressed the index i, and introduced the partition function of the cavity $Z^{(0)}$ and the expectation value $\langle O \rangle^{(0)}$ of an operator O with respect to the cavity. Realizing that $\frac{Z_{\text{eff}} \, Z^{(0)}}{Z}$ is simply a normalization factor, which contains no operators, we have found an exact expression for the local effective action by the combination of (1.21) and (1.25), which reads

$$S_{\text{eff}} = S_0 - \ln \langle e^{-\Delta S} \rangle^{(0)}. \tag{1.26}$$

The first part of the effective action (the local action S_0) contains terms that are of quadratic and quartic order in the Grassmann variables, while the second part (the averaged exponential) contains Grassmann variables to arbitrary large order, which is obvious when we expand this expression into a power series. The logarithm in (1.26) is very helpful to bring the second part of the equation into a more convenient form using the linked cluster theorem. The linked cluster theorem states the following, supposed we have an action S and a perturbation S_{pert} with

$$Z = \int \prod_{i,\sigma} \mathcal{D}[c^{\dagger}_{i\sigma}, c_{i\sigma}] \, e^{-S - S_{\text{pert}}}, \;\; Z_0 = \int \prod_{i,\sigma} \mathcal{D}[c^{\dagger}_{i\sigma}, c_{i\sigma}] \, e^{-S}$$

$$\implies \;\; \ln \frac{Z}{Z_0} = \sum \left(\begin{array}{c} \text{all connected diagrams of a} \\ \text{perturbation expansion in } S_{\text{pert}} \end{array} \right) \tag{1.27}$$

Now, we can apply this theorem to the expectation value in Eq. (1.26) to finally obtain an explicit expression for the the effective action S_{eff}. To understand the result, we perform an expansion of

$$e^{-\Delta S} = \sum_{n=0}^{\infty} \int \prod_{l=1}^{n} d\tau_l \, \Delta S(\tau_l) \tag{1.28}$$

and take into account, that in the expectation value of Eq. (1.26) only even terms of this expansion can survive, since ΔS is linear in cavity operators $c^{\dagger}_{i\sigma}, c_{i\sigma}$[1]. Because we do not consider finite pairing fields in this derivation, the number of Grassmann variables $c^{\dagger}_{0\sigma}$ must also be equal to the number of variables $c_{0\sigma}$ and we only have to consider the respective terms in the expansion (1.28)[2]. After these considerations, we may take a look at the first non-vanishing and non-trivial summand in (1.28), which is the non-vanishing part of the second order contribution (the zeroth order is trivially the unity operator and the expectation value of the first order term vanishes completely), given by

$$\Delta S_2 = \frac{1}{2} \int_0^{\beta} d\tau_1 d\tau_2 \sum_{\sigma} c^{\dagger}_{0\sigma}(\tau_1) \left[\sum_{ij} t_{i0} t_{0j} c_{i\sigma}(\tau_1) c^{\dagger}_{j\sigma}(\tau_2) \right] c_{0\sigma}(\tau_2). \tag{1.29}$$

Looking at Eq. (1.29), we immediately realize, that the missing part of the effective action consists of a sum of connected Green's functions $G_C^{(0)}$ with respect to the cavity action. We can now exactly rewrite the effective action, which takes the form

$$S_{\text{eff}} = S_0 + \sum_{n=1}^{\infty} \int d\tau_1 ... d\tau_n d\tau_1' ... d\tau_n' c^{\dagger}_{0\sigma}(\tau_1) ... c^{\dagger}_{0\sigma}(\tau_n) \mathcal{M}_C^{(n)}(\tau_1 ... \tau_n') c_{0\sigma}(\tau_n') ... c_{0\sigma}(\tau_1'), \tag{1.30}$$

where $\mathcal{M}_C^{(n)}(...)$ is the sum over all connected Green's functions $G_{C,i_1,...i_n,j_1,j_n}^{(0)}(...)$ of order n, weighted with the corresponding hopping parameters $t_{i_1,0}, ... t_{i_n,0}, t_{0,j_1}, ... t_{0,j_n}$, i.e.

$$\mathcal{M}_C^{(n)}(\tau_1 ... \tau_n') = \sum_{i_1,...j_n} G_{C,i_1,...i_n,j_1,...,j_n}^{(0)}(\tau_1 ... \tau_n') \prod_{l=1}^{n} t_{i_l,0} t_{0,j_l}. \tag{1.31}$$

Here, the number of different non-zero hopping amplitudes $t_{i,0}, t_{0,j}$ is proportional to the dimension d and one should note, that the connected Green's functions from the previous expression can be related

---

[1]Note that for fermionic systems (even with superfluid pairing) expectation values of an odd number of creation and annihilation operators are always zero.

[2]This derivation can be straightforwardly extended to include superfluid pairing of fermions but we do not show this here to avoid confusion.

to the full cavity Green's functions by a hierarchy of equations, e.g. the two point connected Green's functions are identical to the full Green's functions and for the four point Green's function, one may use the relation

$$G_{C,i_1,i_2,j_1,j_2}(\tau_1,\tau_2,\tau_1'\tau_2') = G_{i_1,i_2,j_1,j_2}(\tau_1,\tau_2,\tau_1'\tau_2') \tag{1.32}$$

$$-G_{i_1,j_1}(\tau_1,\tau_1')G_{i_2,j_2}(\tau_2,\tau_2') - G_{i_1,i_2}(\tau_1,\tau_2)G_{j_1,j_2}(\tau_1',\tau_2') - G_{i_1,j_2}(\tau_1,\tau_2')G_{i_2,j_1}(\tau_2,\tau_1').$$

So far, we have derived an exact expression for the effective action of an arbitrary lattice site, here denoted as site 0. The effective action in Eq. (1.30) contains only local operators, they must be considered to infinite order and are additionally coupled to very non-trivial matrix elements (those of the matrix $\mathcal{M}$). From this expression we aim now to obtain a useful approximation for the effective action by making use of the large dimension of the system. This expression shall again be exact in the limit of infinite dimensions. From now on, we strictly follow the authors of [53] and explain their steps for the approximation.

If we want to describe non-trivial physics in infinite dimensions, it is necessary to keep the average kinetic energy per particle finite (to be more precise, on the order of the interaction U, otherwise interactions can be treated as an arbitrary small perturbation, resulting in a perfect Fermi liquid). This is achieved by rescaling the hopping parameters $t_{i,j}$ with the dimension. We will now derive the proper scaling scheme to obtain a non-trivial physics in the limit of infinite dimensions as it was first explained by Metzner and Vollhardt in 1989 [133].

The kinetic energy per particle ϵ_{kin} of a d-dimensional fermionic many-particle system at zero-temperature can be expressed as

$$\epsilon_{\text{kin}} = \int d\epsilon \rho_d(\epsilon) f_{\epsilon_F}(\epsilon)\epsilon, \tag{1.33}$$

where we have introduced the density of states of a d-dimensional system

$$\rho_d(\epsilon) = \sum_\alpha \delta(\epsilon - \epsilon_\alpha), \tag{1.34}$$

with α, ϵ_α labeling the eigenstates, the eigenenergies of the system, respectively, and the zero-temperature Fermi-distribution function

$$f_{\epsilon_F}(\epsilon) = \Theta(\epsilon_F - \epsilon), \tag{1.35}$$

such that

$$\int d\epsilon \rho_d(\epsilon) f_{\epsilon_F}(\epsilon) = n \tag{1.36}$$

is the particle number per lattice site. When the eigenstates of the system are separable with respect to each dimension, one can express kinetic energy per particles ϵ, which is distributed according to $\rho_d(\epsilon)$, as the sum of independent variables

$$\epsilon = \sum_{l=1}^{d} \epsilon_l,$$

where every single variable ϵ_l is distributed independently according to the one-dimensional density of states $\rho_1(\epsilon)$. Using the central limit theorem, for the case of the dimension approaching infinity ($d \to \infty$), this leads to a distribution function of

$$\rho_d(\epsilon) \overset{d\to\infty}{=} \frac{1}{\sqrt{\pi d}\sigma} e^{-\frac{(\epsilon-\tilde{\epsilon})^2}{\sqrt{d}\sigma}}, \tag{1.37}$$

where $\tilde{\epsilon} = 0$ is the average and $\sigma = 2t$ is the variance of the one-dimensional density of states. Equation (1.37) shows that the only scaling that preserves the energy from being either infinite or zero in the limit $d \to \infty$ is to scale the hopping t according to $\tilde{t} = Ct/\sqrt{d}$, with a dimension independent constant C, which we choose $C = 1$. For any other choice of the scaling, the density of states would describe a model with an infinite kinetic energy, i.e. a purely metallic system, or with zero kinetic energy, i.e. a system in the atomic limit.

The dimension dependent scaling of the hopping parameters introduced above, i.e. $t \to t/\sqrt{d}$, will also

lead to a specific scaling behavior of the Green's functions $G_{ij\sigma}(\omega)$ with the dimension d. The Green's functions are defined as the matrix elements of the resolvent operator

$$G_{ij\sigma}(\omega) = \langle i\sigma|\mathcal{R}_\omega|j\sigma\rangle = \langle i\sigma|\frac{1}{\omega - H}|j\sigma\rangle = \frac{1}{\omega}\langle i\sigma|\sum_{n=0}^{\infty}\left(\frac{H}{\omega}\right)^n|j\sigma\rangle, \tag{1.38}$$

whereas we used the definition of the Neumann series in the last equality[3]. For off-diagonal matrix elements $|i - j| = l \neq 0$ of the Green's functions, the lowest order non-zero matrix elements in equation (1.38) are those with $n = l$, which are at least proportional to t^l and therefore scale as $d^{-l/2}$. This means, in the limit of large dimensions, the single-particle Green's functions will scale as

$$G_{ij\sigma} \propto d^{-\frac{1}{2}||\mathbf{R}_i - \mathbf{R}_j||}. \tag{1.39}$$

This result is quite important, not only because it will be used further on to analyzed the connected Green's functions in (1.31) but also because it leads to the fact that in infinite dimensions, the self-energy becomes a purely local quantity, which is the essence of the DMFT approximation.
Within diagrammatic perturbation theory in the local interaction U, the self-energy is defined as the sum over all connected, one-particle irreducible diagrams. With the scaling in Eq. (1.39), all contributions to the self-energy that contain non-local Green's functions will vanish in infinite dimensions and the self-energy becomes a purely local quantity

$$\Sigma_{ij\sigma}(\omega) = \delta_{ij}\Sigma_{ii\sigma}(\omega), \tag{1.40}$$

as we stated in the beginning of this chapter[4].
Before we proceed in rescaling the effective action of Eq. (1.30), we have to consider the scaling of the connected Green's functions $G_{C,i_1,\ldots j_n}^{(0)}$. As pointed out in [53], these scale as

$$G_{C,i_1,\ldots j_n}^{(0)} \propto \prod_{l=1}^{n}\sqrt{d}^{-|i_1-i_l|} \times \sqrt{d}^{-|i_1-j_l|}. \tag{1.41}$$

With this, the sum in (1.30) can be further analyzed. For a given order n, in this sum there will always contribute d^m summands with m distinct indices, $1 \leq m \leq 2n$. If two indices of (1.41) are distinct, their distance is at least two lattice sites, which leads to a scaling for the Green's functions of $G_{C,i_1,\ldots j_n}^{(0)} \propto d^{m-1}$, if m indices are distinct. The total scaling of the nth order contribution is given by d^{-n} from the $2n$ rescaled hopping amplitudes, multiplied with $d^m \times d^{1-m} = d$ coming from the Green's functions and therefore in total amounts to $\propto d^{1-n}$. In the limit of infinite dimensions $d \to \infty$, the only non-vanishing term in the sum of Eq. (1.30) is the first order term. With this approximation, the effective action finally reads

$$S_{\text{eff}} = S_0 + \int d\tau d\tau' \sum_{ij\sigma} c_{0\sigma}^\dagger(\tau)t_{i0}t_{j0}G_{ij\sigma}^{(0)}(\tau - \tau')c_{0\sigma}(\tau') \tag{1.42}$$

and by defining the hybridization function Γ_σ as

$$\Gamma_\sigma(\tau) = \sum_{ij} t_{0i}t_{j0}G_{ij\sigma}^{(0)}(\tau), \tag{1.43}$$

the effective action is given by

$$S_{\text{eff}} = -\int d\tau d\tau' \sum_{\sigma} c_{0\sigma}^\dagger(\tau)\left(\delta(\tau - \tau')(-\partial_\tau + \mu) - \Gamma_\sigma(\tau - \tau')\right)c_{0\sigma}(\tau') + U\int d\tau\, n_\uparrow(\tau)n_\downarrow(\tau). \tag{1.44}$$

In this effective action, the hybridization function Γ_σ describes the first order coupling term of a single lattice site to an interacting lattice problem, where the respective lattice site has been removed, of an

---

[3]The states $|i\sigma\rangle$ denote Wannier states at lattice site i for spin σ and we omitted the convergence factor $+i0^+$ in the resolvent operator.

[4]At this point, one should be aware that this is only true for local interactions or iterations that are of density density type but not for non-local exchange interactions

expansion in the dimension d of the system, whereas all higher order terms scale at least as $\mathcal{O}(d^{-1})$.
We now introduce one further quantity, the so-called Weiss function $\mathcal{G}_0$, which compactifies the notation of the effective action. We define

$$\mathcal{G}_{0\sigma}^{-1}(\tau) = \delta(\tau)(-\partial_\tau + \mu) - \Gamma_\sigma(\tau), \tag{1.45}$$

and insert this into the effective action

$$S_{\text{eff}} = -\int d\tau d\tau' \sum_\sigma c_{0\sigma}^\dagger(\tau)\mathcal{G}_{0\sigma}^{-1}(\tau - \tau')c_{0\sigma}(\tau') + U\int d\tau\, n_\uparrow(\tau)n_\downarrow(\tau). \tag{1.46}$$

With this last equation, the effective action derived in this section describes a zero dimensional spinful and interacting system, where the Weiss function has taken over the part of the non-interacting Green's function of this system and the interaction is described by the Hubbard U. From now on, we will call this zero dimensional system the **impurity system** or simply the impurity. Importantly, one should not be confused by the Weiss function, since it is the non-interacting Green's function of the impurity system, but it is **not** the local projection of the non-interacting lattice Green's function. As mentioned before, the hybridization function describes the coupling of the impurity system to an interacting lattice problem and therefore this information is also contained in the Weiss function.

Within the derivation of the effective impurity model, we can identify two important quantities, that coincide for both the lattice and the impurity problem. As we mentioned at the beginning, the reason for deriving an effective action of the above form (1.46) is that we wanted to find a very compact expression for the local interacting Green's functions of the lattice problem as given by (1.20) and (1.22). Looking at these two equations, we can immediately see, that within the DMFT approximation the interacting lattice Green's function $G_{ii\sigma}(\tau)$ exactly coincides with the interacting Green's function $G_{0\sigma}(\tau)$ of the impurity problem. Later, we will demonstrate that the local lattice self-energy is also identical to the self-energy of the impurity problem, which completes the DMFT self-consistency equations.

In the last part, we have introduced the DMFT approximation, which resulted in the insight that the self-energy of a lattice problem with local interactions (as it is the case for the Hubbard model) becomes purely local in infinite dimensions and that the non-local contributions scale at least as $\mathcal{O}(d^{-1})$ and also that the effective action, sufficient to describe all local correlations, takes on the form of a zero dimensional interacting problem, called the impurity. As we will see in the following parts, this is already sufficient to, without any further approximations, construct a fully self-consistent theory to approximately describe the interacting lattice problem in large dimensions, becoming exact in the limit of infinite dimensions.

The physical systems investigated in the later parts of this thesis do not have the translational symmetry of an infinite lattice and therefore always require a real space analysis of a finite system, which was done by using RDMFT, the real space extension of DMFT. To derive the self-consistency equations used in RDMFT is is sufficient to start with all the relations that we have derived so far and therefore the reader may directly jump to the RDMFT section now. However, for completeness, we will also derive the DMFT equations which have been extensively used to investigate a homogeneous lattice system in the thermodynamic limit. This will be done in the residual part of this section but is, as mentioned before, neither necessary to understand the RDMFT equation nor the physics that are presented later in this thesis.

To derive the full set of DMFT equations for translational invariant systems, we precisely follow the steps illustrated in [?]. We start with switching from imaginary-time to Matsubara frequency representation, where

$$f(\tau) = \sum_{n=-\infty}^{\infty} f(i\omega_n)e^{-i\omega_n\tau} \quad \text{and} \quad f(i\omega_n) = \int_0^\beta d\tau f(\tau)e^{i\omega\tau} \tag{1.47}$$

is the transformation between these two representations for an arbitrary function f and $\omega_n = (2n + 1)\pi/\beta$ are the fermionic Matsubara frequencies. In this representation the hybridization function is given by

$$\Gamma_\sigma(i\omega_n) = \sum_{ij} t_{0i}t_{j0}G_{ij\sigma}^{(0)}(i\omega_n) = \sum_{ij} t_{0i}t_{j0}\left(G_{ij\sigma}(i\omega_n) - \frac{G_{i0\sigma}(i\omega_n)G_{0j\sigma}(i\omega_n)}{G_{00\sigma}(i\omega_n)}\right), \tag{1.48}$$

where the last equality can be proven for any lattice, with one lattice site removed, and can for instance be derived by performing an expansion of the Green's functions in the hopping parameters t, as mentioned in [53]. To evaluate the sum in Eq. (1.48) we express the Green's functions in quasi-momentum representation

$$G_{ij\sigma}(i\omega_n) = \frac{1}{L}\sum_k e^{i\mathbf{k}(\mathbf{R_i}-\mathbf{R_j})} G_{\mathbf{k}\sigma}(i\omega_n) = \frac{1}{L}\sum_k e^{i\mathbf{k}(\mathbf{R_i}-\mathbf{R_j})} \frac{1}{i\omega_n + \mu - \Sigma_\sigma(i\omega_n) - \epsilon_\mathbf{k}}, \qquad (1.49)$$

where we already used the $\mathbf{k}$ independence of the self-energy $\Sigma_{\mathbf{k}\sigma}(i\omega_n) = \Sigma_\sigma(i\omega_n)$. The dispersion $\epsilon_\mathbf{k}$ is nothing else but the Fourier transformation of the hopping parameters

$$\epsilon_\mathbf{k} = \sum_i t_{0i} e^{-i\mathbf{k}\mathbf{R}_i}, \qquad (1.50)$$

which leads, when combined with (1.48), to

$$\Gamma_\sigma(i\omega_n) = I_2 - \frac{I_1^2}{I_0}, \qquad (1.51)$$

where we introduced the different sums for convenience

$$I_0 = \frac{1}{L}\sum_\mathbf{k} \frac{1}{\xi - \epsilon_\mathbf{k}}, \qquad (1.52)$$

$$I_1 = \frac{1}{L}\sum_\mathbf{k} \frac{\epsilon_\mathbf{k}}{\xi - \epsilon_\mathbf{k}} = \frac{1}{L}\sum_\mathbf{k} \left(\frac{\epsilon_\mathbf{k} - \xi}{\xi - \epsilon_\mathbf{k}} + \frac{\xi}{\xi - \epsilon_\mathbf{k}}\right) = -1 + \xi I_0, \qquad (1.53)$$

$$I_2 = \frac{1}{L}\sum_\mathbf{k} \frac{\epsilon_\mathbf{k}^2}{\xi - \epsilon_\mathbf{k}} = \frac{1}{L}\sum_\mathbf{k} \left(\frac{\epsilon_\mathbf{k}(\epsilon_\mathbf{k} - \xi)}{\xi - \epsilon_\mathbf{k}} + \frac{\xi\epsilon_\mathbf{k}}{\xi - \epsilon_\mathbf{k}}\right) = -0 + \xi I_1. \qquad (1.54)$$

In these equations, we have used the shortened notation $\xi \equiv i\omega_n + \mu - \Sigma(i\omega_n)$ and made use of the trivial identities

$$\frac{1}{L}\sum_\mathbf{k} = 1 \quad \text{and} \quad \sum_\mathbf{k} \epsilon_\mathbf{k} = 0. \qquad (1.55)$$

Now, with a little bit of algebra, we can rewrite the hybridization function so that it is only in terms of I_0, which is simply the interacting impurity Green's function $G_{0\sigma}(i\omega)$. We obtain

$$\Gamma_\sigma(i\omega_n) = i\omega_n + \mu - \Sigma_\sigma(i\omega_n) - G_{0\sigma}^{-1}(i\omega_n), \qquad (1.56)$$

which, after identifying the Weiss function in Matsubara representation as $\mathcal{G}_{0\sigma}^{-1}(i\omega_n) = i\omega_n + \mu - \Gamma_\sigma(i\omega_n)$ finally reads

$$G_{0\sigma}^{-1}(i\omega_n) = \mathcal{G}_{0\sigma}^{-1}(i\omega_n) - \Sigma_\sigma(i\omega_n). \qquad (1.57)$$

The last equation is nothing but the Dyson equation for the impurity problem, which means that not only the interacting local lattice Green's function is identical to the impurity Green's function but also the local lattice self-energy is identical to the impurity self-energy. This is a remarkable result, especially as no further approximations were necessary in the derivation of these identities. This last identity (1.57) completes the set of four DMFT equations required for the translational invariant lattice. To conclude this section, we shortly review these four equations and explain the DMFT self-consistency procedure. We started by deriving a local effective action, which becomes exact in infinite dimensions and reads

$$S_\text{eff} = -\int d\tau d\tau' \sum_\sigma c_{0\sigma}^\dagger(\tau) \mathcal{G}_{0\sigma}^{-1}(\tau - \tau') c_{0\sigma}(\tau') + U\int d\tau\, n_\uparrow(\tau) n_\downarrow(\tau) \qquad (1.58)$$

and can be used to determine the local correlation functions such as the local interacting Green's function $G_{ii\sigma}(i\omega_n)$. During this derivation, we argued that the self-energy becomes purely local in infinite dimensions, which was rigorously proven by Vollhardt and Metzner [133], i.e.

$$\Sigma_{\mathbf{k}\sigma}(i\omega_n) = \Sigma_\sigma(i\omega_n), \qquad (1.59)$$

which leads to the simplified lattice Dyson equation

$$G_{00\sigma} = \frac{1}{L} \sum_{\mathbf{k}} \frac{1}{i\omega_n + \mu - \Sigma_\sigma(i\omega_n) - \epsilon_{\mathbf{k}}}. \tag{1.60}$$

The last important equation is the identification of the impurity self-energy with the local lattice self-energy, which is best expressed through the impurity Dyson equation

$$\mathcal{G}_{0\sigma}^{-1}(i\omega_n) = G_{00\sigma}^{-1} + \Sigma_\sigma(i\omega_n). \tag{1.61}$$

If the equations (1.60) and (1.61) are fulfilled simultaneously by a Green's function G and self-energy Σ, which result from the impurity action (1.58), a self-consistent solution of the DFMT equations is found and G, Σ are approximate solutions for the interacting lattice problem, which become particular good in large dimensions, i.e. $d \geq 3$. A typical DMFT calculation will start with a guess of the hybridization functions $\Gamma_\sigma(i\omega_n)$ and implement a solver for the non-trivial problem of calculating the impurity Green's function from (1.58). Then iterating the four DMFT equations (1.58), (1.59), (1.60), (1.61) will allow convergence to the self-consistent solution.

1.3   Real-space Dynamical Mean-Field Theory

In the previous section, we introduced the DMFT approximation for a certain class of interacting lattice systems and, in the second part of the section completed the set of required DMFT equations for a homogenous lattice (1.61) by identifying the local lattice self-energy with the impurity self-energy. In this section, we will introduce the real-space extension of DMFT, called real-space dynamical mean-field theory (RDMFT), which can describe inhomogenous lattice systems of finite size, caused for instance by a trapping potential, and will also later be used to analyze systems of infinite size with a larger unit cell than a single lattice site. Recently, RDMFT has been succesfully applied to both, disordered systems, analyzing the competing phases of metal, Mott-insulator and Anderson-insulators [163, 164, 40, 135], as well as finite systems, which were subjected to a confining potential in real-space [147, 166, 59, 84]. The systems that we investigate are described by the Fermi Hubbard model with an inhomogenous distribution of on-site energies ϵ_i and non-uniform hopping parameters t_{ij}, i. e. the Hamiltonian

$$H = -\sum_{ij\sigma} \left(t_{ij} c_{j\sigma}^\dagger c_{i\sigma} + \text{h.c.} \right) - \sum_{i\sigma} (\mu - \epsilon_i) n_{i\sigma} + U \sum_i n_{i\uparrow} n_{i\downarrow}. \tag{1.62}$$

This Hamiltonian was previously used to describe disordered systems [39, 179, 1, 163], where the $\{\epsilon_i\}$ were distributed randomly, or trapped, finite systems as they appear naturally in cold atom experiments. In the following chapters, we will investigate this Hamiltonian with $\{\epsilon_i\}$ representing a trapping potential in the shape of a hard-wall confinement. This will be done to resolve the so-called edge states of the system, which are not present in unconfined systems, described by the Hubbard model for the homogenous case.

One can also justify the use of RDMFT instead of DMFT from a physical point of view. DMFT was formulated for a homogenous system, therefore whenever thermodynamic phases appear that break the translational symmetry of the lattice, the formulation of DMFT in the previous section will not be able to resolve those, simply because it is restricted to homogenous systems. In the cases where translational symmetry is not completely broken but instead the unit cell of the system is just enlarged to two lattice sites (as for instance for an antiferromagnetically ordered phase), it is possible to simply use the original DMFT equations with a modified self-consistency condition. However, if the system is in a lattice symmetry broken phase with hugely enlarged unit cell or even without any translational symmetry remaining (as for instance in an Anderson insulating phase), it is necessary to find a theoretical approach that is able to resolve this effects in real-space, which is the case for the RDMFT approximation.

To derive the RDMFT equations, we start with introducing the Dyson equation for a lattice system in real-space. The non-interacting Green's function in a real-space formulation is determined by the equation

$$(\hat{G}_\sigma^0)^{-1}(i\omega_n) = (\mu + i\omega_n)\,\hat{\mathbf{1}} - \hat{T} - \hat{V}, \tag{1.63}$$

where $\hat{1}$ is the unity operator, $\hat{T}$ is the hopping operator, i.e. $\langle i|\hat{T}|j\rangle = -t_{ij}$ [5], and $\hat{V}$ is the operator with the on-site energies of the corresponding lattice sites, $\langle i|\hat{V}|j\rangle = \delta_{ij}\epsilon_i$. With this equation, we directly come to the Dyson equation in real-space, which reads

$$\hat{G}_\sigma^{-1}(i\omega_n) = (\hat{G}_\sigma^0)^{-1}(i\omega_n) - \hat{\Sigma}_\sigma(i\omega_n) = (\mu + i\omega_n)\,\hat{1} - \hat{T} - \hat{V} - \hat{\Sigma}_\sigma(i\omega_n), \tag{1.64}$$

with the self-energy operator $\langle i|\hat{\Sigma}_\sigma(i\omega_n)|j\rangle = \Sigma_{ij\sigma}(i\omega_n)$. In this equation, we have made use of the fact that, up to now, spin is a good quantum number, since the Hamiltonian (1.62) contains no terms that change the spin of a particle. When we later analyze systems where a single particle's spin is not longer conserved, it is straight forward to extend (1.64) to include these terms and similarly for the derivation of the RDMFT equations.

Now, as in the DMFT section, we want to derive an effective action $S_{\text{eff}}^{(i)}$, which is able to determine the local Green's function on lattice site i, via

$$G_{ii\sigma}(\tau) = \frac{1}{Z_{\text{eff}}^{(i)}} \int \prod_{\sigma'} \mathcal{D}[c_{i\sigma'}^\dagger, c_{i\sigma'}] c_{i\sigma}(\tau) c_{i\sigma}^\dagger e^{-S_{\text{eff}}^{(i)}}. \tag{1.65}$$

Fortunately, the derivation of the effective action and also of the equations (1.48) and (1.40) in the DMFT section have relied only on the fact that the Hamiltonian was formulated on a lattice but not on the translational symmetry of the lattice Hamiltonian itself (this fact just was exploited in the derivation of the last DMFT equation (1.57)). Therefore, we can already define the effective action $S_{\text{eff}}^{(i)}$ as

$$S_{\text{eff}}^{(i)} = -\int d\tau d\tau' \sum_\sigma c_{i\sigma}^\dagger(\tau) \mathcal{G}_{i\sigma}^{-1}(\tau - \tau') c_{i\sigma}(\tau') + U \int d\tau\, n_{i\uparrow}(\tau) n_{i\downarrow}(\tau), \tag{1.66}$$

where the Weiss function $\mathcal{G}_{i\sigma}^{-1}$ is defined as

$$\mathcal{G}_{i\sigma}^{-1}(\tau) = \delta(\tau)(-\partial_\tau + \mu - \epsilon_i) - \Gamma_{i\sigma}(\tau). \tag{1.67}$$

The hybridization function $\Gamma_{i\sigma}(i\omega_n)$ in Matsubara representation is determined, as in the previous section, by

$$\Gamma_{i\sigma}(i\omega_n) = \sum_{lm} t_{0l} t_{m0} G_{lm\sigma}^{(0)}(i\omega_n) = \sum_{lm} t_{0l} t_{m0} \left(G_{lm\sigma}(i\omega_n) - \frac{G_{li\sigma}(i\omega_n) G_{im\sigma}(i\omega_n)}{G_{ii\sigma}(i\omega_n)} \right). \tag{1.68}$$

The self-energy $\Sigma_{ij\sigma}(i\omega_n)$ is again purely local $\Sigma_{ij\sigma}(i\omega_n) = \delta_{ij}\Sigma_{ii\sigma}(i\omega_n)$ but, in contrast to the previous section, may vary from lattice site to lattice site and, due to this, possess an additional dependence on i. The missing step to a closed self-consistency loop, as in the homogenous case, is to relate the impurity self-energy $\Sigma_\sigma^{(\text{imp})}(i\omega_n) = \mathcal{G}_{i\sigma}^{-1}(i\omega_n) - G_{ii\sigma}^{-1}(i\omega)$ to the lattice self-energy $\Sigma_{i\sigma}(i\omega_n)$. Now, we define

$$\hat{\xi}_\sigma(i\omega_n) = (i\omega_n + \mu)\,\hat{1} - \hat{V} - \Sigma_\sigma(i\omega_n) \tag{1.69}$$

as the diagonal (in real-space) part of Eq. (1.64), such that

$$\hat{G}_\sigma^{-1}(i\omega_n) = \hat{\xi}_\sigma(i\omega_n) - \hat{T}. \tag{1.70}$$

For the next few lines, we drop the spin index and Matsubara frequency argument since all operators are diagonal with respect to these and this simplifies the calculation. Rewriting (1.68) then leads to

$$\Gamma_i G_{ii} = \sum_{lm} t_{0l} t_{m0} (G_{lm} G_{ii} - G_{li} G_{im}), \tag{1.71}$$

which we express in matrix notation, exploiting the fact that $\hat{T} = \hat{\xi} - \hat{G}^{-1}$,

$$\begin{aligned}
\Gamma_i G_{ii} &= G_{ii}\langle i|\hat{T}\hat{G}\hat{T}|i\rangle - \langle i|\hat{T}\hat{G}|i\rangle\langle i|\hat{G}\hat{T}|i\rangle \\
&= G_{ii}\langle i|(\hat{\xi} - \hat{G}^{-1})\hat{G}\hat{T}|i\rangle - \langle i|(\hat{\xi} - \hat{G}^{-1})\hat{G}|i\rangle\langle i|\hat{G}(\hat{\xi} - \hat{G}^{-1})|i\rangle \\
&= G_{ii}\langle i|\hat{\xi}\hat{G}(\hat{\xi} - \hat{G}^{-1})|i\rangle - \left(\langle i|\hat{\xi}\hat{G}|i\rangle - 1\right)\left(\langle i|\hat{G}\hat{\xi}|i\rangle - 1\right) \\
&= G_{ii}^2\xi_i^2 - G_{ii}\xi_i - (G_{ii}^2\xi_i^2 - 2G_{ii}\xi_i + 1) \\
&= G_{ii}\xi_i - 1.
\end{aligned} \tag{1.72}$$

---

[5]Here, to be precise, $|j\rangle$ labels a single particle state, describing a particle in the Wannier state $|w_j\rangle$.

This equation can be rearranged and, after reintroducing spin and Matsubara frequency, relates the hybridization function of the impurity to the lattice self-energy and Green's function. Explicitly, we find

$$G_{ii\sigma}(i\omega_n) = \frac{1}{i\omega_n + \mu - \epsilon_i - \Gamma_{i\sigma}(i\omega_n) - \Sigma_{i\sigma}(i\omega_n)}, \tag{1.73}$$

which relates the diagonal parts of lattice Green's function $G_{ii\sigma}$ and lattice self-energy $\Sigma_{ii\sigma}$ to the Weiss functions $\mathcal{G}_{i\sigma}(i\omega_n) = i\omega_n + \mu - \epsilon_i - \Gamma_{i\sigma}(i\omega_n)$ via

$$G_{ii\sigma}^{-1}(i\omega_n) = \mathcal{G}_{i\sigma}^{-1}(i\omega_n) - \Sigma_{i\sigma}(i\omega_n). \tag{1.74}$$

With this last equation, we again found a set of closed equations which describe an ihomogenous interacting lattice system in the limit of large dimensions. The short interpretation of RDMFT is as follows, the equations (1.74) and (1.66) describe a set of L independent, interacting impurities, corresponding to L lattice sites, which are then related to each other by the lattice Dyson equation (1.64) and the approximation of a purely but spatial dependent local self-energy.

At last, we now summarize the numerical procedure to obtain a self-consistent solution of the above equations. Given a set of parameters $\{\mu, \epsilon_i, t_{ij}, U\}$, one follows the iterative scheme:

- Start from a set of initial hybridization functions $\{\Gamma_{i\sigma}(i\omega_n)\}$ to obtain the set of effective actions $\{S_{\text{eff}}^{(i)}\}$, one for each impurity.

- For every effective action $S_{\text{eff}}^{(i)}$, calculate the interacting Green's function $G_{ii\sigma}(i\omega_n)$ by solving the impurity problem (see chapter AIM).

- Obtain the local self-energies, by applying the impurity Dyson equation (1.74) at each site and subsequently insert these into the lattice Dyson equation (1.64).

- Invert the lattice Dyson equation to obtain new local Green's functions $G_{ii\sigma}(i\omega_n)$.

- Finally, determine a new set of hybridization functions $\Gamma_{i\sigma}(i\omega_n)$ by applying using Eq.(1.73) and start again with the first point.

This procedure then is repeated until convergence of the hybridization functions (or self-energies) is reached. During the iteration, the computationally demanding steps are the inversion of the lattice Dyson equation, scaling with $\mathcal{O}(L^3)$, where L is the number of lattice sites and to calculate the local Green's functions as the solutions of the impurity problem. If a good spectral resolution of the Green's functions is required, solving the impurity problem using approximation schemes (which are already quite computationally demanding) is not sufficient and we have to use exact methods, as for instance Numerical Renormalization group or Quantum Monte-Carlo methods, see chapter AIM.

In the following chapters, we will extensively use RDMFT to obtain the self-energies, as well as the spectral functions of interacting Fermions subjected to artificial gauge fields, that turn the hopping parameters complex and spatially dependent and investigate both the infinitely extended as well as finite, trapped systems. Originally, RDMFT was introduced to solve the disordered lattice problem with interactions, as done by Dobrosavljevic *et al.* [40, 135], as well as by Semmler *et al.* [163, 164, **?**], to improve the understanding of Anderson localization with interactions compared to simplified, effective theories. More recently, it has been succesfully used in the context of trapped lattice systems, since the actual experiments with ultracold atoms in optical lattices naturally bring along a trapping potential, strongly influencing the small systems at hand [147, 166, 59, 84].

2. Monte-Carlo Methods in a Nutshell

Monte-Carlo is a generic name for a huge class of computational methods, which are widely used not only in natural sciences but also extensively in other fields like for instance economy. Because of this and, of course, due to its great success in simulating computationally difficult dynamical processes, Monte-Carlo methods are the most well-known computational methods in modern times.

Although Monte-Carlo methods in general are well-known, few are intimate with the concept and working principle behind the method. This might be caused by the fact that today's Monte-Carlo methods are strongly optimized to capture the hardest problems with the least computational effort and may not be understandable for non-specialists. However, as we will see in the following sections, the idea of Monte-Carlo methods (referred to as MC) is very simple and the straight-forward implementation of a Quantum Monte-Carlo (QMC) algorithm (without care for maximizing performance) is not too difficult.

2.1 Monte-Carlo Method Integration

As an introduction to MC, we start with the idea of Monte-Carlo integration. Suppose one simply wants to numerically compute the integral

$$I_n(f) = \int_\Omega dx^n f(x) \tag{2.1}$$

of the function $f : \Omega \to \mathbb{R}$, with $\Omega \subset \mathbb{R}^n$ being a n-dimensional area. Using the standard Simson quadrature procedure the numerical error Δ_ϵ scales with the number of points N, on which the function is explicitly evaluated, with the order of $\mathcal{O}\left(N^{-\frac{4}{n}}\right)$. In contrast, if one picks the N points $\{x_i \in \Omega | i = 1, ..., N\}$ randomly but uniformly distributed and then evaluates the sum

$$J(f, N) = \frac{1}{N} \sum_{i=1}^{N} f(x_i) = \langle f \rangle_u \,, \tag{2.2}$$

where $\langle f \rangle_u$ indicates sampling of f with respect to a uniform distribution, the error is always only of statistical nature and therefore

$$|J(f, N) - I_n(f)| = \mathcal{O}\left(N^{-\frac{1}{2}}\right) \tag{2.3}$$

is completely independent of n. This procedure is called **statistical sampling** of the function f and will converge to the desired integral simply because of the law of large numbers. The scaling of the statistical error is explained in detail in section 2.1.1, however for the moment take (2.3) as a given property of the

method. What can we deduce from this simple example?

From the above equations, we see that, from a scaling point of view, performing statistical sampling of f gives a much better error than Simpson quadrature of f, as soon as the dimensionality of the problem n is larger than 8. However, concluding from this result that statistical sampling is always better than Simpson quadrature would be a dangerous fallacy since the scaling of the error does not tell anything of the error itself. All we know is that for N sufficiently large, the error of both methods is given by

$$\Delta_{\text{Simpson}}(N) = \Delta_{0,\text{Simpson}} N^{-\frac{n}{4}} \quad \text{and} \quad \Delta_{\text{Sampling}}(N) = \Delta_{0,\text{Sampling}} N^{-\frac{1}{2}}, \tag{2.4}$$

with the two unknown prefactors $\Delta_{0,\text{Simpson}}$ and $\Delta_{0,\text{Sampling}}$. Although the scaling of the statistical sampling is very favorable, one expects $\Delta_{0,\text{Simpson}} << \Delta_{0,\text{Sampling}}$ because the structure of f enters the Simpson quadrature but not the statistical sampling procedure. Hence a very large number N of points may be needed in statistical sampling for reasonable accuracy and this number might be much larger than that is needed for a sufficiently small error within Simpson quadrature and therefore statistical sampling is not a priori superior to Simpson.

Although $\Delta_{0,\text{Sampling}}$ is unknown, we can seek to improve it without changing the scaling of the error, by using importance sampling rather than statistical sampling, which takes the structure of f into account for the sampling process. To understand the concept of importance sampling, we illustrate it by a simple example. Suppose the function f is non-zero only on a small part of Ω, then the statistical sampling procedure will pick many points $x \in \Omega$ with $f(x) = 0$ and therefore will waste lots of steps by choosing zeros. The best method here would be to only pick those points x with $f(x) \neq 0$, again randomly but with certain probabilities, which are suitable for the function f. The idea of importance sampling is then to focus the sampling procedure on regions in Ω, where f shows its main features and with this procedure decrease the prefactor of the error $\Delta_{0,\text{Sampling}}$. Formally, we can express this idea by rewriting the integral (2.1) into

$$I_n(f) = \int dx^n f(x) = \int dx^n p(x) \frac{f(x)}{p(x)}, \tag{2.5}$$

which is formally exact. If $p(x)$ is a probability density, i.e. $p(x) \leq 0$, $\forall x \in \Omega$ and $\int_\Omega dx^n p(x) = 1$, we can modulate the sampling procedure by picking N points $x_i \in \Omega$ with the probability $p(x_i)dx$ and then compute the sum

$$J(f, N) = \frac{1}{N} \sum_{i=1}^{N} \frac{f(x_i)}{p(x_i)} = \left\langle \frac{f}{p} \right\rangle_p, \tag{2.6}$$

where $\langle F \rangle_p$ indicates the sampling of F with respect to the probability density p. The scaling of the error of the sampling methods will not be influenced by this change of the method since it results from the sampling of independent stochastic variables which is the case for both statistical sampling and importance sampling. On the other hand, one now expects a much smaller prefactor of the error than for the bare statistical sampling. The challenge of the importance sampling is now to chose the best probability density p since it should both mimic the important details of f to lower the prefactor in the error but, of course, it must also be easy to handle in a computational simulation. For instance one could chose

$$p(x) = f(x) \left(\int dx^n f(x) \right)^{-1}, \tag{2.7}$$

which would mimic $f(x)$ perfectly, but in order to find this density p, one must have already solved the full problem already.

We now generalize the idea of importance sampling to a larger class of integrals. For this, we consider the functions $w, f : \Omega \to \mathbb{R}$, having identical support (i.e. they are non-zero on the same closed subset $\tilde{\Omega} \subset \Omega$, which we refer to in the following as Ω), where Ω is now an abstract set, for instance composed of continuous and also discrete, bounded and also unbounded variables that we call configurations $\mathcal{C} \in \Omega$. As an example, relevant to the calculations in this thesis, this set could be given as $\{(n, s, \tau_1, ..., \tau_n) | n \in \mathbb{N}_0, s = \pm 1, \tau_i \in [0, \beta]\}$, which is a mixture of all the above mentioned cases. For this set, we can define a measure (in the strict mathematical sense) $\mu_{\mathcal{C}}$, which usually coincides with the generalized Lebesgue measure (however in some cases one has to use the Haar measure), such that integrals like

$$\int_\Omega d\mu_{\mathcal{C}} \, w_{\mathcal{C}} \tag{2.8}$$

are well defined and the limit theorems from Lebesgue measure theory apply[1]. The explicit measure will never be important throughout this thesis and we will shorten the integral expression by setting $d\mathcal{C} \equiv d\mu_{\mathcal{C}}$. For the above example of our configuration space Ω, we can write down the integral as

$$\int_{\Omega} d\mathcal{C} = \sum_{n=0}^{\infty} \sum_{s=\pm 1} \prod_{l=1}^{n} \int_{0}^{\beta} d\tau_l. \tag{2.9}$$

Now, the integrals that we are interested are of the form

$$I(w, f) = \frac{\int_{\Omega} d\mathcal{C} f_{\mathcal{C}}}{\int_{\Omega} d\mathcal{C} w_{\mathcal{C}}} = \frac{\int_{\Omega} d\mathcal{C} w_{\mathcal{C}} g_{\mathcal{C}}}{\int_{\Omega} d\mathcal{C} w_{\mathcal{C}}}, \tag{2.10}$$

where we have defined[2] $g_{\mathcal{C}} = \frac{f_{\mathcal{C}}}{w_{\mathcal{C}}}$. The mapping $w_{\mathcal{C}}$ is called the weight function, such that the value of $w_{\mathcal{C}}$ for a certain configuration $\mathcal{C}$ is the respective configuration's weight. Assuming $w_{\mathcal{C}} \geq 0$, $\forall \mathcal{C}$, we can define the probability of a configuration $p_{\mathcal{C}}$ through

$$p_{\mathcal{C}} = \frac{w_{\mathcal{C}}}{\int_{\Omega} d\mathcal{C} \, w_{\mathcal{C}}}. \tag{2.11}$$

The integral $I(w, f)$ can then be solved by importance sampling of g with respect to p, where g is a function of (f, w) and p is a function of w, as defined above, i.e. the sum

$$J(w, f, N) = \frac{1}{N} \sum_{i=1}^{N} g_{\mathcal{C}_i} =: \langle f \rangle_w^{\text{MC}} \tag{2.12}$$

converges to the integral in the limit of $N \to \infty$. In (2.12), we have introduced a new notation. The expression $\langle f \rangle_w^{\text{MC}}$, is shorthand for the sampling of the function f with respect to the **weight function** w, as we have introduced it in the above formalism.

The generalization introduced in the latter paragraph does, on the first view, not seem to simplify the problem of integration of f and even more it is unclear if one can call this importance sampling. The weight function w at this point is arbitrary and a bad choice of w will make the sampling process even worse compared to statistical sampling. However, problems of the form (2.10) are standard problems that appear in statistical physics and the weights $w_{\mathcal{C}}$ are the weights of certain physical configurations $\mathcal{C}$. In other words $w_{\mathcal{C}}$ indicates if a certain configuration plays an important role in the integral or not. Therefore, with the regard on following applications on physical problems, we call also call this importance sampling.

Now, there exist two possibilities:

- If the integral $\int d\mathcal{C} \, w_{\mathcal{C}}$ is known (or can be computed exactly), then one can directly calculate the probabilities $p_{\mathcal{C}}$ and start with the importance sampling of f (this will never be the case in this thesis).

- The integral $\int d\mathcal{C} \, w_{\mathcal{C}}$ can not be computed exactly (small errors may already strongly influence the sampling of f), so one needs to use further tools from stochastics and introduce Markov-Chain Monte-Carlo sampling, as we show in the following chapter.

In this section, we have introduced statistical and importance sampling, which are both direct sampling methods, to evaluate complicated integrals in arbitrary dimensional spaces. We have argued that sampling procedures have a better scaling behavior with the number of step points for large dimensions than Simpson quadrature (and also all other numerical integration procedures). In the next section, we will introduce a little bit of statistical data analysis, to understand the error of the sampling procedure, which is of statistical nature. In the next chapter, we will then introduce Markov-Chain Monte-Carlo (MCMC), which can be applied to a more general set of problems, where the integral over the weight functions does not have to be computed.

---

[1] Our intention here is not to fully cover the mathematical subtleties of stochastic analysis but to introduce a mathematical exact formulation of the problem such that a rigorous mathematical treatment can be applied without any obstacles.

[2] This is well-defined since both functions have the same support.

2.1.1 Statistical Data Analysis for Direct Sampling Procedures

In the previous section, we have introduce direct sampling procedures as a tool to numerically compute complicated integrals on arbitrary dimensional spaces. In this small section, we will briefly discuss the error estimation within sampling procedures, which are of statistical nature and therefore not only numerically but also fundamentally different from errors that come from analytical approximations. Again, we formulate the problem in a general space, denoted by Ω with configurations $\mathcal{C} \in \Omega$. On this space, we consider a probability density $p : \Omega \to \mathbb{R}^+$, with values $p_\mathcal{C}$ and the normalization

$$\int_\Omega d\mathcal{C} \, p_\mathcal{C} = 1. \tag{2.13}$$

Additionally, we consider a mapping (which we will assume is a function) $f : \Omega \to \mathbb{R}$ without any further features. The mean and variance of f with respect to the probability density p are defined as

$$\langle f \rangle_p = \int_\Omega d\mathcal{C} \, p_\mathcal{C} f_\mathcal{C}, \quad \text{(mean)}, \tag{2.14}$$

$$\mathrm{Var}(f) = \langle (f - \langle f \rangle_p)^2 \rangle = \int_\Omega d\mathcal{C} \, p_\mathcal{C} (f_\mathcal{C} - \langle f \rangle_p)^2 = \langle f^2 \rangle_p - \langle f \rangle_p^2, \quad \text{(variance)}. \tag{2.15}$$

From now on we will skip the index p and the integration space Ω. As a direct consequence of these definitions, we can derive the fundamental relations for mean and variance

$$\langle af + b \rangle = a \langle f \rangle + b \quad \text{and} \quad \mathrm{Var}(af + b) = a^2 \, \mathrm{Var}(f), \tag{2.16}$$

for any real parameters a, b.

An important concept in the context of stochastics and Monte-Carlo methods is the concept of independent random variables. In our case, f is a random variable, which we can shortly define as: f takes values $\xi \in \mathbb{R}$ with probability $p(\xi)$ [3]. Consider now another random variable g which is a mapping $g : \Omega' \to \mathbb{R}$, where Ω' may differ from Ω. The elements $\mathcal{C}' \in \Omega'$ are also called configurations and have a certain probability density $p'_{\mathcal{C}'}$. Then, g and f are called independent random variables if and only if

$$P(f = \xi, g = \chi) = P(f = \xi) \cdot P(g = \chi) = p(\xi) \cdot p'(\chi), \tag{2.17}$$

where $P(f = \xi, g = \chi)$ is the probability that f takes the value ξ and at the same time g takes the value χ. In other words, for a certain realization of configurations, if we know the value of g, we have absolutely no information on the value of f and the other way round.

For independent variables f, g, the variance of their sum $\mathrm{Var}(f + g)$ is simply the sum of their variances $\mathrm{Var}(f) + \mathrm{Var}(g)$, since

$$\mathrm{Var}(f+g) = \langle (f+g)^2 \rangle - \langle (f+g) \rangle^2 = \langle (f^2 + 2fg + g^2) \rangle - \langle f \rangle^2 - 2\langle f \rangle \langle g \rangle - \langle g \rangle^2 = \langle f^2 \rangle - \langle f \rangle^2 + \langle g^2 \rangle - \langle g \rangle^2. \tag{2.18}$$

In the second step, we made use of the fact that the expectation value is linear in its components and in the third step, we identified $\langle fg \rangle$ with $\langle f \rangle \langle g \rangle$, which is the case for independent variables.

We now define the random variable F_N which is the sum

$$F_N = \frac{1}{N} \sum_{i=1}^{N} f_i \tag{2.19}$$

of N pairwise independent random variables f_i, but with the same probability density. To bring this into our picture from the previous section, there now exist N identical copies Ω_i with possible configurations $\mathcal{C}_i$ and the f_i are functions $f_i : \Omega_i \to \mathbb{R}$, whereas the configurations $\mathcal{C}_i, \mathcal{C}_j$ are completely independent for $i \neq j$. On the other hand, if (by chance) $\mathcal{C}_i = \mathcal{C}_j$ for any realization, then $f_{i,\mathcal{C}_i} = f_{j,\mathcal{C}_j}$. This directly leads to the two following, very important results

$$\langle F_N \rangle = \frac{1}{N} \langle \sum_{i=1}^{N} f_i \rangle = \frac{\sum_{i=1}^{N} \langle f_i \rangle}{N} = \langle f_i \rangle, \tag{2.20}$$

---

[3] Please note that f has not necessarily to be injective for this definition. There will always exist a well-defined subspace $\Omega_\xi \subset \Omega$ with $f(\Omega_\xi) = \{\xi\}$. Then we define $p(\xi) = \int_{\Omega_\xi} d\mathcal{C} \, p_\mathcal{C}$.

$$\text{Var}(F_N) = \text{Var}(\frac{1}{N} \sum_{i=1}^{N} f_i) = \frac{1}{N^2} \sum_{i=1}^{N} \text{Var}(f_i) = \frac{\text{Var}(f_i)}{N}. \tag{2.21}$$

Here, we made use of the fact that the f_i are independent and identically distributed. On the right side of the two equations it is therefore not important which of the N f_i is inserted in the mean or variance. The random variable F_N has favorable properties, its expectation value is independent of N and equals the expectation values $\langle f_i \rangle$, where the f_i are by definition identical copies of f and therefore the expectation value of F_N is the desired integral of f over the complete space Ω, with probability density p. On the other hand, the variance of F_N decreases with $1/N$, which make F_N sharply peaked around its expectation value, in contrast to f itself, which may be of arbitrary structure. The question is now, how to realize F_N. Fortunately, this question has already been answered if one takes a look at the definition of $J(f, N)$ in the previous section (2.6). As one directly realizes, $J(f, N)$ is identical to F_N and a given realization of $J(f, N)$ is therefore nothing else but a given realization of F_N.

In the last paragraph, we have derived that the variance of $J(f, N)$, as we were using it in the previous chapter, is simply given by

$$\text{Var}(J(f, N)) = \frac{\text{Var}(f)}{N}. \tag{2.22}$$

Now, we have to understand how this is related to the error of $J(f, N)$ at the end of a numerical simulation and how this error has to be understood. For this, we take a look at Chebyshev's inequality, for an arbitrary random variable x with probability density p

$$\text{Var}(x) = \int_\Omega (x - \langle x \rangle)^2 p(x) \, dx \geq \int_{|x - \langle x \rangle| \geq \epsilon} (x - \langle x \rangle)^2 p(x) \, dx \geq \epsilon^2 \int_{|x - \langle x \rangle| \geq \epsilon} p(x) \, dx. \tag{2.23}$$

In this equation, the last integral is nothing but the probability $p(|x - \langle x \rangle| \geq \epsilon)$. Since this result is general, we can do the same for $J(f, N)$ to find

$$\left\{ \begin{array}{c} \text{probability that} \\ |J(f, N) - \langle f \rangle| > \epsilon \end{array} \right\} > 1 - \frac{\text{Var}(f)}{N}. \tag{2.24}$$

In contrast to non-statistical methods, where the error results from approximations and can be made in principle arbitrary small, the error here is of probabilistic nature and can, by coincidence, be arbitrarily large for a particular realization of random variables, this is just very unlikely. The nice result of (2.24) is that one is even able to tune the probabilities by hand, just by changing the number of steps N in the sampling procedure. Nevertheless, it has to be pointed out that the error that we are talking about is a probabilistic one and therefore always must be handled with care. For instance, relying results on a single simulation, although deviations from a small region around the expectation value may be very unlikely, is absolutely dangerous and gives absolutely no control of the error or the result.

One may ask now, so what is the error of direct sampling procedure? As mentioned above, since we are dealing with probabilities there is no direct answer to this question. However, it is established that one can take the standard deviation of the sampling procedure $\sigma(J(f, N))$ which is the square root of the variance

$$\sigma(J(f, N)) = \sqrt{\text{Var}(J(f, N))} = \frac{\sigma(f)}{\sqrt{N}} \tag{2.25}$$

as a measure for the error in terms of probabilities. With a probability of around 68% the result of a numerical sampling will be in the interval $[\langle f \rangle - \sigma, \langle f \rangle + \sigma]$ and with a probability of around 95% the result will be in the interval $[\langle f \rangle - 2\sigma, \langle f \rangle + 2\sigma]$, which is a result from the central limit theorem, that we will not derive in this thesis but is explained in many books on stochastics and is also known from the basic experimental courses on data analysis. Therefore the error (or what we conveniently call the error) is proportional to $\frac{\sigma(f)}{\sqrt{N}}$, which shows us the scaling with N, as we have used it in the previous section and also explains the advantage of importance sampling. The factor $\sigma(f)$ strongly depends on the probability distribution with which the sampling is performed and changing this distribution may change the standard deviation σ by many orders of magnitude [4].

---

[4] An important factor at this point is the size and geometry of Ω. For instance, if Ω is very large, i.e. $\int_\Omega d\mathcal{C} >> 1$ the change of σ will be significant.

In this section, we have derived an expression for the statistical error in a direct sampling process, as previously introduced, which can only be expressed in terms of probabilities. The most convenient and established "error" is the standard deviation σ which can be made arbitrarily small by increasing the number of points N and is a measure of the expected deviation from the mean value of a sampling process. We also have shown, by Chebyshev's inequality, that in the limit of infinite steps N, the sampling recovers exactly the desired integral over f, which to compute was the aim of the current chapter.

2.2   Markov-Chain Monte-Carlo

The direct sampling procedures presented in the last chapter are very easy to understand both from a demonstrative point of view but also from the mathematical side, as one may remember the only necessary ingredients were the weak law of large numbers, the central limit theorem and the Chebyshev inequality. The latter was proven in (2.23) while the weak law of large numbers and the central limit theorem are **the** common theorems from stochastics that every physics student is aware of since his or her undergraduate lectures on data analysis. However, to understand non-direct sampling processes, a little more of stochastics is necessary, which is presented on a minimal level in the next section. Subsequently, we will be able to understand Markov-Chain Monte Carlo processes and the necessary conditions for a successful implementation of these powerful sampling procedures.

2.2.1   Markov-Chains

In this section, we will give a brief introduction to Markov-Chains and the possibility to determine an unknown and complex probability distribution from a running Markov-Chain. For that, in the contrast to the previous section, we will restrict ourselves to a configuration space Ω which is countable (although it may be infinite). This is not a serious restriction, since if Ω was consisting of a subset of continuous variables, we just take a fine grid on this subset such that we end up with a countable number of grid-points to be considered, such that resulting set is countable. Since we can make the grid arbitrarily small, we can find a choice of the grid which does not affect the integrals that we are interested in, i.e. those given by (2.10).

In the following, Ω is countable and $X := (X_n)_{n\in\mathbb{N}}$ is a stochastic process in the space of configurations Ω, i.e. $\forall n$, X_n takes values $\mathcal{C}_n \in \Omega$, whereas the probability $P(X_n = \mathcal{C}_n) = P(X_n = \mathcal{C}_n|(X_0,...X_{n-1}) = (\mathcal{C}_0,...,\mathcal{C}_{n-1}))$ of this event also depends on the values that $X_i, i = 0,...n-1$ has taken in Ω.

Definition 2.1 *(Markov-Chain)*
$X = (X_n)_{n\in\mathbb{N}}$ is called Markov-Chain, if the Markov-condition is fulfilled, i.e.

$$P(X_n = C_n|(X_0,...,X_{n-1}) = (\mathcal{C}_0,...,\mathcal{C}_{n-1})) = P(X_n = C_n|X_{n-1} = \mathcal{C}_{n-1})$$

for all $n \geq 1$ and $\mathcal{C}_0,...,\mathcal{C}_n \in \Omega$ with $P((X_0,...,X_{n-1}) = (\mathcal{C}_0,...,\mathcal{C}_{n-1})) > 0$.

In other words, the stochastic process $X = (X_n)_{n\in\mathbb{N}}$ in every step n only depends on the previous step $n-1$ and does not directly depend on the steps before.

Definition 2.2 *A Markov-Chain $X = (X_n)_{n\in\mathbb{N}}$ is called homogeneous, if*

$$P(X_{n+1} = \mathcal{C}|X_n = \tilde{\mathcal{C}}) = P(X_1 = \mathcal{C}|X_0 = \tilde{\mathcal{C}}) \ \ \forall n \geq 1, \ \mathcal{C}, \tilde{\mathcal{C}} \in \Omega.$$

The **transition matrix** *$P = (p_{\mathcal{C}\tilde{\mathcal{C}}})_{\mathcal{C}\tilde{\mathcal{C}}\in\Omega}$ is the $||\Omega|| \times ||\Omega||$-matrix of the* **transition probabilities**

$$p_{\mathcal{C}\tilde{\mathcal{C}}} = P(X_1 = \mathcal{C}|X_0 = \tilde{\mathcal{C}}).$$

I.e. a Markov-Chain is homogeneous, if the transition probabilities are the same for every step n and do not change as X proceeds.

Remark (Properties of the transition matrix)
The transition matrix from the above definition is a stochastic matrix, i.e. has the properties

- $p_{\mathcal{C}\tilde{\mathcal{C}}} \geq 0 \, \forall \, \mathcal{C}, \tilde{\mathcal{C}} \in \Omega$

- $\sum_{\mathcal{C} \in \Omega} p_{\mathcal{C}\tilde{\mathcal{C}}} = 1 \, \forall \, \tilde{\mathcal{C}} \in \Omega$.

The entries are therefore non-negative (since they represent probabilities) and the sum over a complete row equals 1 since in every step n X_n takes a value in Ω, no matter which value it took in the previous step.

With these definitions, it is very simple to find a formal expression for the probability distribution of X_n for a certain $n \in \mathbb{N}$. Suppose the probability distribution for the variable X_{n-1}, i.e. $P(X_{n-1} = \mathcal{C}) =: \mu_{\mathcal{C}}^{(n-1)}$, is known for all $\mathcal{C} \in \Omega$. Then it is straight forward to compute

$$\mu_{\tilde{\mathcal{C}}}^{(n)} = P(X_n = \tilde{\mathcal{C}}) = \sum_{\mathcal{C} \in \Omega} P(X_n = \tilde{\mathcal{C}}|X_{n-1} = \mathcal{C})P(X_{n-1} = \mathcal{C}) = p_{\tilde{\mathcal{C}}\mathcal{C}}\mu_{\mathcal{C}}^{(n-1)} = (p\mu^{(n-1)})_{\tilde{\mathcal{C}}}. \quad (2.26)$$

Iterative application of (2.26) results in the formal expression for the probability distribution $\mu_{\mathcal{C}}^{(n)}$, which reads

$$\mu_{\mathcal{C}}^{(n)} = (p\mu^{(n-1)})_{\mathcal{C}} = (p^n \mu^{(0)})_{\mathcal{C}}, \quad (2.27)$$

where p^n is the nth power of the transition matrix p and $\mu^{(0)}$ is the initial probability distribution of X_0, which is defined independently of the Markov-Chain.
With these definitions and the properties (2.26), (2.27), we have already found the most general properties of Markov-Chains. From now on, we will only consider homogeneous Markov-Chains and introduce two further fundamental concepts in the framework of Markov-Chains, namely irreducibility and stationarity, which will be fundamental for the successful implementation of Markov-Chain sampling.

Definition 2.3 *(Irreducibility)*

- *Let $\mathcal{C}, \tilde{\mathcal{C}} \in \Omega$ be configurations. The configuration $\tilde{\mathcal{C}} \in \Omega$ **can be reached from** $\mathcal{C} \in \Omega$, if*

$$\exists n \in \mathbb{N}_0, \ such \ that \ (p^n)_{\mathcal{C}\tilde{\mathcal{C}}} > 0.$$

  This is denoted by $\mathcal{C} \rightarrow \tilde{\mathcal{C}}$.

- *$\mathcal{C}$ and $\tilde{\mathcal{C}}$, with $\mathcal{C}, \tilde{\mathcal{C}} \in \Omega$ are said to be communicating, if $\mathcal{C} \rightarrow \tilde{\mathcal{C}}$ and $\tilde{\mathcal{C}} \rightarrow \mathcal{C}$. This is denoted by $\mathcal{C} \leftrightarrow \tilde{\mathcal{C}}$.*

- *A homogeneous Markov-Chain is called irreducible, if $\mathcal{C} \leftrightarrow \tilde{\mathcal{C}}$, $\forall \mathcal{C}, \tilde{\mathcal{C}} \in \Omega$, in other words, if all configurations $\mathcal{C}, \tilde{\mathcal{C}} \in \Omega$ are communicating.*

The last definition is very important for our purpose and therefore we will formulate irreducibility once more in a descriptive definition, which is completely equivalent to Def. (2.3).

Definition 2.4 *(Irreducibility 2)*
A homogeneous Marko-Chain is called irreducible, if for any configuration $\mathcal{C} \in \Omega$ any other configuration $\tilde{\mathcal{C}} \in \Omega$ can be reached with probability larger than zero in a finite number of steps.

In a physics context, the last definition is commonly and mistakenly, referred to as ergodicity, which is however **not** the same as irreducibility. Although in the context of a Markov-Chain sampling they are usually fulfilled at the same time, ergodicity is strictly a requirement on the stationary distribution of a Markov-Chain, while irreducibility is a property of the transition probabilities of a Markov-Chain, as we see from Def. (2.3).

In addition to irreducibility, an important concept that we will now introduce is the concept of a stationary distribution.

Definition 2.5 *(Stationary distribution)*
A probability distribution π on Ω is called **stationary distribution** *with respect to p (the homogeneous Markov-Chain), if*

$$\pi(\mathcal{C}) = \sum_{\tilde{\mathcal{C}} \in \Omega} \pi(\tilde{\mathcal{C}}) p_{\mathcal{C}\tilde{\mathcal{C}}}. \tag{2.28}$$

As we see from (2.28), a stationary distribution, once reached, will never be changed in the subsequent steps of the Markov-Chain, i.e.

$$\exists n \in \mathbb{N}, \text{ with } \mu^n = \pi \Rightarrow \mu^{m+n} = \pi, \ \forall m \in \mathbb{N}.$$

Definition 2.6 *(Reversibility)*
Let π be a probability distribution on Ω. A Markov-Chain is called reversible with respect to π, if

$$\pi(\mathcal{C}) p_{\mathcal{C}\tilde{\mathcal{C}}} = \pi(\tilde{\mathcal{C}}) p_{\tilde{\mathcal{C}}\mathcal{C}}, \ \ \forall \mathcal{C}, \tilde{\mathcal{C}} \in \Omega. \tag{2.29}$$

If a Markov-Chain is reversible with respect to π, then π is a stationary distribution of this Markov-Chain, as we see from summing over both side of the above equality

$$\pi(\mathcal{C}) = \sum_{\tilde{\mathcal{C}} \in \Omega} \pi(\mathcal{C}) p_{\mathcal{C}\tilde{\mathcal{C}}} = \sum_{\tilde{\mathcal{C}} \in \Omega} \pi(\tilde{\mathcal{C}}) p_{\tilde{\mathcal{C}}\mathcal{C}},$$

where in the first equality we have used the properties of a transition matrix p as explained in remark (2.2.1). In order to obtain the fundamental result of this section, the Markov-Chain convergence theorem, we need one last definition.

Definition 2.7 *(Aperiodicity)*
A configuration $\mathcal{C} \in \Omega$ is called **aperiodic**, *if and only if*

$$\exists n \in \mathbb{N}, \ such \ that \ \ \forall m \in \mathbb{N}, \ \ (p^{m+n})_{\mathcal{C}\mathcal{C}} > 0.$$

A Markov-Chain is called aperiodic if all configurations are aperiodic with respect to its transition matrix p.

Until now, we have only introduced concepts from the theory of Markov-Chains and one may ask, what we gain from those. The answer will be given by the following two theorems, that will not be proven in this thesis as their proofs require the understanding of many additional concepts of stochastic processes and stochastic analysis that we do not want to introduce at this point. Instead, we refer the interested reader to mathematical books on stochastic processes, such as [75, 41].

Theorem 2.2.1 *(Uniqueness of the stationary distribution)*
An irreducible Markov-Chain has at most one stationary distribution. If a stationary distribution is found, it is unique.

Theorem 2.2.2 *(Markov-Chain convergence theorem)*
Let $(X_n)_{n \in \mathbb{N}}$ be an irreducible, aperiodic Markov-Chain, with a stationary distribution π. We define $m_{\mathcal{C}}(N) \in \mathbb{N}$ as the number of times the Markov-Chain has passed the configuration $\mathcal{C} \in \Omega$ after N steps in total. Then, we find

$$\lim_{N \to \infty} \frac{m_{\mathcal{C}}(N)}{N} = \pi(\mathcal{C}). \tag{2.30}$$

This result is independent of the starting distribution $\mu^{(0)}$.

The Markov-Chain convergence theorem is a fundamental theorem of stochastic analysis and the cornerstone for all advanced Monte-Carlo methods that are not based on direct sampling. To understand this we shortly review the concepts we have introduced so far. In section 2.1, we posed the quantity we wish to find, which was given by the integral

$$I(w, f) = \frac{\int_{\Omega} d\mathcal{C} \, f_{\mathcal{C}}}{\int_{\Omega} d\mathcal{C} \, w_{\mathcal{C}}} = \int_{\Omega} d\mathcal{C} \, \pi(\mathcal{C}) g_{\mathcal{C}}, \tag{2.31}$$

where $g_{\mathcal{C}} = f_{\mathcal{C}}/w_{\mathcal{C}}$ and we have replaced $p_{\mathcal{C}} = w_{\mathcal{C}} / \int d\mathcal{C}' w_{\mathcal{C}'}$ by $\pi(\mathcal{C})$. We expect that we have no chance to compute the probabilities $\pi(\mathcal{C})$ sufficiently exact without a gigantic effort in programming and computer power, so we ask what can we do to obtain the correct probabilities? The Markov-Chain convergence theorem tells the answer: build a Markov-Chain, which is as simple as possible but fulfills the requirements of the theorem and which has the probability distribution $\pi(\mathcal{C})$ as its stationary distribution. Then after running this Markov-Chain for a sufficiently large number of steps, we will obtain the probability distribution within arbitrary small error. That is exactly what we are going to do in the following section.

2.2.2 The Metropolis algorithm

The aim of this section is to set up a Markov-chain, which is able, through a very simple sample procedure, to determine the probability distribution $\pi(\mathcal{C})$. The probabilities are formally determined by the expression

$$\pi(\mathcal{C}) = \frac{w_{\mathcal{C}}}{\int_{\Omega} d\mathcal{C}' \, w_{\mathcal{C}'}}, \tag{2.32}$$

where we have access to $w_{\mathcal{C}}$ for any configuration $\mathcal{C} \in \Omega$ but because of its complexity, can not compute the integral in the denominator.

A Markov-Chain is determined by its starting distribution $\mu^{(0)}$, which was unimportant for the convergence theorem and its transition matrix p. To successfully obtain the probability distribution π after a Markov-Chain sampling, we have to ensure that π is the stationary distribution with respect to p, and that the Markov-Chain (and therefore p) is irreducible and aperiodic. Aperiodicity can usually be fulfilled easily by setting up a Markov-Chain, which has the property $p_{\mathcal{C}\mathcal{C}} > 0$, i.e. a non-zero probability to stay in a certain configuration. This already ensures aperiodicity of p as one realizes immediately from its definition (2.7).

To ensure that the Markov-Chain has the correct stationary distribution, we use the Metropolis procedure, invented by N. Metropolis et al in their famous 1953 paper [132]. This algorithm uses the fact that a reversible (see Def. (2.6)) Markov-Chain with respect to the probability distribution π, has the same probability distribution as its unique stationary distribution. Since the probabilities are formally known to us, we insert them into (2.29) to get

$$\frac{w_{\mathcal{C}}}{\int_{\Omega} d\mathcal{C}' \, w_{\mathcal{C}'}} p_{\mathcal{C}\tilde{\mathcal{C}}} = \frac{w_{\tilde{\mathcal{C}}}}{\int_{\Omega} d\mathcal{C}' \, w_{\mathcal{C}'}} p_{\tilde{\mathcal{C}}\mathcal{C}} \tag{2.33}$$

or by bringing both transition probabilities on the same side of the equation, we end up with

$$\frac{p_{\tilde{\mathcal{C}}\mathcal{C}}}{p_{\mathcal{C}\tilde{\mathcal{C}}}} = \frac{w_{\mathcal{C}}}{w_{\tilde{\mathcal{C}}}} \quad \text{(Detailed Balance)}. \tag{2.34}$$

This last equation is the celebrated detailed balance condition, which is the simplest but also most powerful procedure to obtain correct transition probabilities $p_{\tilde{\mathcal{C}}\mathcal{C}}$, with the stationary distribution $\pi\mathcal{C} = w_{\mathcal{C}} / \int_{\Omega} d\mathcal{C}' \, w_{\mathcal{C}'}$. Although the space Ω may be very huge, the detailed balance condition can be fulfilled very simply because it connects only the two states $\mathcal{C}$ and $\tilde{\mathcal{C}}$, making no additional restriction on the residual transition probabilities or configurations.

To set up the Metropolis procedure (remember that we have to implement this as a numerical procedure), we use the idea of acceptance-rejection sampling. The transition probabilities are decomposed in a product of two probabilities, namely the proposal and acceptance probability, i.e. $p_{\mathcal{C}\tilde{\mathcal{C}}} = p_{\mathcal{C}\tilde{\mathcal{C}}}^{\text{acc}} p_{\mathcal{C}\tilde{\mathcal{C}}}^{\text{prop}}$. The proposal probabilities can be assigned arbitrary with the only restriction that they must behave as probabilities, i.e.

$$0 \leq p_{\mathcal{C}\tilde{\mathcal{C}}}^{\text{prop}} \leq 1 \quad \text{and} \quad \sum_{\mathcal{C} \in \Omega} p_{\mathcal{C}\tilde{\mathcal{C}}}^{\text{prop}} = 1, \ \forall \mathcal{C}, \tilde{\mathcal{C}} \in \Omega. \tag{2.35}$$

To illustrate the concept of proposal and acceptance probabilities, suppose we are at a certain step of the Markov-Chain in the configuration $\tilde{\mathcal{C}}$, that we now propose a new configuration $\mathcal{C}$ for the next step and the probability of this proposal is given by the proposal probability $p_{\mathcal{C}\tilde{\mathcal{C}}}^{\text{prop}}$. As an example, let us consider an infinitely extended grid, with every grid-point having 4 neighboring grid-points and the grid-points represent possible configurations. In a particular step of the Markov-Chain, we sit on a certain grid-point, which we call $\tilde{\mathcal{C}}$. For the next step of the Markov-Chain, we have to propose a possible configuration $\mathcal{C}$, which we do by allowing only the neighboring grid-points to be reached in a single step of the Markov-Chain but all with the same probability $1/4$. I.e. we simply pick any neighboring point of $\tilde{\mathcal{C}}$ and call this the configuration $\mathcal{C}$. This proposal has nothing to do with the actual probabilities of the configurations, it may even be that some of these neighboring grid-points $\mathcal{C}$ have the actual probability $\pi(\mathcal{C}) = 0$ but this is irrelevant in the proposal of these configurations.

After the proposal of a new configuration for the next step, this configuration can be accepted, with probability $p_{\mathcal{C}\tilde{\mathcal{C}}}^{\text{acc}}$ or can be rejected with probability $1 - p_{\mathcal{C}\tilde{\mathcal{C}}}^{\text{acc}}$. If it is accepted, $\mathcal{C}$ becomes the configuration for the next step in the Markov-Chain. On the other hand, if it is rejected, the old configuration $\tilde{\mathcal{C}}$ stays as the configuration for the next step in the Markov-Chain.

To bring these proposal and acceptance probabilities into the detailed balance equation, we just rewrite (2.34) with these newly introduced probabilities, which then reads

$$\frac{p_{\tilde{\mathcal{C}}\mathcal{C}}^{\text{acc}} p_{\tilde{\mathcal{C}}\mathcal{C}}^{\text{prop}}}{p_{\mathcal{C}\tilde{\mathcal{C}}}^{\text{acc}} p_{\mathcal{C}\tilde{\mathcal{C}}}^{\text{prop}}} = \frac{w_{\mathcal{C}}}{w_{\tilde{\mathcal{C}}}} \Leftrightarrow \frac{p_{\tilde{\mathcal{C}}\mathcal{C}}^{\text{acc}}}{p_{\mathcal{C}\tilde{\mathcal{C}}}^{\text{acc}}} = \frac{w_{\mathcal{C}} p_{\mathcal{C}\tilde{\mathcal{C}}}^{\text{prop}}}{w_{\tilde{\mathcal{C}}} p_{\tilde{\mathcal{C}}\mathcal{C}}^{\text{prop}}}. \tag{2.36}$$

The right side of the right equation is fixed from "outside", both by the weights $w_{\mathcal{C}}, w_{\tilde{\mathcal{C}}}$, which are determined by the problem itself, and by the proposal probabilities $p_{\tilde{\mathcal{C}}\mathcal{C}}^{\text{prop}}, p_{\mathcal{C}\tilde{\mathcal{C}}}^{\text{prop}}$, that we have introduced (and consider for the moment, to be arbitrary).

The Metropolis procedure (or Metropolis algorithm) now proposes the following:

- Suppose the Markov-Chain is in the nth step in configuration $\tilde{\mathcal{C}}$, now pick a new configuration $\mathcal{C}$ from the set of allowed configurations (this set of course depends on $\tilde{\mathcal{C}}$) with probability $p_{\mathcal{C}\tilde{\mathcal{C}}}^{\text{prop}}$.

- This configuration is accepted with the Metropolis probability

$$p_{\mathcal{C}\tilde{\mathcal{C}}}^{\text{acc}} = \min \left\{ 1, \frac{w_{\mathcal{C}} p_{\mathcal{C}\tilde{\mathcal{C}}}^{\text{prop}}}{w_{\tilde{\mathcal{C}}} p_{\tilde{\mathcal{C}}\mathcal{C}}^{\text{prop}}} \right\}. \tag{2.37}$$

- The configuration $\mathcal{C}$ is either accepted, then it is the configuration of the $(n+1)$th step or rejected, then the old configuration $\tilde{\mathcal{C}}$ stays and also becomes the configuration of the $(n+1)$th step.

Using this algorithm, we have already ensured, that $\pi\mathcal{C} = w_{\mathcal{C}} / \int d\mathcal{C}' w_{\mathcal{C}'}$ is the stationary distribution of this Markov-Chain. At this point, it is important to realize that the stationary distribution of the Markov-Chain does, in no way, depend on how complicated (or simple) we chose for the proposal probabilities p^{prop}. As soon as the acceptance probabilities are chosen according to equation (2.37), the stationary distribution of the Markov-Chain stays invariant under the change of the proposal probabilities. This

important fact gives us the freedom to chose the proposal probabilities such that the last condition of the Markov-Chain convergence theorem is fulfilled, which is the irreducibility condition, as defined in Def. (2.3). The irreducibility condition, can on a formal level, be fulfilled by choosing a Markov-Chain that makes π ergodic, which is defined as

Definition 2.8 *(Ergodicity)*
A stationary distribution π of a Markov-Chain is called **ergodic**, *if its support lies in an irreducible component of the Markov-Chain. The* **support** *of a probability distribution π is $supp(\pi) := \{\mathcal{C} \in \Omega | \pi(\mathcal{C}) > 0\}$.*

It is clear, if we had chosen a Markov-Chain such that π is ergodic, then the above choice of the acceptance probabilities would make the Markov-Chain irreducible. In physics, irreducibility is often meant to be equivalent to ergodicity and since we understand that in the context of the Metropolis algorithm both are equivalent, we will from now on always talk about ergodicity. As mentioned before, there is no general recipe to ensure ergodicity in an arbitrary Markov-Chain and therefore this has to be done ad hoc, depending on the distribution π one is interested in. In general, ensuring ergodicity is the most difficult part in setting up a Markov-Chain sampling method because, on the one hand there is no recipe how to actually do that and on the other hand, ergodicity in a mathematical sense is often not sufficient. To illustrate that, we use the following example. Suppose configuration space Ω consists of two distinct irreducible subspaces, i.e. $\Omega = \Omega_1 \cup \Omega_2$ with $\Omega_1 \cap \Omega_2 = \emptyset$ and there exists only a single configuration $\mathcal{C} \in \Omega_1$ from which it is possible to reach Ω_2 during a Markov process. This setup will be ergodic in a mathematical sense, since it will be possible to reach any configuration from any other one in a finite number of steps. In a numerical simulation, if Ω_1 is very large, it will never happen with finite probability, that a Markov-Chain starting in Ω_1 will ever reach a configuration in Ω_2 and therefore the numerical simulation will with finite probability give incredibly wrong results. Of course, this example is an extreme case and no one, familiar with MCMC methods, will set up such a Markov-Chain. It simply illustrates that although a Markov-Chain might look ergodic, it might turn out to be not ergodic "enough" for a numerical simulation. One understands the concept even more clearly, when realizing that the configuration space Ω might be so complex that it is impossible to overview it and the only predictions that one can make are local ones, i.e. on small subsets of Ω which may not even be connected in some manner. Mostly, the only way to verify that a Metropolis algorithm is working, is to perform numerical simulations and test if it is working correctly by benchmarking the results with other analytical and computational methods, which however might only be possible for some limiting cases, where are methods are applicable[5].

Suppose now we have implemented the Metropolis algorithm correctly and have ensured ergodicity. Then the Markov-Chain convergence theorem applies and in a very long Metropolis sampling procedure, we will be able to determine the probability distribution π. But how does this help us to compute the integral

$$I(f, w) = \frac{\int_\Omega d\mathcal{C} \, f_c}{\int_\Omega d\mathcal{C} \, w_c} = \int_\Omega d\mathcal{C} \, \pi(\mathcal{C}) g_\mathcal{C} \tag{2.38}$$

required in this simulation? Of course, it would be possible to apply a direct sampling procedure now, since π is known. But this would be inefficient since we would have to perform a sampling procedure twice and we also would have to store the values of π for every configuration $\mathcal{C}$ in Ω. Also it would be necessary to determine π for every single configuration $\mathcal{C}$ in the Markov-Chain sampling which would take a tremendous amount of computation time.

The idea is to use the Markov-Chain convergence theorem, as we will see. We start with setting up a Markov-Chain as it is described by the Metropolis algorithm. Then we let this Markov- Chain evolve during a numerical sampling procedure but, instead of counting the number of times $m_\mathcal{C}(N)$ every configuration $\mathcal{C} \in \Omega$ has been reached during the sampling, we simply add up the values $g_\mathcal{C}$. For every step n in the Markov-Chain, we know the configuration of this step $\mathcal{C}$, therefore we can compute $g_c = f_\mathcal{C}/w_\mathcal{C}$ and just add this to a variable which we call $J^{(n)}(w, f)$. This means that in every step only two variables have to be determined, first $J^{(n)}(w, f) = J^{(n-1)}(w, f) + g_\mathcal{C}$ and second the step number n (which is just a running integer). After n steps of the Markov-Chain $J^{(n)}(w, f)$ can be expressed as

$$J^{(n)}(w, f) = \sum_{\mathcal{C} \in \Omega} m_\mathcal{C}(n) g_\mathcal{C}. \tag{2.39}$$

---

[5]As for instance exact diagonalization is only applicable to finite systems but not in the thermodynamic limit, whereas a huge class of Monte-Carlo methods is applicable to both finite and infinite systems

In the limit of $n \to \infty$, we can therefore apply the Markov-Chain convergence theorem, which causes the fraction

$$\lim_{n \to \infty} \frac{J^{(n)}(w, f)}{n} = \lim_{n \to \infty} \sum_{\mathcal{C} \in \Omega} \frac{m_{\mathcal{C}}(n)}{n} g_{\mathcal{C}} = \int d\mathcal{C} \, \pi(\mathcal{C}) g_{\mathcal{C}} = I(w, f) \tag{2.40}$$

to converge to the desired integral $I(w, f)$. For a finite number of steps $n < \infty$, we have found an approximate solution for the integral $I(w, f)$ by applying Markov-Chain sampling. The error, however, is again purely statistical in nature and we again can apply error analysis tools, known from stochastics. The main difference here, is that in contrast to direct sampling, the individual steps of the sampling procedure are not independent from each other as it is the case for direct sampling processes. The configuration $\mathcal{C}$ of a certain step n in the Markov-Chain strongly depends on the configuration $\tilde{\mathcal{C}}$ of the previous step $n-1$ and for this reason can not be independent. This means that the error estimation formulas, obtained for the direct sampling have to be modified to cover Markov-Chains. As a conclusion of this section, we present some remarks.

Remarks:

- In the Markov-Chain sampling, all that has to be calculated explicitly are the weights $w_{\mathcal{C}}$ and the functions $f_{\mathcal{C}}$ for certain configurations $\mathcal{C}$ which are passed by the Markov-Chain (the configuration space Ω contains much more points than actually will be passed during a simulation). The computation and subsequent accumulation of $g_{\mathcal{C}}$ shall in the following be called a Monte-Carlo measurement.

- The most difficult part in a Markov-Chain sampling is, as mentioned above, the determination of the proposal probabilities and the possible configurations for the current step to take. This has to be done very carefully and it has to be verified afterwards via simulation if the resulting Markov-Chain is irreducible.

- Often it is computationally demanding to determine the functions $f_{\mathcal{C}}$ (much more than $w_{\mathcal{C}}$), which depends on the physical problem that has to be solved. Since the subsequent steps in the Markov-Chain sampling depend very strongly on each other, not much information is gained by adding $g_{\mathcal{C}}$ in every step and it is often useful to have certain intervals during the sampling process where nothing is summed up and the Markov-Chain just evolves.

- Although the starting configuration of the Markov-Chain $\mu^{(0)}$ was not important for the Markov-Chain convergence theorem, it is clear that it will have an impact on the convergence speed of a Markov-Chain and also on the values of $g_{\mathcal{C}}$ at the very beginning of the sampling process. It is therefore often useful to wait a significant number of steps before starting to accumulate $g_{\mathcal{C}}$. This is often called equilibration of the Markov-Chain.

- The formalism that we used here does not distinguish between classical and quantum mechanical configurations $\mathcal{C}$. In fact, the only difference between classical and quantum Monte-Carlo (QMC) is the fundamental difference in the configuration space but nothing will change in the sampling procedure, as we will see in the next chapter.

- Metropolis sampling is one realization of Markov-Chain sampling, however it is the most well-known and powerful realization. The Metropolis sampling is the basis for all kinds of Monte-Carlo processes, which are mostly either direct implementations of the Metropolis algorithm or extensions with the same basic idea. All the Monte-Carlo processes that are used during this thesis are based on Metropolis sampling, the specific choice of configuration space and the corresponding proposal probabilities is what makes them unique and why they are not simply called Metropolis or Markov-Chain Monte-Carlo.

2.2.3 Statistical Data Analysis for Markov-Chain Sampling Procedures

In the direct sampling procedures, every measurement (i.e. every randomly determined value of $g_{\mathcal{C}}$) was independent from all other measurements, since the bare probabilities were used for the sampling. This

was used in equation (2.18) to express the variance of the sum of the variables in terms of the variance of one single variable. For the Markov-Chain sampling, this is impossible, since the single measurements are not independent from each other. This can again be best understood by the example of a Markov-Chain on a grid. Suppose for every grid-point $\mathcal{C}$, a different value $g_\mathcal{C}$ will be accumulated during the sampling. In a single step of the Markov-Chain, we can move from a certain grid-point to one of its neighbors. This means the measurement of the $(n+1)$th step depends on the nth step because it can only be made on a neighbor of the nth configuration. Therefore, a lot of steps m are necessary in the Markov-Chain, until a configuration $\mathcal{C}$ at step $n+m$ is independent of the configuration $\tilde{\mathcal{C}}$ at step n. This number of steps is usually unknown and in a complicated sampling may also strongly depend on the configurations and vary throughout the sampling procedure, which usually will make it impossible to estimate the number of intermediate, not measured steps m until the next measurement will be independent from the previous one. For the Markov-Chain sampling therefore one has to use slightly more advanced error analysis tools than for the direct sampling, which we will discuss now.

Again, the statistical error of the accumulated variable F_N is expressed through its variance $\text{Var}(F_N)$, where we use the same notation as in the previous data analysis section. F_N is the value accumulated through a Markov-Chain sampling with N measurements during the sample, i.e.

$$F_N = \frac{1}{N} \sum_{i=1}^{N} f_i, \tag{2.41}$$

where the f_i are the individual measurements. Of course, a single sampling procedure to obtain one value F_N takes a lot of time and computer power and therefore repeating this procedure to get a precise variance of F_N is not an option. One has to find error analysis tools, which can be applied on a single run and still give the precise variance of F_N. To do this, we again express the variance of F_N through the single measurements

$$\text{Var}(F_N) = \langle F_N^2 \rangle - \langle F_N \rangle^2 = \frac{1}{N^2} \left(\langle (\sum_{i=1}^{N} f_i)^2 \rangle - \langle \sum_{i=1}^{N} f_i \rangle^2 \right). \tag{2.42}$$

The expectation value $\langle ... \rangle$ is linear in its individual arguments and the f_i are all equally distributed, i.e. $\langle f_i \rangle = \langle f_j \rangle \equiv \langle f \rangle$ and $\text{Var}(f_i) = \text{Var}(f_j) \equiv \text{Var}(f)$ for all $1 \leq i, j \leq N$. The difference to the previous data analysis section is that $\langle f_i f_j \rangle \neq \langle f_i \rangle \langle f_j \rangle$ since they are not independent. This leads to

$$\begin{aligned} \text{Var}(F_N) &= \frac{1}{N^2} \left(\sum_{i,j=1}^{N} \langle f_i f_j \rangle - \langle f_i \rangle \langle f_j \rangle \right) = \frac{1}{N^2} \left(N\,\text{Var}(f) + \sum_{i \neq j} \langle f_i f_j \rangle - \langle f_i \rangle \langle f_j \rangle \right) \\ &= \frac{\text{Var}(f)}{N} \left(1 + \frac{\sum_{i \neq j} (\langle f_i f_j \rangle - \langle f \rangle^2)}{N\,\text{Var}(f)} \right) = \frac{\text{Var}(f)}{N} (1 + 2\tau_A), \end{aligned} \tag{2.43}$$

where we have defined the **auto-correlation time** τ_A as

$$\tau_A = \frac{\sum_{i \neq j} (\langle f_i f_j \rangle - \langle f \rangle^2)}{2N\,\text{Var}(f)}. \tag{2.44}$$

The auto-correlation time contains $N(N-1)$ summands, where it is impossible to make any statement on their behavior during a certain sampling procedure. The best result for the auto-correlation time is that of independent variables, when $\tau_A = 0$ vanishes, on the other hand, for variables which are not independent, there is no argument that prevents τ_A from scaling as $\tau_A = \mathcal{O}(N)$. The latter would be the worst case scenario, because then the total variance $\text{Var}(F_N)$ would be constant and the Markov-Chain sampling would not converge to a fixed value[6]. From the Markov-Chain convergence theorem, we know that a Markov-Chain that is set-up properly (i.e. fulfilling the conditions of (2.2.2)) will converge to a stationary distribution in the limit of infinite steps. From that we directly conclude, that a proper

---

[6]It is obvious that a Markov-Chain, which is converging to a stationary distribution is not allowed to have fixed non-zero variance in the limit of infinite steps.

Markov-Chain will have an auto-correlation time τ_A which does not scale with the number of steps N (at least less than linear order). In a "good" sampling process, for sufficiently large N, τ_A will no longer depend on N and the total standard deviation will again scale as $\sigma(F_N) = \mathcal{O}(N^{-1/2})$. We can also formulate the previous argument from another perspective. As we have seen, a finite auto-correlation time results from non-independent variables f_i, f_j. If we sufficiently increase the number of intermediate sampling steps m between two subsequent measurements, these variables will become independent again and the auto-correlation time vanishes but the number of measurements scales linearly with N, the total number of steps in the sampling. If m is lowered now, the variables are no longer independent and τ_A becomes finite but the number of measurements still scales linearly with N, which means the variance in total may be larger but it is not allowed to depend on N. The only case, when τ_A scales with N is the case when it is impossible to bring τ_A to zero by the increase of m. In this case the measurements will never become independent, no matter how many intermediate steps lie between two measurements, which can only be the case when the Markov-Chain does not converge.

With the introduction of the auto-correlation time, we have found a powerful tool to analyze possible Markov-Chain sampling processes. Suppose we could determine the auto-correlation time τ_A in a certain sampling process. Then we have a direct measure for the Markov-Chain we have constructed: either τ_A remains finite in the limit of infinite steps (i.e. is independent of N for N sufficiently large), such that the Markov-Chain converges to a stationary distribution, or τ_A becomes infinite in this limit, and the Markov-Chain clearly does not converge. The latter means we have made a mistake in the implementation and did not properly ensure ergodicity. If the auto-correlation time is finite, we obtain the error of the sampling process in terms of the standard deviation

$$\sigma(F_N) = \sigma(f)\sqrt{\frac{1 + 2\tau_A}{N}}. \tag{2.45}$$

Although the auto-correlation time is a very powerful quantity, we only benefit from its introduction, if it is possible to determine τ_A during a certain sampling procedure. Finding ways to determine τ_A during a sampling process is therefore the aim of the remainder of this chapter.

Binning Analysis

The most common procedure to obtain the auto-correlation time is to perform binning analysis. Starting with the original set of measurements $f_i^{(0)}$, with $i = 1, ..., N$, we iteratively obtain a "binned" set of measurements by averaging over two consecutive entries:

$$f_i^{(l)} = \frac{1}{2}\left(f_{2i-1}^{(l-1)} + f_{2i}^{(l-1)}\right), \quad \text{with } i = 1, ..., N_l \equiv \frac{N}{2^l}. \tag{2.46}$$

These bin averages $f_i^{(l)}$ are less correlated than the original measurements, since they belong to two distinct (imaginary) measurements with an increased number of intermediate steps $m^{(l)} = 2^l * m^{(0)}$, where $m^{(0)}$ is the number of intermediate steps in the original sampling process. On the other hand, the mean value of the binned averages is always the mean of the original measurements $\sum_i f_i^{(0)}$. We can estimate the error of the binned variables, using the variance formula for independent variables, which we know to be incorrect but, however, converges to the correct error in the limit where the bins become independent of each other. Using (2.45) with $\tau_A = 0$, we obtain

$$\sigma(F_N^{(l)}) \approx \sqrt{\frac{\text{Var}(f_i^{(l)})}{N_l}} = \frac{2^l}{N}\sqrt{\sum_{i=1}^{N_l}\left(f_i^{(l)} - \langle f^{(l)} \rangle\right)^2}. \tag{2.47}$$

Suppose after l steps of applying the binning, the $f_i^{(l)}$ had been independent from each other. Then in the next step of the binning the variables $f_i^{(l+1)}$ would be also independent from each other and the two factors of 2 appearing in $\sigma(F_N^{(l+1)})$ would cancel each other resulting in $\sigma(F_N^{(l+1)}) = \sigma(F_N^{(l)})$. On the other hand, if the $f_i^{(l)}$ had not been independent from each other, $\sigma(F_N^{(l)})$ from Eq. (2.47) would be the wrong expression for the standard deviation, i.e. would underestimate the exact expression. Since in the next binning step, the variables will become "more" independent, (2.47) will be a more realistic expression,

which means that $\sigma(F_N^{(l)})$ will grow with increasing l until it saturates at the point l, where the $f_i^{(l)}$ are completely independent. Therefore the error estimate from (2.47) converges to the correct error estimate

$$\sigma(F_N) = \lim_{l \leftarrow \infty} \sigma(F_N^{(l)}). \tag{2.48}$$

Since in a realistic sampling procedure, the number of available steps have to be finite, one can adjust the number of total steps of the sampling according to the convergence of $\sigma(F_N^{(l)})$, i.e. until

$$|\sigma(F_N^{(l)}) - \sigma(F_N^{(l+1)})| = \epsilon, \tag{2.49}$$

where ϵ is the allowed residual deviation that has to be determined from outside. This binning analysis gives a reliable recipe for estimating errors and autocorrelation times. After convergence against $\sigma(F_N)$ is achieved, the auto-correlation time τ_A can be obtained by rearranging (2.43) via

$$\tau_A = \frac{1}{2}\left(\left(\frac{\sigma(F_N)}{\sigma(F_N^{(0)})}\right)^2 - 1\right). \tag{2.50}$$

The number of steps in the sampling procedure must be chosen at least thus large, that this convergence is achieved, otherwise no error estimation is possible and although one can just use the simple assumption of independent variables and obtain the corresponding error, the correction coming from the fact that the variables are not independent may be several order of magnitude larger than this error obtained from this estimation. This is for instance illustrated in [4] We conclude this section with some remarks.

Remarks:

- The auto-correlation time is a very important tool, as we have seen in the previous section, to give an estimate on the errors of results from a Markov-Chain sampling procedure. However, the name auto-correlation time may be misleading, at least from our point of view. Commonly, τ_A is said to give the number m of intermediate steps necessary to ensure the independence of the measured variables. As we have seen, this number would actually be given by 2^l, where l is the number of binning steps until convergence is observed. This number is usually much larger than the auto-correlation time, which is also what we observed from our Monte-Carlo simulations.

- There exist several important error estimation procedures for Monte-Carlo methods which we are not going to explain since binning was sufficient for our case. One method to mention is the **Jackknife analysis**, explained in [188]. The aim of this method is not to find the auto-correlation time but instead to give a reliable error estimation for variables that are functions of Monte-Carlo results and therefore need to be analyzed with respect to error propagation and cross-correlations in the case of multiple variables.

- Same implementations of Markov-Chain sampling will have different auto-correlation times and it may happen that an algorithm validated with one set of parameters will become non-ergodic when certain parameters are changed. This is for instance the case for spin-systems, when a symmetry broken phase occurs for a given set of parameters. Therefore it is very important to be careful with the analysis for these systems and it may happen that for a given physical system, different algorithms have to be used in different parameter regimes.

2.3 Diagrammatic Monte-Carlo Methods

In this section, a certain class of Monte-Carlo methods is introduced, namely the so-called Diagrammatic Monte-Carlo Methods (DiagMC), which sample Feynman diagrams of a perturbation expansion of the total Hamiltonian $H = H_0 + V$ to obtain the interacting Green's functions of a quantum-mechanical problem. We will start with a short overview on classical Monte-Carlo methods and the difference to quantum Monte-Carlo (QMC) methods, then introduce the idea of DiagMC with the formalism used throughout this thesis and finish with a brief outlook on the famous sign problem arising in QMC applications.

2.3.1   From Classical to Quantum Monte-Carlo

As mentioned already in the previous sections, in general there is no fundamental difference between classical and quantum Monte-Carlo methods, for both cases, after finding the most suitable configuration space, the Metropolis algorithm is applied as introduced before. The main difference is the choice of the configuration space, which is, of course, different for classical and quantum mechanical problems (the keyword for QMC is "world lines"). This difference can be understood very easily by the following example. Consider a system consisting of N interacting particles in a harmonic oscillator. We now first look at a classical system and then switch to the quantum analogue.

For a classical problem, the system is described by a classical Hamiltonian function $H(\{x_1,...,x_N,p_1,...,p_N\})$, which is a function of the individual coordinates and momenta of the particles. The Hamiltonian for N particles in a harmonic oscillator, which are interacting by a two-particle potential $U(x_i, x_j)$ is given by

$$H(\{x_1,...,x_N,p_1,...,p_N\}) = \sum_{i=1}^{N} \frac{p_i^2}{2m} + \frac{1}{2}m\omega^2 x_i^2 + \frac{1}{2}\sum_{i,j} U(x_i, x_j), \tag{2.51}$$

where the N classical momenta $p_i, i = 1, ..., N$ and the N classical coordinates $x_i, i = 1, ..., N$ are independent variables. To now determine the average of a given observable $O(x_1, ...x_N, p_1, ..., p_N)$ which might be a function of all momenta and coordinates (or some subset of those), we have to determine the integral

$$\langle O \rangle = \frac{1}{Z} \int d^N x d^N p \, O(x_1, ...x_N, p_1, ..., p_N) \, e^{-\beta H(\{x_1,...,x_N,p_1,...,p_N\})}, \tag{2.52}$$

where the partition function Z is defined by the integral

$$Z = \int d^N x d^N p \, e^{-\beta H(x_1,...,x_N,p_1,...,p_N)} \tag{2.53}$$

and $\beta = \frac{1}{k_B T}$ is the inverse temperature. The complicated integral from (2.52) can be determined by Markov-Chain Monte-Carlo. A set of possible configurations $\mathcal{C}$ and weights $w_\mathcal{C}$ is directly visible from the form of (2.52). The possible configurations are the momenta and coordinates, i.e. $\mathcal{C} = (x_1, ...x_N, p_1, ...p_N)$ and the possible weights are then given by

$$w_\mathcal{C} = e^{-\beta H_\mathcal{C}} = e^{-\beta H(x_1,...,x_N,p_1,...,p_N)}, \tag{2.54}$$

which leads to the observables

$$g_\mathcal{C} = O(\mathcal{C}) = O(x_1, ..., x_N, p_1, ..., p_N). \tag{2.55}$$

With these definitions, we have found everything necessary for a successful Markov-Chain Monte-Carlo sampling (remember section 2.2.2) except the proposal probabilities which for instance could be distributed uniformly (which would be a bad distribution but we are not interested in the best choice for this example). With our knowledge on Markov-Chain Monte-Carlo from the last section, it is clear that with these simple choices, we have already created a Monte-Carlo method for determining averaged observables for a classical interacting many-body problem.

What changes when switching to a quantum-mechanical many-body problem in the same setup, i.e. interacting quantum particles (but for simplicity with classical statistics) in a harmonic oscillator? In the Hamiltonian all the variables $x_1, ...x_N, p_1, ..., p_N$ are replaced by operators, which can not simply be expressed by numbers, especially not at the same time because p and x are not commuting. To obtain an integral expression for an operator average $\langle O \rangle$, which is also a function of momentum and coordinate operators now, one has to switch to a functional integral representation, i.e.

$$\langle O(x_1, \tau_1, ..., x_N, \tau_N) \rangle = \frac{1}{Z_{\text{QM}}} \int d^N x d^N p \, O(x_1, \tau_1, ..., x_N, \tau_N) e^{-S_{\text{eff}}}, \tag{2.56}$$

with

$$S_{\text{eff}} = \int_0^\beta d\tau \sum_{i=1}^{N} \frac{m}{2} \left(\frac{\partial x_i(\tau)}{\partial \tau} \right)^2 + \frac{m}{2}\omega^2 x_i(\tau) + \frac{1}{2}\sum_{i,j} U(x_i(\tau), x_j(\tau)). \tag{2.57}$$

The partition function Z_{QM} is defined equivalently as

$$Z_{\text{QM}} = \int d^N x d^N p \, e^{-S_{\text{eff}}}. \tag{2.58}$$

In order to find an integral expression for an observable average in the quantum case, it was necessary to switch to functional integral representation, from which another degree of freedom arises, namely the (imaginary) time τ. Therefore possible configurations for the quantum-mechanical problem would be the "classical" configurations $\mathcal{C}_{\text{class}} = (x_1, ..., x_N, p_1, ..., p_N)$, where we call $1/m \frac{\partial x_i}{\partial \tau} = p_i$ together with the time τ, i.e. $\mathcal{C}_{\text{QM}} = (\mathcal{C}_{\text{class}}, \tau)$.

For a quantum mechanical problem, the time is an additional variable in configuration space, whereas this is not the case for a classical problem. Therefore one can either think of totally different configurations (as we will do in the following chapters) for a quantum mechanical problem or one can imagine sampling so-called world lines instead of classical points in configuration space. These "world-lines" are nothing else but the classical variables as a function of τ on a interval $\tau \in [0, \beta]$.

Although we have totally neglected the statistics of the particles in this formalism (we have used classical, distinguishable particles), the main difference from QMC to classical MC is clear from this example, namely the (imaginary) time τ as an essential part of configuration space for QMC algorithms. In the following chapters of this thesis, we will not use world-line sampling and our configurations will be very different from any classical configurations, however, we wanted to illustrate the main difference between QMC and classical MC algorithms, which is **not** a different sampling method but rather a different configuration space Ω.

2.3.2 General Formalism of Diagrammatic Monte-Carlo Methods

For a quantum-mechanical many-body problem, there exist several possibilities to obtain physical quantities, beginning by thermodynamic properties determined by the partition function, static operator averages, such as the density distribution, or dynamic quantities, such as the dynamical structure factor or correlation functions. The most desirable quantities one would determine are the n-body Green's functions of the system, from which every other static or dynamic observable can be determined. One way to determine the Green's functions of a quantum system, is to use diagrammatic Monte-Carlo methods, which can be formulated in both equilibrium and non-equilibrium frameworks. In this section, we will give a brief introduction to the idea of DiagMC methods and the formulation of those with enough detail to describe the later implementation of the continuous time impurity solvers. DiagMC methods are diversely used throughout the scientific community and our aim is not to describe them in great detail or review the most recent developments. However, we would like to emphasize that DiagMC methods, paired with very advanced resummation techniques, have recently regained a great interest in condensed matter physics and are on the way (together with large-size cluster DMFT methods) to solve exactly theoretical models such as, for instance, the Hubbard model at half-filling (see for instance [111, 149, 146]).

The aim of DiagMC methods is to determine the Green's functions $G_{\alpha\alpha'}(\tau)$ of a system described by a Hamiltonian $H = H_0 + V$, where H_0 can be solved exactly (analytically or numerically) and V is an operator that can not easily be diagonalized simultaneously with H_0. The Green's function $G_{\alpha\alpha'}(\tau)$ is then determined by

$$G_{\alpha\alpha'}(\tau) = \frac{1}{Z} \text{Tr} \left(\mathcal{T} e^{-\beta H} c_\alpha(\tau) c_{\alpha'}^\dagger(0) \right), \tag{2.59}$$

where the partition function is

$$Z = \text{Tr} \left(e^{-\beta H} \right) \tag{2.60}$$

and the time-ordering operator $\mathcal{T}$ orders fermionic operators according to their imaginary time, i.e.

$$\mathcal{T} A(\tau) B(\tau') = \theta(\tau - \tau') A(\tau) B(\tau') - \theta(\tau' - \tau) B(\tau') A(\tau) \tag{2.61}$$

for some arbitrary, fermionic operators A, B. In the Heisenberg representation, time-dependence of operators means time-dependence with respect to the total Hamiltonian H, in other words

$$A(\tau) = e^{\tau H} A e^{-\tau H}. \tag{2.62}$$

Equation (2.59) is usually not directly evaluable, since H_0 and V are not simultaneously diagonalizable. Therefore one has to find another expression for the Green's functions. The exponential in (2.59) can be reexpressed using the identities

$$e^{-\beta H} = e^{-\beta H_0} e^{\beta H_0} e^{-\beta H} = e^{-\beta H_0} S(\beta), \tag{2.63}$$

with the definition of

$$S(\tau) = e^{\tau H_0} e^{-\tau H}. \tag{2.64}$$

The operator S can be determined by analyzing the Cauchy problem

$$\partial_\tau S(\tau) = e^{\tau H_0}(H_0 - H)e^{-\beta H} = -e^{\tau H_0} V e^{-\tau H_0} S(\tau) \equiv -V(\tau)S(\tau), \quad S(0) = \mathbb{1}, \tag{2.65}$$

which is formally solved by integration

$$S(\beta) = \mathbb{1} - \int_0^\beta d\tau \, V(\tau)S(\tau). \tag{2.66}$$

In equations (2.65) and (2.66), the time-dependence of $V(\tau)$ is no longer with respect to H but to H_0, this is commonly referred to as the Dirac representation. In the following, we will no longer use the Heisenberg representation. The action of the time-ordering operator $\mathcal{T}$ on other operators is the same in both representations. Iteration of the above equation (2.66) then leads to the Neumann series

$$S(\beta) = \mathbb{1} + \sum_{n=1}^{\infty}(-1)^n \int_0^\beta d\tau_1 \int_0^{\tau_1} d\tau_2 ... \int_0^{\tau_{n-1}} d\tau_n V(\tau_1)...V(\tau_n), \tag{2.67}$$

where it is important to keep the ordering of the operators $V(\tau)$ as in the above equation ($\tau_i \geq \tau_{i+m}$ with $m \in \mathbb{N}$). If one of the operators is in the incorrect order, for instance if $\tau_{i+1} \geq \tau_i$, this belongs to the evolution in negative time direction $\beta \to 0$ and can be corrected by an additional minus sign. It is therefore useful to also apply the time-ordering operator in this context and rewrite

$$S(\beta) = \mathbb{1} + \mathcal{T}\sum_{n=1}^{\infty}(-1)^n \int_0^\beta d\tau_1 \int_0^{\tau_1} d\tau_2 ... \int_0^{\tau_{n-1}} d\tau_n V(\tau_1)...V(\tau_n), \tag{2.68}$$

such that artificial time-ordering is no longer necessary since the time-ordering operator introduces minus signs whenever they are necessary (i.e. when operators are ordered incorrectly). With the time-ordering operator present in (2.68) it is also no longer necessary to keep the bounds of the integration as in (2.68), and instead all of the limits for the integrals become 0 to β with the inclusion of the combinatorial factor $n!$ that corrects for overcounting. The result is the Dyson series

$$S(\beta) = \mathbb{1} + \mathcal{T}\sum_{n=1}^{\infty}\frac{(-1)^n}{n!} \int_0^\beta d\tau_1 \int_0^\beta d\tau_2 ... \int_0^\beta d\tau_n V(\tau_1)...V(\tau_n) = \mathcal{T}e^{-\int_0^\beta d\tau \, V(\tau)}. \tag{2.69}$$

The last equality is a formal reexpression of the Dyson series, but it must be emphasized that this is only shorthand for the whole series since it is impossible to express the exponential without using the infinite Dyson series (the exceptions are only the trivial cases when V and H_0 are simultaneously diagonalized). With this reformulation, the Green's function can be expressed as the solution of the following problem:

$$G_{\alpha\alpha'}(\tau) = \frac{\mathrm{Tr}\left(e^{-\beta H_0}\,\mathcal{T}e^{-\int_0^\beta d\tau' V(\tau')}\, c_\alpha^\dagger(\tau)c_{\alpha'}(0)\right)}{\mathrm{Tr}\left(e^{-\beta H_0}\,\mathcal{T}e^{-\int_0^\beta d\tau' V(\tau')}\right)} = \frac{\left\langle \mathcal{T}e^{-\int_0^\beta d\tau' V(\tau')}\, c_\alpha^\dagger(\tau)c_{\alpha'}(0)\right\rangle_0}{\left\langle \mathcal{T}e^{-\int_0^\beta d\tau' V(\tau')}\right\rangle_0}, \tag{2.70}$$

where

$$\langle ... \rangle_0 = \mathrm{Tr}\left(e^{-\beta H_0}...\right)$$

denotes the average with respect to H_0. Equation (2.70) is already of very similar form as (2.31) , which was the starting point for the Metropolis algorithm and took the form

$$G_{\mathrm{MC}} = \frac{\int_\Omega d\mathcal{C} \, w_\mathcal{C} g_\mathcal{C}}{\int_\Omega d\mathcal{C} \, w_\mathcal{C}}. \tag{2.71}$$

We must now find a possible set of configurations and weights to implement a Monte-Carlo sampling computing the Green's functions. A possible way to do this is to express the partition function through the infinite Dyson series again. This leads to

$$Z = \left\langle \mathcal{T} e^{-\int_0^\beta d\tau V(\tau)} \right\rangle_0 = \sum_{n=0}^\infty \frac{(-1)^n}{n!} \int_0^\beta d\tau_1 ... \int_0^\beta d\tau_n \left\langle \mathcal{T} \prod_{l=1}^n V(\tau_l) \right\rangle_0 \equiv \int_\Omega d\mathcal{C} \, w_\mathcal{C}, \qquad (2.72)$$

where we have identified the configurations $\mathcal{C}$ and the respective weights $w_\mathcal{C}$ according to

$$\mathcal{C} = (n, \tau_1, ..., \tau_n), \quad \text{and} \quad d\mathcal{C} w_\mathcal{C} = \frac{(-1)^n}{n!} \left\langle \mathcal{T} \prod_{l=1}^n V(\tau_l) d\tau_l \right\rangle_0. \qquad (2.73)$$

The factor

$$\left\langle \prod_{l=1}^n V(\tau_l) \right\rangle_0$$

in the definition of the weights above will usually be very difficult to determine and looking from a diagrammatic point of view, one immediately realizes that this expectation value is already the sum over all Feynman diagrams for a given perturbation order n. Therefore it is also possible, starting from the definition of the configurations and weights (2.73) to construct new configurations and weights by decomposition or resummation of old weights. For instance, suppose V is of quartic order in fermionic operators, then for a given perturbation order n, there exist $2n!$ labeled Feynman diagrams. A possible choice for configurations and weights then could be

$$\mathcal{C} = (n, k, \tau_1, ..., \tau_n), \quad \text{and} \quad d\mathcal{C} w_\mathcal{C} = \frac{(-1)^n}{n!} (n\text{th order diagram } \#k) \prod_{l=1}^n d\tau_l, \qquad (2.74)$$

where $1 \leq k \leq 2n!$ labels the individual Feynman diagrams at perturbation order n. The last example can be seen as the starting point for any diagrammatic Monte-Carlo method. Commonly, it is not the bare labeled diagrams that are sampled but instead resummation techniques are applied, for instance it is possible to resum all diagrams of a given structure, ending up with either bold-lined diagrams[7] or diagrams with renormalized interactions. As already mentioned, the possible realizations for diagrammatic Monte-Carlo methods is very diverse and for our purpose it is not necessary to go into further details. We will always use configurations and weights as defined in (2.73). As pointed out above, this can be understood as a diagrammatic Monte-Carlo method, where the resummation is done such that all diagrams of a given perturbation order are contained in the weight $w_\mathcal{C}$.

The last missing ingredient for the implementation of the Metropolis algorithm (except the proposal probabilities which have again to be designed for every problem individually) are the $g_\mathcal{C}$'s. We write the Green's functions as

$$G_{\alpha\alpha'}(\tau) = \frac{\int_\Omega d\mathcal{C} \, w_\mathcal{C} g_{\mathcal{C},\alpha\alpha'}(\tau)}{\int_\Omega d\mathcal{C} \, w_\mathcal{C}}, \qquad (2.75)$$

from which it is clear that for $\mathcal{C} = (n, \tau_1, ... \tau_n)$

$$g_{\mathcal{C},\alpha\alpha'}(\tau) = \frac{\frac{(-1)^n}{n!} \left\langle \mathcal{T} c_\alpha^\dagger(\tau) c_{\alpha'}(0) \prod_{l=1}^n V(\tau_l) d\tau_l \right\rangle_0}{\frac{(-1)^n}{n!} \left\langle \mathcal{T} \prod_{l=1}^n V(\tau_l) d\tau_l \right\rangle_0} = \frac{\left\langle \mathcal{T} c_\alpha^\dagger(\tau) c_{\alpha'}(0) \prod_{l=1}^n V(\tau_l) \right\rangle_0}{\left\langle \mathcal{T} \prod_{l=1}^n V(\tau_l) \right\rangle_0}. \qquad (2.76)$$

The numerical value of $g_{\mathcal{C},\alpha\alpha'}(\tau)$ can be obtained on two distinct ways, either via a direct calculation, as we will do it in the later chapters or again by using diagrammatics. For the latter, one simply has to remember that w_c includes all diagrams resulting from nth order perturbation theory and therefore $g_{\mathcal{C},\alpha\alpha'}(\tau)$ contains all $(n+1)$th order diagrams from a diagrammatic expression of the Green's function $G_{\alpha\alpha'}(\tau)$ (connected **and** disconnected). With the definition of the $g_\mathcal{C}$'s, the weights $w_\mathcal{C}$ and the configurations $\mathcal{C}$, we have done the preface for the implementation of the continuous-time quantum Monte-Carlo solvers that we explain in the following sections. We conclude this section with a brief introduction of the sign problem, which usually arises in quantum Monte-Carlo processes.

---

[7] In our example this would mean that in the sampling process, the interacting Green's functions are already included instead of the non-interacting ones.

2.3.3   The Sign Problem in Monte-Carlo Processes

From the definition of possible weights in the previous section, i.e. $w_\mathcal{C}$ being diagrams. It becomes clear that some of the $w_\mathcal{C}$ may become negative when dealing with fermions, since fermionic diagrams are not strictly positive in contrast to the bosonic case. Therefore $\pi(\mathcal{C})$ is negative, which excludes it from being a probability and no Markov-Chain can be created by using the weights. It is possible to circumvent this problem by realizing that $w_\mathcal{C} = |w_\mathcal{C}|\mathrm{sign}(w_\mathcal{C})$ and rewriting the expression for the Green's function sampling as

$$G_{\alpha\alpha}(\tau) = \frac{\int_\Omega d\mathcal{C}\, w_\mathcal{C}\, g_{\mathcal{C},\alpha\alpha'}(\tau)}{\int_\Omega d\mathcal{C}\, w_\mathcal{C}} = \frac{\int_\Omega d\mathcal{C}\, |w_\mathcal{C}|\mathrm{sign}(w_\mathcal{C}) g_{\mathcal{C},\alpha\alpha'}(\tau)}{\int_\Omega d\mathcal{C}\, |w_\mathcal{C}|}\, \frac{\int_\Omega d\mathcal{C}\, |w_\mathcal{C}|}{\int_\Omega d\mathcal{C}\, |w_\mathcal{C}|\mathrm{sign}(w_\mathcal{C})} = \frac{\tilde{G}_{\alpha\alpha}(\tau)}{\langle\mathrm{sign}\rangle}, \quad (2.77)$$

where we have defined the positive weighted Green's function

$$\tilde{G}_{\alpha\alpha}(\tau) \equiv \frac{\int_\Omega d\mathcal{C}\, |w_\mathcal{C}|\mathrm{sign}(w_\mathcal{C}) g_{\mathcal{C},\alpha\alpha'}(\tau)}{\int_\Omega d\mathcal{C}\, |w_\mathcal{C}|} \tag{2.78}$$

and the average sign

$$\langle\mathrm{sign}\rangle \equiv \frac{\int_\Omega d\mathcal{C}\, |w_\mathcal{C}|\mathrm{sign}(w_\mathcal{C})}{\int_\Omega d\mathcal{C}\, |w_\mathcal{C}|}. \tag{2.79}$$

Both the average sign and the positive weighted Green's function can be determined in a single sampling procedure according to the positive weights $|w_\mathcal{C}|$ without any approximation. At first glance, this might solve the problem of negative weights $w_\mathcal{C}$ completely and avoiding negative weights in Monte-Carlo would never be an issue. However, the important fact that makes Monte-Carlo superior to many other methods is that the Monte-Carlo error is under control. Now suppose the sampling error $\tilde{\Delta}(N)$ of $\tilde{G}_{\alpha\alpha}(\tau)$ was obtained in a Monte-Carlo simulation with N subsequent MC measurements. This error can be expressed as

$$\tilde{\Delta}(N) = \frac{\tilde{\Delta}_0}{\sqrt{N}}, \tag{2.80}$$

where the prefactor $\tilde{\Delta}_0$ is unimportant for the moment. Now, the error $\Delta(N)$ of the Green's function resulting from the same Monte-Carlo sampling would, according to (2.77), be given by

$$\Delta(N) = \frac{\tilde{\Delta}(N)}{\langle\mathrm{sign}\rangle} = \frac{\tilde{\Delta}_0}{\sqrt{\langle\mathrm{sign}\rangle^2 N}}. \tag{2.81}$$

This error is the error belonging to a direct Monte-Carlo sampling of the Green's function with a reduced number of steps $\tilde{N} = \langle\mathrm{sign}\rangle^2 N$. To obtain an error comparable to N Monte-Carlo steps in systems with positive weights, one has to perform an increased number of $\frac{N}{\langle\mathrm{sign}\rangle^2}$ steps in a system that shows also negative weights (i.e. when $\langle\mathrm{sign}\rangle < 1$). This means, although negative signs are handled by (2.77) without restrictions on a formal level, it may be that the number of necessary Monte-Carlo steps to obtain an acceptable error is increasing up to an intractable number, which makes Monte-Carlo simulations very inefficient or even impossible. To understand how severe this increase of necessary Monte-Carlo steps can become for fermionic systems, we take a short look at the average sign (2.79) for a DiagMC sampling as introduced in the previous section. Then

$$\langle\mathrm{sign}\rangle = \frac{\int_\Omega d\mathcal{C}\, w_\mathcal{C}}{\int_\Omega d\mathcal{C}\, |w_\mathcal{C}|} = \frac{Z}{Z_B} = e^{-\beta V(f_F - f_B)}, \tag{2.82}$$

where Z_B is the partition function of a corresponding (fictive) bosonic system, β is the inverse temperature and V is the volume of the system and f_F, f_B are the free energies per volume of the fermionic, bosonic system, respectively. From (2.82), it is clear that the average sign of a system decreased exponentially with the system size and the inverse temperature. This fact means that simple, straightforwardly implemented quantum simulations of larger fermionic systems at sufficiently deep temperatures become impossible and is the limiting problem for exact quantum simulations of interacting fermion systems on the basis of Monte-Carlo processes. Very often, this is referred to as the sign problem of QMC methods. However, recently developed DiagMC methods (also called bold-line diagrammatic Monte-Carlo methods, BoldDiagMC) have found a perfect way to make use of the sign problem [149, 150]. Although the idea is rather simple, the implementation therefore is, however, very demanding:

- Imagine the configuration space Ω consisting of the bare diagrams, as in the example from the previous section.

- Now, construct new configurations $\tilde{\mathcal{C}}_i = \{\mathcal{C}_{i1}, ...\mathcal{C}_{in}\}$ consisting of several old configurations, such that $w_{\tilde{\mathcal{C}}_i} = \sum_{l=1}^{n} w_{\mathcal{C}_{il}} \to 0$ for most of the new configurations $\tilde{\mathcal{C}}_i$.

- Perform a Monte-Carlo sampling with the few residual, non-zero weights $w_{\tilde{\mathcal{C}}_i}$, where the sign problem is much less severe, resulting from the effectively decreased system size.

On the first view, this procedure seems very artificial. However, it turns out that this kind of Monte-Carlo sampling can be achieved by applying resummation techniques, already known from diagrammatic treatments of condensed matter systems and that these methods are indeed quite powerful.

With this brief introduction of the sign problem, we conclude the more general part on Monte-Carlo and diagrammatic Monte-Carlo methods and come to the derivation of the so-called continuous-time quantum Monte-Carlo methods, which will be used to solve the Anderson impurity model from section (3.1).

3. The Anderson Impurity Model and Continuous-Time Monte-Carlo Methods

In this chapter, we will introduce the Anderson Impurity model (AIM), a famous theoretical model describing two interacting fermionic particles coupled to a non-interacting bath. The AIM was first introduce to describe the Kondo-effect in solid state systems and its great importance was even increased after one realized that the same model is strongly connected to the DMFT approximation, as we will see in the following sections. To successfully apply the DMFT equations, it is essential in every iteration to calculate the correlation functions of an AIM and use these in the iterative DMFT procedure. Therefore, we are interested in theoretical (computational) methods to determine those correlation functions. In this chapter, we will discuss two such methods. First, the exact diagonalization of a quantum system with only few degrees of freedom and, second, Continuous-Time Quantum Monte-Carlo (CT-QMC) methods which are able to determine exact correlation functions for arbitrary bath sizes without any additional computational cost. This last point is very important, since, as we will see, reducing the bath to a finite number of quantum states decreases the spectral resolution of the DMFT approximation dramatically.

3.1 The Anderson Impurity Model

Our interest in the Anderson Impurity model (sometimes also called single impurity Anderson model, SIAM) results from the fact that we have to determine the corresponding correlation functions in order to use them during the DMFT iterations. Depending on the physics that are investigated (i.e. repulsive interactions, attractive interactions, superfluidity or spin orbit coupling), the Hamiltonian of the AIM that we are considering slightly changes but the general structure will always stay the same.

The AIM is a theoretical model describing two interacting fermionic particles (which we will label with spin indices $\sigma = \uparrow, \downarrow$), both coupled to a non-interacting bath. It is usually expressed through the Hamiltonian

$$H_{\text{AIM}} = H_{\text{loc}} + H_{\text{hyb}} + H_{\text{bath}}, \tag{3.1}$$

consisting of the local Hamiltonian

$$H_{\text{loc}} = -\sum_{\sigma} \mu_\sigma n_\sigma + U n_\uparrow n_\downarrow, \tag{3.2}$$

the Hamiltonian of the non-interacting bath, with the bath operators creation and annihilation operators $d_{\sigma\alpha}^\dagger$ and $d_{\sigma\alpha}$,

$$H_{\text{bath}} = \sum_{\sigma,\alpha} \epsilon_{\sigma,\alpha} d_{\sigma\alpha}^\dagger d_{\sigma\alpha} \tag{3.3}$$

and the hybridization with the bath

$$H_{\text{hyb}} = \sum_{\sigma,\alpha} V_{\sigma,\alpha} c_\sigma^\dagger d_{\sigma\alpha} + \text{h.c.}. \tag{3.4}$$

The bath energies $\epsilon_{\sigma,\alpha}$ are real parameters, while the hybridization parameters $V_{\sigma,\alpha}$ may be complex. The chemical potential μ_σ is allowed to be different for the different components $\sigma = \uparrow, \downarrow$ in order to describe population imbalance.

As for the lattice problem, we would like to find an effective action S_{eff}, which only contains the two components $\sigma = \uparrow, \downarrow$ such that all states α have been integrated out, so that the interacting Green's functions of the last two components can be written as

$$G_\sigma(\tau) = \frac{1}{Z_{\text{eff}}} \int \prod_{\sigma'} \mathcal{D}[c_{\sigma'}^\dagger, c_{\sigma'}] c_\sigma(\tau) c_\sigma^\dagger e^{-S_{\text{eff}}}. \tag{3.5}$$

In contrast to the previous chapter, the expression of these Green's functions via an effective action can be formulated by an exact transformation and the exact effective action can be determined analytically from the parameters $\{V_{\sigma,\alpha}, \epsilon_{\sigma,\alpha}\}$. To prove this, we start with the complete action the AIM, S_{AIM},

$$S_{\text{AIM}} = S_{\text{loc}} + S_{\text{hyb}} + S_{\text{bath}}, \tag{3.6}$$

where we again have separated this into a local part, the pure bath and the hybridization between local part and bath

$$S_{\text{loc}} = \int d\tau \sum_\sigma c_\sigma^\dagger(\tau) \left(\partial_\tau - \mu_\sigma\right) c_\sigma(\tau) + U \int d\tau n_\uparrow(\tau) n_\downarrow(\tau), \tag{3.7}$$

$$S_{\text{bath}} = \int d\tau \sum_{\sigma,\alpha} d_{\sigma\alpha}^\dagger(\tau) \left(\partial_\tau + \epsilon_{\sigma,\alpha}\right) d_{\sigma\alpha}(\tau) \tag{3.8}$$

and

$$S_{\text{bath}} = \int d\tau \sum_{\sigma,\alpha} V_{\sigma,\alpha} c_\sigma^\dagger(\tau) d_{\sigma\alpha}(\tau) + \text{h.c.}. \tag{3.9}$$

To diagonalize this expression in the time domain (i.e. to get rid of the derivative ∂_τ) and simplify the following steps, we switch to Matsubara frequency representation, where the single parts of the action read

$$S_{\text{loc}} = \sum_{n=-\infty}^{\infty} \sum_\sigma c_\sigma^\dagger(i\omega_n)\left(i\omega_n - \mu_\sigma\right) c_\sigma(i\omega_n) + U \sum_{n,n',n''} c_\uparrow^\dagger(i\omega_n) c_\downarrow^\dagger(i\omega_n') c_\downarrow(i\omega_n'') c_\uparrow(i\omega_n + i\omega_n' - i\omega''),$$
$$\tag{3.10}$$

$$S_{\text{bath}} = \sum_{n=-\infty}^{\infty} \sum_{\sigma,\alpha} d_{\sigma\alpha}^\dagger(i\omega_n)\left(i\omega_n + \epsilon_{\sigma,\alpha}\right) d_{\sigma\alpha}(i\omega_n), \tag{3.11}$$

$$S_{\text{bath}} = \sum_{n=-\infty}^{\infty} \sum_{\sigma,\alpha} V_{\sigma,\alpha} c_\sigma^\dagger(i\omega_n) d_{\sigma\alpha}(i\omega_n) + \text{h.c.}. \tag{3.12}$$

To integrate out the $d_{\sigma\alpha}^\dagger, d_{\sigma\alpha}$ degrees of freedom, we make use of the integration law for Grassmann variables, which states

$$\int \mathcal{D}[\xi^*, \xi] e^{-\sum_{\lambda\mu} \xi_\lambda^* M_{\lambda\mu} \xi_\mu + \sum_\lambda (\bar{\eta}_\lambda \xi_\lambda + \xi_\lambda^* \eta_\lambda)} = (\det M) \; e^{\sum_{\lambda\mu} \bar{\eta}_\lambda (M^{-1})_{\lambda\mu} \eta_\mu}. \tag{3.13}$$

By defining the indices $\lambda \equiv (\sigma, \alpha, i\omega_n)$, the matrix $M_{\sigma,\alpha,i\omega_n} = i\omega_n - \epsilon_{\sigma,\alpha}$ and the Grassmann variables $\eta_{\sigma,\alpha,i\omega_n} = V_{\sigma\alpha}^* c_\sigma(i\omega_n)$, we can integrate out the bath degrees of freedom and find

$$\int \prod_{\alpha,\sigma} \mathcal{D}[d_{\alpha\sigma}^\dagger, d_{\alpha\sigma}] e^{-S_{\text{AIM}}} = \left(\prod_{\sigma,\alpha,n} (i\omega_n + \epsilon_{\sigma,\alpha})\right) e^{-S_0 + \sum_{\sigma,\alpha,n} c_\sigma^\dagger(i\omega_n)\left(\frac{|V_{\sigma\alpha}|^2}{i\omega + \epsilon_{\sigma,\alpha}}\right) c_\sigma(i\omega_n)}. \tag{3.14}$$

The prefactor of this expression results from the determinant in (3.13) but doesn't play any role (except when one is interested in the thermodynamics of the AIM) since it can be absorbed into Z_{eff} in (3.5). In the last step, we will find the hybridization function of the AIM

$$\Gamma_\sigma(i\omega_n) = \sum_\alpha \frac{|V_{\sigma\alpha}|^2}{i\omega_n + \epsilon_{\sigma\alpha}}, \tag{3.15}$$

with which we can again define a Weiss function $\mathcal{G}_\sigma$ by

$$\mathcal{G}_\sigma^{-1}(i\omega_n) = i\omega_n - \mu_\sigma - \Gamma_\sigma(i\omega_n) = i\omega_n - \mu_\sigma - \sum_\alpha \frac{|V_{\sigma\alpha}|^2}{i\omega_n + \epsilon_{\sigma\alpha}}. \tag{3.16}$$

Here, the Weiss function has no further index than σ since it is not yet associated with any lattice site of the system as it was the case in the previous chapter. Inserting the Weiss function into the effective action leads to

$$S_{\text{eff}} = \int d\tau d\tau' \sum_\sigma c_\sigma^\dagger(\tau) \mathcal{G}_\sigma^{-1}(\tau - \tau') c_{\tau'} + U \int d\tau n_\uparrow(\tau) n_\downarrow(\tau), \tag{3.17}$$

which looks identical to the effective impurity action of the DMFT equations (1.58).

We have found two representations of the AIM effective action, from which we can obtain the correlation functions with respect to the $c_\sigma^\dagger, c_\sigma$ degrees of freedom. First, the action defined by (3.6), which is local in time but has additional degrees of freedom of the bath that we are not interested in, and second, the effective action defined by (3.17), which has no additional degrees of freedom but is non-local in time due to the non-local hybridization functions $\Gamma_\sigma(\tau)$. In the following sections, we will work with both representations, depending on the computational method that we are interested in. However, one should note that the effective action coming from the DMFT equation (i.e. that which we wish to solve) has the representation (3.17) and can therefore only be fully captured by (3.6) if the bath is infinitely large[1]. The residual (but nevertheless main part) of this chapter, we will derive computational methods to solve the AIM model or, more precisely, calculating the correlation functions, which appears rather simple but still demands for very advanced methods to be solved exactly. This difficulty simply arises from the non-locality in time of the hybridization function and must not be circumvented by any approximation (otherwise DMFT would simplify to a static Mean-Field theory).

3.1.1 Exact Diagonalization

Exact Diagonalization (ED) is a very simple, yet often used approximation to solve the AIM presented in the previous section. As we have seen, one representation of the AIM is that of an interacting, two level system, coupling to an infinite bath. If the bath was finite (which we take as about $4 - 6$ bath orbitals), one possibility to solve the AIM would be to numerically implement the Hamiltonian as a matrix (in a given complete basis of states) and diagonalize it numerically. Here, the size of the matrix (the number of states) scales exponentially with the number of orbitals, which makes ED impossible for larger systems. On the other hand, DMFT produces a Weiss function $\mathcal{G}$, from which all the parameters $\{V_{\sigma\alpha}, \epsilon_{\sigma\alpha}\}$ would have to be determined. This would also be an impossible task for a large system[2] and therefore it is only possible to use ED as an approximate method, where the approximation itself comes from the restriction to a finite bath. When restricting oneself to a finite system, the explicit numbers for the bath energies and hybridization parameters are obtained from a least squares fit to the DMFT Weiss function and subsequent diagonalization of the resulting matrix. In this thesis, ED is never used as an impurity solver for DMFT iterations and therefore, we will not go further into the details of this method. However, we used ED to benchmark the Monte-Carlo methods described in the following sections and numerically implemented during the work on this thesis. For this benchmarking, we reverse the problem by choosing some arbitrary parameters $\{V_{\sigma\alpha}, \epsilon_{\sigma\alpha}\}$, and then determining the Weiss function $\mathcal{G}$ (which in this direction is exactly possible by (3.16)) and comparing Monte-Carlo and ED results. In this case, no approximation is made and both results are exact and should be equivalent an so we are able to verify the Monte-Carlo algorithm.

---

[1]The Weiss function is a bounded function on a finite interval, i.e. $\tau \in [-\beta, \beta]$, which means it belongs to a separable but **infinite dimensional** space, which can only be fully reproduced by taking into account an infinite number of bath orbitals.

[2]Neither the space of Green's functions nor the basis functions $\frac{|V|^2}{\epsilon - i\omega}$ posses a mathematical structure that allows for a systematic determination of the parameters $\{V_{\sigma\alpha}, \epsilon_{\sigma\alpha}\}$.

3.2   Continuous-Time Auxiliary Field Quantum Monte-Carlo Algorithm

In this section, we derive the continuous-time auxiliary field quantum Monte-Carlo algorithm (CT-AUX), as an impurity solver for the Anderson impurity model, based on Monte-Carlo sampling and an auxiliary field decomposition of the interaction part of the AIM. Continuous-time solvers, based on an auxiliary field method were first developed by Rombouts *et al.* [154, 155] in 1998 for small Hubbard lattices. Monte-Carlo solvers on the Basis of a Trotter decomposition, the so-called Hirsch-Fye algorithms [86], have been used much earlier to treat a small number of magnetic impurities in metals. The formulation of CT-AUX that we present in this section has been developed by Emanuel Gull *et al.* in 2008 [65] and is presented in detail in [65, 67, 70]. We will mainly follow the original derivation, i.e. [65], while we present some of the calculations in more detail. In particular, we present an exact derivation of the weight formulas based on functional integration, whereas the derivation in the original publications is based on approximative formulas, developed for the Hirsch-Fye algorithm. The resulting weight formulas are, however, identical. The CT-AUX impurity solvers have been used also in cluster DMFT approximations [190, 111], where a cluster of multiple sites $N = 4, 8, 32, ...$ has been used as the "impurity". In this approaches, the self-energy becomes momentum-dependent and the results become exact with increasing cluster size. The CT-AUX algorithm is perfectly suited for cluster problems, because a cluster implementation is straight-forward, as we will see at the end of this section. However, our intention is to use CT-AUX as an impurity solver for the RDMFT approximation, for which it is useful because it is an exact method to solve the impurity problem and it can be extended to a more general class of systems, including spin-orbit coupling or superfluid pairing, as we will see in the succeeding chapters.

3.2.1   Configurations, Weights and Measurement Factors

In this part, we will identify the configurations $\mathcal{C}$ for the CT-AUX algorithm and derive analytic formulas for the weights $w_{\mathcal{C}}$ and measurement factors $g_{\mathcal{C}}$ by applying functional integration and matrix algebra tools to the AIM. The aim of the CT-AUX impurity solver is to compute the Green's functions of the AIM, described by the Hamiltonian (3.1)

$$H = -\sum_{\sigma} \mu_{\sigma} n_{\sigma} + U n_{\uparrow} n_{\downarrow} + \sum_{\sigma,\alpha} \epsilon_{\sigma,\alpha} d_{\sigma\alpha}^{\dagger} d_{\sigma\alpha} + \sum_{\sigma,\alpha} V_{\sigma,\alpha} c_{\sigma}^{\dagger} d_{\sigma\alpha} + \text{h.c.}, \tag{3.18}$$

with the creation and annihilation operators for the bath states $d_{\sigma\alpha}^{\dagger}, d_{\sigma\alpha}$ and the impurity states $c_{\sigma}^{\dagger}, c_{\sigma}$, with $\sigma = \uparrow, \downarrow$. The corresponding functional integral representation of the AIM, with the bath degrees of freedom integrated out, is determined by the effective action (3.6), (3.17)

$$S_{\text{eff}} = \int d\tau d\tau' \sum_{\sigma} c_{\sigma}^{\dagger}(\tau) \mathcal{G}_{\sigma}^{-1}(\tau - \tau') c_{\tau'} + U \int d\tau n_{\uparrow}(\tau) n_{\downarrow}(\tau). \tag{3.19}$$

We will start the formulation of the CT-AUX algorithm in operator representation and later switch to functional integral representation, which leads to more general results and allows for an exact calculation of the weights $w_{\mathcal{C}}$.

Following the derivation presented in section (2.3.2), we decompose the Hamiltonian H into an exactly solvable part H_0 and the additional part V, i.e. $H = H_0 + V$. The specific choice of V determines the CT-QMC method one has to use to solve the AIM. The idea of the CT-AUX solver is to chose V such that $-V$ has a positive spectrum. If this is the case, the weights $w_{\mathcal{C}}$ will become positive for any configuration $\mathcal{C}$ as can be seen from (2.73) and there will be no sign problem occurring during the MC sampling process[3]. The simplest choice of V will be

$$V = U \left(n_{\uparrow} n_{\downarrow} - \frac{n_{\uparrow} + n_{\downarrow}}{2} \right) - \frac{K}{\beta}, \tag{3.20}$$

---

[3]To be precise, when the operator V is chosen such that it possesses a positive spectrum, it is possible to find a Hubbard-Stratonovich transformation, such that all weights are positive [154].

where the role of the positive parameter K will become clear soon. The choice of V in (3.20) results from the fact that the operator part is zero for zero or double occupancy of the impurity and takes the value $-U/2$ for a singly occupied impurity. The resulting Hamiltonian

$$H_0 = H - V \tag{3.21}$$

is quadratic in fermionic operators and leads to solvable Gaussian integrals in a functional integral formulation. To further proceed, we apply a discrete Hubbard-Stratonovich transformation to V, which can be found for any bounded operator with a finite number of different eigenvalues (see for instance [142]) and was in the context of CT-QMC solver first introduced by Rombouts [155]

$$-V = -U\left(n_\uparrow n_\downarrow - \frac{n_\uparrow + n_\downarrow}{2}\right) + \frac{K}{\beta} = \frac{K}{\beta}\sum_{s=\pm 1} e^{\gamma s(n_\uparrow - n_\downarrow)}, \tag{3.22}$$

where the positive parameter γ is defined by

$$\cosh(\gamma) = 1 + \frac{U\beta}{2K} \quad \Leftrightarrow \quad \gamma = \ln\left(1 + \frac{U\beta}{2K} + \sqrt{\left(1 + \frac{U\beta}{2K}\right)^2 - 1}\right). \tag{3.23}$$
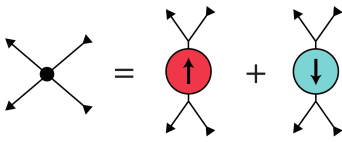
Figure 3.1: Schematic illustration of the discrete Hubbard-Stratonovich transformation. The four point vertex on the left side is replaced by the sum of vertices on the right.

Equality in (3.22) can be checked by letting the left and right side of the equation act on the basis states $\mathcal{B} = \{|0\rangle, |\uparrow\rangle, |\downarrow\rangle, |\uparrow\downarrow\rangle\}$ of the impurity, which are the eigenstates of the left and right operators with the same corresponding eigenvalues, which proves identity since $\mathcal{B}$ is a complete basis.

To further simplify the resulting expression for the weight factors, we perform a transformation according to

$$e^{\gamma s \sigma n_\sigma} = e^{\gamma s \sigma} c_\sigma \sigma_+^\dagger c_\sigma c_\sigma^\dagger = e^{\gamma s \sigma} - (e^{\gamma s \sigma} - 1) c_\sigma c_\sigma^\dagger. \tag{3.24}$$

In this equation, we have introduced the spin variable σ to be used as a number. Whenever σ takes the place of a variable, it is identified as $\sigma \equiv +1$ for $\uparrow$ and $\sigma = -1$ for $\downarrow$. The reason for bringing the creation operators in front of the annihilation operators, is to bring them into correct order for a switch to functional integral representation, where at equal times $c_\sigma^\dagger$ is considered to at infinitesimal smaller time than c_σ. We can now again rewrite the operator $-V$ as

$$-V = \frac{K}{\beta}\sum_{s=\pm 1} e^{\gamma s(n_\uparrow - n_\downarrow)} = \frac{K}{\beta}\sum_{s=\pm 1}\prod_{\sigma=\uparrow,\downarrow}\left[e^{\gamma s \sigma} - (e^{\gamma s \sigma} - 1) c_\sigma c_\sigma^\dagger\right]. \tag{3.25}$$

In the DiagMC section, using a perturbation expansion in V, the weights $w_\mathcal{C}$ were found to be

$$d\mathcal{C}w_\mathcal{C} = \frac{1}{n!}\left\langle \mathcal{T}\prod_{l=1}^{n} -V(\tau_l)d\tau_l \right\rangle, \tag{3.26}$$

where n was the current perturbation order and part of the configuration $\mathcal{C} = (n, \tau_1, ..., \tau_n)$. One has to keep in mind, that for this expression the expectation value including the time ordering operator $\mathcal{T}$ means that all permutations of the n distinct times $\tau_i, i = 1, ...n$ must be averaged and multiplied with the corresponding sign (-1 or $+1$ depending on the ordering). In our version of the algorithm, we will only pick one realization of these permutations, which will be the time ordered one. Therefore, the factor $n!$ in the denominator can be dropped and by using (3.25), the weights become

$$d\mathcal{C}w_\mathcal{C} = \left\langle \prod_{l=1}^{n}\sum_{s_l=\pm 1}\prod_{\sigma=\uparrow,\downarrow}\left[e^{\gamma s_l \sigma} - (e^{\gamma s_l \sigma} - 1) c_\sigma(\tau_l)c_\sigma^\dagger(\tau_l)\right]\right\rangle_0 \left(\frac{Kd\tau}{\beta}\right)^n, \tag{3.27}$$

where we have, for convenience, skipped the index l for the infinitesimal times $d\tau_l$.

We can realize two facts, leading to a further simplification of the above expression. First, for every time $\tau_l, l = 1, ..., n$, there exists a corresponding classical spin $s_l = \pm 1$ over which is summed in (3.27). To remove the sum over the classical spins from the weights, we enlarge the configuration $\mathcal{C}$ to be $[\mathcal{C} = (n, \tau_1, s_1, ..., \tau_n, s_n)]$ which means the summation over the classical spins becomes part of the sampling process and has no longer to be performed to obtain the weight factors $w_{\mathcal{C}}$. Second, when looking at the Hamiltonian H_0, we see it can be decomposed into a sum of three commuting operators, namely

$$H_0 = \frac{K}{\beta} + \sum_\sigma H_0^\sigma, \tag{3.28}$$

where H_0^σ contains only quadratic operators with index σ and therefore commutes with $H_0^{-\sigma}$. The weights are therefore a product of the individual weights of the spin components $\sigma = \uparrow, \downarrow$, leading to

$$d\mathcal{C} w_{\mathcal{C}} = \prod_{\sigma=\uparrow,\downarrow} \left\langle \prod_{l=1}^n \left[e^{\gamma s_l \sigma} - (e^{\gamma s_l \sigma} - 1) c_\sigma(\tau_l) c_\sigma^\dagger(\tau_l) \right] \right\rangle_0^\sigma e^{-K} \left(\frac{K d\tau}{\beta} \right)^n, \tag{3.29}$$

with the factor e^{-K} coming from the first term in (3.28) and $\langle ... \rangle_0^\sigma$ denoting the average with respect to H_0^σ.

Now, we switch to functional integral representation to compute the operator averages in the weight factors[4]. With this, the average in (3.29) transforms to

$$\left\langle \prod_{l=1}^n \left[e^{\gamma s_l \sigma} - (e^{\gamma s_l \sigma} - 1) c_\sigma(\tau_l) c_\sigma^\dagger(\tau_l) \right] \right\rangle_0^\sigma = \int \mathcal{D}[c_\sigma^\dagger, c_\sigma] e^{-S_{0\text{eff}}^\sigma} \prod_{l=1}^n \left[e^{\gamma s_l \sigma} - (e^{\gamma s_l \sigma} - 1) c_\sigma(\tau_l) c_\sigma^\dagger(\tau_l) \right], \tag{3.30}$$

where the non-interacting, effective action for spin σ reads

$$S_{0\text{eff}}^\sigma = \int_0^\beta d\tau d\tau' c_\sigma^\dagger(\tau) \left((\mathcal{G}_\sigma)^{-1}(\tau - \tau') \right) c_\sigma(\tau'), \tag{3.31}$$

and the non-interacting impurity Green's function is

$$(\mathcal{G}_\sigma)^{-1}(\tau) = \delta\tau(\partial_\tau - \mu_\sigma + \frac{U}{2}) - \Gamma_\sigma(\tau). \tag{3.32}$$

It is important to note that, the factor $U/2$ has been added here, which is valid only for the CT-AUX algorithm and is usually not present in the definition of the non-interacting impurity Green's function. This factor comes from the subtraction of $U/2n_\sigma$ in the definition of V in (3.22). The interacting Green's functions obtained by the sampling procedure again will coincide with the original impurity Green's functions.

We will now switch to a more general notation to compute the weight factors for the most general case, e.g. also directly applicable to generalized Grassmann variables like in Nambu notation or to cluster formulations, as we will see later. To do so, we introduce the matrices S, A, B with their elements

$$S_{ij} = (\mathcal{G}^{-1})_{i,j}(\tau_i - \tau_j), \quad A_{ij} = \delta_{ij} e^{\gamma s_i \sigma_i}, \quad B_{ij} = \delta_{ij}(1 - e^{\gamma s_i \sigma_i}), \tag{3.33}$$

---

[4]It would also be possible to obtain expression for the weight factors by applying Wick's theorem or using approximate formulas as in [65] or all other literature. However, using functional integrals is simply the most convenient way for us to deal with many-particle problems

where the indices i, j have to be understood as general indices, labeling for instance times, spins, lattice sites and so forth, and the Kronecker delta not only makes A and B diagonal but also shall be zero for unoccupied quantum states and times[5]. Then the integral to be computed is the Grassmann integral

$$
\begin{aligned}
\mathcal{I} &= \int \mathcal{D}[\zeta^*, \zeta] e^{-\zeta_i^* S_{ij} \zeta_j} \prod_l (A_{ll} - A_{ll} B_{ll} \zeta_l \zeta_l^*) \\
&= (\prod_l A_{ll}) \int \mathcal{D}[\zeta^*, \zeta] e^{-\zeta_i^* S_{ij} \zeta_j} \prod_l (1 + \zeta_l^* B_{ll} \zeta_l) = (\prod_l A_{ll}) \int \mathcal{D}[\zeta^*, \zeta] e^{-\zeta_i^* S_{ij} \zeta_j} e^{\zeta_l^* B_{ll} \zeta_l} \\
&= \det(A) \int \mathcal{D}[\zeta^*, \zeta] e^{-\zeta_i^* (S_{ij} - B_{ij}) \zeta_j} = \det(A) \det(S - B) \\
&= \det(A) \det(\mathbb{1} - BS^{-1}) \det(S) \qquad\qquad\qquad\qquad\qquad\qquad\qquad\qquad (3.34)
\end{aligned}
$$

The infinite matrix BS^{-1} consists of exactly n non-zero rows, where n is the perturbation order, leading to $\mathbb{1} - BS^{-1}$ being mainly diagonal with the exception of the n completely filled rows. Now we interchange the columns of $\mathbb{1} - BS^{-1}$ such that these n columns are the first n of the resulting matrix and the resulting determinant has to multiplied by $(-1)^m$, where m is the number of necessary permutations perform this interchange of columns. To get rid of this factor, we perform the same number of permutations to the rows of the resulting matrix, such that the prefactor becomes unity. The resulting matrix from these two operations is of the following structure

$$
M = \begin{pmatrix} \tilde{\mathbb{1}} - \tilde{B}\tilde{S}^{-1} & T \\ 0 & \mathbb{1} \end{pmatrix}, \qquad\qquad\qquad\qquad\qquad (3.35)
$$

where $\tilde{B}\tilde{S}^{-1}$ is the restriction of BS^{-1} to rows l and columns l' such that B has non-zero elements B_{ll} and $B_{l'l'}$, resulting from the interchanges of rows and columns and $\tilde{\mathbb{1}}$ is the n by n unity matrix. T is a non-zero matrix for which we do not care and $\mathbb{1}$ is the infinite dimensional unity matrix. Therefore, the desired determinant

$$
\det(\mathbb{1} - BS^{-1}) = (-1)^{2m} \det(M) = \det(\tilde{\mathbb{1}} - \tilde{B}\tilde{S}^{-1}) \det \mathbb{1} = \det(\tilde{\mathbb{1}} - \tilde{B}\tilde{S}^{-1}) \qquad (3.36)
$$

is identical to the determinant of the $n \times n$ matrix $\tilde{\mathbb{1}} - \tilde{B}\tilde{S}^{-1}$ and we find

$$
\mathcal{I} = \det(S) \det(\tilde{A} - \tilde{A}\tilde{B}\tilde{S}^{-1}). \qquad\qquad\qquad\qquad\qquad (3.37)
$$

The determinant of the infinite dimensional matrix S is just a constant and is independent of the elements of A and B and therefore the same for all weight factors. Its physical meaning is that of the non-interacting partition function Z_0.

With the result from this short detour, we can come back to the calculation of the average in (3.30), which we can easily identify as

$$
\int \mathcal{D}[c_\sigma^\dagger, c_\sigma] e^{-S_{0\text{eff}}^\sigma} \prod_{l=1}^n \left[e^{\gamma s_l \sigma} - (e^{\gamma s_l \sigma} - 1) c_\sigma(\tau_l) c_\sigma^\dagger(\tau_l) \right] = Z_{0\sigma} \det(N_\sigma^{-1}(\{s_i, \tau_i\})), \qquad (3.38)
$$

with the inverse configuration matrix

$$
N_\sigma^{-1}(\{s_i, \tau_i\}) = \tilde{A} - \tilde{A}\tilde{B}\tilde{S}^{-1} = e^{\Gamma_\sigma} - (e^{\Gamma_\sigma} - \mathbb{1}) G_{0\sigma} \qquad\qquad\qquad (3.39)
$$

consisting of the diagonal matrix

$$
(e^{\Gamma_\sigma})_{lm} = (\tilde{A})_{lm} = \delta_{lm} e^{\gamma s_l \sigma} \qquad\qquad\qquad\qquad\qquad (3.40)
$$

and the reduced Green's function

$$
(G_{0\sigma})_{lm} = (\tilde{S}^{-1})_{lm} = \mathcal{G}_\sigma(\tau_l - \tau_m). \qquad\qquad\qquad\qquad (3.41)
$$

---

[5]This means that for perturbation order n, only n diagonal elements of A and B are non-zero and the infinite residual elements are all equal to zero.

Finally, the weights $w_{\mathcal{C}}$ for a configuration $\mathcal{C} = (n, \tau_1, s_1, ..., \tau_n, s_n)$ can be written down as

$$d\mathcal{C}w_{\mathcal{C}} = e^{-K} \left(\frac{Kd\tau}{\beta} \right)^2 \prod_\sigma Z_{0\sigma} \det(N_\sigma^{-1}(\{s_i, \tau_i\})). \tag{3.42}$$

The weights are defined in terms of a inverse matrix N^{-1} merely by convention. For the weights a determinant has to be computed and the determinant of N^{-1} is the inverse determinant of N. In contrast, for the measurements, we will need the matrix N and not N^{-1} and therefore will always compute and store the matrix N instead of N^{-1}.

The next step in our derivation of the CT-AUX algorithm will be the computation of the measurement factors $g_{\mathcal{C}}$, which we will again perform in functional integral representation. According to (2.76), the measurement factors are obtained by the integrals

$$g_{\mathcal{C},\alpha\alpha'}(\tau) = \frac{\left\langle \mathcal{T} c_\alpha^\dagger(\tau) c_{\alpha'}(0) \prod_{l=1}^n V(\tau_l) \right\rangle_0}{\left\langle \mathcal{T} \prod_{l=1}^n V(\tau_l) \right\rangle_0}. \tag{3.43}$$

Since the AIM is diagonal in the spins σ, we can again separately determine spin up and spin down, while the interchanging term will be zero. This leads to the measurement factors in functional integral representation

$$g_{\mathcal{C},\sigma}(\tau) = \frac{\int \mathcal{D}[c_\sigma^\dagger, c_\sigma] e^{-S_{0\mathrm{eff}}^\sigma} c_\sigma(\tau) c_\sigma^\dagger(0) \prod_{l=1}^n \left[e^{\gamma s_l \sigma} - (e^{\gamma s_l \sigma} - 1) c_\sigma(\tau_l) c_\sigma^\dagger(\tau_l) \right]}{\int \mathcal{D}[c_\sigma^\dagger, c_\sigma] e^{-S_{0\mathrm{eff}}^\sigma} \prod_{l=1}^n \left[e^{\gamma s_l \sigma} - (e^{\gamma s_l \sigma} - 1) c_\sigma(\tau_l) c_\sigma^\dagger(\tau_l) \right]}. \tag{3.44}$$

We now switch again to a simplified expression using the matrices S, A, B defined above. Equation (3.44) corresponds to the integral

$$\begin{aligned} \mathcal{J} &= \frac{\int \mathcal{D}[\zeta^*, \zeta] e^{-\zeta_i^* S_{ij} \zeta_j} \prod_l (A_{ll} - A_{ll} B_{ll} \zeta_l \zeta_l^*) \zeta_x \zeta_y^*}{\int \mathcal{D}[\zeta^*, \zeta] e^{-\zeta_i^* S_{ij} \zeta_j} \prod_l (A_{ll} - A_{ll} B_{ll} \zeta_l \zeta_l^*)} \\ &= \frac{1}{\det(S) \det(\tilde{A} - \tilde{A}\tilde{B}\tilde{S}^{-1})} \det(\tilde{A}) \int \mathcal{D}[\zeta^*, \zeta] e^{-\zeta_i^* (S_{ij} - B_{ij}) \zeta_j} \zeta_x \zeta_y^* \\ &= (S - B)_{x,y}^{-1}, \end{aligned} \tag{3.45}$$

where we performed the same transformations as in (3.34) and simple integration rules for Gaussian integrals of Grassmann variables. The aim is now to relate the matrix element in (3.45) to an expression that we can deal with. Therefore, we start rearranging the matrix $(S - B)$ using the fact that S as well as $(1 - BS^{-1})$ are invertible[6], while B is not. We find

$$\begin{aligned} (S - B)^{-1} &= S^{-1}(1 - BS^{-1})^{-1} = S^{-1} + S^{-1} \left[(1 - BS^{-1})^{-1} - 1 \right] \\ &= S^{-1} + S^{-1}(1 - BS^{-1})^{-1} \left[1 - (1 - BS^{-1}) \right] \\ &= S^{-1} + S^{-1}(1 - BS^{-1})^{-1} BS^{-1}, \end{aligned} \tag{3.46}$$

which can be further simplified by looking at the structure of $(1 - BS^{-1})$ and B. From the previous calculations we know, when working in the permuted basis, that

$$(1 - BS^{-1}) = \begin{pmatrix} \tilde{1} - \tilde{B}\tilde{S}^{-1} & T \\ 0 & 1 \end{pmatrix} \quad \text{and} \quad B = \begin{pmatrix} \tilde{B} & 0 \\ 0 & 0 \end{pmatrix} \tag{3.47}$$

and therefore the matrix product

$$(1 - BS^{-1})^{-1} B = \begin{pmatrix} (\tilde{1} - \tilde{B}\tilde{S}^{-1})^{-1} & X \\ 0 & 1 \end{pmatrix} \begin{pmatrix} \tilde{B} & 0 \\ 0 & 0 \end{pmatrix} = \begin{pmatrix} (\tilde{1} - \tilde{B}\tilde{S}^{-1})^{-1}\tilde{B} & 0 \\ 0 & 0 \end{pmatrix} \tag{3.48}$$

---

[6]The matrix S is invertible since its inverse is the Green's function, and the matrix $(1 - BS^{-1})$ is invertible as long as the weights are larger than zero, while configurations with zero weight are simply not considered.
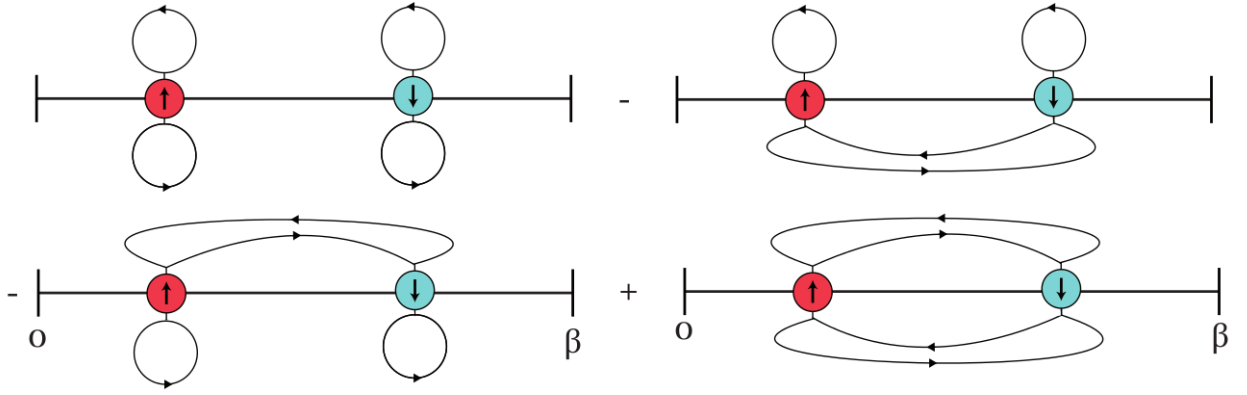
Figure 3.2: Illustration of the four distinct diagrams forming the weight factor $w_{\mathcal{C}}$ for a configuration $\mathcal{C} = (n = 2, s_1 = \uparrow, \tau_1, s_2 = \downarrow, \tau 2)$ consisting of a classical up- and down-spin. Since the interaction is only of density-density type, there are only $(n!)^2 = 4$ instead of $(2n)! = 24$ diagrams contributing to $w_{\mathcal{C}}$.

vanishes completely on the subspace where no configurations have been inserted. On the subspace with non-zero matrix elements of B, B and also A are invertible and we can insert the matrix $\tilde{A}$ into this equation, leading to

$$(\mathbb{1} - BS^{-1})^{-1}B = \begin{pmatrix} (\tilde{A} - \tilde{A}\tilde{B}\tilde{S}^{-1})^{-1}\tilde{A}\tilde{B} & 0 \\ 0 & 0 \end{pmatrix} = \begin{pmatrix} N_\sigma(\{s_i, \tau_i\})(e^{\Gamma_\sigma} - \mathbb{1}) & 0 \\ 0 & 0 \end{pmatrix}. \quad (3.49)$$

This can be translated back to the configuration measurements $g_{\mathcal{C}}$ directly, leading to

$$g_{\mathcal{C}\sigma}(\tau_x - \tau_y) = (S - B)^{-1}_{x,y} = \mathcal{G}_\sigma(\tau_x - \tau_y) + \mathcal{G}_\sigma(\tau_x - \tau_i)\left[N_\sigma(\{s_i, \tau_i\})(e^{\Gamma_\sigma} - \mathbb{1})\right]_{i,j}\mathcal{G}_\sigma(\tau_j - \tau_y). \quad (3.50)$$

With this, we have derived the formulas for the weights $w_{\mathcal{C}}$ and the measurement factors $g_{\mathcal{C}}$ and found the proper configurations $\mathcal{C} = (n, s_1, \tau_1, ..., s_n, \tau_n)$, which are the necessary ingredients for a Markov-Chain sampling. The only required informations are the non-interacting Green's functions $\mathcal{G}_\sigma$ of the impurity and the computation of the parameters e^γ and $e^{-\gamma}$ at the beginning of the sampling process.

3.2.2 The Sampling Procedure

For the sampling procedure, the proposal probabilities have to be found such that ergodicity (see chapter Markov-Chains) of the Markov-Chain is guaranteed. Since the configurations $\mathcal{C} = (n, s_1, \tau_1, ..., s_n, \tau_n)$ consist of the perturbation order n and n tuples $(\tau_i, s_i) \in [0, \beta] \times \{-1, 1\}$ one possible choice of changing a configuration $\mathcal{C} = (n, s_1, \tau_1, ..., s_n, \tau_n)$ would be to either increase the perturbation order by one to $n + 1$ by inserting a randomly chosen tuple (τ_{n+1}, s_{n+1}) or to decrease the perturbation order by one to $n - 1$ by removing a existing tuple $(\tau_i, s_i), i = 1, ...n$. These will, in fact, be the updates that we chose for the Metropolis algorithm. The probabilities will be called the removal probability for decreasing the perturbation order $n + 1 \rightarrow n$ and the insertion probability for the increase of the perturbation order $n \rightarrow n + 1$. The corresponding probabilities are decomposed into a proposal probability and an acceptance probability, i.e. $p(n \rightarrow n \pm 1) = p^{\text{acc}}(n \rightarrow n \pm 1)p^{\text{prop}}(n \rightarrow n \pm 1)$. For an insertion of a tuple (τ, s), a random time is picked from the interval $[0, \beta]$ with uniform probability distribution the corresponding probability is $p_1 = \frac{d\tau}{\beta}$ [7]. The spin s is independently and uniformly chosen from the set $\{-1, 1\}$ with probability $p_2 = 1/2$. The proposal probability for inserting a tuple (τ, s) therefore becomes $p^{\text{prop}}(n \rightarrow n+1) = p_1 p_2 = \frac{d\tau}{2\beta}$ and is independent of n. On the other hand, when removing a tuple (τ_i, s_i) from the configuration $\mathcal{C} = (n + 1, ...)$, this tuple must be chosen to be part of the existing $n + 1$. This is again chosen uniformly, leading to $p^{\text{prop}}(n+1 \rightarrow n) = \frac{1}{n+1}$. This choice of proposal probabilities, allowing

---

[7]Practically, it is impossible to chose τ in a continuous interval for instance because every random number generator only retains discrete values and $d\tau$ has to be understood as the width of the single intervals from which τ is chosen.

for insertion and removal of pairs (s, τ) seems to fulfill ergodicity, since any configuration $\mathcal{C} = (n, ...)$ can be reached from any other configuration $\mathcal{C}' = (n', ...)$ in $n + n'$ steps with finite probability by removing all n' tuples and inserting n distinct ones (of course, many other possible ways exist to reach $\mathcal{C}$ from $\mathcal{C}'$). With the weight factors from the previous section (3.42)

$$d\mathcal{C}w_\mathcal{C} = e^{-K} \left(\frac{K d\tau}{\beta} \right)^n \prod_\sigma Z_{0\sigma} \det(N_\sigma^{-1}(\mathcal{C})), \tag{3.51}$$

the acceptance probabilities can be obtained via the detailed balance condition (2.34)

$$\frac{p^{\mathrm{acc}}(n \to n+1)}{p^{\mathrm{acc}}(n+1 \to n)} = \frac{2\beta}{(n+1)d\tau} \frac{w_{n+1}}{w_n}, \tag{3.52}$$

leading to the ratio

$$\frac{p^{\mathrm{acc}}(n \to n+1)}{p^{\mathrm{acc}}(n+1 \to n)} = \frac{K}{n+1} \prod_\sigma \frac{\det(N_\sigma^{-1}(n+1))}{\det(N_\sigma^{-1}(n))}, \tag{3.53}$$

where we have used a shorthand notation and replaced $\mathcal{C}, \mathcal{C}'$ by $n, n+1$, respectively. The acceptance
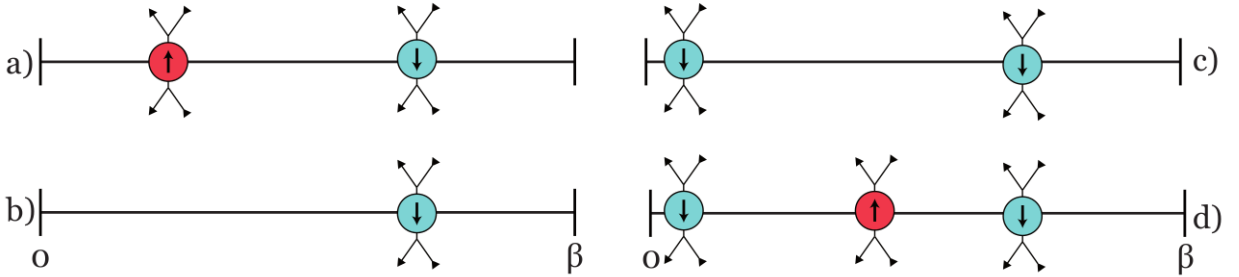
Figure 3.3: Schematic picture of four possible subsequent steps in the Markov-Chain of a CT-AUX sampling. a) starts with two distinct auxiliary spins at distinct times, in the next move, the spin-up vertex is removed (b) and another spin-down vertex is inserted (c). In the following step, a spin-up vertex is inserted again but at a distinct time (d).

probabilities are then determined according to the Metropolis formula (2.37) as

$$p^{\mathrm{acc}}(n \to n+1) = \min \left\{ 1, \frac{K}{n+1} \prod_\sigma \frac{\det(N_\sigma^{-1}(n+1))}{\det(N_\sigma^{-1}(n))} \right\}, \tag{3.54}$$

$$p^{\mathrm{acc}}(n+1 \to n) = \min \left\{ 1, \frac{n+1}{K} \prod_\sigma \frac{\det(N_\sigma^{-1}(n))}{\det(N_\sigma^{-1}(n+1))} \right\}. \tag{3.55}$$

The updates introduced above have been found to ensure ergodicity for all the parameter regimes, the CT-AUX algorithm has been applied to [67]. However, it may useful to implement also other possible moves of the Markov- Chain, which can reduce the auto-correlation time and may be much faster that the proposed insertion and removal updates. For instance one possible move is to flip an existing spin variable, i.e. going from configuration $\mathcal{C} = (n, s_1, \tau_1, ..., s_i, \tau_i, ..., s_n, \tau_n)$ to configuration $\mathcal{C} = (n, s_1, \tau_1, ..., -s_i, \tau_i, ..., s_n, \tau_n)$.

Because of the symmetry of the Hamiltonian in the classical spins, these moves should always have an sufficiently large probability and therefore be accepted (and required) very often, which reduces the auto-correlation time significantly. The other advantage of these moves is that they are much faster performed than an insertion or removal of a tuple (s, τ). However, the disadvantage is that they only contribute minimally to the ergodicity, since the subspace that is reachable with spin-flipping updates is very small compared to the complete configuration space. There also exist other possible Markov-Chain moves for this problem, however the most important are the insertion and removal updates that have been discussed

in this part. At the end, one can never be completely sure that ergodicity is ensured with these updates for the whole parameter regime of the AIM and therefore the sampling process has always to be reviewed when starting to investigate a new physical regime with Monte-Carlo solvers.

Steps of the Sampling Process

The individual steps of the sampling process are illustrated in the CT-AUX flow diagram in Fig. 3.4.
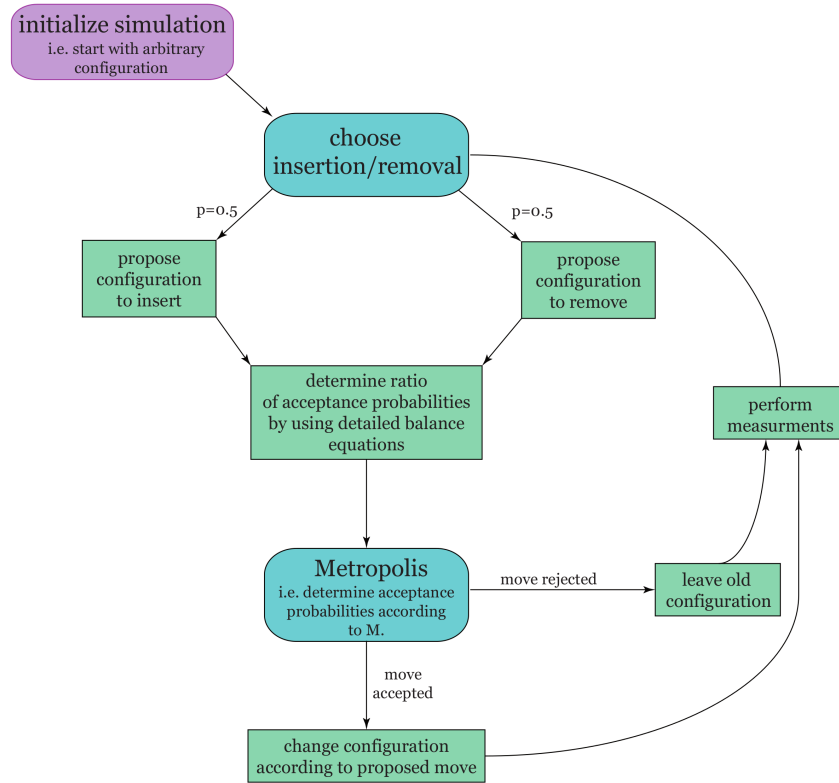

Figure 3.4: Monte-Carlo flow diagram for the CT-AUX algorithm.

- Initialization: At the beginning of the sampling process one possible configuration must be determined (from outside) as the starting configuration to initialize the sampling procedure.

- For the current configuration $\mathcal{C}$ a possible update has to be chosen, either the insertion or the removal of a tuple (τ, s). Where both have the same probability to not influence the detailed balance formulas above.

- A new configuration must be proposed, either with a tuple (τ, s) less or more, depending on the previous step.

- The acceptance probability for this new configuration is determine according to the Metropolis probabilities ((3.54) and (3.55)).

- Either the new configuration is accepted, then the old configuration will be replaced or the new configuration is rejected, then the old configuration stays unchanged and the new configuration is discarded.

- A measurement of the observables, i.e. the $g_{\mathcal{C}}$'s, is performed (these may be many observables).

- The whole procedure except the initialization is repeated.

Of course, this just the most simple example for a running CT-AUX algorithm. In between, there may be implemented additional updates, such as the spin-flip updates discussed above. Another important point, already discussed in chapter 2 is whether it makes sense to measure the observables in every single step or if the gain in accuracy is much worse than the loss in computation speed. Therefore, Fig. 3.4 illustrates the basic principle of the CT-AUX sampling and a realistic sampling would look quite different, although the basic principle remains unchanged.

In the previous two sections, we have derived all the necessary formulas and the basic Monte-Carlo algorithm to determine the interacting Green's functions of the AIM as it was described above. We will extend these formulas a cluster of impurities, which are coupled to each other, and impurities which are no longer diagonal in the spin index, either caused by spin-mixing processes or superfluid pairing and show explicit calculations for these systems in the following chapter. In this chapter, before we come to the derivation of a distinct Monte-Carlo solver, we will derive efficient matrix manipulation formulas for the CT-AUX solver, which speed up the calculations of the matrices N_σ and the weights $w_\mathcal{C}$ incredibly.

3.2.3   Fast Matrix Manipulations

The formulas for the weights and measurements in the previous section strongly depended on the matrices N_σ, N_σ^{-1} respectively. In this section, we will derive formulas how to determine the ratio of the weights for a removal or an insertion $n \to (n \pm 1)$ for the case that the matrices $N_\sigma^{(n)}$ are known and show how to determine the new matrices $N_\sigma^{(n\pm1)}$ after a move has been accepted. The structure of the $n \times n$ matrix $N_\sigma^{(n)}$ is determined by equation (3.39), stating

$$(N_\sigma^{(n)})^{-1}_{ij} = \delta_{ij}e^{\gamma s_i \sigma} - (e^{\gamma s_i \sigma} - 1)G_{0\sigma}(\tau_i - \tau_j). \tag{3.56}$$

For the acceptance probability for insertion of the tuple (s, τ), the ratio

$$\mathcal{R} = \frac{\det(N_\sigma^{(n+1)})^{-1}}{\det(N_\sigma^{(n)})^{-1}} \tag{3.57}$$

is required. The updated matrix $(N_\sigma^{(n+1)})^{-1}$ can then be written as

$$(N_\sigma^{(n+1)})^{-1} = \begin{pmatrix} (N_\sigma^{(n)})^{-1} & Q \\ R & S \end{pmatrix}, \tag{3.58}$$

where the $n \times 1$ vector Q, the $1 \times n$ vector R and the scalar S are defined as

$$Q_l = -(e^{\gamma s_l \sigma} - 1)G_{0\sigma}(\tau_l - \tau), \tag{3.59}$$

$$R_l = -(e^{\gamma s \sigma} - 1)G_{0\sigma}(\tau - \tau_l), \tag{3.60}$$

with $1 \leq l \leq n$ and

$$S = e^{\gamma s \sigma} - (e^{\gamma s \sigma} - 1)G_{0\sigma}(0^+). \tag{3.61}$$

The ratio (3.57) can be rewritten as

$$\mathcal{R} = \det \begin{pmatrix} N_\sigma^{(n)} & 0 \\ 0 & 1 \end{pmatrix} \det \begin{pmatrix} (N_\sigma^{(n)})^{-1} & Q \\ R & S \end{pmatrix} = \det \begin{pmatrix} \mathbb{1} & N_\sigma^{(n)}Q \\ R & S \end{pmatrix} = S - RN_\sigma^{(n)}Q. \tag{3.62}$$

For the acceptance probability of an insertion, the matrices $N_\sigma^{(n)}$ are required and the vectors R, Q as well as the scalar S have to be determined. Then the probability is given by the vector matrix product of (3.62). If the insertion is accepted, the matrix $N_\sigma^{(n+1)}$ must be computed. Similar to $(N_\sigma^{(n+1)})^{-1}$, we write

$$N_\sigma^{(n+1)} = \begin{pmatrix} \tilde{P} & \tilde{Q} \\ \tilde{R} & \tilde{S} \end{pmatrix} \tag{3.63}$$

and compute the matrix product

$$
\begin{aligned}
\mathbb{1} &= N^{(n+1)}(N^{(n+1)})^{-1} = \left(\begin{array}{cc} \tilde{P} & \tilde{Q} \\ \tilde{R} & \tilde{S} \end{array} \right) \left(\begin{array}{cc} (N^{(n)})^{-1} & Q \\ R & S \end{array} \right) \\
&= \left(\begin{array}{cc} (N^{(n)})^{-1}\tilde{P} + Q\tilde{R}^{(3)} & (N^{(n)})^{-1}\tilde{Q} + \tilde{S}Q^{(1)} \\ R\tilde{P} + \tilde{R}S^{(4)} & R\tilde{Q} + S\tilde{S}^{(2)} \end{array} \right).
\end{aligned}
\tag{3.64}
$$

Formula 3.64 contains four different equations, stating

$$
(1) \qquad (N^{(n)})^{-1}\tilde{Q} + \tilde{S}Q = 0 \;\Leftrightarrow\; \tilde{Q} = -N^{(n)}Q\tilde{S},
\tag{3.65}
$$

$$
(2) \qquad R\tilde{Q} + S\tilde{S} = 1 \;\Leftrightarrow\; \tilde{S}(S - RN^{(n)}Q) = 1 \;\Leftrightarrow\; \tilde{S} = \frac{1}{S - RN^{(n)}Q},
\tag{3.66}
$$

$$
(3) \qquad (N^{(n)})^{-1}\tilde{P} + Q\tilde{R} = \mathbb{1} \;\Leftrightarrow\; \tilde{P} = N^{(n)}(\mathbb{1} - Q\tilde{R}),
\tag{3.67}
$$

$$
(4) \qquad R\tilde{P} + \tilde{R}S = 0 \;\Leftrightarrow\; RN^{(n)}(\mathbb{1} - Q\tilde{R}) + \tilde{R}Q = 0 \;\Leftrightarrow\; \tilde{R} = -RN^{(n)}\tilde{S}.
\tag{3.68}
$$

Combining these equations, leads to the desired equations which, step by step, determine the matrix $N^{(n+1)}$:

$$
\begin{aligned}
\tilde{S} &= (S - RN^{(n)}Q)^{-1}, & (3.69) \\
\tilde{Q} &= -N^{(n)}Q\tilde{S}, & (3.70) \\
\tilde{R} &= -\tilde{S}RN^{(n)}, & (3.71) \\
\tilde{P} &= N^{(n)} + \tilde{Q}\tilde{S}^{-1}\tilde{R}. & (3.72)
\end{aligned}
$$

For a removal, the steps to determine the weights and the updated matrix are even simpler. Suppose the removal of the lth tuple (s_l, τ_l) has been proposed. Without loss of any information, the matrix $N^{(n+1)}$ can be rearranged such that the lth and $(n + 1)$th component interchange position. Then the ratio of the determinants is simply determined by

$$
\mathcal{R} = S - RN^{(n)}Q = \tilde{S}^{-1}.
\tag{3.73}
$$

And the updated matrix $N^{(n)}$ is determined by rearranging (3.73) to

$$
N^{(n)} = \tilde{P} - \tilde{Q}\tilde{S}^{-1}\tilde{R},
\tag{3.74}
$$

where $\tilde{Q}, \tilde{R}$ are simply the column, row vectors corresponding to the index l.

The weight ratios and update formulas never require the inversion of a matrix or the computation of a determinant, only matrix vector multiplications and therefore the whole procedure scales with n^2 the perturbation order squared, which makes this algorithm very efficient. As we have previously seen in the measurement factors there is also only required a matrix vector multiplication with the matrix $N^{(n)}$ and the non-interacting Green's functions. This simplicity in the computation of all required ingredients for the sampling and measurement procedure confirms the choice of the proposal probabilities from the previous section. With this rather technical aspect of the efficient computation of weight ratios and updates, we finish this introductory section on the CT-AUX algorithm. For further developments, technical details and efficiency analysis, we refer to the literature, i.e. [70, 65, 69, 64, 67].

3.2.4 Benchmarking and Performance Analysis

When implementing a new numerical method, one has to ensure both that the algorithm achieves correct results, i.e. by comparing the results to other numerical methods[8], and that the algorithm has good performance, i.e. is accurate and fast enough for the desired application. To analyze the first point, we compared the results of the CT-AUX algorithm for the interacting Green's functions of an Anderson impurity model with finite bath size $S = 6$ to the exact results obtained from diagonalization of the Hamiltonian. A set of results, together with a Monte-Carlo error analysis is shown in Fig. 3.5, where a good agreement between MC and ED results can be found. Note that CT-AUX is an exact method
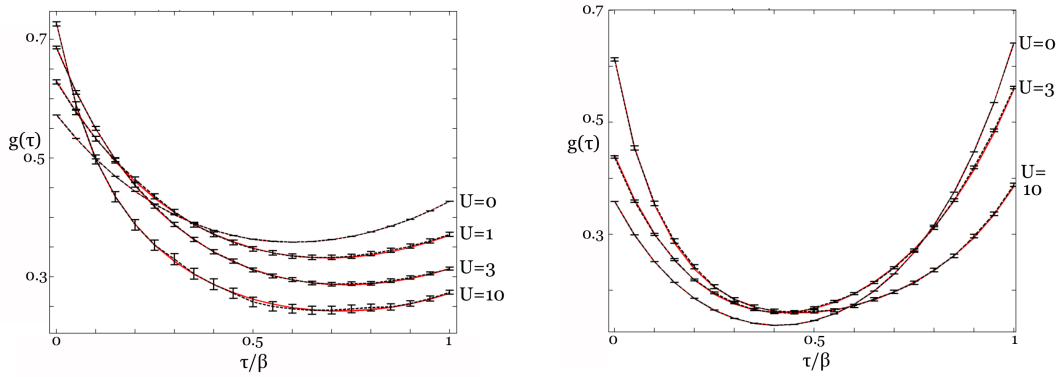
Figure 3.5: Comparison of Green's functions for the AIM with three bath states for every spin σ for different interaction strengths U at $\beta = 1$. The black dashed lines are the Monte-Carlo results, obtained with the CT-AUX algorithm and the red lines are the exact results from diagonalization of the Hamiltonian. The error bars are obtained from a converged binning analysis. For interactions $U = 0, 1, 3$, the calculation used 10^6 Monte-Carlo steps, for $U = 10$ we used 10^7 sampling steps. Left: Bath energies $\epsilon_\sigma = (1, -1, 1)$, hybridization parameters $V_\sigma = (1, -1, 1)$. Right: Bath energies $\epsilon_\sigma = (3, 2, 1)$, hybridization parameters $V_\sigma = (1, 2, 3)$.

and the error can be made arbitrary small by increasing the number of Monte-Carlo iterations. Another important point is the speed of the algorithm or in other words, the necessary time to obtain acceptable results from numerical calculations. This has been done by E. Gull *et al.* [65] for both the CT-AUX and CT-HYB impurity solvers [70] by analyzing the size of the matrices N_σ during the CT-AUX samplings (and M_σ for CT-HYB). The majority of time during the sampling is spent on the manipulations of these matrices, which means the speed of the algorithm mainly depends on how fast these manipulations can be performed and therefore on the size of these matrices. The growth of the matrix size is shown in Fig. 3.6 for CT-AUX, CT-HYB and Hirsch-Fye algorithms, where the latter is not explained in this thesis. However, from our simulations we do not fully agree with their conclusion, since it is not obvious that small matrix sizes are desirable. It is clear that the size can be directly connected to the speed of the algorithm, on the other hand, small matrices mean strong fluctuations in the measurements and therefore much more sampling steps are required to obtain the same accuracy than for larger matrices, where the fluctuations are much smaller. Therefore a compromise has to be found between small matrix sizes with fast updates and larger matrices but more accurate measurements. The average perturbation order $\langle n \rangle$ (which is the average size of the matrices) can be influenced by the parameter K, introduced to the CT-AUX algorithm at the beginning, by the formula [67, 70]

$$\langle n \rangle = K - \beta U \langle n_\uparrow n_\downarrow - (n_\uparrow + n_\downarrow)/2 \rangle, \tag{3.75}$$

which means it can be adjusted by a proper choice of K. For small $U < 5\beta$ we chose $K = 5$ and otherwise $K = 1$, which seemed to be a better choice than keeping $\langle n \rangle$ and therefore the matrices as small as possible. Further and much more detailed analysis can for instance be found in [69, 67, 70].

3.3 Continuous-Time Hybridization Expansion Quantum Monte-Carlo Algorithm

In this section, the continuous-time hybridization expansion algorithm (CT-HYB) is derived. This algorithm is in some sense complementary to the previously introduced CT-AUX, since it is not an expansion in the interaction as for the latter, but an expansion in the hybridization function. This algorithm was

---

[8]This may be only possible in some limiting cases, when other methods, such as for instance exact diagonalization, can be applied.
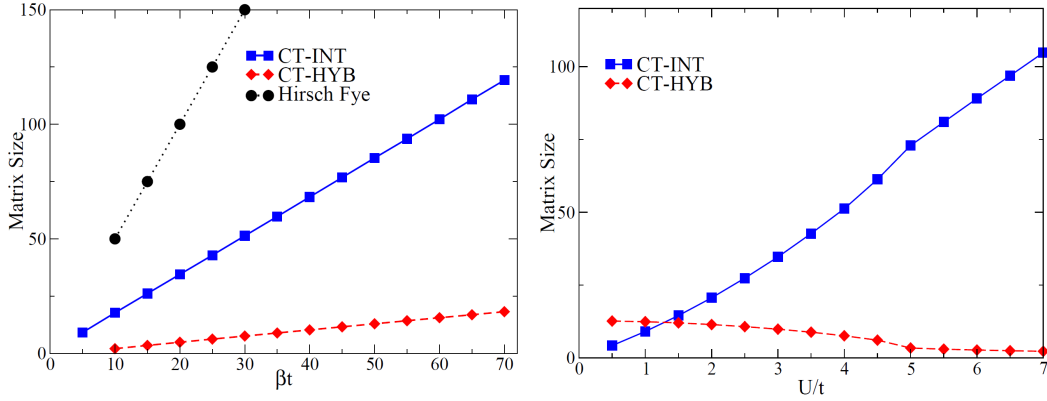
Figure 3.6: Average perturbation order of the CT-AUX algorithm (blue line, here denoted as CT-INT) as a function of (left) βt, where the ratio $U/t = 4$ is kept fixed and (right) as a function of U/t when $\beta t = 30$ is kept fixed. The value t enters the AIM through the hybridization function $\Gamma(\tau)$, which corresponds to a 3-dimensional Hubbard Hamiltonian with hopping t. The matrix size increases almost linearly with the factor βU, which can also be obtained from (3.75). Figure from [70].

developed as impurity solver for the AIM [189, 191] to treat parameter regimes with large interactions much more efficient than it is done for the CT-AUX solver [192]. It is also perfectly suited for extended impurity model, consisting of multiple orbitals not coupled via the hybridization function but via the interaction, as it was done in [191, 193]. As for the CT-AUX solver, we will stick to the basic formulation of the configurations, weights and observables and derive the general sampling procedure and leave extensions and improvements of this solver to the next chapter.

3.3.1 Configurations, Weights and Observables

To find the configurations and weights, we follow an opposite way as for the CT-AUX solver, namely, we start with a functional integral formulation of the AIM and switch back to operator notation after an expansion of the effective action exponential in the hybridization function. The effective action of the AIM reads (3.6)

$$
\begin{aligned}
S_{\text{eff}} &= \int d\tau \left[\sum_\sigma c_\sigma^\dagger(\tau)(\partial_\tau - \mu_\sigma)c_\sigma(\tau) + U n_\uparrow(\tau)n_\downarrow(\tau) \right] - \int d\tau d\tau' \sum_\sigma c_\sigma^\dagger(\tau)\Gamma_\sigma(\tau - \tau')c_\sigma(\tau') \\
&= S_0 - \int d\tau d\tau' \sum_\sigma c_\sigma^\dagger(\tau)\Gamma_\sigma(\tau - \tau')c_\sigma(\tau') \quad\quad\quad (3.76)
\end{aligned}
$$

where the first part (i.e. S_0) is local in time, i.e. has a direct operator correspondence. The second part, the hybridization, is non-local in time since it results from the integration over the infinite bath. The idea is now, to expand the partition function in terms of the hybridization function Γ. In the expansion,

we denote n_σ as the perturbation order of spin σ and $n = n_\uparrow + n_\downarrow$ as the total perturbation order. The partition function in the functional integral representation is given by the integral

$$
\begin{aligned}
Z &= \int \mathcal{D}[c^\dagger, c\,] e^{-S_{\text{eff}}} \\
&= \int \mathcal{D}[c^\dagger, c\,] e^{-S_0} \left[\prod_{\sigma=\uparrow\downarrow} \sum_{n_\sigma=0}^{\infty} \frac{1}{n_\sigma!} \prod_{l_\sigma=1}^{n_\sigma} \int d\tau_l^{c_\sigma^\dagger} d\tau_l^{c_\sigma} \, c_\sigma^\dagger(\tau_l^{c_\sigma^\dagger}) \Gamma_\sigma(\tau_l^{c_\sigma^\dagger} - \tau_l^{c_\sigma}) c_\sigma(\tau_l^{c_\sigma}) \right] \\
&= \sum_{n_\sigma=0}^{\infty} \frac{1}{n_\uparrow! n_\downarrow!} \left[\prod_{\sigma=\uparrow\downarrow, l=1}^{n_\sigma} \int d\tau_l^{c_\sigma^\dagger} d\tau_l^{c_\sigma} \, \Gamma_\sigma(\tau_l^{c_\sigma^\dagger} - \tau_l^{c_\sigma}) \right] \\
&\quad \times \int \mathcal{D}[c^\dagger, c\,] e^{-S_0} \prod_{\sigma=\uparrow\downarrow, l=1}^{n_\sigma} c_\sigma^\dagger(\tau_l^{c_\sigma^\dagger}) c_\sigma(\tau_l^{c_\sigma}).
\end{aligned}
\tag{3.77}
$$

The functional integral on the right side of this equation has a direct operator correspondence and we can rewrite the integral as an time-ordered operator average $\langle ... \rangle_0$ with respect to the Hamiltonian

$$
H_0 = -\sum_\sigma \mu_\sigma n_\sigma + U n_\uparrow n_\downarrow,
\tag{3.78}
$$

resulting in the expression

$$
\begin{aligned}
Z &= \sum_{n_\sigma=0}^{\infty} \frac{1}{n_\uparrow! n_\downarrow!} \left[\prod_{\sigma=\uparrow\downarrow, l=1}^{n_\sigma} \int d\tau_l^{c_\sigma^\dagger} d\tau_l^{c_\sigma} \, \Gamma_\sigma(\tau_l^{c_\sigma^\dagger} - \tau_l^{c_\sigma}) \right] \left\langle \mathcal{T} \prod_{\sigma=\uparrow\downarrow, l=1}^{n_\sigma} c_\sigma^\dagger(\tau_l^{c_\sigma^\dagger}) c_\sigma(\tau_l^{c_\sigma}) \right\rangle_0 \\
&= \sum_{n_\sigma=0}^{\infty} \frac{1}{(n_\uparrow! n_\downarrow!)^2} \left[\prod_{\sigma=\uparrow\downarrow, l=1}^{n_\sigma} \int d\tau_l^{c_\sigma^\dagger} d\tau_l^{c_\sigma} \, \det\left(M_\sigma^{-1}(\{\tau_l^{c_\sigma^\dagger}, \tau_l^{c_\sigma}\}) \right) \right] \\
&\quad \times \left\langle \mathcal{T} \prod_{\sigma=\uparrow\downarrow, l=1}^{n_\sigma} c_\sigma^\dagger(\tau_l^{c_\sigma^\dagger}) c_\sigma(\tau_l^{c_\sigma}) \right\rangle_0.
\end{aligned}
\tag{3.79}
$$

In the last step, the matrix $M_\sigma^{-1}(\{\tau_l^{c_\sigma^\dagger}, \tau_l^{c_\sigma}\})$ has been introduced, which contains the elements

$$
\left(M_\sigma^{-1}(\{\tau_l^{c_\sigma^\dagger}, \tau_l^{c_\sigma}\}) \right)_{ij} = \Gamma_\sigma(\tau_i^{c_\sigma^\dagger} - \tau_j^{c_\sigma}),
\tag{3.80}
$$

which leads to $n_\sigma!$ products instead of a single one and enforces the additional factor $1/(n_\sigma!)$ in equation (3.79). Note that the sign of the determinant exactly cancels with the sign that results from the time-ordering operator and so there is no sign problem. The integrals and the two sums over the perturbation order for spin-up and spin-down operators in (3.79) are supposed to be sampled by the Monte-Carlo process, which identifies the configurations $\mathcal{C} = (n_\uparrow, n_\downarrow, \{(\tau_l^{c_\sigma^\dagger}, \tau_{l_\sigma}^{c_\sigma}) | l_\sigma = 1, ..., n_\sigma, \sigma = \uparrow\downarrow\}$, consisting of the perturbation orders $n_\uparrow, n_\downarrow$ for spin up, spin down and the $2n_\sigma$ times $(\tau_l^{c_\sigma^\dagger}, \tau_{l_\sigma}^{c_\sigma})$ for the respective creation and annihilation operators. In the Monte-Carlo procedure, the creation operators will be integrated in a time-ordered form, as well as the annihilation operators but the ordering of creation operators with respect to annihilation operators will not be performed. This cancels exactly the factors $1/(n_\sigma)^2$ from equation (3.79) above and leads to the formula for the weights

$$
d\mathcal{C} \, w_\mathcal{C} = \prod_\sigma (d\tau)^{2n_\sigma} \det\left(M_\sigma^{-1}(\{\tau_l^{c_\sigma^\dagger}, \tau_l^{c_\sigma}\}) \right) \left\langle \prod_{\sigma=\uparrow\downarrow, l_\sigma=1}^{n_\sigma} c_\sigma^\dagger(\tau_l^{c_\sigma^\dagger}) c_\sigma(\tau_l^{c_\sigma}) \right\rangle_0.
\tag{3.81}
$$

The next step is then to find an analytic expression for the trace

$$
\left\langle \prod_{\sigma=\uparrow\downarrow, l_\sigma=1}^{n_\sigma} c_\sigma^\dagger(\tau_l^{c_\sigma^\dagger}) c_\sigma(\tau_l^{c_\sigma}) \right\rangle_0 = \sum_{n_\uparrow, n_\downarrow=0,1} \langle n_\uparrow, n_\downarrow | e^{-\beta H_0} \left(\prod_{\sigma=\uparrow\downarrow, l_\sigma=1}^{n_\sigma} c_\sigma^\dagger(\tau_l^{c_\sigma^\dagger}) c_\sigma(\tau_l^{c_\sigma}) \right) | n_\uparrow, n_\downarrow \rangle,
\tag{3.82}
$$

which is rather easy, since for any configuration $\mathcal{C}$, only of the four summands in the trace will be non-zero. As mentioned above, the creation operators stay time-ordered with respect to annihilation operators and therefore in the product in (3.82) either all operators for a given spin component are ordered as $c_\sigma(\tau_{n_\sigma}^{c_\sigma})c_\sigma^\dagger(\tau_{n_\sigma}^{c_\sigma^\dagger}), ..., c_\sigma(\tau_1^{c_\sigma})c_\sigma^\dagger(\tau_1^{c_\sigma^\dagger})$ or as $c_\sigma^\dagger(\tau_{n_\sigma}^{c_\sigma^\dagger})c_\sigma(\tau_{n_\sigma}^{c_\sigma}), ..., c_\sigma^\dagger(\tau_1^{c_\sigma^\dagger})c_\sigma(\tau_1^{c_\sigma})$, where the latter introduces a factor of (-1) because of the changed ordering. A trace of the first product in the space of spin σ, i.e. $n_\sigma = \{0, 1\}$, will have only one non-zero contribution, namely from the state $|n_\sigma = 1\rangle$, whereas in the second product the non-vanishing contribution results from the state $|n_\sigma = 0\rangle$, which clearly illustrates for the statement above that only a single state $|n_\uparrow, n_\downarrow\rangle$ contributes to the trace (3.82). The configurations $\mathcal{C}$ are best understood in terms of a segment picture of the impurity, which we now introduce.

The non-zero trace-factor for the product $c_\sigma(\tau_{n_\sigma}^{c_\sigma})c_\sigma^\dagger(\tau_{n_\sigma}^{c_\sigma^\dagger}), ..., c_\sigma(\tau_2^{c_\sigma})c_\sigma^\dagger(\tau_2^{c_\sigma^\dagger})c_\sigma(\tau_1^{c_\sigma})c_\sigma^\dagger(\tau_1^{c_\sigma^\dagger})$ belongs to the state $|n_\sigma = 0\rangle$, i.e. at time $\tau = 0$ the impurity is unoccupied. Then at time $\tau = \tau_1^{c_\sigma^\dagger}$ a spin-σ particle is inserted and stays in the impurity until it is removed at $\tau = \tau_1^{c_\sigma}$ and the impurity is empty again until at $\tau_2^{c_\sigma^\dagger}$ a particle is inserted again and so on. These time intervals when the impurity is occupied by a spin up or spin down particle are called segments and uniquely define the configurations $\mathcal{C}$. When the trace factor belongs to the occupied state $|n_\sigma = 1\rangle$, we can interpret the respective product $c_\sigma^\dagger(\tau_{n_\sigma}^{c_\sigma^\dagger})c_\sigma(\tau_{n_\sigma}^{c_\sigma}), ..., c_\sigma^\dagger(\tau_1^{c_\sigma^\dagger})c_\sigma(\tau_1^{c_\sigma})$ as starting with an occupied impurity, i.e. with an occupied interval $[0, \tau_1^{c_\sigma}]$, and also end with an occupied impurity, i.e. with the interval $[\tau_{n_\sigma}^{c_\sigma^\dagger}, \beta]$. Combining these two intervals, the result is a single interval $[\tau_{n_\sigma}^{c_\sigma^\dagger}, \tau_1^{c_\sigma}]$, which belongs to a segment that winds around and crosses the interval boundaries from β to zero. For such segments, an additional factor (-1) has to be introduced, as explained above, because of exchanged ordering.

In the segment picture, the trace-factor can be determined in terms of segment properties and is given by
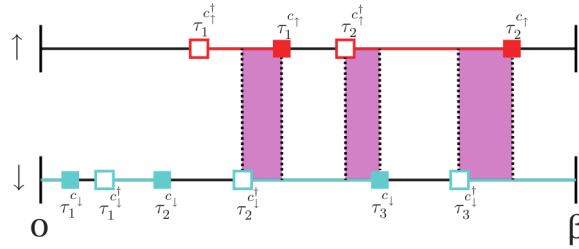
Figure 3.7: Illustration of a configuration $\mathcal{C}$ in the segment picture. There are two pairs of annihilation and creation operators for spin up and three pairs of annihilation and creation operators for spin down occupying the impurity for different times. The filled squares stand for annihilation operators, whereas the empty squares denote creation operators. Colored lines depict a filled impurity. The prefactors for the trace of this configuration would be (-1) since for the down spins one segment crosses the $\beta, 0$ line. The occupation time τ_σ^{occ} for spin σ would be the total length of all lines with the corresponding color and the double occupation time τ^{double} is the total width of the violet blocks, which indicate the time spans when the impurity is doubly occupied.

$$\left\langle \prod_{\sigma=\uparrow\downarrow, l_\sigma=1}^{n_\sigma} c_\sigma^\dagger(\tau_l^{c_\sigma^\dagger})c_\sigma(\tau_l^{c_\sigma}) \right\rangle_0 = (-1)^{\sum_\sigma s_\sigma} e^{\mu \sum_\sigma \tau_\sigma^{\text{occ}} - U\tau^{\text{double}}}, \tag{3.83}$$

where s_σ is the number of segments for spin σ, which cross the $0, \beta$ boundary ($s_\sigma = 0, 1$), τ_σ^{occ} is the total length of all segments for spin σ and τ^{double} is the total overlap of the occupied segments of the different spins or in other words the total time in which the impurity is doubly occupied. One should note that for the case when $n_\sigma = 0$, i.e. at zero perturbation order we must also distinguish between a completely filled or a completely empty impurity in order to always have a single contribution from the trace above as for all higher perturbation orders. This can be done by decomposing the corresponding Monte-Carlo configuration $\mathcal{C}$ into two distinct configuration, i.e. a "filled" impurity and an "empty" impurity. A typical configuration is illustrated in Fig. 3.7, explaining the trace-factor's ingredients.

Up to now, the configurations $\mathcal{C}$ and their corresponding weights $w_\mathcal{C}$ have been identified. The config-
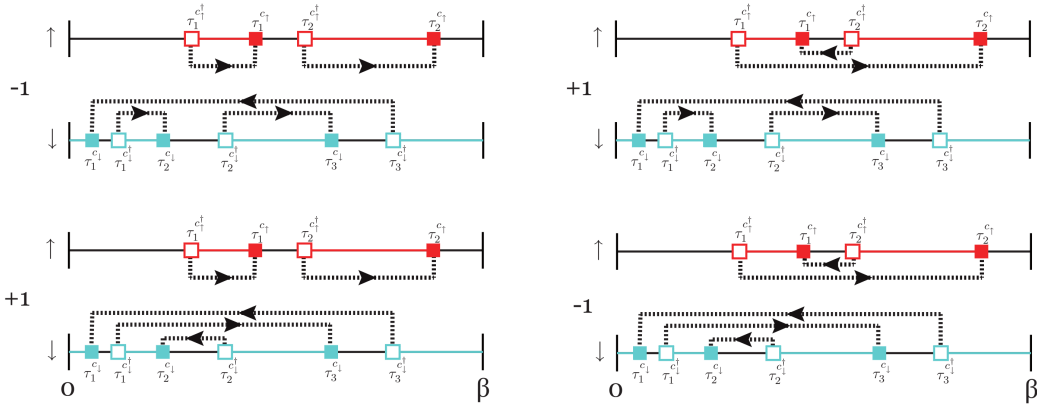
Figure 3.8: Subset of diagrams contributing to the weight $w_{\mathcal{C}}$ of a configuration $\mathcal{C} = (n_{\uparrow} = 2, n_{\downarrow} = 3), ...)$. In front of every diagram, there is the corresponding prefactor $(-1)^{s+d}$ which comes from the determinant (d) and from the trace factor (s) and can be determined by counting the number n_R of hybridization lines that are reversed in time, i.e. $s + d = n_R$.

urations $\mathcal{C} = (n_{\uparrow}, n_{\downarrow}, \mathcal{S}_1^{\uparrow}, ..., \mathcal{S}_{n_{\uparrow}}^{\uparrow}, \mathcal{S}_1^{\downarrow}, ..., \mathcal{S}_{n_{\downarrow}}^{\downarrow})$ contain the perturbation order n_{σ} for spin σ and the n_{σ} distinct segments $\mathcal{S}_i^{\sigma} = (\tau_i^{c^{\dagger}_{\sigma}}, \tau_i^{c_{\sigma}})$ for both spin components. The corresponding weight is then determined by

$$d\mathcal{C}\, w_{\mathcal{C}} = (-1)^{\sum_{\sigma} s_{\sigma}} e^{\mu \sum_{\sigma} \tau_{\sigma}^{\mathrm{occ}} - U\tau^{\mathrm{double}}} \prod_{\sigma} (d\tau)^{2n_{\sigma}} \det\left(M_{\sigma}^{-1}(\{\tau_l^{c^{\dagger}_{\sigma}}, \tau_l^{c_{\sigma}}\})\right). \tag{3.84}$$

Note that the prefactor $(-1)^{s_{\sigma}}$ in this expression does not cause an explicit sign problem, since it cancels with the sign of the determinant $\det(M_{\sigma})^{-1}$, which is positive when no segment crosses $\beta, 0$ and becomes negative otherwise. The last point results from the fact that

$$\Gamma_{\sigma}(\tau) > 0 \text{ for } \tau > 0, \text{ and } \Gamma_{\sigma}(-\tau) = -\Gamma_{\sigma}(\beta - \tau), \tag{3.85}$$

which is clear by definition of Γ in (3.15).

After the weights and configurations are found, the next step is to determine the observables $g_{\mathcal{C}}$, which we will not do directly but instead in a more subtle way. An arbitrary Green's function $g(\tau)$ can, by using the identity $g(\tau) = -g(\beta + \tau)$, be re-expressed as

$$g(\tau) = \int d\tau' d\tau'' \Delta(\tau' - \tau'' - \tau) g(\tau' - \tau''), \tag{3.86}$$

where we have introduced the delta-function

$$\beta \Delta(\tau' - \tau'' - \tau) = \left. \begin{array}{l} \delta(\tau' - \tau'' - \tau), \text{ for } \tau' > \tau'' \\ -\delta(\beta + \tau' - \tau'' - \tau), \text{ for } \tau' < \tau'' \end{array} \right\}. \tag{3.87}$$

The Green's function for spin $\bar{\sigma}$ is then determined by

$$
\begin{aligned}
G_{\bar{\sigma}}(\tau) &= \int d\tau' d\tau'' \Delta(\tau' - \tau'' - \tau) G_{\bar{\sigma}}(\tau' - \tau'') \\
&= \frac{1}{Z} \int d\tau' d\tau'' \Delta(\tau' - \tau'' - \tau) \langle \mathcal{T} c_{\bar{\sigma}}(\tau') c_{\bar{\sigma}}^{\dagger}(\tau'') \rangle,
\end{aligned} \tag{3.88}
$$

which, remembering the effective action in (3.76), can be formulated as

$$G_{\bar{\sigma}}(\tau) = \frac{1}{Z} \int d\tau' d\tau'' \Delta(\tau' - \tau'' - \tau) \frac{\partial Z}{\partial \Gamma_{\bar{\sigma}}(\tau'' - \tau')}. \tag{3.89}$$

With the definition of $g_\mathcal{C}$, it is immediately clear from this expression, that

$$
\begin{aligned}
g_{\bar\sigma\mathcal{C}}(\tau) &= \int d\tau' d\tau'' \Delta(\tau' - \tau'' - \tau) \frac{1}{w_\mathcal{C}} \frac{\partial w_\mathcal{C}}{\partial \Gamma_{\bar\sigma}(\tau'' - \tau')} \\
&= \int d\tau' d\tau'' \Delta(\tau' - \tau'' - \tau) \det(M_{\bar\sigma}(\{\tau_l^{c_{\bar\sigma}^\dagger}, \tau_l^{c_{\bar\sigma}}\})) \frac{\partial \det(M_{\bar\sigma}^{-1}(\{\tau_l^{c_{\bar\sigma}^\dagger}, \tau_l^{c_{\bar\sigma}}\}))}{\partial \Gamma_{\bar\sigma}(\tau'' - \tau')}.
\end{aligned}
\tag{3.90}
$$

Combining the rules for functional differentiation, i.e.

$$
\frac{\partial \Gamma_\sigma(\tau_i - \tau_l)}{\partial \Gamma_{\bar\sigma}(\tau'' - \tau'')} = \delta(\tau_i - \tau_l - \tau'' + \tau') \delta_{\sigma\bar\sigma},
\tag{3.91}
$$

and matrix inversion

$$
M_{ij} = \frac{\det(\tilde M^{-1})(ji)}{\det(M^{-1})} = \frac{1}{\det(M^{-1})} \frac{\partial \det(M^{-1})}{\partial (M^{-1})_{ji}},
\tag{3.92}
$$

where we used the cofactors $(\tilde M^{-1})(ji)$ for the matrix inversion, which has a possible representation as the derivative of the determinant with respect to the corresponding matrix element $(M^{-1})_{ji}$, we finally obtain the formula for the observables:

$$
g_{\bar\sigma\mathcal{C}}(\tau) = \Delta(\tau_i^{c_{\bar\sigma}} - \tau_j^{c_{\bar\sigma}^\dagger} - \tau)(M_{\bar\sigma}(\{\tau_l^{c_{\bar\sigma}^\dagger}, \tau_l^{c_{\bar\sigma}}\}))_{ji}.
\tag{3.93}
$$

The delta-function in this formula must either be measured on a fine grid in τ-space, i.e. on a discretized time interval $[0, \beta]$ or, as we will do, the observables have to be performed in another representation which is much more suitable for continuous, smooth functions (see chapter ...). The average occupation $\langle n_\sigma \rangle$ for the σ-component and the average double occupancy $\langle n_\uparrow n_\downarrow \rangle$ are other observables, which can be directly measured in the Monte-Carlo sampling, which becomes clear when taking the derivatives

$$
\beta \langle n_\sigma \rangle = \frac{1}{Z} \frac{\partial Z}{\partial \mu_\sigma} \quad \text{and} \quad \beta \langle n_\uparrow n_\downarrow \rangle = -\frac{1}{Z} \frac{\partial Z}{\partial U}.
\tag{3.94}
$$

As above, this leads to the observables

$$
n_{\sigma\mathcal{C}} = \frac{1}{\beta w_\mathcal{C}} \frac{\partial w_\mathcal{C}}{\partial \mu_\sigma} = \frac{\tau_\sigma^{\text{occ}}}{\beta} \quad \text{and} \quad (n_\uparrow n_\downarrow)_\mathcal{C} = -\frac{1}{\beta w_\mathcal{C}} \frac{\partial w_\mathcal{C}}{\partial U} = \frac{\tau^{\text{double}}}{\beta},
\tag{3.95}
$$

which can be accumulated without any effort during the Monte-Carlo sampling and are determined more accurately than the Green's functions since they are static variables.

With all the necessary ingredients, namely the configurations, the weights and the observables, we can skip and jump to the next section and set up the Markov-Chain and determine the acceptance probabilities for the sampling process.

3.3.2   The Sampling Procedure

In the previous section, we introduced the configurations $\mathcal{C}$ in the segment representation, where the segments denote pairs of creation and annihilation operators $\left(c_\sigma^\dagger(\tau_l^{c_\sigma^\dagger}), c_\sigma(\tau_l^{c_\sigma}) \right)$, which occupy the σ-state of the impurity in the time interval $[\tau_l^{c_\sigma^\dagger}, \tau_l^{c_\sigma}]$. Subsequently, we expressed the Monte-Carlo weights and observables in terms of these segments.

In this section, we will decide the allowed moves of the Markov-Chain sampling process, which we choose to be the insertion and removal of segments and the insertion and removal of anti-segments, all together sufficient to obtain ergodicity [9]. We start with the discussion of the insertion and removal of segments as possible updates. According to the Metropolis procedure, the transition probabilities $p_{\mathcal{C}\tilde{\mathcal{C}}}$ for moving from configuration $\tilde{\mathcal{C}}$ to configuration $\mathcal{C}$ is decomposed into a product $p_{\mathcal{C}\tilde{\mathcal{C}}} = p_{\mathcal{C}\tilde{\mathcal{C}}}^{\text{prop}} p_{\mathcal{C}\tilde{\mathcal{C}}}^{\text{acc}}$ of a proposal probability $p_{\mathcal{C}\tilde{\mathcal{C}}}^{\text{prop}}$ and an acceptance probability $p_{\mathcal{C}\tilde{\mathcal{C}}}^{\text{acc}}$, whereas the proposal probability will be defined by the possible moves of the Markov-Chain and the acceptance probabilities are then determined by the Metropolis rule (ref Metropolis).
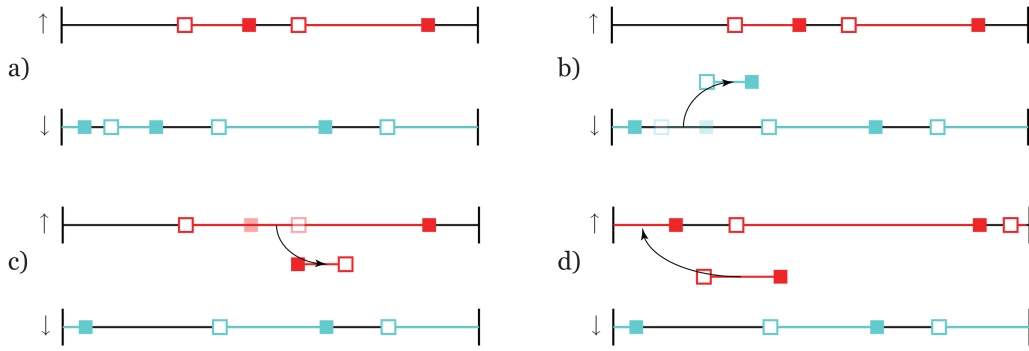
Figure 3.9: Illustration of four subsequent possible steps in the Markov-Chain sampling. First, in a), the chain starts with a configuration $\mathcal{C}$ consisting of two segments for spin-up and three segments for spin-down. In the next step of the Markov-Chain, b), a specific spin-down segment is removed. In step c), an anti-segment for the spin-up component is removed, leading to the merging of the two present segments into a single one, and finally, in d), a distinct spin-up segment is inserted again.

Suppose the current configuration $\mathcal{C}$ consists of n_σ segments, occupying the σ-state of the impurity. Then with probability $p = 0.5$ we pick a spin-component $\sigma = \{\uparrow, \downarrow\}$ to update. Possible updates are either to insert a new segment into a free time interval or to remove one of the n_σ existing segments from the impurity. For the insertion, which will be chosen with probability $p = 0.5$, a time $\tau^{c_\sigma^\dagger}$ has to be selected at which the creation operator $c_\sigma^\dagger(\tau^{c_\sigma^\dagger})$ shall be inserted into the impurity. This time is chosen from the interval $[0, \beta]$ with uniform distributed probability, i.e. $p = \frac{d\tau}{\beta}$. After the time $\tau^{c_\sigma^\dagger}$ has been determined, the algorithm has to check if the impurity is empty or occupied at this time. If the impurity is occupied, this move is rejected and the sampling then proceeds with the next step, otherwise when the impurity is empty, the length $l_{\max}$ of the empty time interval from time $\tau^{c_\sigma^\dagger}$ to the starting time of the next segment is determined. The annihilation operator $c_\sigma(\tau^{c_\sigma})$ is then inserted at a uniformly chosen time τ^{c_σ} in the interval $[\tau^{c_\sigma^\dagger}, \tau^{c_\sigma^\dagger} + l_{\max}]$, i.e. with probability $p = \frac{d\tau}{l_{\max}}$. The proposal probability for the insertion of this segment is then determined by the product of the two probabilities $p^{\text{prop}}(n_\sigma \rightarrow n_\sigma + 1) = \frac{d\tau^2}{\beta l_{\max}}$. On the other hand, for $n_\sigma + 1$ segments occupying the impurity, the probability to uniformly pick a certain segment to remove is simply $p^{\text{prop}}(n_\sigma + 1 \rightarrow n_\sigma) = \frac{1}{n_\sigma + 1}$. With this, the detailed balance condition states

$$
\begin{aligned}
\frac{p^{\text{acc}}(n_\sigma \rightarrow n_\sigma + 1)}{p^{\text{acc}}(n_\sigma + 1 \rightarrow n_\sigma)} &= \frac{p^{\text{prop}}(n_\sigma + 1 \rightarrow n_\sigma)}{p^{\text{prop}}(n_\sigma \rightarrow n_\sigma + 1)} \frac{w_{n_\sigma + 1}}{w_{n_\sigma}} \\
&= \frac{(n_\sigma + 1)}{\beta l_{\max}} e^{\mu_\sigma \delta\tau_\sigma^{\text{occ}} - U\delta\tau^{\text{double}}} \left| \frac{\det(M_\sigma^{-1}(n_\sigma + 1))}{\det(M_\sigma^{-1}(n_\sigma))} \right|,
\end{aligned}
\tag{3.96}
$$

where in the last step, the formula for the weights (3.84) was inserted and we introduced the quantities $\delta\tau_\sigma^{\text{occ}}$ and $\delta\tau^{\text{double}}$ which are the change in the occupation time and double occupation time between the two configurations. Note that we took the absolute value of the determinant ratio since we have shown previously that the prefactors $(-1)^s$ coming from the determinants cancel with the prefactors from the trace-factor, see (3.81). The Metropolis condition fixes these probabilities to

$$
p^{\text{acc}}(n_\sigma \rightarrow n_\sigma + 1) = \min\left\{ 1, \frac{(n_\sigma + 1)}{\beta l_{\max}} e^{\mu_\sigma \delta\tau_\sigma^{\text{occ}} - U\delta\tau^{\text{double}}} \left| \frac{\det(M_\sigma^{-1}(n_\sigma + 1))}{\det(M_\sigma^{-1}(n_\sigma))} \right| \right\},
\tag{3.97}
$$

$$
p^{\text{acc}}(n_\sigma + 1 \rightarrow n_\sigma) = \min\left\{ 1, \frac{\beta l_{\max}}{(n_\sigma + 1)} e^{-\mu_\sigma \delta\tau_\sigma^{\text{occ}} + U\delta\tau^{\text{double}}} \left| \frac{\det(M_\sigma^{-1}(n_\sigma))}{\det(M_\sigma^{-1}(n_\sigma + 1))} \right| \right\}.
\tag{3.98}
$$

By including updates that insert and remove segments, ergodicity has been obtained on a formal level since any configuration $\mathcal{C} = (n_\uparrow, n_\downarrow, ...)$ can be reached from any other configuration $\tilde{\mathcal{C}} = (\tilde{n}_\uparrow, \tilde{n}_\downarrow, ...)$

---

[9]Please note that the insertion and removal of segments alone is not sufficient to obtain ergodicity, i.e. the insertion and removal of antisegments is required for the Markov chain and not a tool that simply improves the sampling procedure.

in $N = n_\uparrow + n_\downarrow + \tilde{n}_\uparrow + \tilde{n}_\downarrow$ steps. However, it turns out that the insertion and removal of segments does not guarantee ergodicity in finite sampling processes. This fact can also be conjectured from the fact that a completely empty impurity and a completely filled impurity are not treated on equal footing with these kind of updates as it is very unlikely to insert a segment spanning the whole time interval $[0, \beta]$. This can be adjusted by considering a complementary set of updates, namely the insertion and removal of so-called anti-segments. While a segment is nothing but a time interval $(\tau^{c_\sigma^\dagger}, \tau^{c_\sigma})$ for which the impurity is occupied, an anti-segment is just a contrary time interval $(\tau^{c_\sigma}, \tau^{c_\sigma^\dagger})$ for which the impurity is unoccupied. To express this in the segment picture, the insertion of an anti-segment $(\tilde{\tau}^{c_\sigma}, \tilde{\tau}^{c_\sigma^\dagger})$ is nothing but the splitting of a single segment $(\tau^{c_\sigma^\dagger}, \tau^{c_\sigma})$ into two distinct segments $(\tau^{c_\sigma^\dagger}, \tilde{\tau}^{c_\sigma})$ $(\tilde{\tau}^{c_\sigma^\dagger}, \tau^{c_\sigma})$, while the removal of an anti-segment $(\tilde{\tau}^{c_\sigma}, \tilde{\tau}^{c_\sigma^\dagger})$ is the recombination of two subsequent segments into a single one. The update probabilities are then determined by the formulas (3.97) and (3.98) since the anti-segment moves follow completely the same procedure as the segment moves and the weights are identical[10]. As for the CT-AUX solver, further updates can also be implemented in the CT-HYB solver, which lead to a decrease of the auto-correlation times but are not required for ergodicity. A set of such updates would be the possibility to not only insert and remove (anti-) segments but also to allow for shifting segments in time or to shift only the starting- or end point of a segment in time. These updates are implemented straight-forwardly by using the detailed balance condition and are not derived here. However, in some situations a complete exchange of the segments for the two different components is required, especially when the system is approaching magnetically ordered phases [67].

Steps of the Sampling Process

The Monte-Carlo flow diagram for the CT-HYB solver is very similar to the diagram for the CT-AUX solver, Fig. 3.4. The steps are as follows:

1. Initialization: At the beginning of the sampling process one possible configuration must be predetermined as the starting configuration to initialize the sampling procedure.

2. For the current configuration $\mathcal{C}$ a possible update has to be chosen, either the insertion/removal of a segment $(\tau^{c_\sigma^\dagger}, \tau^{c_\sigma})$ or insertion/removal of an anti-segment $(\tau^{c_\sigma}, \tau^{c_\sigma^\dagger})$. Where all four of those possibilities have the same probability to not influence the detailed balance formulas above.

3. A new configuration must be proposed, either with one segment $(\tau^{c_\sigma^\dagger}, \tau^{c_\sigma})$ less or more (or one anti-segment less or more), depending on the previous step.

4. The acceptance probability for this new configuration is determined according to the Metropolis probabilities (3.97) and (3.98).

5. Either the new configuration is accepted and the old configuration replaced, or the new configuration is rejected, and the old configuration stays unchanged (i.e. the new configuration is discarded).

6. A measurement of the observables, i.e. the $g_\mathcal{C}$'s, is performed (these may be many observables).

7. Go back to step 2, until the specified number of iterations has been achieved.

Finally, after deriving the configurations, weights and observables in the previous chapter and setting up the sampling procedure, we will also compare the CT-HYB solver with exact diagonalization to check whether it is working correctly or not. In Fig. 3.10, we show a comparison between ED and CT-HYB Green's functions for two distinct hybridization functions, determined by the bath energies ϵ_σ and hybridization parameters V_σ, which are chosen to be the same for both spin components. Together with these results, the performance of the CT-HYB algorithm can be discussed in the same way as the CT-AUX solver from Fig. 3.6, which shows the average perturbation order in dependence of βt and βU. Since CT-HYB is an expansion in the hybridization, it does not scale with U but rather with the factor βt, which is

---

[10]In fact they are only identical after a rearrangement of the matrix M has been performed, since, in contrast to the segment insertion/removal, for the anti-segment insertion/removal the inserted/removed columns do not belong to the same segments. Although this is a trivial modification of the matrix M after the insertion/removal of an anti-segment it must not be forgotten or neglected since it totally changes the measurements.
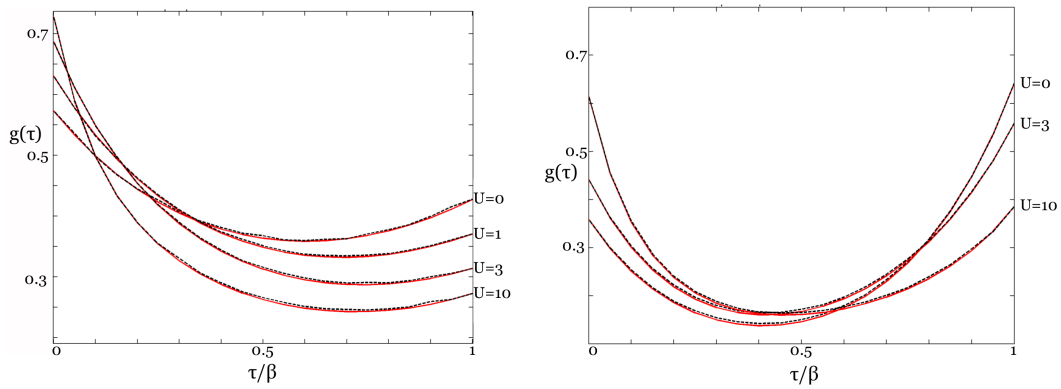
Figure 3.10: Comparison of the interacting Green's function $g(\tau) = G_\sigma(\tau)$ of an AIM with finite number of bath orbitals $S = 3$ obtained from a CT-HYB algorithm and the exact results from diagonalization of the Hamiltonian. The accuracy does not depend on the interaction parameter U, since CT-HYB is an expansion in the hybridization. The Green's functions have been obtained for (left) bath energies $\epsilon_\sigma = (1, -1, 1)$ and hybridization parameters $V_\sigma = (1, -1, 1)$ and (right) bath energies $\epsilon_\sigma = (3, 2, 1)$ and hybridization parameters $V_\sigma = (1, 2, 3)$. Although a very small number of sampling steps, $N = 10^6$, was used, the agreement is already very good and can be improved by taking the usual number of steps $N = 10^8$, which turned out to be optimal for most simulations that we performed.

the Hubbard hopping parameter and indirectly proportional to the hybridization.

In this chapter, we have found the basic formalism for the continuous-time Monte-Carlo impurity solvers CT-HYB and CT-AUX, for which we will discuss several extensions and improvements in the following chapter and which we will use later in combination with RDMFT to investigate the properties of fermionic lattice models with artificial gauge fields.

4. Extensions and Improvements to the CT-QMC Methods

The continuous-time Monte-Carlo impurity solvers introduced in the previous chapter, namely the CT-AUX and the CT-HYB solver, were so far only discussed for the case of a single impurity and with spin a good quantum number, i.e. without terms that mix the spins, as they would occur for systems which show superfluid ordering or spin-changing hopping parameters. In this chapter, we will discuss both, the extension of the CT-AUX and the CT-HYB solvers to systems with superfluid pairing and spin-changing hopping processes. We will also extend the CT-AUX solver to cluster impurities, containing more than just a single lattice site. Additionally, improvements of the measurements in the CT-HYB solver are discussed, which allow for a direct measurement of the self-energy [74] and which perform the measurements in a different basis compared to the previous chapter, i.e. the measurements will be performed in a polynomial basis instead of the discretized imaginary-time interval [16].

4.1   CT-AUX on a L-site Cluster

So far, the impurities that have been considered to be solved by the CT-AUX algorithm only consisted of two quantum states, i.e. spin-up and spin-down, which were interacting with each other and both coupled to a non-interacting bath[1]. Now, we will introduce an additional degree of freedom to the system, which can be seen as a spatial one. The Hamiltonian of the extended system is given by

$$H = \sum_{i,j\sigma} t_{ij} c_{i\sigma}^\dagger c_{j\sigma} + \text{h.c.} + \sum_i U n_{i\uparrow} n_{i\downarrow} - \mu(n_{i\uparrow} + n_{i\downarrow}) + \sum_{i\sigma} c_{i\sigma}^\dagger \hat{V}_{i\sigma} + \text{h.c.} + H_{i\sigma}^{\text{bath}}, \qquad (4.1)$$

where the operators $\hat{V}_{i\sigma}$ and $H_{i\sigma}^{\text{bath}}$ are defined as

$$\hat{V}_{i\sigma} = \sum_{\mathbf{k}} V_{\mathbf{k}}^{(i\sigma)} d_{i\sigma\mathbf{k}}, \quad V_{\mathbf{k}}^{(i\sigma)} \in \mathbb{C} \qquad (4.2)$$

and

$$H_{i\sigma}^{\text{bath}} = \sum_{\mathbf{k}} \epsilon_{\mathbf{k}}^{i\sigma} d_{i\sigma\mathbf{k}}^\dagger d_{i\sigma\mathbf{k}}, \quad \epsilon_{\mathbf{k}}^{i\sigma} \in \mathbb{R} \qquad (4.3)$$

and the index $i = 1, ..., L$ labels the L additional quantum states. For the case of $L = 1$, this clearly reduces to the AIM discussed in the previous section. For $L > 1$, the Hamiltonian (4.1) describes a system

---

[1] In a functional integral representation, the bath is equivalent to a hybridization Γ, which is non-local in time.

of L impurities $i = 1, ..., L$, which are coupled to a non-interacting bath $H_{i\uparrow}^{\text{bath}} + H_{i\downarrow}^{\text{bath}}$ via the hybridization operators $\hat{V}_{i\sigma}$. Additionally the impurities are coupled to each other via the "hopping" t_{ij} which is left arbitrary for the case of this derivation.

Similar to section 3.2, the Hamiltonian is decomposed as

$$H = H_0 + \sum_i W_i, \tag{4.4}$$

where the operators W_i are chosen as

$$W_i = U\left(n_{i\uparrow}n_{i\downarrow} - \frac{n_{i\uparrow} + n_{i\downarrow}}{2}\right) - \frac{K}{\beta}, \tag{4.5}$$

thereby implicitly defining H_0 as

$$H_0 = H - \sum_i W_i, \tag{4.6}$$

which leads to H_0 being quadratic in the fermionic operators $c_{i\sigma}^\dagger, d_{i\sigma\mathbf{k}}^\dagger$. From the commutation relation

$$[W_i, W_j] = 0, \quad \forall i, j \tag{4.7}$$

one directly infers the important result

$$[H, W_j] = [H_0, W_j], \quad \forall j. \tag{4.8}$$

Next, we would like to express the partition function in terms of time-ordered operators $S_i(\beta)$, following the procedure in section 2.3.2. Rewriting the exponential of the Hamiltonian (4.1) as

$$e^{-\beta H} = e^{-\beta(H - W_i)}e^{\beta(H - W_i)}e^{-\beta H} = e^{-\beta(H - W_i)}S_i(\beta) \tag{4.9}$$

defines the operator

$$S_i(\tau) = e^{\tau(H - W_i)}e^{-\tau H}, \tag{4.10}$$

which solves the Cauchy problem according to

$$\partial_\tau S_i(\tau) = e^{\tau(H - W_i)}(H - W_i - H)e^{-\tau H} = -e^{\tau(H - W_i)}W_i e^{-\tau(H - W_i)}S_i(\tau) = -W_i(\tau)S_i(\tau), \quad S(0) = \mathbb{1}. \tag{4.11}$$

Because of (4.8), $W_i(\tau)$ simplifies to

$$W_i(\tau) = e^{\tau(H - W_i)}W_i e^{-\tau(H - W_i)} = e^{\tau H_0}W_i e^{-\tau H_0} \tag{4.12}$$

and the formal solution of (4.11) is given by (compare (2.65), (2.66) and (2.69))

$$S_i(\beta) = \mathcal{T}e^{-\int_0^\beta d\tau \, W_i(\tau)}. \tag{4.13}$$

The residual exponential in equation (4.9) can now be rewritten again, leading to

$$e^{-\beta(H - W_i)} = e^{-\beta(H - W_i - W_j)}e^{\beta(H - W_i - W_j)}e^{-\beta(H - W_i)} = e^{-\beta(H - W_i - W_j)}S_j(\beta), \tag{4.14}$$

with

$$S_j(\tau) = e^{\beta(H - W_i - W_j)}e^{-\beta(H - W_i)} \tag{4.15}$$

being determined by the Cauchy problem

$$\partial_\tau S_j(\tau) = e^{\tau(H - W_i - W_j)}(H - W_j - W_i - H + W_i)e^{\tau(H - W_i)} = -W_j(\tau)S_j(\tau), \quad S_j(0) = \mathbb{1}. \tag{4.16}$$

Again, because of (4.8),

$$W_j(\tau) = e^{\tau(H - W_i - W_j)}W_j e^{-\tau(H - W_i - W_j)} = e^{\tau H_0}W_j e^{-\tau H_0}, \tag{4.17}$$

which leads to the formal solution of (4.16) being

$$S_j(\beta) = \mathcal{T}e^{-\int_0^\beta d\tau\, W_j(\tau)}.\tag{4.18}$$

This solution is independent of whether the same step has been performed for W_i before or not, since in the time-dependence of $W_j(\tau)$ only the quadratic Hamiltonian H_0 is present. After performing the above steps L times for all different states $i = 1,...,L$, the partition function can be expressed as

$$Z = \langle e^{-\beta H} \rangle = \langle e^{-\beta H_0} \prod_{i=1}^{L} S_i(\beta) \rangle,\tag{4.19}$$

with $S_i(\beta)$ defined by (4.13). To deal with $S_i(\beta)$ during a Monte-Carlo simulation, we rewrite it in terms of the well-known Neumann series (2.67)

$$S_i(\beta) = \sum_{n_i=0}^{\infty} (-1)^n \int_0^\beta d\tau_1^i \int_0^{\tau_1^i} d\tau_2^i ... \int_0^{\tau_{n_i-1}^i} d\tau_n^i W_i(\tau_1^i)...W_i(\tau_{n_i}^i).\tag{4.20}$$

This can also be done for the time-ordered product in equation (4.19), leading to

$$
\begin{aligned}
\prod_{i=1}^{L} S_i(\beta) &= \prod_{i=1}^{L} \left[\sum_{n_i=0}^{\infty} (-1)^{n_i} \int_0^\beta d\tau_1^i \int_0^{\tau_1^i} d\tau_2^i ... \int_0^{\tau_{n_i-1}^i} d\tau_{n_i}^i W_i(\tau_1^i)...W_i(\tau_{n_i}^i) \right] \\
&= \sum_{n=0}^{\infty} \sum_{\mathcal{L}\{n_i\}=n} (-1)^n \int_0^\beta d\tau_1 \int_0^{\tau_1} d\tau_2 ... \int_0^{\tau_{n-1}} d\tau_n \prod_{i=1}^{L} \left(W_i(\tau^\#) \right)^{n_i},
\end{aligned}\tag{4.21}
$$

where we introduced $\sum_{\mathcal{L}\{n_i\}=n}$, which is the sum over all possible realizations of the set $\{n_i\}$ such that $\sum_i n_i = n$ and the placeholders $\tau^\#$, which are the imaginary times that have to be determined by the order in which the operators are introduced in the Monte-Carlo procedure[2].

For any W_i in (2.68), the discrete Hubbard-Stratonovich transformation (3.22) can be performed, introducing n additional classical spins $s_l = \pm 1, l = 1,...n$, as in section 3.2. The only difference between here and the corresponding expression for the single-site impurity (Eq. (3.26) and following) is the additional index i. For that reason, all the computations from the previous sections can be performed analogously by replacing the tuples (τ_l, s_l) by the triples (τ_l, s_l, x_l), where $x_l = 1,...,L$ labels the additional quantum state i. This leads to a change of the configurations from $\mathcal{C} = (n, \tau_1, s_1,...,\tau_n, s_n)$ in the previous section to $\mathcal{C} = (n, \tau_1, s_1, x_1,...,\tau_n, s_n, x_n)$, which leaves the results obtained in the functional integral formalism completely unchanged.

The weights $w_\mathcal{C}$ of the configurations $\mathcal{C} = (n, \tau_1, s_1, x_1,...,\tau_n, s_n, x_n)$ are determined by the formula

$$w_\mathcal{C} = e^{-LK} \left(\frac{K d\tau}{\beta} \right)^n \prod \sigma Z_{0\sigma} \det\left(N_\sigma^{-1}(\{\tau_l, s_l, x_l\}) \right)\tag{4.22}$$

with the matrix

$$N_\sigma^{-1}(\{\tau_l, s_l, x_l\}) = e^{\Gamma_\sigma} - (e^{\Gamma_\sigma} - \mathbb{1})\mathbf{G}_{0\sigma}\tag{4.23}$$

consisting of the diagonal matrix

$$\left(e^{\Gamma_\sigma} \right)_{lm} = \delta_{lm} e^{\gamma s_l \sigma}\tag{4.24}$$

and the Green's function

$$\left(\mathbf{G}_{0\sigma} \right)_{lm} = \mathcal{G}_{\sigma x_l x_m}(\tau_l - \tau_m).\tag{4.25}$$

As one realizes from (4.22) and (4.25), the only difference for the cluster problem compared to the single site impurity is that the Green's functions have an additional dependence on the indices x_l, x_m. The Green's functions are determined by

$$\mathcal{G}_{\sigma x_l x_m}^{-1}(\tau) = \left\{ \begin{array}{ll} \delta(\tau)(\partial_\tau - \mu_\sigma + U/2) - \Gamma_{\sigma x_l}(\tau) & \text{for } x_l = x_m \\ \delta(\tau) t_{x_l x_m} & \text{for } x_l \neq x_m \end{array} \right\}.\tag{4.26}$$

---

[2]In the last equality of (4.21), it seems that a factor $1/L!$ is missing because we switched from a sum in which only the L individual parts $i = 1,...,L$ are time ordered with respect to each other to a fully time ordered representation. We did not account for this term, since in the Monte-Carlo procedure there will be always an implicit ordering between distinguishable states i, j with $i = j$ such that (4.21) with respect to the MC procedure is the correct expression for the product on the left of (4.21)

As for the weights $w_{\mathcal{C}}$, the measurement formulas stay formally unaffected and read

$$g_{\mathcal{C}\sigma x_l x_m}(\tau) = \mathcal{G}_{\sigma x_l x_m}(\tau) + \mathcal{G}_{\sigma x_l x_i}(\tau - \tau_i)\left[N_\sigma(\{\tau_j, s_j, x_j\})(e^{\Gamma_\sigma} - \mathbb{1})\right]_{i,j}\mathcal{G}_{\sigma x_j x_m}(\tau_j), \qquad (4.27)$$

where $g_{\mathcal{C}\sigma x_l x_m}(\tau)$ is the interacting Green's function belonging to configuration $\mathcal{C}$, as in the previous section.

With this, the measurement and weight formulas are determined and one can directly start with the sampling procedure. The sampling is equivalent to the sampling procedure of the single site CT-AUX method, based on insertion and removal of auxiliary spins s_i. The only difference for the cluster problem is that a new configuration contains the triple (τ_i, s_i, x_i), whereas x_i has to be chosen from the set $\{1, ..., L\}$. Performing this according to a uniform distribution, i.e. with probability $1/L$, there occurs an additional factor $1/L$ in the proposal probabilities, which leads to a modification of the probability ratio of equation (3.53), which has to be multiplied by a factor L. These minor changes are already sufficient to solve cluster impurity problems with the CT-AUX method. However, there is one important difference between the single site and the cluster problem, namely the weights $w_{\mathcal{C}}$ can become negative in the cluster problem, while they were always positive for the single site problem. As pointed out in section 2.3.3, the average sign decreases with the size of the system, which leads to a sign problem, that increases with the cluster size. This restricts the cluster version of CT-AUX intermediate cluster size and interaction strengths, which is also pointed out in [68, 67]. The cluster version of the CT-AUX method introduced above in combination with cluster formulations of DMFT have been used successfully to analyze momentum selective phase transitions in two-dimensional systems, such as the momentum selective Mott-transition [68, 64] and the pseudogap transition for attractive interactions [121, 122]. For these investigations, the parameters t_{ij} were chosen such that they reproduce a certain dispersion relation in discretized momentum space instead of mimicking the real-space hopping from lattice site to lattice site. This leads to the possibility of addressing several regions in momentum space that are expected to be sensitive to the specific phase of the system. The cluster formulation of CT-AUX was not used to investigate physical systems in the context of this thesis, however, since its formulation and implementation is straightforward after it has been done for single-site CT-AUX, we briefly introduced this method in this section.

4.2   Spin-Mixing Formulation of CT-AUX

For the Anderson impurity model as considered up to now, the spin σ has been a good quantum number since the interactions did not change the spin and both spin components coupled to a distinct set of bath states. It is easy to imagine that this does not cover the full range of possible physics for a single-site impurity model. Consider for instance a realization of the Hubbard model which has additional hopping terms, including a possible spin flip of a particle hopping from lattice site i to the neighboring lattice site j. This would lead to a system without having spin as a good quantum number. As we saw in the previous chapter, the action of the AIM can be considered as the local effective action of a lattice problem, where all lattice site but one have been integrated out. Therefore it is immediately clear that for such a model the corresponding AIM would have to contain couplings of the impurity states to bath states with opposite spin as well. In this section, we will derive the corresponding impurity solver for such systems. The Hamiltonian we are considering has the form

$$H = -\sum_\sigma \mu_\sigma n_\sigma + Un_\uparrow n_\downarrow + \sum_\sigma c_\sigma^\dagger (\hat{V}_\sigma + \hat{W}_{\bar{\sigma}}) + \text{h.c.} + \sum_\sigma H_\sigma^{\text{bath}}, \qquad (4.28)$$

where we have introduced the non-hermitian operators $\hat{V}_\sigma$ and $\hat{W}_{\bar{\sigma}}$, which are defined as

$$\hat{V}_\sigma = \sum_{\mathbf{k}} V_{\mathbf{k}}^\sigma d_{\sigma\mathbf{k}} \qquad (4.29)$$

and

$$\hat{W}_{\bar{\sigma}} = \sum_{\mathbf{k}} W_{\mathbf{k}}^{\bar{\sigma}} d_{\bar{\sigma}\mathbf{k}} \qquad (4.30)$$

and the bath Hamiltonian $H^{\text{bath}} = H^{\text{bath}}_\downarrow + H^{\text{bath}}_\uparrow$, with

$$H^{\text{bath}}_\sigma = \sum_{\mathbf{k}} \epsilon^\sigma_{\mathbf{k}} d^\dagger_{\sigma\mathbf{k}} d_{\sigma\mathbf{k}}. \tag{4.31}$$

The normal hybridization operator $\hat{V}_\sigma$ introduces a coupling of the spin σ to the bath states $(\sigma, \mathbf{k})$ via the hybridization parameters $V^\sigma_{\mathbf{k}} \in \mathbb{C}$, whereas the anomalous hybridization operator $\hat{W}_{\bar{\sigma}}$ introduces a coupling of the spin σ to the bath states with opposite spin $(\bar{\sigma}, \mathbf{k})$ via the anomalous hybridization parameters $W^{\bar{\sigma}}_{\mathbf{k}} \in \mathbb{C}$.

Switching to a functional integral representation and integrating out the bath degrees of freedom, the effective impurity action corresponding to the Hamiltonian (4.28) is given by

$$S_{\text{eff}} = \int d\tau d\tau' \left(c^\dagger_\uparrow(\tau), c^\dagger_\downarrow(\tau) \right) \hat{\mathcal{G}}^{-1}(\tau - \tau') \begin{pmatrix} c_\uparrow(\tau') \\ c_\downarrow(\tau') \end{pmatrix} + U \int d\tau\, n_\uparrow(\tau) n_\downarrow(\tau), \tag{4.32}$$

where the matrix of Green's functions is defined as

$$\hat{\mathcal{G}}^{-1}(\tau) = \delta(\tau) \begin{pmatrix} \partial_\tau - \mu_\uparrow & 0 \\ 0 & \partial_\tau - \mu_\downarrow \end{pmatrix} + \begin{pmatrix} \Gamma_{\uparrow\uparrow}(\tau) & \Gamma_{\uparrow\downarrow}(\tau) \\ \Gamma_{\downarrow\uparrow}(\tau) & \Gamma_{\downarrow\downarrow}(\tau) \end{pmatrix}. \tag{4.33}$$

The hybridization functions are obtained according to the description in section 3.1, equation (3.13), i.e.

$$\Gamma_{\sigma\sigma}(i\omega_n) = \sum_{\mathbf{k}} \frac{|V^\sigma_{\mathbf{k}}|^2 + |W^{\bar{\sigma}}_{\mathbf{k}}|^2}{i\omega_n - \epsilon^\sigma_{\mathbf{k}}} \tag{4.34}$$

and

$$\Gamma_{\sigma\bar{\sigma}}(i\omega_n) = \sum_{\mathbf{k}} \frac{V^\sigma_{\mathbf{k}}(W^\sigma_{\mathbf{k}})^*}{i\omega_n - \epsilon^\sigma_{\mathbf{k}}} + \frac{W^{\bar{\sigma}}_{\mathbf{k}}(V^{\bar{\sigma}}_{\mathbf{k}})^*}{i\omega_n - \epsilon^{\bar{\sigma}}_{\mathbf{k}}}, \tag{4.35}$$

fulfilling the relation $(\Gamma_{\sigma\bar{\sigma}}(i\omega_n))^* = \Gamma_{\bar{\sigma}\sigma}(-i\omega_n)$.

As in the derivation of the CT-AUX algorithm, we decompose the Hamiltonian (4.28) into an exactly solvable part H_0 and the residual part V, i.e. $H = H_0 + V$. The choice of the operator V and the subsequent transformations are completely equivalent as described in detail in the CT-AUX section 3.2.1, i.e. equations (3.20)-(3.25), such that the weights are obtained via

$$d\mathcal{C} w_{\mathcal{C}} = \frac{1}{n!} \left\langle \mathcal{T} \prod_{l=1}^n -V(\tau_l) d\tau_l \right\rangle_0 \tag{4.36}$$

and the configurations $\mathcal{C}$ stay unchanged, namely are given as $\mathcal{C} = (n, \tau_1, s_1, ... \tau_n, s_n)$ with the perturbation order n and the n tuples $(\tau_i, s_i), i = 1, ..., n$.

The explicit calculation of this expectation value can be performed according to our derivation of the weight formulas in the CT-AUX section. However, instead of showing the detailed calculation with slight modifications again, we can derive the weight formulas in a diagrammatic picture. The weight factor as given by (4.36) is the n-th order term of a perturbation expansion in the interaction and therefore it is clear how to express this term in a diagrammatic picture, as we have shown in Fig. 3.2 for a specific configuration of the standard CT-AUX. The single addition that must be made to this picture, is that the anomalous propagators $\mathcal{G}_{\uparrow\downarrow}(\tau)$ are non-zero and therefore must be considered in the diagrammatic picture.

Fig. 4.1 shows additional diagrams compared to the non-spin-mixing CT-AUX method, contributing to the weight factor (4.36). The weights for a given configurations $\mathcal{C} = (n, \tau_1, s_1, ..., \tau_n, s_n)$ are obtained via

$$d\mathcal{C} w_{\mathcal{C}} = e^{-K} \left(\frac{K d\tau}{\beta} \right)^2 Z_0 \det(N^{-1}(\{s_i, \tau_i\})), \tag{4.37}$$

where Z_0 is the non-interacting partition function, which is no longer simply the product of spin-up and spin-down partition function, and the $2n \times 2n$ matrix $N^{-1}(\{s_i, \tau_i\})$ is defined by

$$N^{-1}(\{s_i, \tau_i\}) = e^\Gamma - (e^\Gamma - \mathbb{1})\hat{G}_0, \tag{4.38}$$
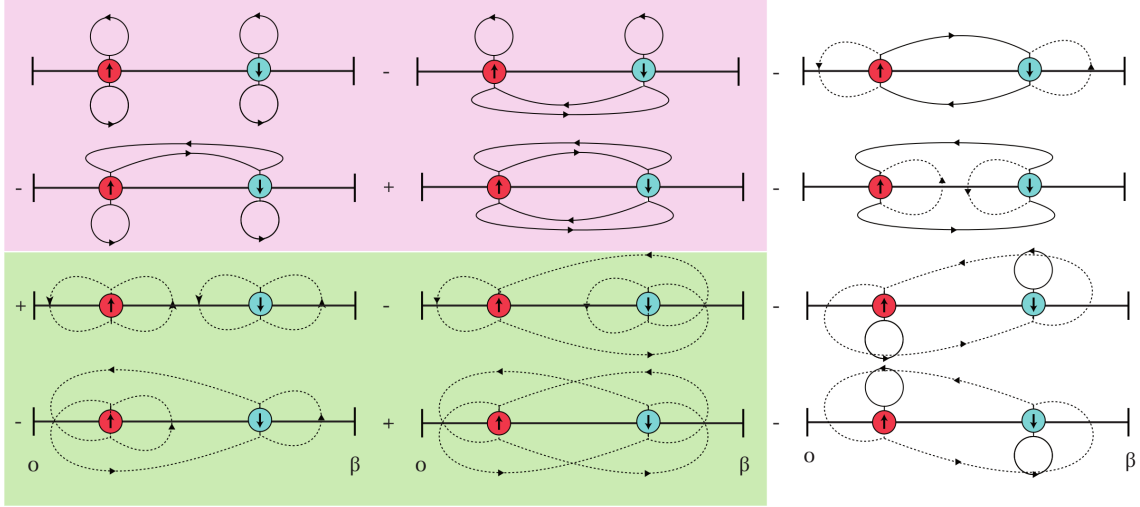
Figure 4.1: Illustration of 12 of the $(2n)! = 24$ distinct diagrams contributing to the weight factor $w_{\mathcal{C}}$ at perturbation order $n = 2$ with finite anomalous Green's functions $G_{\sigma\bar{\sigma}}(\tau)$. The spin conserving normal Green's functions are depicted with straight lines while the spin mixing anomalous Green's functions are drawn as dotted lines. The four diagrams in the violet region are those four diagrams which do not involve spin-mixing terms and therefore are the only ones that would contribute for the standard CT-AUX algorithm. In the green region, are the four diagrams that consist of spin-mixing terms only. The four diagrams on the right side consist of both spin-mixing and spin-conserving terms, which is also the case for the 12 remaining diagrams which we have not drawn here.

with the $n \times n$ distinct, 2×2 dimensional blocks

$$(e^{\Gamma})_{lm} = \delta_{lm} \begin{pmatrix} e^{\gamma s_l} & 0 \\ 0 & e^{-\gamma s_l} \end{pmatrix} \tag{4.39}$$

and

$$(\hat{G}_0)_{lm} = \begin{pmatrix} \mathcal{G}_{\uparrow\uparrow}(\tau_l - \tau_m) & \mathcal{G}_{\uparrow\downarrow}(\tau_l - \tau_m) \\ \mathcal{G}_{\downarrow\uparrow}(\tau_l - \tau_m) & \mathcal{G}_{\downarrow\downarrow}(\tau_l - \tau_m) \end{pmatrix}. \tag{4.40}$$

One immediately realizes that for $\mathcal{G}_{\downarrow\uparrow}(\tau_l - \tau_m) = \mathcal{G}_{\uparrow\downarrow}(\tau_l - \tau_m) = 0$ the determinant factorizes to a product of determinants for the distinct spin components only and therefore to the well-known expression from the CT-AUX without spin-mixing terms.

In the notation of the 2×2 blocks, as used above, the Monte-Carlo observables can be expressed in an equivalent manner to the measurement formulas in terms of the matrix N and the non-interacting Green's functions, leading to

$$g_{\mathcal{C}}(\tau) = \hat{\mathcal{G}}(\tau) + \hat{\mathcal{G}}(\tau - \tau_i) \left[N(\{s_i, \tau_i\})(e^{\Gamma} - \mathbb{1}) \right]_{i,j} \hat{\mathcal{G}}(\tau_j), \tag{4.41}$$

where the $\left[N(\{s_i, \tau_i\})(e^{\Gamma} - \mathbb{1}) \right]_{i,j}$ refers to the 2×2 dimensional sub-block i, j of the matrix $N(\{s_i, \tau_i\})(e^{\Gamma} - \mathbb{1})$ and $g_{\mathcal{C}}(\tau)$ is the block of interacting Green's functions

$$g_{\mathcal{C}}(\tau) = \begin{pmatrix} g_{\uparrow\uparrow\mathcal{C}}(\tau) & g_{\uparrow\downarrow\mathcal{C}}(\tau) \\ g_{\downarrow\uparrow\mathcal{C}}(\tau) & g_{\downarrow\downarrow\mathcal{C}}(\tau) \end{pmatrix} \tag{4.42}$$

corresponding to the configuration $\mathcal{C}$. Again, these formulas simplify to the CT-AUX measurement formulas for systems without spin-mixing, as soon as the anomalous Green's functions $\mathcal{G}_{\sigma\bar{\sigma}}$ are equal to zero.

After obtaining the weight and measurement formulas, the sampling procedure is totally equivalent to section 3.2.2 except that the weights and measurements have to be determined according to (4.37), (4.41), respectively. Fig. 4.2 shows a comparison of interacting Green's functions obtained via the extended CT-AUX method with Green's functions obtained from exact diagonalization of Hamiltonian of the corresponding Anderson impurity model, i.e. (4.28).
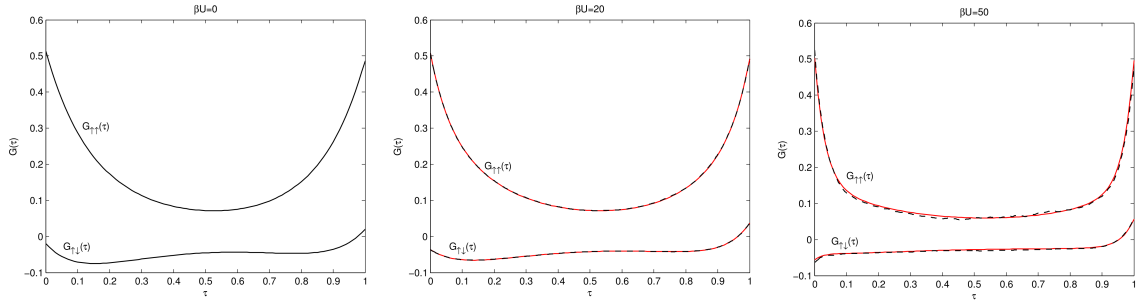
Figure 4.2: Interacting Green's functions $G_{\uparrow\uparrow}$ and $G_{\uparrow\downarrow}$ obtained from Monte-Carlo sampling (dashed lines) and exact diagonalization (red lines) of an Anderson impurity model, with fixed filling but different interaction strengths βU. For strong interactions one can identify small deviations of the MC result from the exact result because all figures have been obtained with 10^6 sampling steps, which is clearly too few for strong interactions $\beta U = 50$.

4.3 Superfluid Formulation of CT-AUX

To properly describe systems with attractive interactions, i.e. with an interaction Hamiltonian

$$H' = -Un_\uparrow n_\downarrow, \tag{4.43}$$

one has to allow for superfluid pairing, i.e. the anomalous Green's functions

$$\Delta(\tau) = \langle c_\uparrow^\dagger(\tau) c_\downarrow^\dagger \rangle \tag{4.44}$$

can become finite. To allow for a this, the Anderson impurity model must contain terms which don't conserve of particle number. The AIM we consider for this problem is given by the Hamiltonian

$$H = -\sum_\sigma \mu_\sigma n_\sigma - Un_\uparrow n_\downarrow + \sum_\sigma c_\sigma^\dagger \hat{V}_\sigma + \text{h.c.} + H^{\text{bath}}, \tag{4.45}$$

where the hybridization operator $\hat{V}_\sigma$ is defined as usual

$$\hat{V}_\sigma = \sum_{\mathbf{k}} V_{\mathbf{k}}^\sigma d_{\sigma\mathbf{k}} \tag{4.46}$$

and the bath Hamiltonian contains the symmetry breaking terms

$$H^{\text{bath}} = \sum_{\mathbf{k}} \left(d_{\uparrow\mathbf{k}}^\dagger, d_{\downarrow\mathbf{k}} \right) \begin{pmatrix} \epsilon_{\uparrow\mathbf{k}} & \Delta_{\mathbf{k}} \\ \Delta_{\mathbf{k}}^* & -\epsilon_{\downarrow\mathbf{k}} \end{pmatrix} \begin{pmatrix} d_{\uparrow\mathbf{k}} \\ d_{\downarrow\mathbf{k}}^\dagger \end{pmatrix}. \tag{4.47}$$

Integrating out the bath degrees of freedom, this leads to an effective impurity action

$$S_{\text{eff}} = \int d\tau d\tau' \left(c_\uparrow^\dagger(\tau), c_\downarrow(\tau) \right) \hat{\mathcal{G}}^{-1}(\tau - \tau') \begin{pmatrix} c_\uparrow(\tau') \\ c_\downarrow^\dagger(\tau') \end{pmatrix} - U \int d\tau\, n_\uparrow(\tau) n_\downarrow(\tau), \tag{4.48}$$

with the matrix of Green's functions

$$\hat{\mathcal{G}}^{-1}(\tau) = \delta(\tau) \begin{pmatrix} \partial_\tau - \mu_\uparrow & 0 \\ 0 & \partial_\tau + \mu_\downarrow \end{pmatrix} + \begin{pmatrix} \Gamma_{\uparrow\uparrow}(\tau) & \Delta_0(\tau) \\ \Delta_0^*(\tau) & -\Gamma_{\downarrow\downarrow}(-\tau) \end{pmatrix}. \tag{4.49}$$

The hybridization functions can be obtained from the parameters of the impurity model according to the formula (3.13), leading to

$$\Gamma_{\sigma\sigma}(i\omega) = \sum_{\mathbf{k}} \frac{|V_{\mathbf{k}}^\sigma|^2 (i\omega_n + \bar{\sigma}\epsilon_{\bar{\sigma}})}{(i\omega_n - \epsilon_\downarrow)(i\omega_n + \epsilon_\uparrow) - |\Delta_{\mathbf{k}}|^2} \tag{4.50}$$

and

$$\Delta_0(i\omega) = \sum_{\mathbf{k}} \frac{|V_{\mathbf{k}}^\sigma|^2 \Delta_{\mathbf{k}}}{(i\omega_n - \epsilon_\downarrow)(i\omega_n + \epsilon_\uparrow) - |\Delta_{\mathbf{k}}|^2}. \tag{4.51}$$

In order to determine the configurations, weights and observables for the sampling procedure, we perform a particle-hole transformation for the spin-down component of the system, i.e. defining new operators

$$\left. \begin{array}{l} \tilde{c}_\downarrow^\dagger = c_\downarrow \\ \tilde{c}_\downarrow = c_\downarrow^\dagger \end{array} \right\} \quad \Rightarrow \quad \{\tilde{c}_\downarrow, \tilde{c}_\downarrow^\dagger\} = \{c_\downarrow, c_\downarrow^\dagger\} = 1 \tag{4.52}$$

$$\tilde{n}_\downarrow = 1 - n_\downarrow. \tag{4.53}$$

These fermionic operators can now be inserted into the effective action, leading to

$$S_{\text{eff}} = \int d\tau d\tau' \left(c_\uparrow^\dagger(\tau), \tilde{c}_\downarrow^\dagger(\tau) \right) \tilde{\mathcal{G}}^{-1}(\tau - \tau') \begin{pmatrix} c_\uparrow(\tau') \\ \tilde{c}_\downarrow(\tau') \end{pmatrix} + U \int d\tau \, n_\uparrow(\tau) \tilde{n}_\downarrow(\tau), \tag{4.54}$$

which is the effective action for a spin-mixing system with repulsive interactions and non-interacting Green's functions, which are determined via

$$\tilde{\mathcal{G}}^{-1}(\tau) = \begin{pmatrix} \delta(\tau)(\partial_\tau - \mu_\uparrow - U) + \Gamma_{\uparrow\uparrow}(\tau) & \Delta_0(\tau) \\ \Delta_0^*(\tau) & \delta(\tau)(\partial_\tau + \mu_\downarrow) - \Gamma_{\downarrow\downarrow}(-\tau) \end{pmatrix}. \tag{4.55}$$

With these representation, the configurations, weights and observables can be directly obtained from the previous section about the spin-mixing CT-AUX method. The sampling procedure remains the same as for the original CT-AUX without any off-diagonal terms in the hybridization. The superfluid CT-AUX method has been used by Koga *et al.* [105, 106] to investigate the Hubbard model with attractive interactions, but they used a slightly different scheme by directly calculating the weights in an operator picture and applying formulas from the Hirsch-Fye [86] impurity solver in the continuum limit. This changes the weights and measurement formulas compared to the ones obtained above but leaves the sampling procedure unchanged.

4.4   Spin-Mixing Formulation of CT-HYB

In this section, we derive the spin-mixing version of the hybridization expansion solver, CT-HYB, which can, for instance, be used in combination with DMFT to investigate the Hubbard model with spin-mixing hopping terms and strong interactions. This solver can be discussed very briefly after the work from the previous sections, i.e. the very detailed discussion of the CT-HYB solver in Sec. 3.3 and the derivation of the spin-mixing CT-AUX solver. The Anderson impurity model of consideration is the same as introduced in the CT-AUX section, i.e. in equation (4.28), leading to the effective action

$$\begin{aligned} S_{\text{eff}} &= \int d\tau (c_\uparrow^\dagger(\tau), c_\downarrow^\dagger(\tau)) \begin{pmatrix} \partial_\tau - \mu_\uparrow & 0 \\ 0 & \partial_\tau - \mu_\downarrow \end{pmatrix} \begin{pmatrix} c_\uparrow(\tau) \\ c_\downarrow(\tau) \end{pmatrix} + \int d\tau U n_\uparrow(\tau) n_\downarrow(\tau) \\ &\quad - \int d\tau d\tau' (c_\uparrow^\dagger(\tau), c_\downarrow^\dagger(\tau)) \begin{pmatrix} \Gamma_{\uparrow\uparrow}(\tau - \tau') & \Gamma_{\uparrow\downarrow}(\tau - \tau') \\ \Gamma_{\downarrow\uparrow}(\tau - \tau') & \Gamma_{\downarrow\downarrow}(\tau - \tau') \end{pmatrix} \begin{pmatrix} c_\uparrow(\tau') \\ c_\downarrow(\tau') \end{pmatrix} \\ &= S_0 - \int d\tau d\tau' (c_\uparrow^\dagger(\tau), c_\downarrow^\dagger(\tau)) \begin{pmatrix} \Gamma_{\uparrow\uparrow}(\tau - \tau') & \Gamma_{\uparrow\downarrow}(\tau - \tau') \\ \Gamma_{\downarrow\uparrow}(\tau - \tau') & \Gamma_{\downarrow\downarrow}(\tau - \tau') \end{pmatrix} \begin{pmatrix} c_\uparrow(\tau') \\ c_\downarrow(\tau') \end{pmatrix}, \end{aligned} \tag{4.56}$$

thereby defining the action S_0, which is local in time and does not mix different spins. The corresponding Hamiltonian

$$H_0 = -\sum_\sigma \mu_\sigma n_\sigma + U n_\uparrow n_\downarrow \tag{4.57}$$

is diagonal in the local Fock space. The CT-HYB algorithm is based on an expansion of the exponential of the effective action (4.56) in terms of the hybridization functions. Since the Hamiltonian (4.57) is diagonal in the particle number of the impurity, time evolution generated by this Hamiltonian will leave the occupation of the impurity invariant. Therefore, the segment picture of the original CT-HYB algorithm is also a good choice for the configurations of the spin-mixing algorithm. An expansion in the hybridization will now, due to the off-diagonal terms in the hybridization, generate terms which, for a certain spin σ, contain more creation operators than annihilation operators. However, these terms will give zero contribution to the weights, since H_0 is diagonal in the particle number and the trace can be expressed in the particle number basis. Following the steps of the CT-HYB derivation, i.e. equations (3.79)-(3.84), it becomes immediately clear that the weights in the segment picture can be found to be

$$d\mathcal{C}\ w_{\mathcal{C}} = (-1)^{\sum_{\sigma} s_{\sigma}} e^{\mu \sum_{\sigma} \tau_{\sigma}^{\mathrm{occ}} - U\tau^{\mathrm{double}}} (d\tau)^{2(n_{\uparrow}+n_{\downarrow})} \det\left(M^{-1}(\{\tau_l^{c_{\sigma}^{\dagger}}, \tau_l^{c_{\sigma}}\})\right),\tag{4.58}$$

where the factor

$$(-1)^{\sum_{\sigma} s_{\sigma}} e^{\mu \sum_{\sigma} \tau_{\sigma}^{\mathrm{occ}} - U\tau^{\mathrm{double}}}\tag{4.59}$$

is the local trace and completely equivalent to the original CT-HYB method. In difference to the original CT-HYB, the determinant of M^{-1} can not be separated into a product of determinants containing the two distinct spins only. The meaning of the determinant is to sum up all distinct diagrams that can be drawn in the segment representation, where hybridization lines connect the starting and ending points of the segments in the impurity for given configuration, as explained in Fig. 3.8. The number of possible diagrams has now been enlarged from $n_{\uparrow}! n_{\downarrow}!$ in the original method to $(n_{\uparrow}+n_{\downarrow})!$ in the spin-mixing formulation of the hybridization expansion. Fig. 4.3 illustrates a set of diagrams contributing to the weight factor when spin-mixing is included.
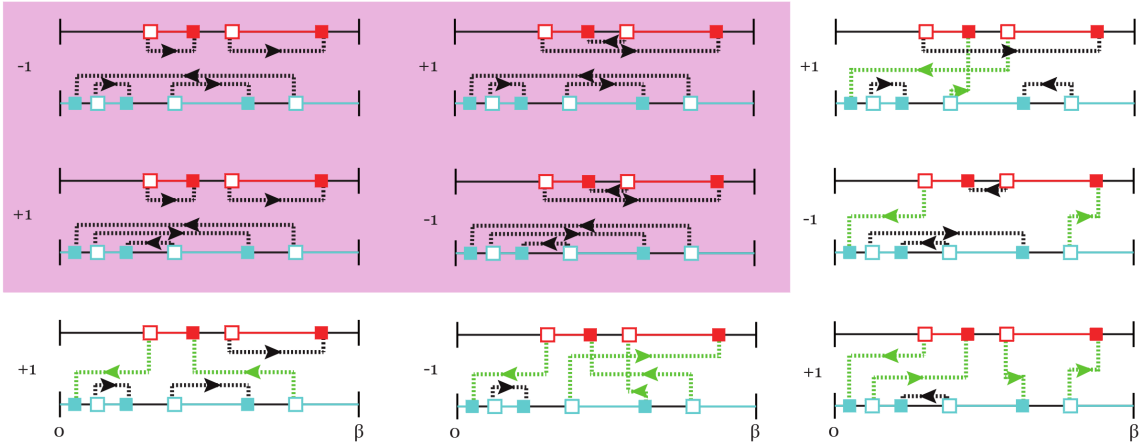

Figure 4.3: Illustration of 9 of the $(n_{\uparrow}+n_{\downarrow})! = 120$ distinct diagrams contributing to the weight factor $w_{\mathcal{C}}$ at perturbation order $n_{\uparrow} = 2$ and $n_{\downarrow} = 3$ with finite anomalous hybridization functions $\Gamma_{\sigma\bar{\sigma}}(\tau)$. The spin conserving (normal) hybridization functions are depicted with dotted black lines while the spin mixing anomalous hybridization functions are drawn as dotted green lines. Filled squares indicate annihilation operators for spin-up (red), spin-down (blue), respectively, while empty squares indicate creation operators. The four diagrams in the violet region are those diagrams which do not involve spin-mixing terms and therefore are the only ones of the shown set of diagrams that would contribute for the standard CT-HYB solver. All of the 120 diagrams for this configuration are covered by the determinant of the $(n_{\uparrow}+n_{\downarrow}) \times (n_{\uparrow}+n_{\downarrow})$ matrix M^{-1}, as defined in (4.60)-(4.62).

A formal derivation as in section 3.3, shows that the $(n_{\uparrow}+n_{\downarrow}) \times (n_{\uparrow}+n_{\downarrow})$ matrix M^{-1} can be expressed as

$$M^{-1}(\{\tau_l^{c_{\sigma}^{\dagger}}, \tau_l^{c_{\sigma}}\}) = \begin{pmatrix} M_{\uparrow}^{-1}(\{\tau_l^{c_{\uparrow}^{\dagger}}, \tau_l^{c_{\uparrow}}\}) & F_{\uparrow\downarrow}(\{\tau_l^{c_{\uparrow}^{\dagger}}, \tau_l^{c_{\downarrow}}\}) \\ F_{\downarrow\uparrow}(\{\tau_l^{c_{\downarrow}^{\dagger}}, \tau_l^{c_{\uparrow}}\}) & M_{\downarrow}^{-1}(\{\tau_l^{c_{\downarrow}^{\dagger}}, \tau_l^{c_{\downarrow}}\}) \end{pmatrix},\tag{4.60}$$

consisting of the different blocks $M_\uparrow^{-1}$, $F_{\uparrow\downarrow}$, $F_{\downarrow\uparrow}$ and $M_\downarrow^{-1}$. Where M_σ^{-1} is a $n_\sigma \times n_\sigma$ matrix, defined via

$$\left(M_\sigma^{-1}(\{\tau_l^{c_\sigma^\dagger}, \tau_l^{c_\sigma}\})\right)_{ij} = \Gamma_{\sigma\sigma}(\tau_i^{c_\sigma^\dagger} - \tau_j^{c_\sigma}), \tag{4.61}$$

and $F_{\sigma\bar\sigma}$ is a $n_\sigma \times n_{\bar\sigma}$ matrix, with the elements

$$\left(F_{\sigma\bar\sigma}(\{\tau_l^{c_\sigma^\dagger}, \tau_l^{c_{\bar\sigma}}\})\right)_{ij} = \Gamma_{\sigma\bar\sigma}(\tau_i^{c_\sigma^\dagger} - \tau_j^{c_{\bar\sigma}}). \tag{4.62}$$

In addition to the change in the weight factors $w_\mathcal{C}$, the observables must also be computed according to modified formulas as soon as spin mixing processes are considered. Completely analogous to the derivation of the measurement formulas in the original CT-HYB algorithm, we can determine the measurement formulas for the spin mixing case. By defining

$$\Delta(\tau' - \tau'' - \tau) = \begin{cases} \frac{1}{\beta}\delta(\tau' - \tau'' - \tau), & \text{for } \tau' > \tau'' \\ -\frac{1}{\beta}\delta(\beta + \tau' - \tau'' - \tau), & \text{for } \tau' < \tau'' \end{cases} \tag{4.63}$$

as in the CT-HYB section and the inverse matrix of M^{-1} as consisting of the blocks

$$M = \begin{pmatrix} \tilde{M}_\uparrow & \tilde{F}_{\uparrow\downarrow} \\ \tilde{F}_{\downarrow\uparrow} & \tilde{M}_\downarrow \end{pmatrix}, \tag{4.64}$$

where $\tilde{M}_\sigma$ is the upper-left, lower-right $n_\sigma \times n_\sigma$ block and $\tilde{F}_{\sigma\bar\sigma}$ is the upper-right, lower-left $n_\sigma \times n_{\bar\sigma}$ block of the matrix M, which is stored during the sampling[3]. The observables for the diagonal part of the interacting Green's functions is then obtained via

$$g_{\sigma\sigma}\mathcal{C}(\tau) = \sum_{ij} \Delta(\tau_i^{c_\sigma} - \tau_j^{c_\sigma^\dagger} - \tau)\left(\tilde{M}_\sigma\right)_{ij}, \tag{4.65}$$

while the off-diagonal parts are determined via

$$g_{\sigma\bar\sigma}\mathcal{C}(\tau) = \sum_{ij} \Delta(\tau_i^{c_{\bar\sigma}} - \tau_j^{c_\sigma^\dagger} - \tau)\left(\tilde{F}_{\bar\sigma\sigma}\right)_{ij}, \tag{4.66}$$

where the order of σ and $\bar\sigma$ is very important in the last equality. After determining the observables and weights for the spin-mixing system, the sampling process stays unaffected, and is described in section 3.3.2. We can also consider the superfluid formulation of the CT-HYB algorithm, which can be obtained, as for CT-AUX, by applying the particle-hole transformation to the spin-down operators. This is straightforward to calculate and is therefore not mentioned explicitly within this thesis. Another important extension of CT-HYB is to consider multi-orbital impurities and also to include interactions not only of density-density type but also exchange interactions. This has been done by Werner *et al.* [191], for instance to apply DMFT to the Kondo lattice or to multiple band models [114, 23]. On the other hand it is also possible to find a cluster formulation of the CT-HYB solver, as explained by Haule *et al.* [82, 83] and used to investigate strongly interacting superfluid systems. However, the extensions to CT-AUX and CT-HYB introduced in this and the previous chapters have been proven to be sufficient for our investigations of topological phases in the modified Hofstadter model.

4.5   Improvements for CT-HYB

In this last section of this chapter, we will introduce some improvements for the measurement process for the hybridization expansion impurity solver, namely the orthogonal polynomial representation of the observables, as introduced in [16], and a direct measurement of the self-energy within the CT-HYB algorithm, first discussed in [74]. These improvements will be discussed only for the original CT-HYB algorithm, as derived in section 3.3, – the generalization to the spin-mixing case is straight-forward.

---

[3] One should note that $\tilde{M}_\sigma$ is, of course, not simply the inverse of M_σ but instead has to be obtained by inversion of the whole matrix M, as it are the same for $\tilde{F}$.

4.5.1 Observables in the Legendre Polynomials Basis

The observables $g_{\mathcal{C}}(\tau)$ in the CT-HYB algorithm have been shown to be proportional to a δ-function in imaginary time, i.e. have to be obtained during a sampling procedure according to (3.93)

$$g_{\sigma \mathcal{C}}(\tau) = \sum_{ij} \Delta(\tau_i^{c_\sigma} - \tau_j^{c_\sigma^\dagger} - \tau)(M_\sigma(\{\tau_l^{c_\sigma^\dagger}, \tau_l^{c_\sigma}\}))_{ji}, \tag{4.67}$$

with the generalized δ-function

$$\beta\Delta(\tau' - \tau'' - \tau) = \begin{cases} \delta(\tau' - \tau'' - \tau), & \text{for } \tau' > \tau'' \\ -\delta(\beta + \tau' - \tau'' - \tau), & \text{for } \tau' < \tau'' \end{cases}. \tag{4.68}$$

To compute the observables numerically, one has to implement a discretized imaginary time interval on a fine grid and define the δ-function on this grid. This procedure is very problematic, since the grid size has a huge influence on the measurements. As one can easy imagine, a grid that is too coarse has a very bad resolution for the Green's functions, whereas a fine grid is very sensitive to errors coming from a finite number of Monte-Carlo steps, e.g. a grid point maybe is hit too many or too few times during the simulation. Another reason that the measurement formula (4.67) is unattractive is that the statistical errors, which are unavoidable in a MC simulation, may lead to spiky Green's functions, which are hard to handle in a combination of CT-HYB and DMFT. Therefore, it is much more convenient not to measure the Green's functions directly, but instead to measure the coefficients of the Green's functions in a polynomial representation. This was first suggested by Boehnke *et al.* [16] and will be briefly reviewed in the following part of this section.

The Legendre polynomials $\{\mathcal{L}_l(x)|\ l \in \mathbb{N}_0\}$ form a complete set of orthogonal functions on the interval $x \in [-1, 1]$, fulfilling the relations for orthogonality

$$\int_{-1}^{1} dx \mathcal{L}_l(x) \mathcal{L}_m(x) = \delta_{lm} \frac{2}{2l+1} \tag{4.69}$$

and completeness

$$\sum_{l=0}^{\infty} \mathcal{L}_l(x) \mathcal{L}_l(x') = \delta(x - x'). \tag{4.70}$$

As seen from (4.69), the Legendre polynomials are chosen to be normalized to $\frac{2}{2l+1}$ instead of unity. This simplifies the numerical procedure, as the Legendre polynomials can be shown to fulfill the recursive relation

$$(l+1)\mathcal{L}_{l+1}(x) = (2l+1)x\mathcal{L}_l(x) - l\mathcal{L}_{l-1}(x) \tag{4.71}$$
$$\mathcal{L}_0(x) = 1, \quad \mathcal{L}_1(x) = x, \tag{4.72}$$

which can directly be used to compute the value of $\mathcal{L}_l(x_0)$ for $x_0 \in [-1, 1]$ for all coefficients $0 \le l\ L_{\max}$ recursively [4]. The Green's function $G_\sigma(\tau)$ can be expressed as

$$G_\sigma(\tau) = \sum_{l=0}^{\infty} g_{\sigma,l}\ \mathcal{L}_l(x(\tau)), \tag{4.73}$$

with the argument $x(\tau) = 2\tau/\beta - 1$ and the coefficients $g_{\sigma,l} \in \mathbb{R}$. The coefficients are obtained by applying the orthogonality relation (4.69) in combination with (4.73), leading to

$$g_{\sigma,l} = \frac{2l+1}{\beta} \int_0^\beta d\tau\ \mathcal{L}_l(x(\tau)) G_\sigma(\tau). \tag{4.74}$$

Therefore, knowing the Green's function $G_\sigma(\tau)$ on the interval $[0, \beta]$ is equivalent to knowing all the coefficients $g_{\sigma,l}$ for $l \in \mathbb{N}_0$. However, in a numerical simulation, one is forced to truncate this series

---

[4] Note that computing the polynomials on a fine grid at the beginning of a simulation and then interpolating the values for x_0 in every single step is computationally not faster than to apply the recursive relations (4.71), (4.72) for every step.

to a finite number of these coefficients. This is not a serious problem, since it is easy to prove that the coefficients $g_{\sigma,l}$ scale as

$$g_{\sigma,l} = \mathcal{O}\left(\frac{1}{\sqrt{l}}\right) \tag{4.75}$$

for the case when $G_\sigma(\tau)$ is a smooth function[5]. This means that the coefficients can be restricted to $0 \leq l \leq L_{\max}$, where $L_{\max}$ has to be chosen sufficiently large (we use $L_{\max} = 40$). In a Monte-Carlo simulation, the observable of interest has been switched now from the imaginary time Green's function $G_\sigma(\tau)$, which had to be measured on a discretized time grid without any clear estimations for the grid size, and the size of the individual grid points to the coefficients $g_{\sigma,l}$, which are discretized by definition, with the clear scaling behavior of (4.75). The Green's functions are determined by the equation

$$G_\sigma(\tau) = \frac{\sum_{\mathcal{C}} w_{\mathcal{C}} \, g_{\sigma\mathcal{C}}(\tau)}{\sum_{\mathcal{C}} w_{\mathcal{C}}}, \tag{4.76}$$

where $\sum_{\mathcal{C}}$ is the sum over all configurations $\mathcal{C}$ as explained in section 2.3.2. Applying (4.74) to equation (4.76) directly leads to

$$g_{\sigma,l} = \frac{\sum_{\mathcal{C}} w_{\mathcal{C}} \, g_{\sigma,l\mathcal{C}}}{\sum_{\mathcal{C}} w_{\mathcal{C}}}, \tag{4.77}$$

with the configurations coefficients $g_{\sigma,l\mathcal{C}}$, determined via

$$
\begin{aligned}
g_{\sigma,l\mathcal{C}} &= \frac{2l+1}{\beta} \int_0^\beta d\tau \, \mathcal{L}_l(x(\tau)) g_{\sigma\mathcal{C}}(\tau) \\
&= \frac{2l+1}{\beta} \sum_{ij} (M_\sigma(\{\tau_l^{c_\sigma^\dagger}, \tau_l^{c_\sigma}\}))_{ji} \int_0^\beta d\tau \, \Delta(\tau_i^{c_\sigma} - \tau_j^{c_\sigma^\dagger} - \tau) \, \mathcal{L}_l(x(\tau)) \\
&= \sum_{ij} (M_\sigma(\{\tau_l^{c_\sigma^\dagger}, \tau_l^{c_\sigma}\}))_{ji} \, \tilde{\mathcal{L}}_l(x(\tau_i^{c_\sigma} - \tau_j^{c_\sigma^\dagger})).
\end{aligned}
\tag{4.78}
$$

Here, we defined the modified Legendre polynomials

$$\tilde{\mathcal{L}}_l(x(\tau)) = \begin{cases} \mathcal{L}_l(x(\tau)) & \text{for } \tau > 0 \\ -\mathcal{L}_l(x(\tau+\beta)) & \text{for } \tau < 0 \end{cases}. \tag{4.79}$$

The measurement of the Legendre polynomial coefficients $g_{\sigma,l\mathcal{C}}$ is numerically very simple to implement and doesn't require much more computation time compared to the measurement of the Green's functions on a grid. However, by using a polynomial representation one always obtains smooth Green's functions and the information that is lost by placing a finite cut-off $L_{\max}$ can be much better estimated than for the case of a discretized time interval in the original formulation of CT-HYB. Except for the benchmarking calculations of section 3.3, all calculations using CT-HYB have been performed with measurements in the polynomial representation, where the gain in accuracy compared to the original formulation is huge compared to effort of its implementation. For a more detailed discussion about the polynomial representation, also involving higher order correlation functions and measurements in the Matsubara frequency representation, we refer the reader to [16].

4.5.2   Direct Self-Energy Measurement for the CT-HYB Algorithm

In section 1.3, we saw that for the DMFT procedure both the interacting impurity Green's function $G_\sigma(i\omega_n)$ as well as the impurity self-energy $\Sigma_\sigma(i\omega_n)$ are required. While the interacting Green's functions are obtained directly via solving the impurity problem, the self-energy has to be determined via the Dyson equation

$$\Sigma_\sigma(i\omega_n) = \mathcal{G}_\sigma^{-1}(i\omega_n) - G_\sigma^{-1}(i\omega_n). \tag{4.80}$$

---

[5]In [16], a scaling of $\mathcal{O}(1/l)$ was found, which results from their distinct definition of the coefficients $g_{\sigma,l}$. However, for our definition of the coefficients, i.e. equation (4.74), the correct scaling is instead (4.75).

The problem with this equation in the context of a numerical Monte-Carlo simulation is that $G_\sigma(i\omega_n)$ can only be determined within statistical error. It is a well-known problem that these small errors, when inverting the Green's function and subtracting the non-interacting Green's function, can lead to large errors in the self-energy and can oscillate with iteration number of the DMFT process, especially in the intermediate frequency region. To overcome this problem, one would prefer to measure the self-energy directly during a Monte-Carlo simulation. However, this is not possible, at least not without an unfeasibly large effort. Fortunately, the quantity $F_\sigma(\tau) := (G_\sigma \Sigma_\sigma)(\tau)/U$ can be measured directly without much effort, which reduces the problem of finding the self-energy to a simple division $\Sigma_\sigma(i\omega_n) = U F_\sigma(i\omega_n)/G_\sigma(i\omega_n)$, in which the errors in both functions do not cause larger problems. In the context of the hybridization expansion solver, this procedure was first suggested by Hafermann *et al.* [74], however, it is a well-known feature that has been first introduced by Bulla *et al.* [22] in the context of Numerical Renormalization Group (NRG).

The derivation of the corresponding measurement formulas is rather easy, the only requirement is the equation of motion for the interacting Green's function, which in the context of the AIM reads,

$$\int d\tau' \mathcal{G}_\sigma^{-1}(\tau - \tau') G_\sigma(\tau' - \tau'') = \delta(\tau - \tau'') + U \underbrace{\int d\tau' \delta(\tau - \tau') \left\langle \mathcal{T} c_\sigma(\tau') c_\sigma^\dagger(\tau'') n_{\bar\sigma}(\tau'') \right\rangle}_{F(\tau - \tau'')}. \quad (4.81)$$

Transforming (4.81) to Matsubara frequency representation leads to

$$\mathcal{G}_\sigma^{-1}(i\omega_n) G_\sigma(i\omega_n) = 1 + U F_\sigma(i\omega_n), \quad (4.82)$$

from which we can identify $U F_\sigma(i\omega_n) = \Sigma_\sigma(i\omega_n) G_\sigma(i\omega_n)$, by comparison to the Dyson equation. Therefore, in the sampling procedure, we should also accumulate the additional observable

$$F_\sigma(\tau - \tau') = \left\langle \mathcal{T} c_\sigma(\tau) c_\sigma^\dagger(\tau') n_{\bar\sigma}(\tau') \right\rangle. \quad (4.83)$$

In the segment picture of the CT-HYB algorithm, this observable is almost trivial to sample, once the interacting Green's functions are also measured. Suppose in the Monte-Carlo sampling, the configuration of the present step is $\mathcal{C}$. If in this configuration, the impurity is not occupied with a spin $\bar\sigma$ for the time τ', then $n_{\bar\sigma}(\tau') = 0$ and configuration $\mathcal{C}$ does not contribute to $F_\sigma(\tau - \tau')$. On the other hand, if for the configuration $\mathcal{C}$ the spin $\bar\sigma$ is present in the impurity, $n_{\bar\sigma}(\tau') = 1$ and this configuration has the same contribution to $F_\sigma(\tau - \tau')$ as it would have to $G_\sigma(\tau - \tau')$, as one can see from (4.83). This result allows us to determine the observables $f_{\sigma\mathcal{C}}(\tau)$, such that

$$F_\sigma(\tau) = \frac{\sum_{\mathcal{C}} w_{\mathcal{C}} \, f_{\sigma\mathcal{C}}(\tau)}{\sum_{\mathcal{C}} w_{\mathcal{C}}}, \quad (4.84)$$

which can just be done by implementing the indicator mentioned above ($\bar\sigma$ is occupied, unoccupied) in the observables for the Green's functions. The observables $f_{\sigma\mathcal{C}}(\tau)$ are then defined as

$$f_{\sigma\mathcal{C}}(\tau) = \sum_{ij} \underbrace{\Delta(\tau_i^{c_\sigma} - \tau_j^{c_\sigma^\dagger} - \tau)(M_\sigma(\{\tau_l^{c_\sigma^\dagger}, \tau_l^{c_\sigma}\}))_{ji}}_{g_{\sigma\mathcal{C}}(\tau)} \times \mathcal{I}_{\bar\sigma}(\tau_j^{c_\sigma^\dagger}), \quad (4.85)$$

with the indicator function

$$\mathcal{I}_{\bar\sigma}(\tau_j^{c_\sigma^\dagger}) = \begin{cases} 0 & \text{if } \bar\sigma \text{ is unoccupied at time } \tau_j^{c_\sigma^\dagger} \\ 1 & \text{if } \bar\sigma \text{ is occupied at time } \tau_j^{c_\sigma^\dagger} \end{cases}. \quad (4.86)$$

The accumulation of the observables $f_{\sigma\mathcal{C}}(\tau)$ makes no extra computational effort when at the same time the interacting Green's functions are measured, since the result from this measurement is simply multiplied by zero or unity. On the other hand, the self-energies obtained from the division $\Sigma_\sigma(i\omega_n) = F_\sigma(i\omega_n) G_\sigma(i\omega_n)$ are much more accurate and much smoother than the ones obtained via the Dyson equation (4.80) and therefore the more direct measurement of the self-energies is much more preferable. For further comments on improved measurement schemes for the CT-HYB algorithm, we refer the reader to [74], where improved measurements for the vertex function are also discussed in further detail. However, for our purpose the derivation of the simplest of these improved measurement schemes is sufficient since we have not investigated more sophisticated observables than the single-particle correlation functions.

5. Ultracold Atoms in Optical Lattices

The discoveries of modern many-body cooling techniques such as laser cooling and evaporative cooling have lead to the achievement of Bose-Einstein condensation (BEC) [6, 5, 17] and the realization of Fermi degeneracy [184, 162, 37] with ultracold, dilute bosonic and fermionic gases, from which a wealth of research was performed. Recently, however one of the main focuses in the field of atomic and molecular physics has switched from non-interacting, single-particle physics to the exploration of correlated, many-body physics, where statistics and interactions are the dominant physical effects [15]. The first step towards realizing a quantum simulator as proposed by R. Feynman was achieved. In his seminal publication [47], Feynman discussed that a classical computer, however implemented, will experience an exponential slowdown when simulating systems that are inherently quantum mechanical in nature. He proposed to use an universal quantum simulator instead, which would not face this problem at all. Nowadays, cold atom experiments represent a keystone for the realization of a universal quantum simulator in two distinct ways. On one hand, they are deeply involved in setting up a so-called quantum computer, or quantum Turing machine, as proposed by D. Deutsch [38], which could simulate quantum physics without the problems of exponential slowing down by making use of the so-called "quantum parallelism". On the other hand, ultracold atom experiments are very clean realizations of model Hamiltonians, where the parameters of the underlying model can be tuned with very high precision. Therefore, simulating model Hamiltonians, such as those from condensed matter physics, with ultracold atoms and exploring these quantum systems in experiment is another, more direct, realization of a universal quantum simulator as proposed by R. Feynman. The latter idea has been realized by loading ultracold atoms into optically created crystal lattices and thereby perfectly simulating the bosonic [95, 60] and fermionic Hubbard model [107]. Together with the tunability of the inter-particle interactions due to Feshbach resonances, a large number of theoretical models from condensed matter physics and many-body theory have been realized, including for instance one-dimensional hard-core bosons in the Tonks-Girardeau regime [103], bosons in the lowest Landau level [19] and with dipolar interactions [61], fermionic vortex lattices [202] and many more. Recently, artificial gauge fields have been successfully implemented in optical lattice experiments [123, 124, 2, 177], simulating strong magnetic fields with flux quanta at the order of the particle density. This has paved the way for simulating topological non-trivial phases, such as the quantum Hall (QH) [104, 63, 80], the quantum spin Hall (QSH) [10, 101, 110] and the fractional quantum Hall effect [185, 116] in cold atom experiments. This development is very promising towards gaining a deeper insight in the open issue of the interplay of strong correlations and topology of the system. A great advantage of cold atom experiments with artificial gauge fields is the perfect realization of theoretical models, e.g. the Hofstadter Hamiltonian [87], which describes particles on a square lattice subjected to a strong magnetic field. Therefore, simulating these models with cold atom experiments allows for a detailed comparison of theoretical predictions and experimental observations. In this chapter, we briefly discuss the realization of the Hubbard model for ultracold fermionic and bosonic atoms in optical lattices and possible measurement techniques, such as time-of-flight measurements and Bragg spectroscopy.

5.1   Optical Lattice Potentials

Neutral atoms in an oscillating electric field will experience an energy shift due to the AC Stark effect. This second order effect describes how the electric field induces an oscillating dipole moment in the atoms, which in turn interacts with the electric field and therefore causing the above mentioned energy shift. The induced electric dipole moment $\mathbf{d}(t)$ of an atom in an oscillating electromagnetic field is described by

$$\mathbf{d}(t) = \alpha(\omega)\mathbf{E}(t), \tag{5.1}$$

where $\alpha(\omega)$ is the polarizability of the atom, which is a function of the frequency ω of the electric field $\mathbf{E}(t)$. The resulting conservative potential is determined via [62]

$$V_{\text{dip}} = -\frac{1}{2}\text{Re}\langle \mathbf{d} \cdot \mathbf{E}\rangle_t = -\frac{1}{2}\text{Re}(\alpha(\omega))\langle \mathbf{E}^2\rangle_t, \tag{5.2}$$

where the time average $\langle ...\rangle_t$ leads to a static dipole potential in the limit of stationary atoms (which is reasonable when the time-scale for the center-of-mass motion of the atom is much slower than the oscillating frequency of the electric field). The polarizability of the atom is commonly discussed in an (effective) two level system, subjected to a classical electromagnetic field. In this model, the excited state has an energy difference ω_0 with respect to the ground state and a finite decay rate Γ_e, which leads to the polarizability being a complex number. Due to this, the conservative part of the potential is determined by the real part of α, as in (5.2). In terms of the effective two level system, the potential (5.2) can be expressed as [62]

$$V_{\text{dip}} = \frac{\hbar \Omega_R \delta}{\delta^2 + \Gamma_e^2/4} I(\mathbf{x}). \tag{5.3}$$

Here, Ω_R is the Rabi frequency associated with the effective model, $\delta = \omega - \omega_0$ is the detuning of the electric field with respect to the energy difference of the two level system and $I(\mathbf{x})$ is the time averaged intensity of the electric field. Depending on the sign of δ, the potential can be chosen to be attractive or repulsive by varying the frequency of the electric field[1]. Commonly, the different detunings are denoted as red for $\delta < 0$, i.e. for $V_{\text{dip}} < 0$ being attractive, and blue for $\delta > 0$, i.e. for $V_{\text{dip}} < 0$ being a repulsive potential.

To create an optical lattice potential in a certain direction (which we denote as the x-direction), two counterpropagating laser beams with identical frequency and intensity are spatially overlayed. For equal polarization vectors, this results in

$$\mathbf{E}^2(\mathbf{r}, t) = 4E_0 \cos^2(\omega t) \cos^2(k_x x), \tag{5.4}$$

with the electric field strength E_0 and wave vector k_x. Time-averaging of the $\cos(\omega t)$ leads to a factor $1/2$, such that the lattice potential in x-direction is described by

$$V_{\text{dip}}(\mathbf{r}) = s\, E_R \cos^2(k_x x) = s\, E_R \cos^2(\pi x/a_x), \tag{5.5}$$

where we introduced the dimensionless lattice strength s, the recoil energy[2] $E_R = \hbar^2 \pi^2/2ma_x^2$ and the lattice constant in x-direction a_x, which determines the length of the unit cell of the lattice. To construct a two- or three-dimensional lattice potential, additional pairs of counterpropagating laser beams can be added in the y- and or z-direction, leading to an optical lattice potential

$$V_{\text{dip}}(\mathbf{r}) = s_x\, \cos^2(\pi x/a_x) + s_y\, \cos^2(\pi y/a_y) + s_z\, \cos^2(\pi z/a_z), \tag{5.6}$$

where we allow for different strengths s_i and lattice constants a_i for the different directions.

In the previous discussion of the optical lattice potential, the laser beams which create the lattice potential in the x-direction have been considered to be infinitely extended in the y- and z-direction. However, these laser beams typically have a Gaussian shaped intensity profile in the plane orthogonal to the propagation direction. Since the potential (5.2) is proportional to the laser intensity, it has also a Gaussian shape.

---

[1] However, the detuning also influences the imaginary part of α, which induces a dissipative part of the potential and scales as δ^{-2}. To maximize the life-time of the physical systems in experiments, the detuning has to be chosen such that the dissipative effects can be neglected for sufficiently long time-scales.

[2] In the following, E_R will be set to unity.

Therefore, the systems that can be simulated using ultracold atoms in combination with optical lattices are finite systems, that are too small to be considered as being in the thermodynamic limit. Depending on the sign of the lattice potential, the finite laser beams lead to an additional confining (red detuned lasers) potential or to a repulsion of the atoms from the center (blue detuned lasers)[3]. In any case, the simulated systems are confined to a finite region in space, typically modeled with an additional harmonic potential, leading to

$$V_{\text{dip}}(\mathbf{r}) = \sum_{i=1}^{3} s_i \ \cos^2(\pi x_i/a_{x_i}) + \sum_{i=1}^{3} V_i x_i^2 = V_{\text{latt}}(\mathbf{r}) + V_{\text{trap}}(\mathbf{r}), \tag{5.7}$$

where V_{latt} is the bare lattice potential and V_{trap} the trapping potential, which is the leading order term of the Gaussian potential[4]. For many physical effects, this trapping potential must be included for both theoretical and experimental investigations and we will discuss its effect on topological insulating systems in Sec. 6.3.

For the content of this thesis, it is also relevant that in optical lattice experiments lattice models with dimensions lower than three can be simulated, as it is for instance necessary to investigate the integer quantum Hall effect. This is done by applying a two-dimensional lattice potential and confining the system in the residual direction, for instance by a dipole trap. If the energy gap between the excited states and the ground state in the trap is much larger than the temperature of the system, it is effectively confined to two dimensions, since excitations in the third direction are very unlikely to occur. Another possibility to create two-dimensional systems is to use a three-dimensional lattice as described by (5.5) but to increase the strengths of the lattice potential in one direction such that tunneling in this direction is severely reduced. The resulting setup is then an array of two-dimensional layers, where each layer represents a two-dimensional optical lattice. Both methods have been successfully used to experimentally explore the physics in two-dimensional lattice systems [14].

5.2 Interactions and Feshbach Resonances

The interest in optical lattice experiments with ultracold atoms results not only from the high tunability of the lattice potential to which the particles are exposed to but also from the ability to precisely tune the inter-particle interactions, allowing for the experimental simulation of many-body effects, such as collective excitations or spontaneous ordering in the many-particle system. The (two-particle) interactions between neutral atoms result from the short-ranged van der Waals force, which shows a characteristic $1/r^6$ decay for sufficiently large distances r between two particles. Commonly, in the limit of dilute gases and very low temperatures, the interactions between particles are described within the framework of scattering theory. For sufficiently low energies and densities, an expansion of the two-particle scattering process in terms of partial waves reveals that when the energy scales involved in the scattering process are sufficiently low, only s-wave scattering dominates. In this case all higher order contributions are negligible and the interaction is sufficiently well described by the s-wave scattering length a_s [55, 15]. The s-wave state is spatially symmetric, which implies that two bosonic particles of the same internal quantum state can interact with each other, while for fermions only two particles in distinct internal quantum states can interact because of the symmetric, anti-symmetric two-particle wave functions, respectively. The s-wave scattering length can theoretically be obtained by taking the limit

$$a^2 = \lim_{k \to 0} \frac{\sigma_{\text{tot}}}{4\pi}, \tag{5.8}$$

where σ_{tot} is the total elastic cross section and k is the difference in momentum of the two particles [113]. However, since the exact interaction potential between two atoms is likely unknown and very hard to determine, it is much more convenient to measure the scattering length directly in experiments. The interaction potential can be modeled by an arbitrary pseudo potential, which is required to reproduce the correct scattering length in the low energy limit. Commonly, the pseudo potential is chosen as [55]

$$V(\mathbf{r} - \mathbf{r}') = \frac{2\pi a_s}{m} \delta(\mathbf{r} - \mathbf{r}'), \tag{5.9}$$

---

[3]In this case, additional trapping potentials are needed, as for instance optical dipole traps.

[4]By overlaying different laser beams, more complicated trapping potentials are possible, however, the harmonic potential is the common approximation for deep lattices.

with the reduced mass of the particles m.

An important tool to experimentally tune the strength of the inter-particle interactions independently of other experimental parameters is the use of Feshbach resonances. By making use of Feshbach resonances, it is possible to adjust the scattering length to very large values compared to the inter-atomic distance or to change the sign of a_s, thereby making the particles attracting each other, by applying an additional magnetic field. The occurrence of Feshbach resonances is due to the fact that the scattering particles are atoms and therefore have many internal degrees of freedom allowing for inelastic scattering processes.
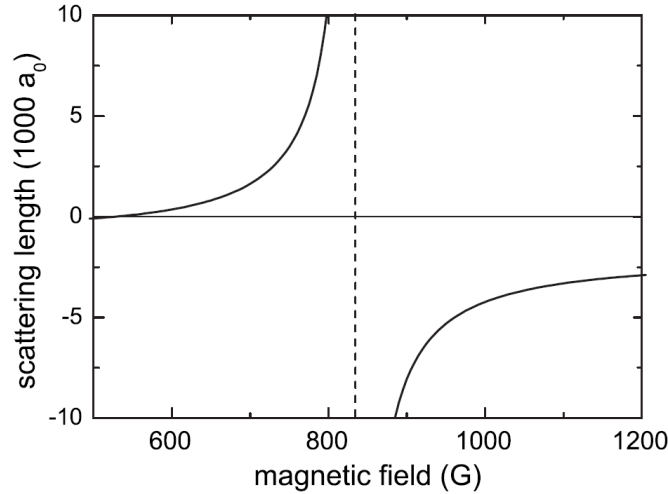
Figure 5.1: Scattering length between two hyperfine states of ^{6}Li as a function of the external magnetic field B. The Feshbach resonance is located at $B_0 = 834$G and the width of the resonance is approximately $\Delta B = 300$G. The off-resonant scattering length $a_{s0} = -1405 a_B$ (a_B is the Bohr radius) is exceptionally large for this configuration. Figure from Ref. [15].

In a two-atom scattering process, whenever the energy associated with an elastic scattering process (referred to as open channel) approaches the energy of a bound state (referred to as closed channel), the two atoms can temporarily form a bound state, which significantly influences the scattering properties. For the theoretical treatment of these effect, a single-channel analysis, i.e. considering elastic scattering processes only, is not sufficient and one has to consider a multi-channel scattering problem [176]. For the multi-channel problem, the resulting scattering length depends on the energies of the different channels [181, 183, 137], which in turn can be tuned by an external magnetic field B. The resulting scattering length can approximately be described by the formula

$$a_s(B) = a_{s0}\left(1 - \frac{\Delta B}{B - B_0}\right),\tag{5.10}$$

where the effective parameters ΔB and B_0 are being considered as the width of the resonance and the field strength at resonance, respectively [137], and have to be determined in experiment, as well as the off-resonant scattering length a_{s0}. In Fig. 5.1 magnetic field dependence of the scattering length is shown for the case of ^{6}Li.

5.3   Hubbard Parameters for Optical Lattices

We have discussed the single-particle potential set up by the lasers, i.e. described by equation (5.7), and the effective interaction potential (5.9). However, many-body physics is commonly expressed in the second quantization framework, therefore we now briefly discuss the second quantized Hamiltonian of the interacting system, which is the Hubbard Hamiltonian, discussed in section 1.1, and also the Bose-Hubbard Hamiltonian, describing interacting fermions or bosons, respectively. Equation (5.7) expresses

the single-particle potential of the system in terms of a trapping potential V_{trap} and a periodic lattice potential V_{lat}, the latter being defined as

$$V_{\text{lat}}(\mathbf{r}) = \sum_{i=1}^{3} s_i \ \cos^2(\pi x_i / a_{x_i}),$$

(5.11)

in units of the recoil energy E_R. In the regime of sufficiently deep lattices, i.e. $s \gtrsim 5$ the lattice potential is the dominant potential for determining the physics in the center of the trap, i.e. for sufficiently small particle numbers in the system. Because of this, the Hamiltonian of the system is conveniently expressed either in terms of Bloch states $|\alpha, \mathbf{k}\rangle$, which are the eigenstates of the Hamiltonian

$$H_{\text{lat}} = \frac{\mathbf{p}^2}{2m} + V_{\text{lat}}$$

(5.12)

and labeled with the band index $\alpha \in \mathbb{N}$ and the quasi-momentum $k_i \in [-\pi/a_i, \pi/a_i]$, or in terms of Wannier states $|\alpha, l\rangle$, which are obtained from the Bloch states via Fourier transformation

$$|\alpha, l\rangle = \frac{1}{\sqrt{L}} \sum_{\mathbf{k}} e^{i\mathbf{k}\mathbf{R}_l} |\alpha\mathbf{k}\rangle$$

(5.13)

and for appropriate choice of phase factors are maximally localized around lattice site l[5]. The eigenvalue equation for the lattice Hamiltonian then reads

$$H_{\text{lat}}|\alpha, \mathbf{k}\rangle = \epsilon_\alpha(\mathbf{k})|\alpha, \mathbf{k}\rangle,$$

(5.14)

where $\epsilon_\alpha(\mathbf{k})$ is a smooth function in terms of the quasi-momentum $\mathbf{k}$, but is well separated in energy for different band indices, i.e. features band gaps

$$\Delta_{\alpha,\alpha'} \equiv \min |\epsilon_\alpha(\mathbf{k}) - \epsilon_{\alpha'}(\mathbf{k})| > 0$$

for $\alpha \neq \alpha'$. This makes the set of Wannier states a good basis, since although they mix all possible quasi-momenta, they respect the separation of the system into distinct bands. Now, including the spin σ as a label for the particles internal degree of freedom, the single-particle Hamiltonian

$$H = \frac{\mathbf{p}^2}{2m} + V_{\text{lat}} + V_{\text{trap}}$$

(5.15)

can be expressed in the basis of Wannier states $|\alpha, l, \sigma\rangle$ according to

$$H = - \sum_{\alpha,l,m,\sigma} |\alpha, l, \sigma\rangle t^\alpha_{l,m} \langle \alpha, m, \sigma| + \sum_{\alpha,\alpha',l,m,\sigma} |\alpha, l, \sigma\rangle V^{\alpha,\alpha'}_{l,m} \langle \alpha', m, \sigma|,$$

(5.16)

with the matrix elements of the lattice Hamiltonian

$$t^\alpha_{l,m} = -\langle \alpha, l, \sigma| \left(\frac{\mathbf{p}^2}{2m} + V_{\text{lat}} \right) |\alpha, m, \sigma\rangle = -\sum_{\mathbf{k}} e^{i\mathbf{k}(\mathbf{R}_l - \mathbf{R}_m)} \epsilon_\alpha(\mathbf{k}),$$

(5.17)

which respect the separation of the system into distinct bands[6], and the matrix elements of the trapping potential

$$V^{\alpha,\alpha'}_{l,m} = \langle \alpha, l, \sigma| V_{\text{trap}} |\alpha', m, \sigma\rangle,$$

(5.18)

which are not diagonal with respect to the band index α. Here, the laser potentials that we are considering do not make a distinction for the different internal states of the particles and therefore there is no additional dependence on σ in the matrix elements of the Hamiltonian[7]. When the band gap $\Delta_{1,\alpha'}$

---

[5]Maximally localized in this context means that the Wannier states $|\alpha, l\rangle$ are the most localized states in the subspace of fixed band index α.

[6]The minus sign in (5.17) is convention, leading to the matrix elements being positive.

[7]There exist experiments which make use of optical potentials, which distinguish between the different hyperfine states of the atoms and therefore would have additional dependence on σ in the matrix elements of the Hamiltonian. A corresponding model is discussed in Sec. 5.4.

between the first band ($\alpha = 1$) and all higher bands $\alpha' > 1$ is much larger than the typical interaction energy and the temperature of the system and the trapping potential is very flat[8], it is sufficient to express the resulting low energy physics in a lowest band approximation, i.e. neglecting all contributions from $\alpha > 1$. This approximation relies on the fact that the energetically well separated quantum states in the higher bands are only sparsely populated, thereby having no influence on the physics of the system, which is dominated by the hugely populated states in the first band[9], therefore we only consider quantum states from the lowest band and drop the index α further on. The Wannier states $|l, \sigma\rangle$ are localized around lattice site l and decay exponentially with the distance, which leads to the matrix elements $t_{l,m}$ and $V_{l,m}$ in equation (5.16) also decaying exponentially in the distance $|l - m|$. For the case of optical lattice potentials this decay is so strong, that taking only nearest neighbor matrix elements, i.e. those with $|l - m| = 1$ into account, is a perfectly reasonable approximation [95]. For the matrix elements of the trapping potential (5.18), it is sufficient to only consider the local matrix elements, where $l = m$, since the non-local matrix elements decay even faster than for the hopping matrix elements, caused by the lack of a "non-local" operator like the momentum operator in (5.17). Combining all the discussed simplifications and approximations and subsequently switching to the language of second quantization, the Hamiltonian of the system without interactions reads

$$H = - \sum_{\langle l,m \rangle, \sigma} t_{l,m} c_{l\sigma}^\dagger c_{m\sigma} + \sum_{l,\sigma} V_{l,l} c_{l\sigma}^\dagger c_{l\sigma}, \qquad (5.19)$$

where the creation and annihilation operators $c_{l\sigma}^\dagger, c_{l\sigma}$ create or annihilate a particle with spin σ at lattice site l and $\langle l, m \rangle$ means that only the sum over nearest neighbors l, m is evaluated.

The non-interacting Hamiltonian (5.19) is the same for both bosonic and fermionic particles in an optical lattice. The nature of the particles only enters the Hamiltonian in form of the different commutation relations of the creation and annihilation operators, i.e. the fermionic operators anti-commute

$$\{c_{l\sigma}, c_{m\sigma'}^\dagger\} = c_{l\sigma} c_{m\sigma'}^\dagger + c_{m\sigma'}^\dagger c_{l\sigma} = \delta_{lm} \delta_{\sigma\sigma'}, \qquad (5.20)$$

whereas the bosonic operators commute

$$[c_{l\sigma}, c_{m\sigma'}^\dagger] = c_{l\sigma} c_{m\sigma'}^\dagger - c_{m\sigma'}^\dagger c_{l\sigma} = \delta_{lm} \delta_{\sigma\sigma'}. \qquad (5.21)$$

As we saw in the previous section, bosonic atoms with the same internal quantum state can interact via s-wave scattering, while for fermions only atoms with different internal quantum states can interact with each other via s-wave scattering. Therefore the simplest interacting bosonic systems are those having no internal degrees of freedom, while for fermions the simplest systems are those which are described by atom with two possible internal quantum states, which can be seen as the spin of the particle $\sigma = \uparrow\downarrow$. For the bosonic system (without internal degrees of freedom), the interacting part of the Hamiltonian is described as

$$H_{\text{Int}} = \frac{1}{2} \sum_{l,m,s,t} U_{lmst} c_l^\dagger c_m^\dagger c_t c_s, \qquad (5.22)$$

whereas for fermions, it reads

$$H_{\text{Int}} = \frac{1}{2} \sum_{l,m,s,t,\sigma\sigma'} U_{lmst} c_{l\sigma'}^\dagger c_{m\sigma}^\dagger c_{t\sigma} c_{s\sigma'}, \qquad (5.23)$$

with the matrix elements

$$U_{lmst} = \frac{2\pi a_s}{m} \int w_l^*(\mathbf{r}) w_m^*(\mathbf{r}) w_s(\mathbf{r}) w_t(\mathbf{r}) d\mathbf{r}, \qquad (5.24)$$

according to (5.9) the same for bosonic and fermionic particles. For sufficiently deep lattices, the Wannier functions $w_l(\mathbf{r}) = \langle \mathbf{r}|l \rangle$ at site l again have almost no overlap with their neighboring sites, such that it

---

[8] All of which is fulfilled in optical lattice experiments [15].

[9] For a discussion of the influence of second order processes on the matrix elements in a lowest band approximation see for instance [13, 127]

is reasonable to only take into account the purely local parts of the interaction, i.e. the matrix elements with $l = m = s = t$. Then the interacting Hamiltonian reads

$$H_{\text{Int}} = \frac{U}{2} \sum_l n_l (n_l - 1) \tag{5.25}$$

for bosonic particles and

$$H_{\text{Int}} = U \sum_l n_{l\uparrow} n_{l\downarrow}, \tag{5.26}$$

for fermionic particles. The Hubbard interaction parameter U is then defined according to

$$U = \frac{2\pi a_s}{m} \int |w_l(\mathbf{r})|^4 d\mathbf{r}. \tag{5.27}$$

Adding the interactions to the single-particle Hamiltonian (5.19), we obtain the inhomogeneous Bose-Hubbard model

$$H = - \sum_{\langle l,m \rangle} t_{l,m} c_l^\dagger c_m + \sum_l V_{l,l} c_l^\dagger c_l + \frac{U}{2} \sum_l n_l (n_l - 1) \tag{5.28}$$

for a system of interacting single-component Bosons and the inhomogeneous Fermi-Hubbard model

$$H = - \sum_{\langle l,m \rangle, \sigma} t_{l,m} c_{l\sigma}^\dagger c_{m\sigma} + \sum_{l\sigma} V_{l,l} c_{l\sigma}^\dagger c_{l\sigma} + U \sum_l n_{l\uparrow} n_{l\downarrow} \tag{5.29}$$

for a system of interacting two-component Fermions in optical lattices. Indeed, despite the approximations made to obtain (5.28) and (5.29), optical lattices filled with one species of interacting bosons have been shown to be a near perfect realization of the Bose-Hubbard model [95, 60], i.e. of (5.28). Similarly the same statement holds for a two-species system of interacting fermions and (5.29), as shown in theory and experiment, for instance in [90, 159, 88].

5.4 Artificial Gauge Fields for Neutral Atoms in Optical Lattices

Ultracold Atoms in Optical Lattices can be seen as perfect experimental realizations of theoretical models from condensed matter physics, such as the fermionic or bosonic Hubbard model, as we have seen in the last chapter. This was proven by many experiments, which resolved for instance the Fermi-surface of non-interacting Fermions [45, 107], the metallic and Mott-insulating phase of interacting Fermions [98, 159] and the superfluid-Mott insulator transition for interacting Bosons [60]. An important class of theoretical models are those, which explain the emergence of topologically non-trivial phases, such as the quantum Hall effect or the quantum spin Hall effect, which we will discuss in the following chapter. Such models are for instance the Hofstadter model [87], the Kane-Mele model [99] or the Bernevig-Hughes-Zhang model [9]. All of them have in common, that the hopping parameters corresponding to the kinetic energy in these models show complex phases, corresponding to a non-trivial gauge potential. The gauge potential results either from external magnetic fields, which leads to a spatially dependent but Abelian gauge potential or from intrinsic spin-orbit coupling, for instance of Rashba type, which leads to homogeneous but non-Abelian gauge potentials.

The experimental simulation of these theoretical models with cold atoms is rather complicated, as, on one hand, the atoms themselves are neutrally charged such that an external magnetic field does not affect the hopping of the particles at all and, on the other hand, the atoms do not show any kind of natural spin-orbit coupling, such that for both effects, the gauge potential has to be introduced to the atoms artificially [96, 143, 54, 34]. This leads to the topic of artificial gauge fields for neutral atoms, which has gained much interest because of the promising possibility to investigate topological phases in cold atom experiments where, in contrast to condensed matter, all experimental relevant parameters can be controlled from the experimentalist. Since the realization of artificial gauge fields has come into focus of theorists and experimentalists, a plethora of publications has proposed how to implement several kinds of

gauge potentials in cold atom experiments [123, 124, 119, 28, 57, 96, 143, 54, 34], reaching from the creation of artificial effective magnetic fields, to optical flux lattices and even time-reversal invariant non-Abelian gauge fields. Here, we will focus on a proposal by Goldman *et al.* [57], which focuses on the realization of a combination of Abelian and non-Abelian artificial gauge field for a two-component fermionic system on an atom chip. The model proposed in this letter is the model that the theoretical investigations in the following chapters will be focused on. The proposed setup uses a combination of Raman-assisted tunneling and an alternating Zeeman lattice, which we will explain in the following.

5.4.1   Raman Transitions in the Λ-system

Consider an atomic system consisting of three internal states, two low energy states $\{|g_1\rangle, |g_2\rangle\}$ with energies ω_1, ω_2 lying close to each other and a high energy excited state $|e\rangle$ with a much larger energy ω_e, where the two low energy states are coupled to the excited state via two far off-resonant laser beams. The frequency of the first laser is denoted as $\omega_1^L = \omega_e - \omega_1 + \delta_1$, where δ_1 is the detuning from the transition frequency, while the frequency of the second laser can be written as $\omega_2^L = \omega_e - \omega_2 + \delta_2$, with the second detuning δ_2.

It is more convenient to switch to a rotating frame [25], which simplifies the view on the situation
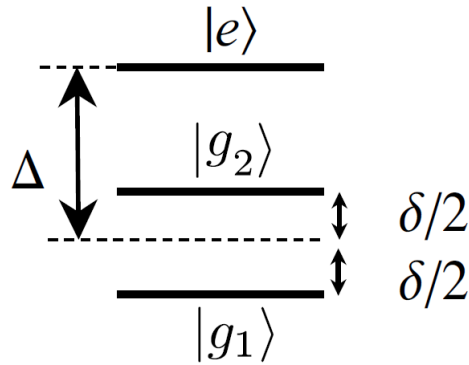
Figure 5.2: Illustration of the Λ-system in an energy level diagram. The two low energy states $|g_1\rangle, |g_2\rangle$ are separated by an energy difference δ and the excited state $|e\rangle$ is separated from both states by the energies $\Delta \pm \delta/2$.

introduced above. In a rotating frame, the two low energy states are separated by an energy difference $\delta = \delta_2 - \delta_1$ and the excited state is separated from the states $|g_1\rangle, |g_2\rangle$ by the energies $\Delta \pm \delta/2$, where $\Delta = \delta_2 + \delta_1$, see Fig. 5.2. After performing a rotating wave approximation (see for instance [151]), an effective, Rabi-type model is obtained, which is described by the Hamiltonian

$$H_{\text{Rabi}} = \frac{1}{2} \begin{pmatrix} -\delta & 0 & \Omega_a^* \\ 0 & \delta & \Omega_b^* \\ \Omega_a & \Omega_b & 2\Delta \end{pmatrix}, \tag{5.30}$$

where Ω_i, $i = a, b$ is the corresponding Rabi-frequency $\Omega_i = |\Omega_i|e^{i\phi_i}$ with the spatially dependent phase $\phi_i = \mathbf{k}_i\mathbf{r}$. In the following, we consider $|\Delta| >> |\delta|, |\Omega_i|$, i.e. very large detuning of the lasers. Then, starting with a state $|\psi\rangle$ without any population of the excited state, the excited state will stay almost completely unpopulated during the time evolution. Exploiting this fact, an effective model for the low energy states only can be derived. Assuming a state

$$|\psi(t)\rangle = \begin{pmatrix} \alpha(t) \\ \beta(t) \\ \gamma(t) \end{pmatrix}, \tag{5.31}$$

the Schrödinger time-evolution of this state is determined according to

$$
i\partial_t \begin{pmatrix} \alpha(t) \\ \beta(t) \\ \gamma(t) \end{pmatrix} = H_{\text{Rabi}} \begin{pmatrix} \alpha(t) \\ \beta(t) \\ \gamma(t) \end{pmatrix} = \frac{1}{2} \begin{pmatrix} -\delta\alpha(t) + \Omega_a^*\gamma(t) \\ \delta\beta(t) + \Omega_b^*\gamma(t) \\ 2\Delta\gamma(t) + \Omega_a\alpha(t) + \Omega_b\beta(t) \end{pmatrix}.
\tag{5.32}
$$

For stationary $\gamma(t)$, i.e. $\partial_t\gamma = 0$, the third row of (5.32) requires

$$
\gamma(t) = -\frac{\Omega_a}{2\Delta}\alpha(t) - \frac{\Omega_b}{2\Delta}\beta(t),
\tag{5.33}
$$

which allows us to replace $\gamma(t)$ by α and β[10]. Replacing γ by (5.33) in equation (5.32) leads to an effective time-evolution for the α and β coefficients.

$$
i\partial_t \begin{pmatrix} \alpha(t) \\ \beta(t) \end{pmatrix} = \tilde{H}_{\text{Rabi}} \begin{pmatrix} \alpha(t) \\ \beta(t) \end{pmatrix},
\tag{5.34}
$$

with the simplified Rabi Hamiltonian

$$
\tilde{H}_{\text{Rabi}} = -\frac{1}{2} \begin{pmatrix} \delta + \frac{|\Omega_a|^2}{2\Delta} & \Omega_R^* \\ \Omega_R & -\delta + \frac{|\Omega_b|^2}{2\Delta} \end{pmatrix},
\tag{5.35}
$$

where the Rabi frequencies Ω_R are defined as

$$
\Omega_R = \frac{\Omega_a\Omega_b^*}{2\Delta} = |\Omega_R|e^{i(\mathbf{k}_a - \mathbf{k}_b)\mathbf{r}},
\tag{5.36}
$$

leading to the Hamiltonian in (5.35) being spatially dependent. Typically, the laser beams which drive the transitions from the low energy states to the excited states have to be chosen to account for the internal structure of the atoms, e.g. for different angular momenta of different interal states, which was not discussed here. A set of laser beams realizing the Hamiltonian (5.35) for a set of two distinct internal states $|g_1\rangle, |g_2\rangle$ of an atom is called a Raman setup, or a set of Raman lasers. The transitions are called Raman transitions.

5.4.2   Zeeman Lattice plus Raman Beams

The system we consider consists of atoms with two different hyperfine states $|g_1\rangle, |g_2\rangle$[11], which are confined to two dimensions (see section 5.1). In the x-direction, two laser beams are creating a lattice with lattice potential

$$
V_x(x) = s_x \cos^2(\pi x/a_x),
\tag{5.37}
$$

which acts equally on both hyperfine states. In the y-direction, a Zeeman lattice is build by implementing stripes of constant magnetic field along the x-direction but with alternating sign in the y-direction [57]. The both hyperfine states, due to their distinct internal spin, feel a lattice potential in the y-direction. In contrast to the lattice in x-direction, the lattice in the y-direction is state dependent, i.e. $|g_1\rangle$ feels a maximum in the potential at the place where $|g_2\rangle$ feels a minimum and vice versa. Additionally, there is a total energy shift B between the two hyperfine states. In the proposal of [57], the Zeeman lattice is created on an atom chip by current carrying wires, oriented in the x-direction, such that the current travels in the opposite direction in two neighboring wires. Approximating the Zeeman lattice by a cos-function, which is sufficient for the tight-binding approximation, then leads to the lattice potential

$$
V(x,y) = V_x(x)\mathbb{1} + V_y(y)\sigma_z + B\sigma_z,
\tag{5.38}
$$

---

[10]It is evident that the choice of γ in (5.33) is itself time dependent and therefore not self-consistent with the assumption [25, 94]. However, the approximation is well established since it leads to results in good agreement with exact solutions. For a detailed analysis, see [20]

[11]There must be more than two internal states for these atoms, however, we consider all others to be essentially unpopulated.

where σ_z is the Pauli z-matrix, acting on the subspace of the two hyperfine states and

$$V_y(y) = s_y \cos^2(\pi y/a_y) \tag{5.39}$$

is the potential for the first hyperfine state. To create a square lattice in the end, we chose $a_y = 2a_x = 2a$. The Hamiltonian for the Zeeman lattice configuration then reads

$$H_0 = \frac{\mathbf{p}^2}{2m}\mathbb{1} + V_x(x)\mathbb{1} + V_y(y)\sigma_z + B\sigma_z. \tag{5.40}$$

In the x-direction, a particle can hop from one lattice site to the next lattice site without changing the internal state and therefore the system is described by a tight-binding model in the x-direction. On the other hand, hopping from one lattice site to a neighboring site in the y-direction requires the change of the particle's hyperfine state because of the alternating potential in this direction. Without changing the hyperfine state, the particle can only hop to the next nearest neighbor, which is strongly suppressed due to a small spatial overlap and therefore, without additional potentials that change the hyperfine states of the particles, no hopping in y-direction takes place.

To allow for tunneling in the y-direction, additional operators are required, which change the internal state of the particles. Equation (5.35) exactly describes such an operator, which is the operator describing two Raman beams acting on the system. Adding these two Raman beams, leads to the total Hamiltonian of the system

$$H = \frac{\mathbf{p}^2}{2m}\mathbb{1} + V_x(x)\mathbb{1} + V_y(y)\sigma_z + B\sigma_z + \tilde{H}_{\text{Rabi}} \tag{5.41}$$

which contains diagonal and off-diagonal terms in the hyperfine states. The corresponding tight-binding Hamiltonian in second quantization can now be expressed as

$$H = \sum_{\langle i,j\rangle,\sigma,\sigma'} t_{ij}^{\sigma\sigma'} c_{i\sigma}^\dagger c_{j\sigma'}, \tag{5.42}$$

where i,j label the lattice sites of the two-dimensional system and the sum is running only over pairs of nearest neighbors. The index $\sigma = g_1, g_2$ labels the two hyperfine states. For hopping in the x-direction, only the hopping amplitudes between equal hyperfine states are non-zeros, while for the y-direction only hopping amplitudes between distinct hyperfine states are non-zero, due to the Raman coupling.

As shown in (5.36), the off-diagonal terms in the Hamiltonian (5.42) carry a position dependent phase factor $e^{i(\mathbf{k}_a - \mathbf{k}_b)\cdot\mathbf{r}}$, which can be adjusted by changing the wave-vectors of the Raman beams $\mathbf{k}_{a,b}$. To realize phase factors which break time-reversal symmetry, i.e. realize quantum Hall physics, one can realize the Landau gauge by adjusting the phase factor such that they depend on the x-coordinate only. Then the hopping matrix elements in the x-direction would obtained by the common formula

$$t_{ij}^x = \int w(\mathbf{r})H_{11}w(\mathbf{r} + a_x\mathbf{e}_x)d\mathbf{r} = t^x, \tag{5.43}$$

with H_{11} being the first matrix element of the Hamiltonian (5.41) and $\mathbf{e}_x$ the unit vector in x-direction. Therefore, the hopping elements in the x-direction can be chosen purely real and are uniform.

On the other hand, the hopping matrix elements in the y-direction are defined according to

$$t_{ij}^y = \int w(\mathbf{r})H_{12}w(\mathbf{r} + a_y/2\mathbf{e}_y)d\mathbf{r} = \frac{|\Omega_R|}{2}\int w(\mathbf{r})e^{i(k_a - k_b)x}w(\mathbf{r} + a_y/2\mathbf{e}_y), \tag{5.44}$$

where we have already exploited that the Raman beams are chosen such that the phase factor only depends on the x-coordinate. Solving the equations above leads to the hopping matrix elements for the y-direction being

$$t_{ij}^y = t^y\, e^{i2\pi\alpha x_i} \tag{5.45}$$

with uniform magnitude and spatial dependent phase $e^{i2\pi\alpha x_i}$, where $\alpha = (k_a - k_b)a_y/2\pi = (k_a - k_b)a/4\pi$. The absolute value of the hopping amplitude in x- and y- direction can be tuned independently, allowing the realization of the desired case of $t^y = t^x \equiv t$ by adjusting the experimental parameters. On the other, the "flux" parameter α can be adjusted the same way, allowing for the special cases, where

$\alpha = p/q$ with $p, q \in \mathbb{N}$ and therefore realizing the celebrated Hofstadter model with cold atoms[12]. The two-component system introduced here can effectively be seen as a single-component system, since, due to the fact that the two hyperfine states feel an opposite potential in the y-direction, a given column in the x-direction will only be populated by a single hyperfine state. In other words, every even column will be occupied with atoms in the hyperfine state $|g_1\rangle$, while every odd column will be populated only with atoms in the hyperfine state $|g_2\rangle$, such that the double occupancy of every lattice site is zero, due to the Pauli principle. This leads to the fact that the system can be treated as an effective single particle system of atoms in just a single internal state, which we call $|g\rangle$.

5.5   Time-Reversal Invariant Topological Insulators with Cold Atoms

In the previous section, we introduced a possible realization of artificial Abelian gauge fields for ultracold atoms in optical lattices. In this section, we discuss very briefly how this system can be generalized to two-component systems, including non-Abelian gauge fields. The Hamiltonian, which is to be realized, is the time-reversal invariant generalization of the Hofstadter model with two component fermions, in second quantization stating

$$H = -t \sum_{x,y} \mathbf{c}^\dagger_{x+1,y} e^{i2\pi\gamma\sigma_x} \mathbf{c}_{x,y} + \mathbf{c}^\dagger_{x,y+1} e^{i2\pi\alpha\sigma_z x} \mathbf{c}_{x,y} + \text{h.c.}. \tag{5.46}$$

Here, we introduced the vector notation of the creation operators on a lattice site at coordinates (x, y), $\mathbf{c}^\dagger_{x,y} = (c^\dagger_{x,y,\uparrow}, c^\dagger_{x,y,\downarrow})$ and the real parameter γ which tunes the non-Abelian phase, proportional to the Pauli matrix σ_x, which mixes the spin. The spatial dependent phase $e^{i2\pi\alpha\sigma_z x}$ has opposite sign for both components, which leaves the Hamiltonian time-reversal symmetric and therefore allows for quantum spin Hall physics. After introducing the Hofstadter model in the last section, the experimental realization of its time-reversal invariant generalization (5.46) is, in principle, straight forward.
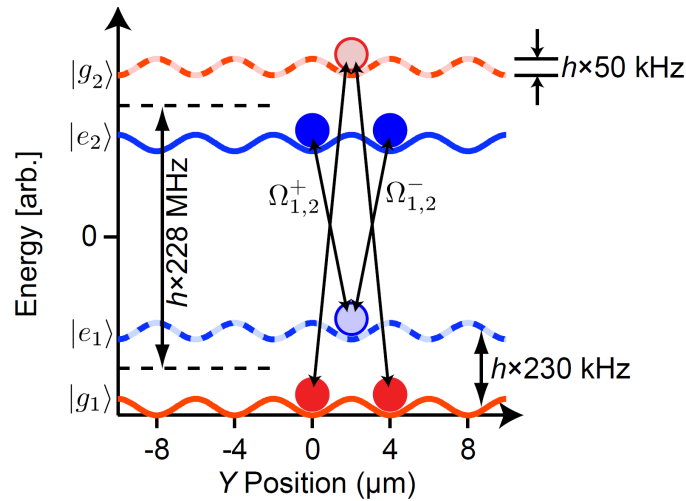
Figure 5.3: Illustration of the Raman assisted tunneling in the y-direction of the lattice. The Raman beams couple either the states $|g_1\rangle$ and $|g_2\rangle$ or the states $|e_1\rangle$ and $|e_2\rangle$. The lattices for both components are alternating, such that tunneling only happens due to the Raman beams, which imprint a phase to the particle according to (5.36). Figure from Ref. [57].

The first step is to experimentally realize a copy of the Hofstadter system with a set of new hyperfine states $|e_1\rangle, |e_2\rangle$, coupled by two distinct Raman beams in the same lattice as the original system. Then the

---

[12]For a discussion of the Hofstadter model and how the spatially dependent phases effect the single-particle physics of the system, we refer to the next chapter. The aim of this chapter was simply to explain one experimental realization of artificial gauge fields in optical lattice experiments on a very basic level.

fluxes α, α' of the two systems can be tuned independently, and one can realize the special case $\alpha = -\alpha'$. If these two systems are uncoupled but located in the same lattice, the Hamiltonian (5.46) is realized for the special choice of $\gamma = 0$. To tune the parameter γ to values larger than zero, it is sufficient to also allow for Raman assisted tunneling in the x-direction by choosing an appropriate phase of the Rabi frequencies (5.36) for the corresponding transitions. An illustration of the system with $\gamma = 0$ is depicted in Fig. 5.3, taken from Ref. [57], also showing realistic experimental parameters.

The experimental schemes to achieve artificial gauge fields in optical lattices presented in this chapter have been introduced on a very basic level, without going into any details of the current experimental issues, that emerge when trying to realize these gauge fields within optical lattices. For more details about the experimental realization of certain classes of gauge fields and the path towards the realization of more general systems, we refer the reader to [123, 124, 125, 120, 2, 177].

6. ℤ-Topological Insulators in Optical Lattices

ℤ-topological insulators are known as bulk insulating systems, which can be classified in terms of a ℤ quantum number ν. For $\nu = 0$ these systems are topologically equivalent to an ordinary insulator and therefore topologically trivial. On the other hand for $\nu \neq 0$ these systems are topologically equivalent to a quantum Hall system with the corresponding topological quantum number. All realizations of ℤ topological insulators can be discussed in terms of the corresponding quantum Hall system. In this chapter, we will introduce the quantum Hall effect on a very general level, without focusing on a specific Hamiltonian, and discuss the Chern topological invariant and the bulk-boundary correspondence. After that, we introduce the Hofstadter model, which is a lattice model in tight-binding approximation that is able to show quantum Hall phases. The main part of this chapter will then be the discussion of the realization of ℤ topological phases with ultracold atoms, which is published as an article [21].

6.1 The Quantum Hall Effect

In the Quantum Hall effect, the transverse Hall conductivity of a two-dimensional electronic system subjected to high magnetic fields is found to be quantized according to $\sigma_{xy} = Ne^2/h$, where N is a topological invariant integer, which is called the total Chern number of the occupied bands [182, 104, 141]. Since its first experimental detection [104], the quantum Hall effect has been established as the textbook example of a topological non-trivial insulator, i.e. an insulator that is, from a topological point of view, not equivalent to the vacuum state which would be the case for an ordinary band insulator [78]. In this section, we will discuss the quantum Hall effect from a topological point of view by briefly reviewing the TKNN invariant [182] and Berry phase [11], and also discuss the emergence of gapless boundary states, so-called edge states, at interfaces where the topology of the system changes.

6.1.1 TKNN Invariant and Berry Phase for the QHE

The difference between an ordinary insulator (ordinary refers to the conductivity tensor being identical to zero) and a quantum Hall state in terms of topology has been explained by Thouless *et al.* [182] (TKNN) in a seminal paper from 1982, which we will shortly review here. The essential result of the TKNN paper is that the transverse Hall conductance σ_{xy} for a bulk insulating system can be expressed as

$$\sigma_{xy} = N\frac{e^2}{h}, \tag{6.1}$$

where $N \in \mathbb{N}$ is an integer, the so-called total Chern number of the occupied bands, which is a topological invariant.

In linear response theory, the transverse Hall conductivity σ_{xy} of a fermionic lattice system is described by the Kubo formula[1]

$$\sigma_{xy} = \frac{i\hbar}{V} \sum_{n>0} \frac{\langle \psi_n | j_x | \psi_0 \rangle \langle \psi_0 | j_y | \psi_n \rangle}{(E_n - E_0)^2} - \frac{\langle \psi_0 | j_x | \psi_n \rangle \langle \psi_n | j_y | \psi_0 \rangle}{(E_n - E_0)^2}, \tag{6.2}$$

where $|\psi_n\rangle, |\psi_0\rangle$ label the many-particle excited states and ground state, E_n, E_0 are the corresponding eigenenergies of the lattice Hamiltonian and $j_\alpha, \alpha = x, y$ is the current operator for the α-direction, see for instance [32]. TKNN expressed the Hall conductivity in terms of the eigenstates of the system, which are the Bloch states $|u_\alpha(\mathbf{k})\rangle$ with band index α and quasi-momentum $\mathbf{k} \in \mathcal{B}$, where $\mathcal{B}$ is the first Brillouin zone. The expression they found for the Hall conductivity (in a more convenient formulation) states

$$\sigma_{xy} = \frac{e^2}{2\pi h} \sum_{\epsilon_\alpha < \epsilon_F} \int_{\mathcal{B}} d\mathbf{k} \, i \left(\langle \partial_{k_x} u_\alpha(\mathbf{k}) | \partial_{k_y} u_\alpha(\mathbf{k}) \rangle - \langle \partial_{k_y} u_\alpha(\mathbf{k}) | \partial_{k_x} u_\alpha(\mathbf{k}) \rangle \right), \tag{6.3}$$

where the integral runs over the complete Brillouin zone and the sum covers the occupied bands. The quantization of the Hall conductivity then comes from the fact that the integrand is the so-called Berry curvature, which is an anti-symmetric second rank tensor or, in other words, a $2n$-form (with $n = 1$) over a two-dimensional space M (which we leave unspecified). According to the Chern-Gauss-Bonnet theorem [31], the integral over the complete Brillouin zone in (6.3) returns the value

$$\sigma_{xy} = \frac{e^2}{2\pi h} \sum_{\epsilon_\alpha < \epsilon_F} 2\pi \chi(M_\alpha) \tag{6.4}$$

where $\chi(M_\alpha)$ is the Euler characteristic of the subset M_α, which is the αth magnetic Brillouin zone of the system, embedded in the first total Brillouin zone. Since the Euler characteristic is always an integer, i.e. $\chi(M_\alpha) = n_\alpha \in \mathbb{N}_0$, the Hall conductivity finally reads

$$\sigma_{xy} = \frac{e^2}{h} N, \quad \text{with} \quad N = \sum_\alpha n_\alpha. \tag{6.5}$$

The TKNN paper has two essential results, first the Hall conductivity is proven to be strictly quantized as soon as the Fermi energy of the system is located in a bulk gap and as long as linear response theory is applicable and, second, the mathematical reason for the quantization of the Hall conductance is deeply related to the topology of the of the Bloch functions $|u_\alpha(\mathbf{k})\rangle$ and therefore of the Hamiltonian that describes the physical system. The topological properties of an underlying system have to be understood as global properties, which can not be easily changed by small perturbations of the system (in contrast to geometrical properties, which are defined locally) and therefore the quantization of the Hall conductance is very robust against external perturbations which cannot change the topology [182].

The Berry curvature

$$\mathcal{F}_\alpha(\mathbf{k}) = i \left(\langle \partial_{k_x} u_\alpha(\mathbf{k}) | \partial_{k_y} u_\alpha(\mathbf{k}) \rangle - \langle \partial_{k_y} u_\alpha(\mathbf{k}) | \partial_{k_x} u_\alpha(\mathbf{k}) \rangle \right) \tag{6.6}$$

in Eq. (6.4) is closely related to another very important physical quantity, namely the Berry phase (or geometric phase) γ_α [11], which is defined as the closed path integral over the first Brillouin zone

$$\gamma_\alpha = \oint \mathcal{A}_\alpha(\mathbf{k}) d\mathbf{k} = \oint i \langle u_\alpha(\mathbf{k}) | \nabla_{\mathbf{k}} | u_\alpha(\mathbf{k}) \rangle d\mathbf{k}. \tag{6.7}$$

As one directly sees,

$$\nabla \times \mathcal{A}_\alpha(\mathbf{k}) = i \nabla \times \langle u_\alpha(\mathbf{k}) | \nabla_{\mathbf{k}} | u_\alpha(\mathbf{k}) \rangle d\mathbf{k} = \mathcal{F}_\alpha(\mathbf{k}) \tag{6.8}$$

and therefore, by applying Stoke's theorem

$$\gamma_\alpha = \oint \mathcal{A}_\alpha(\mathbf{k}) d\mathbf{k} = \int_{\mathcal{B}} \nabla \times \mathcal{A}_\alpha(\mathbf{k}) d\mathbf{k} = \int_{\mathcal{B}} \mathcal{F}_\alpha(\mathbf{k}) d\mathbf{k}. \tag{6.9}$$

---

[1]Here we restrict ourselves to the real part of the zero frequency conductivity, i.e. $\sigma_{xy} \equiv \text{Re}(\sigma_{xy}(\omega = 0))$.

This, according to (6.3), relates the Berry phase γ_α directly to the Hall conductance σ_{xy}. The Berry phase allows for a physically more appealing explanation of the quantized Hall conductance, as we will sketch shortly. Suppose there are no degeneracies along a closed loop in the Brillouin zone, such that the Bloch functions $|u_\alpha(\mathbf{k})\rangle$ accumulate a well defined phase $e^{i\phi}$ when the quasi-momentum $\mathbf{k}$ is transported adiabatically along this closed loop in the Brillouin zone. The accumulated phase is then identical to the Berry phase, i.e. $\phi = \gamma_\alpha$, and must be an integer multiple of 2π such that the states are left unchanged after the adiabatic evolution along a closed path [182]. In the TKNN paper, the quantization of the Hall conductance was explained by using Berry's phase rather than the Chern-Gauss-Bonnet theorem. While using the latter leads to a more rigorous proof [141] of the quantization, it also requires much more mathematical background on the theory of fiber bundles on complex valued manifolds.

The TKNN invariant (6.5) nicely describes the quantization of the Hall conductance σ_{xy} in cases when the Fermi energy is located in a bulk gap of the infinite system. However, it requires a well defined Brillouin zone, which only exists for translationally invariant, infinitely sized systems. For the theoretical description of finite system the so-called edge states play an essential role, which are states that are energetically located in the bulk gap of the infinite system and spatially localized along the boundary of the finite system, thereby carrying the Hall current along this boundary. In the next section we will focus on finite systems and discuss the emergence of these edge states and their relevance for the QHE and topological insulators in general.

6.1.2 Topological Edge States and the Bulk Boundary Correspondence

In the previous section, we identified the quantum Hall effect as a topological feature of an infinite system. To drive a quantum Hall system, or more general, a topological non-trivial system, into a topologically trivial system, the topology of the system must be changed. In general, changing the topology is possible by allowing bulk bands, which were formerly well separated by a bulk gap such that the Chern number of both bands was well defined, touch each other at certain points in the Brillouin zone. When two bands touch each other, the Chern number, i.e. the topology, of the individual bands is no longer well defined. Further deformation of the system will lead to splitting of the bands, such that the Chern number is well defined again but may have changed during the process of deformation.

Now imagine a finite topologically non-trivial system. The boundary of the system can be seen as an interface between a topologically non-trivial system to a topologically trivial system, namely the vacuum. Somewhere on the way from the center to the boundary of the system, the energy gap has to vanish, since this is required for changing the topological invariant from a finite integer to zero. Therefore, there will exist low energy states, which are bound to the region where the energy gap vanishes. From a topological point of view, these low energy states must also be very robust against external perturbations since, as with the Chern number of the infinite system, they exist due to purely topological arguments. As first shown by Halperin [77], these low energy states are located close to the boundary of the system, decaying exponentially into the bulk and are therefore referred to as (topological) edge states. Moreover, the edge states are chiral, which means they propagate in one direction only along a given edge of the system, and therefore are responsible for the strictly quantized Hall conductance in finite systems. The chirality of the edge states is also the reason for their robustness against external perturbations or interactions, as backscattering processes can only occur when two or more states are counterpropagating. Without backscattering, hybridization or localization of the states is impossible.

Since the introduction of edge states by Halperin [77] and the introduction of the TKNN invariant for the bulk system [182], many publications have proven that the Hall conductance obtained from the infinite system via TKNN coincides with the one obtained from the analysis of the edge states in finite system, which is known as the bulk-boundary correspondence [79, 71, 44].

We will now derive a very simple expression for the quantized Hall conductance in terms of edge states. For this purpose, we imagine a two-dimensional lattice system on a cylindrical geometry, which consists of M_y lattice sites and lattice spacing a_y in the y-direction and M_x lattice sites and lattice spacing a_x in the x-direction. While the system shall be translationally invariant in the y-direction, it is confined in the x-direction[2]. The confining potential shall not be specified, the only restriction we make for this potential is that it still allows for a clear distinction between bulk bands and bulk gaps, while the latter may now

---

[2]This is realized by periodic boundary conditions in the y-direction and choosing the Landau gauge for the vector potential $\mathbf{A}$.

contain gapless edge states which connect the different bulk bands of the system and are located close to the boundary of the system, i.e. states from different boundaries have no real space overlap. Because the system is translationally invariant in the y-direction, the quasi-momentum k_y remains a good quantum number, such that the eigenstates and eigenenergies of the system can be labeled as $|\psi_\alpha(k_y)\rangle$, $\epsilon_\alpha(k_y)$, respectively, where α is an additional label but not a band index. Fig. 6.1 shows the integrated spectral density

$$\rho(k_y, \omega) = \sum_\alpha \langle \psi_\alpha(k_y)| \frac{1}{\omega - H + i0^+} |\psi_\alpha(k_y)\rangle \tag{6.10}$$

of possible systems, where one can clearly distinguish between bulk band regions and bulk gap regions, which are now traversed by gapless edge states. The particles in the system are considered to be electrons,
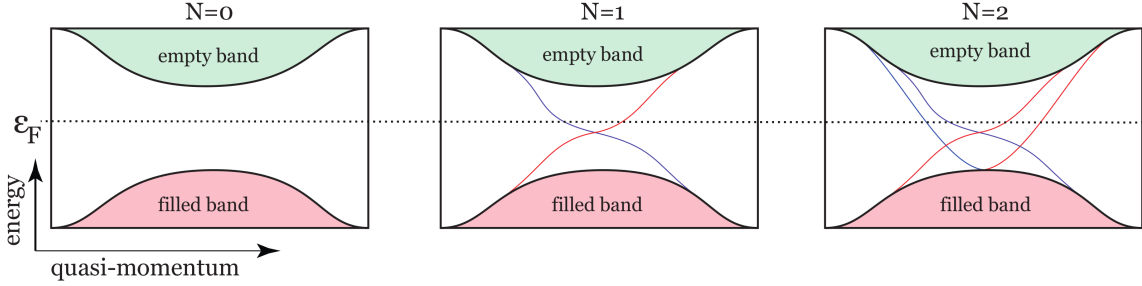
Figure 6.1: Schematic illustration of the band structure of a finite system for different topological invariants $N = 0, 1, 2$ (from left to right). The red region indicates a completely filled band, while the green region indicates a empty band in between the two bands, there is a bulk gap, filled with single edge modes, which are located at the left (red) and right (blue) boundary of the system. The Fermi energy is located in the bulk gap, such that the system finds itself in a normal insulator for $N = 0$, in quantum Hall state for $N = 1$ and in a quantum Hall state with increased Hall conductance for $N = 2$. The topological invariant N is obtained according to Eq. (6.18).

with the elementary charge $q = -e$ and a Fermi energy located in a bulk gap. Now, a voltage V_x is applied in the x-direction, which is sufficiently small, such that the energy $E_V = |eV_x| << \Gamma$ is much smaller than the bulk gap. This voltage leads to a linearly shifted chemical potential along the x-direction, i.e.

$$\mu(x) = \epsilon_F - eV_x \frac{x}{M_x}, \tag{6.11}$$

such that the difference in the chemical potential between the left and the right boundary of the system is $\Delta\mu = eV_x$. Since the bulk of the system is gapped, the change in the chemical potential does not influence the bulk at all. On the other hand, there are gapless states at the edges of the system, which will change their occupation according to the changed chemical potential. Therefore, since the chemical potential is larger at the left edge, there will be more states populated on the left edge than on the right edge, leading to an asymmetry in the current on both sides and therefore to a net current density j_y in the whole system. This current density is determined by

$$j_y = \frac{I_y}{M_y a_y} = -\frac{e}{M_y a_y} \sum_{\alpha'} v_{\alpha'}(k_y) = -\frac{e}{\hbar M_y a_y} \sum_{\alpha'} \frac{\partial \epsilon_{\alpha'}(k_y)}{\partial k_y}, \tag{6.12}$$

where I_y is the total current in the y-direction, $v_\alpha(k_y) = \partial_{k_y} \epsilon_\alpha(k_y)/\hbar$ is the velocity associated with the state $|\psi_\alpha(k_y)\rangle$ and the sum runs over all states α' that are occupied on the left side but unoccupied on the right side of the system. In the limit of a weak perturbation, this can be simplified to

$$j_y = -\frac{e}{\hbar M_y a_y} \frac{\partial \epsilon_F(k_y)}{\partial k_y} \Delta n, \tag{6.13}$$

where $\epsilon_F(k_y)$ is the energy of the edge states at the Fermi surface and Δn is the number of additionally occupied states. The chemical potential on the left boundary of the system has changed by $\Delta\mu = eV_x$, due

to the applied voltage. The number of additionally occupied states in the energy interval $[\epsilon_F, \epsilon_F + eV_x]$ shall now be expressed in terms of the voltage. Therefore, we rewrite the change in the chemical potential in terms of the k-space volume Δk_y that is available due to the energy change

$$eV_x = \Delta\mu = \left| \frac{\partial \epsilon_F(k_y)}{\partial k_y} \right| \Delta k_y. \tag{6.14}$$

In the last equation, the absolute value of the derivative of the dispersion is taken because both the k-space volume and the energy shift are defined as being positive. The number of states in this k-space volume is straight-forward to determine. In a lattice of M_y sites, with lattice spacing a_y, the quasi-momentum k_y is distributed over M_y equally distributed values in the interval $[-\pi/a_y, \pi/a_y]$ and therefore

$$\Delta k_y = \frac{2\pi \Delta n}{M_y a_y}. \tag{6.15}$$

Combining equations (6.13)-(6.15) leads to the Hall current

$$j_y = -\frac{e^2}{2\pi\hbar} \frac{\partial \epsilon_F(k_y)}{\partial k_y} \left(\left| \frac{\partial \epsilon_F(k_y)}{\partial k_y} \right| \right)^{-1} V_x = -\frac{e^2}{h} \mathrm{sgn}\left(\frac{\partial \epsilon_F(k_y)}{\partial k_y} \right) V_x \tag{6.16}$$

and therefore to the Hall conductance

$$\sigma_{xy} = \frac{j_y}{V_x} = -\frac{e^2}{h} \mathrm{sgn}\left(\frac{\partial \epsilon_F(k_y)}{\partial k_y} \right) \tag{6.17}$$

which is evidently quantized in terms of e^2/h. This derivation for the Hall conductance was performed for the case where a single edge state is present on the left edge of the system. For the case of multiple edge modes, this derivation can easily be extended to represent the contribution of every single edge mode to the Hall conductance as long as they are well separated in k-space. Therefore, the combined Hall conductance for an arbitrary number of edge states is given by the sum

$$\sigma_{xy} = -\frac{e^2}{h} \sum_\alpha \mathrm{sgn}\left(\frac{\partial \epsilon_\alpha(k_y)}{\partial k_y} \right), \tag{6.18}$$

where α labels the edge modes crossing the Fermi edge and $\epsilon_\alpha(k_y)$ is the dispersion of the α-mode at the Fermi edge.

The derivation of Eq. (6.18) presented in this thesis is very simple and does not directly rely on any topological arguments, however, the presence of edge states, which is required for a non-zero value of σ_{xy}, is a result of the topology of the system, as argued above. However, the integer

$$\nu = \sum_\alpha \mathrm{sgn}\left(\frac{\partial \epsilon_\alpha(k_y)}{\partial k_y} \right) \tag{6.19}$$

can also be interpreted in terms of topology, as pointed out by Hatsugai [79]. In his analysis, he found that (6.19) is the winding number of the edge states on a Riemann surface, which is obtained by analytically continuing the energy onto the complex plane. Additionally, Hatsugai showed that this number is identical to the total Chern number of the occupied bands and therefore proved the bulk-boundary correspondence. Whereas Eq. (6.18) is independent of the confining potential, the formulas for the Hall conductance in [79] are derived only for the case of open boundaries but without a trapping potential. While we present a generalized formulation of the Hall conductance for finite systems (6.18), which is formally equivalent to the one obtained in [79] for the open system, no proof exists for the bulk-boundary correspondence to hold for arbitrary confining potentials. For a certain confining potential, the bulk-boundary correspondence has then to be validated individually by either numerical or analytical calculations (see section 6.3 for the case of potentials relevant in optical lattice experiments).

6.2   The Hofstadter Model

So far, the discussion of the quantum Hall effect was based on topological arguments and the existence of a band structure and did not rely on the explicit form of the underlying Hamiltonian. In this section, we will discuss the famous Hofstadter model, which was introduced by Douglas Hofstadter in 1976 [87]. In the context of the quantum Hall effect, two theoretical models have been of great importance, the two-dimensional electron gas (2DEG) subjected to a perpendicular magnetic field and the Hofstadter model, which in its initial formulation describes spinless fermions in a two-dimensional lattice potential with an perpendicular external magnetic field in the tight-binding approximation. The first-quantized Hamiltonian for this system reads

$$H = \frac{(\mathbf{p} - \frac{e}{c}\mathbf{A})^2}{2m} + V(x, y), \tag{6.20}$$

where $\mathbf{A}$ is the vector potential determining the magnetic field according to $\mathbf{B} = \nabla \times \mathbf{A}$ and $V(x, y)$ is the two-dimensional lattice potential in the x-y-plane. In the following, we choose the Landau gauge, i.e. $\mathbf{A} = Bx\mathbf{e}_x$ such that $\mathbf{B} = B\mathbf{e}_z$ is perpendicular to the plane. According to the original formulation by Peierls [144], the second-quantized Hamiltonian in the tight-binding approximation is given by

$$H = -t \sum_{\langle i,j \rangle} e^{i\phi_{ij}} c_i^\dagger c_j, \tag{6.21}$$

where $c_j^\dagger$ creates a particle in the Wannier state j, which is defined as the Fourier transform of the Bloch eigenstates of Hamiltonian (6.20) but without a magnetic field. The so-called Peierls' phases ϕ_{ij} have to be chosen such that a particle hopping on a closed path along the unit cell governs the phase

$$\Phi = \phi_{12} + \phi_{23} + \phi_{34} + \phi_{41} = Ba_x a_y, \tag{6.22}$$

for an illustration see Fig. 6.2 A common choice of the phases, which is often also referred to as the Landau gauge, is

$$\phi_{ij} = \begin{cases} 2\pi\alpha x_i & \text{for hopping in the y-direction} \\ 0 & \text{for hopping in the x-direction} \end{cases}, \tag{6.23}$$

where the parameter $\alpha = Ba_x a_y/2\pi$ is referred to as the flux through the unit cell.
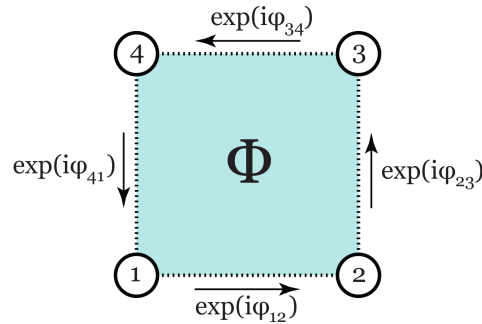
Figure 6.2: A particle hopping around a unit cell of the fluxless system, enclosed by the lattice sites $1 - 4$, accumulates the phase $\Phi = 2\pi\alpha$ according to Eq. (6.22). Modifying the phases π_{ij} does not influence the physics described by the Hofstadter model as long as Φ stays invariant under these modifications, which results from the gauge-freedom of the vector potential.

For α being rational, i.e. $\alpha = p/q$ with $p, q \in \mathbb{N}$, the unit cell of the system is enlarged an consists of q unit cells of the fluxless system (the system without magnetic field obviously has $\alpha = 0$), which leads to a splitting of the lowest band into q so-called magnetic bands of the system and the Brillouin zone to be $\mathcal{B} = [-\pi/a_x q, \pi/a_x q] \times [-\pi/a_y, \pi/a_y]$. For the case of odd q, these bands are well separated by an

energy gap, while for the case of even q the two bands at zero energy are touching each other at q points in the Brillouin zone, leading to so-called Dirac points in the spectrum with a linear dispersion close to these points, however, the residual $q - 2$ bands are again well separated from each other and from the zero energy bands by non-zero band gaps. For non-rational flux α the spectrum shows a fractal structure, as pointed out in [87]. The spectrum of the Hofstadter model as a function of the flux α is known as the Hofstadter butterfly and shown in Fig. 6.3.

In the context of the quantum Hall effect, the Hofstadter model with rational flux is particular interesting
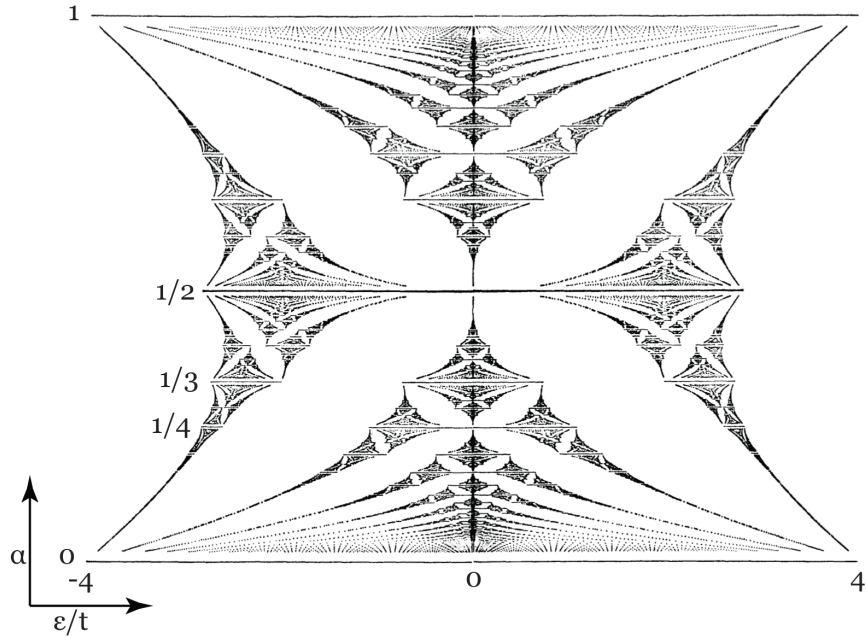
Figure 6.3: Energy spectrum of the Hofstadter model in terms of the flux parameter α (6.23), which is referred to as the Hofstadter butterfly. One clearly identifies the separation of the eigenenergies into q bands for the case when $\alpha = p/q$ with p, q, coprime and the fractal structure for the case when α is irrational. Figure taken from [87] with slight modification of the axis labels.

because it always shows a quantum Hall phase as soon as the chemical potential is placed in the band gap between two distinct magnetic bands.

The Hofstadter model is particular interesting for cold atom experiments, since it is the simplest model on a cubic lattice that realizes topological phases, in this case the quantum Hall effect. In the next section, we analyze the properties of Hofstadter models describing neutral particles in optical lattice potentials subjected to artificial gauge fields, which mimic a magnetic field for charged particles as described in section 5.4. As we will show, it is possible to realize quantum Hall physics in optical lattices by experimentally realizing the optical lattice version of the Hofstadter Hamiltonian.

6.3 Effects of Smooth Boundaries on Topological Edge Modes in Optical Lattices

M. Buchhold, D. Cocks, and W. Hofstetter

The following section discusses the effects of smooth boundaries of the edge states of a topological non-trivial system, which can be implemented with cold atom experiments. This paper was written in collaboration with Daniel Cocks and Walter Hofstetter and was published in Physical Review A with the title "Effects of Smooth Boundaries on Topological Edge Modes in Optical Lattices".

Since the experimental realization of synthetic gauge fields for neutral atoms, the simulation of topologically non-trivial phases of matter with ultracold atoms has become a major focus of cold atom experiments. However, several obvious differences exist between cold atom and solid state systems, for instance the small size of the atomic cloud and the smooth confining potential. In this chapter we show that sharp boundaries are not required to realize quantum Hall or quantum spin Hall physics in optical lattices and, on the contrary, that edge states which belong to a smooth confinement exhibit additional interesting properties, such as spatially resolved splitting and merging of bulk bands and the emergence of robust auxiliary states in bulk gaps to preserve the topological quantum numbers. In addition, we numerically validate that these states are robust against disorder. Finally, we analyze possible detection methods, with a focus on Bragg spectroscopy, to demonstrate that the edge states can be detected and that Bragg spectroscopy can reveal how topological edge states are connected to the different bulk bands.

Ultracold atoms in optical lattices provide a unique experimental setup for studying properties of solid state systems in a very clean and well controlled fashion [15, 29]. Particularly interesting in this context is the experimental implementation of artificial gauge fields for neutral atoms, as discussed in section 5.4 and in [15, 123, 124, 119, 28], simulating for instance time-reversal symmetry breaking magnetic fields [96, 140, 167, 170, 54, 97] or a coupling of the atom's internal spin degree to its angular momentum [34, 125, 56, 120]. The realization of these effects will open a path for precise simulations of a large class of topologically non-trivial systems such as quantum Hall (QH) or quantum spin Hall (QSH) phases[3]. Creating topological states of matter with cold atoms is particularly attractive because of the precise control of physical parameters such as the hopping amplitude and interaction strength, allowing the possibility to observe strongly interacting topological phases in lattice experiments. However the implementation of artificial gauge fields for neutral atoms is only one experimental challenge in simulating topological phases in optical lattices [156, 143, 2, 177]. Experiments must overcome the difficulties provided by the finite size of the lattice and the soft boundary of the system, caused by a trapping potential that is smoothly varying in space. Finite size leads to a finite overlap of spatially separated counterpropagating edge states and therefore to possible backscattering processes, decreasing the robustness of the edge states against external perturbations [173, 172]. While this is not a very serious restriction for optical lattice potentials, which are relatively pure, the effects of the soft boundary of the optical lattice system may significantly change the properties of the edge states characterizing topological insulators in finite systems. Whereas recent publications identify the soft boundaries as an unwanted restriction or propose how to avoid them by implementing artificial sharp boundaries to their system [57], we demonstrate in this chapter that soft boundaries will lead to interesting additional features, either not present or at least not visible in systems with sharp boundaries. For this purpose, we investigate different trap shapes and geometries, which are realizable in optical lattices and discuss their specific influence on the cold atom system.

This chapter is organized in the following way. First, in Sec. 6.3.1, we present the theoretical model under consideration, a QH Hamiltonian in the tight-binding approximation for spin polarized fermions confined in an additional trapping potential. In Sec. 6.3.2, we present our results for the stripe geometry, discussing in detail the properties of the edge states in systems with a hard wall boundary, a harmonic trap and a quartic trapping potential. In Sec. 6.3.3, we study the shape of the edge states in a completely trapped system and investigate the suitability of several detection methods as tools to probe the system experimentally, including Bragg spectroscopy.

6.3.1   The Hofstadter Model for Cold Atoms

The model we consider is similar to the ones proposed in [96, 54], experimentally realizing time-reversal symmetry breaking topological insulators with ultracold atomic gases. This model describes a two-dimensional (2D) system of spin-polarized fermionic atoms subjected to a square optical lattice, experiencing an artificial Abelian gauge field $\mathbf{A}$ that induces an artificial uniform magnetic field perpendicular to the lattice, $\mathbf{B} = B\mathbf{e_z}$, which is similar to the celebrated Hofstadter Hamiltonian [87] on the lattice, see previous section. In our system, the gauge field $\mathbf{A}$ enters the first-quantized Hamiltonian of the system in form of the minimal coupling $\mathbf{p} \rightarrow \mathbf{p} - \frac{e}{c}\mathbf{A}$, which leads to the Hamiltonian:

$$H = (\mathbf{p} - \frac{e}{c}\mathbf{A})^2/2m + W(\mathbf{x}) + V(\mathbf{x}). \tag{6.24}$$

---

[3]For a brief introduction into the QSH effect, see the next chapter

Hamiltonian (6.24) contains the optical lattice potential W and a spatially dependent scalar potential V which allows for the inhomogeneity of the lattice, caused by the finite width of the laser beams creating the lattice or additional external potentials such as a harmonic trap or an artificial hard wall boundary. For the moment we leave the detailed shape of V arbitrary, and only assume that the non-local matrix elements of V are negligible (i.e. $\langle l|V|m\rangle = \delta_{l,m}\langle l|V|l\rangle$, where $\langle l|$ is the Wannier state at lattice site l), which is reasonable in our case since the potential is either varying slowly compared to the lattice spacing a, or is a step function. The second quantized form of Hamiltonian (6.24) in the tight binding approximation then reads

$$H = -t \sum_{l,m} c_l^\dagger e^{i2\pi\phi_{l,m}} c_m + \sum_l V_l c_l^\dagger c_l. \tag{6.25}$$

The operator $c_l^\dagger$ here denotes the fermionic creation operator at lattice site l, with its respective annihilation operator c_l. The first term is the well known nearest neighbor (NN) hopping with amplitude t, and is complex due to the Peierls phases $2\pi\phi_{l,m}$ that are a result of the gauge field, see Sec. 6.2. The second term corresponds to the inhomogeneity V with the local matrix elements $V_l \equiv \langle l|V|l\rangle$. The phases $\phi_{l,m} = \frac{1}{2\pi}\int_l^m \mathbf{A}\cdot d\mathbf{l}$ are not uniquely defined by the magnetic field and depend on the gauge chosen. Here, we choose the common Landau gauge $\mathbf{A} = (0, Bx, 0)$, which leads to $\phi_{l,m} = \alpha \cdot x_l(\delta_{y_l,y_m+1} - \delta_{y_l,y_m-1})$, where x_l and y_l are the coordinates of lattice site l with lattice spacing $a = 1$ and $\alpha = \frac{\Phi}{\Phi_0}$ represents the flux per plaquette in units of the magnetic flux quantum, $\Phi_0 = h/e$, see Eq. (6.23). Setting $e = \hbar = 1$, we obtain $\alpha = \frac{B}{2\pi}$ for the square lattice. Throughout the rest of this chapter we choose the hopping t as the natural energy unit of our system. In the following sections we will restrict our analysis to the case where $\alpha = 1/6$ or $\alpha = 2/5$ respectively. Our results for these two cases can easily be generalized to other cases where $\alpha = p/q$, with $p, q \in \mathbb{N}$, and where topological edge states are predicted [80].

The experimental realization of a similar model was proposed in [57], where the authors consider a spinful fermionic system subjected to an artificial gauge field that simulates a magnetic field of the form $\mathbf{B} = \mathbf{B}\sigma\mathbf{e_z}$, where $\sigma = \pm 1$ is the spin quantum number. This model preserves time-reversal invariance and therefore allows for the realization of QSH phases in optical lattices. Because of the time-reversal symmetry, our analysis also applies to this model when spin remains a good quantum number, and we will mention the corresponding QSH phases throughout the text. A brief introduction to QSH physics can be found in the succeeding chapter. So far, we have not accounted for a Zeeman splitting due to an external magnetic field, a spin-orbit coupling or a staggering potential, all realizable in optical lattices [57], see section 5.5. The physics caused by these additional effects are indeed very interesting and leaving them out may seem quite restrictive, but the results we discuss in this chapter are quite general and require only that the states are topological and do not rely on the detailed nature of the edge states.

6.3.2 Edge States in Cylindrical Geometries

The defining property of topological insulators in a semi-infinite system is the emergence of gapless edge states which are localized at one edge and robust against perturbations of the system, e.g. potential or magnetic disorder. Furthermore, the presence of these states is the origin of the currents measured in QH [104, 63, 80] and QSH samples [10, 101, 110] which are well known to be strictly quantized when S_z is a good quantum number. Topological phases are typically distinguished by the transport properties of the edge states, specifically by the quantized charge (or mass for neutral atoms) that is transported at a single edge [108, 78]. One method of determining the topological quantum number for a given system is therefore to calculate the energy spectrum on a cylindrical geometry and to evaluate the transport properties of the edge states directly, as described in Sec. 6.1.2. Alternatively, one may determine the topological quantum numbers from the dispersion relation of filled bands [71] or the corresponding eigenstates [79, 182, 78] in the corresponding infinite system.

In this section we will focus on a cylindrical geometry and determine the spectral functions of the system of interest via exact diagonalization of the Hamiltonian for a finite system of size 100×100. We discuss the properties of the edge states of the system by analyzing the integrated spectral function in quasi-momentum space and real space for several kinds of boundaries and show the robustness of the edge states against perturbations by switching on a disordered potential.
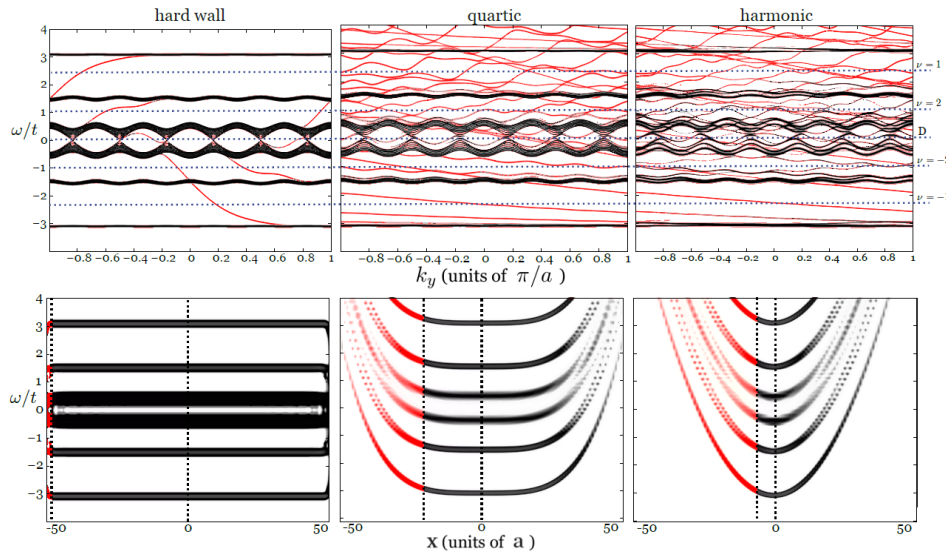
Figure 6.4: Integrated spectral function for a system described by (6.25) with flux $\alpha = 1/6$ and stripe geometry with 100×100 lattice sites. The stripe geometry is infinitely extended in the y-direction and as long as translational invariance is not broken along this direction, the Hamiltonian can be expressed in terms of k_y and x. In this case, a 100×100 lattice corresponds to 100 lattice sites in the x-direction and k_y being chosen on a 100 points grid in the interval $[-\pi/a, \pi/a]$. Three experimentally relevant confinements of the form $V(x) = V_0(x/L)^\delta$ are shown: a) hard wall, $\delta \to \infty$, b) quartic confinement, $\delta = 4$ and c) harmonic confinement, $\delta = 2$. The spectra in the upper row, $\rho_L(k_y, \omega)$, show the k_y-dependence along the periodic direction, integrated over the left half of the confinement direction, see text, and the real space spectra of the lower row, $\tilde{\rho}(x, \omega)$, show the x-dependence along the confinement direction. To the right of the figure are the transport coefficients, calculated using (6.26) with the Fermi edge set to the corresponding dotted line. For hard wall and quartic confinement there is an appreciable number of bulk bands and the edge states are clearly distinguishable, whereas within harmonic confinement we consider almost all of the states to be edge states. In each case we indicate left edge states in red (gray), while the remaining bulk states are shown in black, corresponding to the left half of the cylinder in real space, see lower plots. Two possible approaches exist for designation of edge and bulk states in softly confined systems. As seen in the upper row, energy regions with well defined topological quantum numbers can be identified in the spectrum. The corresponding states can be designated as part of the edge, and the remaining ones as the bulk. Alternatively, we can define the edge as the point at which no states have energies within the range of energies covered by states at the center of the trap. We use the latter designation, although there is little difference between the two methods.

6.3.2.1   Identification of Topological Invariants

Topological phases can be characterized either by analyzing the band structure properties of the infinite system, or in terms of the transport properties of the system in a confined geometry. While the first approach is insensitive to the specific shape of the confining potential, the latter may in principle strongly depend on these details. In this section we discuss the properties of edge states at an infinite wall boundary, realized by open boundary conditions at the edges of the cylinder, henceforth referred to as stripe geometry. For this kind of boundary the topological quantum number of the infinite system is equivalent to the transport coefficient ν of the finite system, a relation known as the bulk-boundary correspondence [79, 71]. The coefficient ν counts the difference in number of forwards-moving and backwards-moving

states at the Fermi edge, which represents the net transport for low-energy excitations and hence the quantized edge current I_E [80] and (6.18). Explicitly we have [4]

$$\nu_m = \sum_{\alpha_m} \text{sign}(\partial_{k_y} \epsilon_{\alpha_m}(k_y)), \tag{6.26}$$

where α_m labels the states at the Fermi edge with energy $\epsilon_{\alpha_m}(k_y) = \epsilon_F$ and $m = L, R$ for the left and right edge, respectively. Eq. (6.26) can be obtained by applying the well-known Laughlin argument to a cylindrical geometry and subsequently following the procedure described in [79] or by following the our derivation in the previous chapter (6.18), whereas the latter has the advantage that no specific shape of the confining potential has to be assumed. For the gauge $\mathbf{A} = (0, Bx, 0)$, the single particle Hamiltonian (6.24) obeys the symmetry $H(\mathbf{x}, \mathbf{p}) = H(-\mathbf{x}, -\mathbf{p})$, which leads to $\nu_L = -\nu_R$. Throughout this thesis we will only consider the Hall transport coefficient for the left edge $\nu \equiv \nu_L$, which is identical to the topological $\mathbb{Z}$ quantum number of the infinite system and determines the Hall conductance $\sigma_{xy} = -\nu e^2/h$, see Eq. (6.18). The topological $\mathbb{Z}_2$ quantum number ν_2, which indicates QSH phases in the corresponding spin-1/2 system [57] can then be obtained, if S_z is a good quantum number, by [196, 198]

$$\nu_2 = |\nu| \mod 2. \tag{6.27}$$

If $\nu_2 = 1$ the system will exhibit a QSH phase. In this section we make an explicit distinction between an "edge state" and an "edge mode". An edge state always refer to an eigenstate of the Hamiltonian that is localized to one edge, whereas an edge mode refers to a series of edge states that are smoothly connected in momentum-space. Although this distinction is not necessary for hard-wall systems, it is required for soft boundary systems.

6.3.2.2 Cylindrical Geometry with Open Boundary Conditions

We first consider a system described by (6.25) with a step potential V that is zero for $|x| \leq L_x/2$ and infinite elsewhere, with L_x sufficiently large, providing a hard-wall boundary at the edges of the cylinder. Since the quasi-momentum in the y-direction is a well-defined quantum number and we are interested in transport coefficients for this direction, it is convenient to represent the spectrum of the system in terms of the integrated spectral density $\rho_L(k_y, \omega) \equiv \int_{-L/2}^{0} dx \rho(x, x, k_y, \omega)$, where the spectral function is defined as

$$\rho(x, x', k_y, \omega) = -2\text{Im}\langle x, k_y| \frac{1}{\omega - H + i0^+} |x', k_y\rangle, \tag{6.28}$$
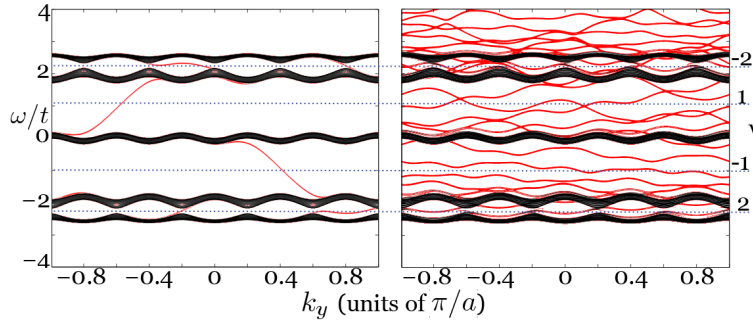
Figure 6.5: Integrated spectral function $\rho_L(k_y, \omega)$ for a system described by (6.25) with flux $\alpha = 2/5$ and hard-wall (left) and quartic (right) confinement. Edge states are shown in red (gray), while bulk states are shown in black.

We integrate only over the left half of the system in real space, so as to separate the left from the right edge states [5]. In Fig. 6.4a), upper, the integrated spectral density $\rho_L(k_y, \omega)$ is shown for $\alpha = 1/6$. One can

---

[4]Please note that the stripe geometry has the discrete translational invariance of an infinite lattice in y-direction and therefore the quasi-momentum k_y is a well defined quantum number.

[5]The integrated spectral function for the full system can be obtained from $\rho(k_y, \omega) = \rho_L(k_y, \omega) + \rho_R(k_y, \omega)$, where $\rho_R(k_y, \omega)$ is the integrated spectral function for the right half of the system, which fulfills $\rho_R(k_y, \omega) = \rho_L(-k_y, \omega)$.
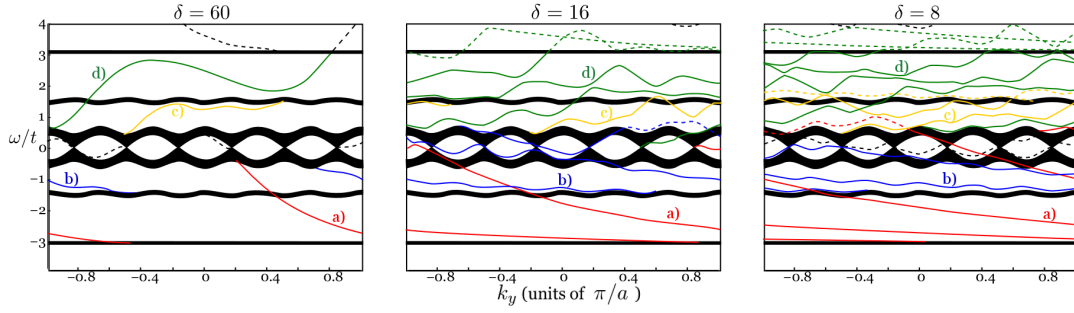
Figure 6.6: False color diagram of the integrated spectral density $\rho_L(k_y, \omega)$ for a system described by (6.25) with flux $\alpha = 1/6$, stripe geometry, and a confining potential, $V(x) = V_0(x/L)^\delta$. Bulk bands are indicated in black and edge modes as colored curves, also marked as $(a), (b), (c), (d)$. There exist several true crossings and avoided crossings in the spectra which combine to preserve the topological invariants for any confinement exponent δ. Auxiliary states of the corresponding edge modes are shown with dashed curves. The auxiliary states do not influence the topological phases of the system, since they always come in pairs with opposing velocities.

identify the bulk states which are grouped into six thick bands and the edges states, which close the gaps between the bands. To determine the transport coefficients and possible topological phases, we place the Fermi edge in a bulk gap and apply (6.26) to the dispersion of the edge states.

There are several phases visible in this system. If the Fermi edge lies within a bulk band, the system is in a trivial metallic phase. If the Fermi edge lies between the third and fourth band, there are a set of Dirac points with a linear dispersion and the phase is a semi-metal. In the bulk gaps, which lie between the other bands, the edge modes place the system in a quantum Hall phase with $\nu = -1$ and -2 for the first and second bulk gap, respectively, and inverted for the third, fourth bulk gap. In shorthand, we can specify the phases between the bands by $\text{gap}_{1/6} = \{-1, -2, D, 2, 1\}$, where D represents Dirac points. In the analogous spin-1/2 system, $\nu = \pm 1$ indicates a QSH phase whereas $\nu = \pm 2$ corresponds to a normal insulator, due to lack of topological protection. In addition we also investigate the case where $\alpha = 2/5$, see Fig. 6.5 for which we find $\text{gap}_{2/5} = \{2, -1, 1, -2\}$. Note that there are no Dirac points for $\alpha = 2/5$. The differences between $\text{gap}_{1/6}$ and $\text{gap}_{2/5}$ appear as different real space behaviors within soft confining potentials that are not visible within a hard-wall confinement, as we demonstrate in the next section.

6.3.2.3   Cylinder with Soft Boundaries

With soft boundaries, it becomes relevant to look at the spectra of the system in real space along the x axis, $\tilde{\rho}(x, \omega) = \int dk_y \, \rho(x, x, k_y, \omega)$, as well as the partially integrated spectra in quasi-momentum space along the k_y axis, $\rho_L(k_y, \omega)$. The quasi-momentum spectra allows us to extract transport coefficients and discuss the dispersion of the edge modes. On the other hand, the real space spectrum exhibits some unusual features for different trapping conditions. We consider a lattice of size 100×100 and trapping geometries of the form $V(x) = V_0(x/L)^\delta$ where $V_0 = 10t$ and $L = 50a$ is chosen such that $V(x = 50a) = V(x = -50a) = 10t$ which is larger than the energy spanned by the infinite system $\sim 8t$. Three particular values of δ are relevant to experiment: $\delta \to \infty$ which reproduces hard-wall boundary conditions, $\delta = 4$ for quartic confinement and $\delta = 2$ for harmonic confinement. In most optical lattice experiments, the confining potential is a result of the Gaussian envelope of the finite beam width of the lasers and in the center of the trap we may approximate this confinement by its leading order harmonic term. However, it is has been suggested [72] that one can remove the harmonic term by superimposing an anti-trapping Gaussian beam of different detuning to the trapping beam, which then promotes the quartic term to the leading order approximation of the trapping potential, i.e. $V(x) \propto x^4$. This scheme was realized in optical lattice experiments to improve quantum phase diffusion experiments [195, 194]. We investigate these trapping geometries below in further detail.

1. General features and preservation of topological invariants

In Fig. 6.4, we show a comparison between $\rho_L(k_y, \omega)$ and $\tilde{\rho}(x, \omega)$ for $\alpha = 1/6$ and hard wall, quartic and harmonic confinements that are relevant to experiment. One can see that the potential does not gap the system, and edge modes continue to connect the bands. The transport coefficients of the soft boundary systems, indicated to the right of Fig. 6.4, are insensitive to the trapping potential. In other words, there exist energy ranges in which we can identify a transport coefficient, which is identical for all confinements we consider.

Comparing the k_y-dependent soft-boundary spectra of the upper row in Fig. 6.4, we make two observations: 1) we can readily identify highly degenerate regions of bulk bands in the hard-wall and quartic confinements, and 2) we find that the dispersion of edge modes that are present within quartic confinement do not change noticeably when changing the confinement to the harmonic trap. In contrast, the rest of the spectrum is significantly modified, such that the ratio of bulk to edge states is very small. To define such a bulk region in the soft boundary system, we assume the edge begins at a distance from the trap center where none of the states at this point overlap in energy with any of the states in the very center of the trap (i.e. at $x = 0$).

Analogously, we can clearly identify a bulk region from the x-dependent spectra in the bottom row of Fig. 6.4 for the quartic trap, but not in the case of the harmonic trap. From this we conclude that the quartic trap is likely the best trapping potential for observing effects of both the bulk system and topological edge states in an experimental setup, if it is not feasible to artificially implement hard wall boundaries as proposed, for example, in [57]. Furthermore, we observe no overlap between states of different edges, which has been proposed to destroy edge states via couplings between the edges [173]. This again shows that the edge states are topologically protected and robust against external changes in the potential.

In Fig. 6.5, we also show a comparison of $\rho_L(k_y, \omega)$ for the case where $\alpha = 2/5$ between a hard wall (left column) and a quartic confined system (right column). We again calculate the transport coefficients of both systems and list these next to the plots to show that these also coincide for all trapping potentials.

To better understand the details of the rather complicated spectra of the quartic trap, we choose to follow the edge modes of the hard-wall confinement by smoothly varying the trapping exponent δ. We show plots for $\delta = 60, 16, 8$ and $\alpha = 1/6$ in Fig. 6.6, where we have artificially colored the spectra to indicate each edge mode. $\delta = 60$ represents a very steep trap, and is almost identical to the hard-wall case: with the color designation, one sees that the blue and yellow edge states are only present in the 2nd and 3rd bulk gaps, respectively, whereas the red (marked as (a)) and green edge states (b) span two bulk gaps. As the confinement is made softer, we see that an edge mode may cross the BZ more than once, and that the energy range of the edge states changes, e.g. with $\delta = 8$ the red state (a) now extends into the 3rd bulk gap. However, whenever this occurs, the state forms an avoided crossing at some higher energy with a different edge state and is forced downwards in energy, a process which preserves the value of the topological invariants. We represent this in the false color diagram by a dotted line for parts of the edge states that are non-topological, i.e. not connecting different bulk bands. For $\delta = 16, 8$, we can consistently see this occurring in the most energetic edge mode (colored green, (b)), which extends above the highest bulk band, and forms an avoided crossing with the non-topological edge state created by the effect of the trapping on the highest bulk band.

Note that, due to the trapping potential, several edge states that belong to the same edge mode may exist for one value of energy.

2. Merging and splitting of edge states

When the number of edge modes changes, as the Fermi edge crosses a bulk band in the hard-wall boundary system, either an edge mode must be created, or an edge mode must merge into either the bulk band itself or with another edge mode. In the soft-boundary system we can see some very non-trivial behavior that shows the complexity of these processes.

We first focus on the real space spectra of the $\alpha = 2/5$ flux system under quartic confinement, see Fig. 6.7. In the lowest gap, we see that two different edge modes, which evolve between the first and second bulk

band, merge into a single edge mode, which evolves between the second and third bulk band. In the hard wall system, this mode is localized to a single site in the x-direction and can only be observed in quasi-momentum space. In the quartic trap, the edge states leaving the first bulk band follow the shape of the quartic potential and one may expect the same for the states leaving the second bulk band. As one sees in Fig. 6.7, this is not the case. The states leaving the second bulk band immediately start to merge with the edge states from the first bulk band and the result is only a single mode at each edge, evolving between the second and third bulk band. Although it is not possible to determine topological invariants from real-space spectra, we can link this merging behavior to the k_y-space spectra of Fig. 6.5 and see that it leads to the correct topological quantum number $\nu = -1$. The same effect is again observable between the fourth and fifth bulk band. Interestingly, the merging of these modes does not take place via a simple overlap of the states, but a gap in real space with negligible spectral weight exists between the states originating from the bands and the newly-formed edge mode.

In the $\alpha = 1/6$ flux system, we also see the opposite effect: the splitting of a single bulk band, to connect edge modes of different bands which are energetically well separated. In Fig. 6.4, the integrated spectral density $\tilde{\rho}(x, \omega)$ shows that the modes leaving the second and fifth bulk bands each split into two curves, where a single eigenstate has large amplitudes on two spatially separated lattice sites. We interpret this splitting as a process that facilitates the connection between different bands which we observe in Fig. 6.6. For example, the outer part of the mode leaving the second bulk band can be seen to merge at higher energies with the mode that is a product of the third and fourth bands. This connection between the bands is analogous to the avoided crossings that we observe in the k_y-dependent spectra in Fig. 6.6. This very non-trivial behavior of modes within the outer region of the system, combined with transport coefficients which are identical to the topological quantum numbers, given by the transport coefficients of the infinite system, indicates that the soft edge states are of topological origin. To further verify this, we address in section 6.3.2.4 the robustness of these states against perturbations in terms of a disordered background potential.

3. Relation of Edge States and Bulk Bands

When we look more closely at the dispersion of the edge modes, we can see an interesting connection to the bulk bands of the system. We focus on the quasi-momentum spectra for the case $\alpha = 1/6$ shown in Fig. 6.6 for increasing confinement exponent δ.

The dispersion of an edge mode leaving a given bulk band can be described on two different quasi-momentum scales. For a small range of k_y, the dispersion mimics that of its associated bulk band, and this behavior becomes more prominent for smaller δ. This can be seen for the lowest edge modes, colored red (a) and blue (b), e.g. the red (a) mode has a locally flat dispersion, mirroring the flatness of the lowest band. However, when avoided crossings have occurred, such as for the yellow (c) and green (d) edge modes, the dispersion of an edge mode cannot simply be described by one band alone and corresponds to a mixture of bands.

On the other hand, considering the Brillouin zone as a whole, the edge modes become more flat in momentum space, the smoother the confining potential is in real space. This flattening is a direct result of the number of accessible sites at the edge. The number of lattice sites, n_{edge}, that are available for an edge state between e.g. the first and the second bulk band, is the number of sites i that fulfill $\epsilon_1 - \epsilon_0 \lesssim V(x_i) \lesssim \epsilon_2 - \epsilon_0$, where ϵ_1 (ϵ_2) are the maximum (minimum) energies of the first and second bulk band, respectively, and ϵ_0 is the minimum energy of the first bulk band [172]. In the hard wall system, $n_{\text{edge}} = 1$ but becomes larger the smoother the confining potential becomes in real space. An interesting result for the $\alpha = 1/6$ flux per plaquette, is that the flatter the potential becomes, the flatter the lowest gap edge modes become, with a corresponding increase of the effective mass of system's excitations:

$$m^* \equiv \left(\frac{\partial^2}{\partial k_y^2} \epsilon(k_y) \right)^{-1} \to \infty. \tag{6.29}$$

This is generally true for soft confinements, as pointed out in [172], but the edge state structure in the case $\alpha = 1/6$ allows this feature even for relatively steep potentials.
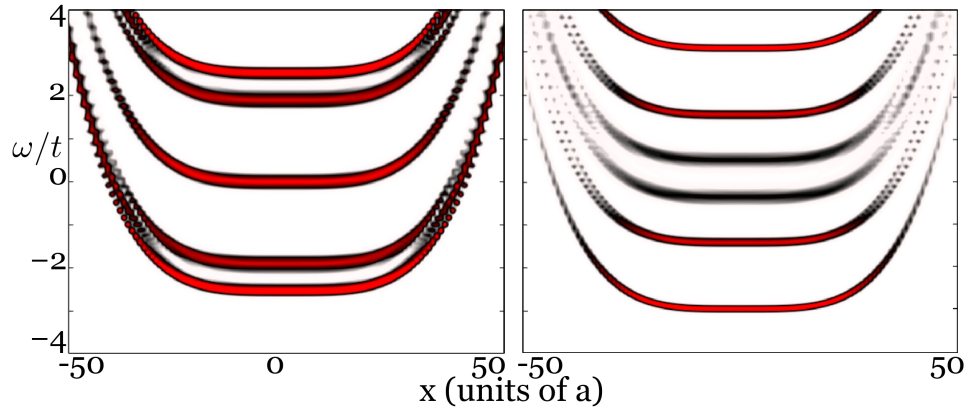
Figure 6.7: Integrated spectral density $\tilde{\rho}(x, \omega)$ for a system described by Eq. 6.25 on a 100×100 lattice with quartic confinement V. In the left figure, the flux is chosen to be $\alpha = 2/5$, while in the right figure $\alpha = 1/6$. In the left figure, the edge states leaving the second bulk band immediately merge with the edge states of the first bulk band to form a state spatially localized between the bulk bands with the correct transport coefficient. In the right figure, the states leaving the second bulk band split up, i.e. they localize to more than one point in space. The inner part of these states merges with the edge states of the third band at higher energies. Similar behavior is observed for the 3rd, 4th and 5th band. As pointed out in the text, this non-trivial behavior is an indication of the topological origin of the edge states.

6.3.2.4 Robustness of Soft Edge States in Stripe Geometries

One of the most important properties of topological edge states is their robustness against even large perturbations, which leads to clearly detectable quantized Hall conductance in impure experimental setups. In optical lattice experiments which are, by construction, very clean realizations of condensed matter Hamiltonians, perturbations such as disorder are usually not an issue. However, since disordered potentials can be implemented in a controlled manner [12, 46, 157], it is of interest to thoroughly investigate how robust the edge states are against these kinds of perturbation. Here, we address this question for soft boundaries. The general argument, which illustrates the robustness of edge states in condensed matter systems, is the lack of possible backscattering processes [78]. Counter-propagating edge states are localized on opposite edges of the system and are very well separated spatially. Therefore, in huge condensed matter systems, these states have vanishing spatial overlap and backscattering from impurities is completely suppressed. In contrast, in finite systems different edge states from opposite edges will have a finite overlap in real space, which theoretically allows for backscattering processes, and therefore disorder may lead to the opening of a gap in the spectrum. However, as we will see from our numerical results, even in very small systems (≈ 60 lattice sites in x-direction) this effect is not observable.

To verify the robustness of the soft edge states numerically, we perturb the system described by Eq. 6.25 by adding a disordered background potential

$$V_{\text{disorder}} = \sum_l \Delta_l c_l^\dagger c_l, \qquad (6.30)$$

where Δ_l is distributed randomly, either by a binary distribution, $\Delta_l \in \{0, \Delta_{\text{max}}\}, \forall l$, or by a uniform distribution, $\Delta_l \in [0, \Delta_{\text{max}}], \forall l$ [6]. For all realizations, we found that the edge states stay robust and still connect the different bulk band regions without opening a gap up to disorder strengths of about $\Delta_{\text{max}} \approx 0.5t$ for binary disorder and even larger strengths for uniform disorder.

For example, in Fig. 6.8 the integrated partial spectral density $\rho_L(k_y, \omega)$ is shown for a 120×60 lattice system with uniformly distributed Δ_l and $\Delta_{\text{max}} = 0.5t$. There is clearly no gap in the spectrum and

---

[6] In the presence of a disordered background potential, translational invariance in the y-direction is broken and therefore, to mimic a semi-infinite system, we diagonalize the Hamiltonian of the system on a $L_x \times L_y$ lattice with periodic boundary conditions in the y-direction (i.e. $\psi(x, y) = \psi(x, y + L_y)$, where $\psi(x, y)$ is the single-particle wave function).
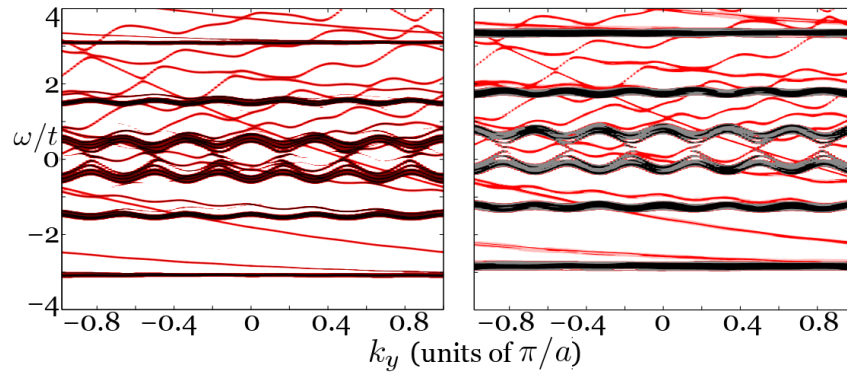
Figure 6.8: Integrated partial spectral density $\rho_L(k_x, \omega)$ of a system described by Eq. 6.25 on a 120×60 lattice with $\alpha = 1/6$. Right: with an additional binary disordered potential, given by Eq. 6.30 and $\Delta_{\max} = 0.5t$. Left: with the disordered potential being set to zero. The robust edge states are still clearly pronounced and gapless, while the former bulk bands are smeared out and show a mobility gap (not shown here but obtainable from the Anderson-localized bulk eigenstates).

although quasi-momentum is no longer a good quantum number, the edge states in momentum space are very sharply centered around a particular value of k_y and remain delocalized in the y-direction as they were for the system without disorder [7]. In contrast, some of the bulk states now consist of many quasi-momentum components (not shown in our figure) and therefore become localized to a region much smaller than the system size, which can be termed Anderson localization.

We have also addressed larger systems with larger boundary regions. These systems contain more and more edge states in a given bulk gap, which may possibly lead to different backscattering processes between edge states located at the same edge and therefore open gaps in the spectrum after disorder is introduced. To exclude these possibilities, we studied system sizes of up to 60×240 lattice sites without finding any indication of gaps in the spectrum or localization of the edge states up to disorder strengths of $\Delta_{\max} = 0.5t$.

6.3.3 Detection Methods

So far we focused on a semi-infinite system with stripe geometry. However, realistic systems in optical lattice experiments are confined to a finite region in all dimensions by the finite beam width of the lasers. In this section, we determine the spatial wave functions of a 2D system trapped in both the x- and y-directions and discuss possible detection methods of the resulting edge states.

6.3.3.1 Eigenstates of the Completely Trapped System

We determine the eigenstates of a system with a confining potential V that varies in the x- and y-directions

$$V(x,y) = V_0 \left[\left(\frac{x}{L}\right)^\delta + \left(\frac{y}{L}\right)^\delta \right]. \tag{6.31}$$

The parameter δ determines the shape of the trap and the possible eigenstates. For $\delta \to \infty$ the system is again confined by hard walls in both directions, while for $\delta = 4$ and $\delta = 2$ the system is in a quartic and harmonic confinement, respectively. For harmonic confinement, we expect the eigenstates that are extended over various lattice sites to be circularly symmetric, whereas in the quartic case the potential is no longer circularly symmetric and the states take on a shape that is sometimes referred to as a squircle

---

[7]At this point, one has to keep in mind that we are investigating the properties of a finite system, which has per construction only localized eigenstates. Localization or delocalization therefore means confinement to few lattice sites or an extension over various sites and must be understood from the context.
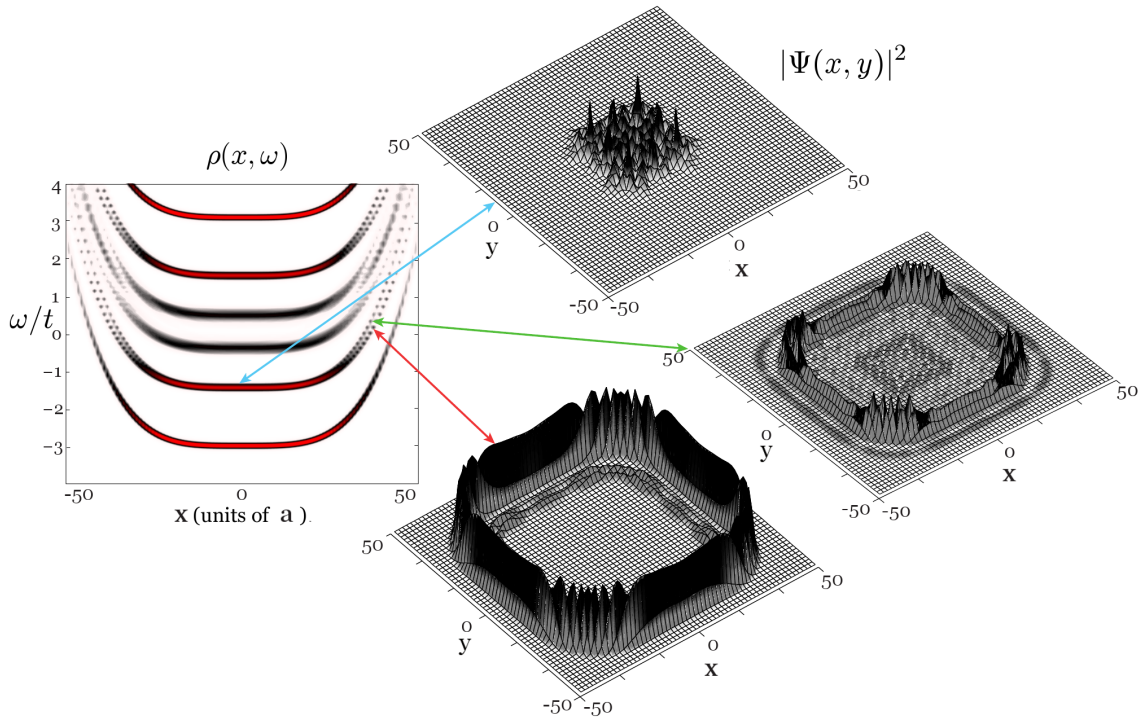
Figure 6.9: Wave function $|\Psi(x,y)|^2$ as a function of the lattice spacing a of different eigenstates of the system within complete quartic confinement. The real space spectral density shown to the left is a cross section of the complete system: $\rho(x, y = 0, \omega)$. Three particular eigenstates have been shown, and their energies indicated by arrows to the spectral density. The wave functions belong to a) a bulk region and b) and c) to a pair of edge states splitting up after leaving the second bulk band.

[128]. For this analysis we again will restrict ourselves to a system with 100×100 lattice sites and a trapping potential with a minimum value of $V_0 = 10t$ along each edge of the lattice. We again focus on $\alpha = 1/6$.

In Fig. 6.9, we clearly see the different real space distribution of edge states compared to bulk states. The bulk states are delocalized over a region of about 30×30 lattice sites, while the edge states for a given energy follow the isolines of the quartic potential, and are strongly confined to these regions. Comparing figures b) and c) for the completely trapped system one can see the splitting of the edge states leaving the second bulk band as the two states have a weak overlap with one another. The shape of the edge states in the quartic confinement looks similar to that which one would expect in the hard wall system (like those explicitly shown in [57]) and differs only at the very corners of the system. We therefore expect similar single particle excitations for the quartic confinement as for the hard wall confinement when probing the edge states in experiment.

The situation slightly changes when looking at the harmonically confined system. There, the confining potential is circularly symmetric and one may expect that the eigenstates reflect this symmetry. The wave functions of the harmonically confined system are shown in Fig. 6.10. As already seen from the spectral density plotted in Fig. 6.4, the former bulk region is tightly confined to very few lattice sites in the center of the trap, which makes it difficult to define a bulk region in the harmonic trap. On the other hand, the edge states chosen reflect the radial symmetry of the trapping potential and again are localized along the isolines of the trapping potential. This already indicates that for the harmonic confinement we expect very different excitation dynamics than for the quartic and hard wall confinement, where significant parts of the eigenstates are quasi-one-dimensional.

For harmonic confinement, one can solve the continuum model analytically in the absence of the lattice [131, 27] and the resulting wave functions are quite similar to those from the lattice calculation. The major difference in the continuum case is that no edge states from different bulk bands merge, since the
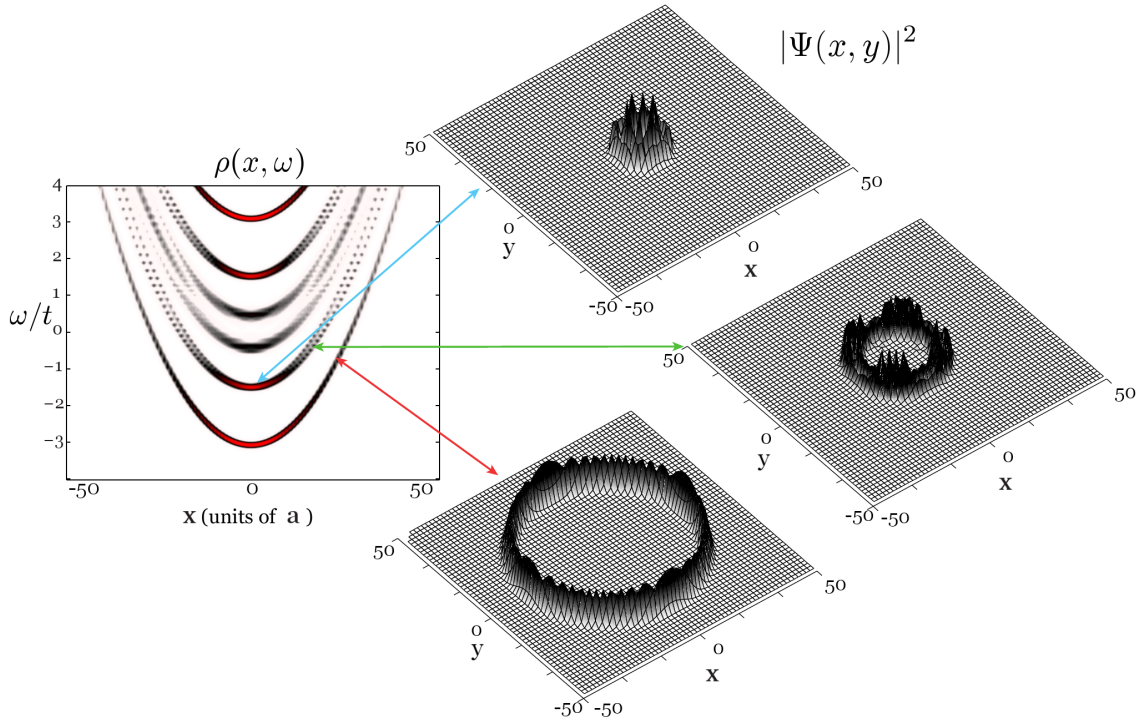
Figure 6.10: As in figure 6.9 but with complete harmonic confinement. The three states are shown from a) a bulk region and b) and c) edge states of states belonging to different bulk bands. Spatial coordinates in units of the lattice spacing a.

hall conductivity always increases by one when passing a bulk band and the different bulk bands are not connected. Additionally, angular momentum is only a good quantum number in the continuum case.

6.3.3.2 Bragg Spectroscopy

An important question concerning topological non-trivial phases in ultracold atoms is whether the edge states are detectable with existing experimental tools. Due to the lack of stationary transport in optical lattice experiments, it is not feasible to directly measure the Hall conductance, and one has to consider alternative approaches [172, 158]. Several possibilities for detecting edge states or topological quantum numbers in optical lattice experiments have been proposed. Some require careful experimental implementation such as Bragg [126, 58] or Raman spectroscopy [35] and others take advantage of easily accessible observables like time-of-flight (ToF) patterns or density profiles. Density profile measurements were proposed by Umucalilar *et al.* [186] to directly separate the bulk and edge densities between different bands. However, as already pointed out in [172], these profiles do not show the required structure, as can be seen in Fig. 6.4 (lower): the bulk bands all occupy approximately the same real space extent. Hence, this method is not applicable to topological systems in general. Alternatively, ToF measurements have been proposed by Zhao *et al.* [200] to exhibit minima and maxima that depend on the topological number of the system. While this is true for the specific cases they were investigating and also for our system in the case of $\alpha = 1/6$, we found that it is not valid in the case of $\alpha = 2/5$ and therefore cannot be reliably used as a detection method in experiment. In contrast, Alba *et al.* [3] propose using ToF measurements as a method to identify skyrmions, by focusing on topological properties of pseudo-spin vectors within the Hamiltonian on the Bloch sphere. However, this method focuses on bulk properties rather than the edge modes that we consider here.

We choose to focus instead on Bragg spectroscopy, which probes the dynamical structure factor $S(q, \omega)$ of the underlying system. Bragg scattering of topological insulators in optical lattices has been previously considered for the case of the quantum anomalous Hall effect [126]. However, no inhomogeneity of the

lattice was considered. Recently, Goldman *et al.* [58] have investigated Bragg spectroscopy theoretically, considering shaped lasers to probe angular momentum states within circularly symmetric traps. While this is a novel implementation to enhance the detection of edge states, we demonstrate that one is able to observe edge states using a simple linear Bragg coupling which, due to technical limitations, may be the only option available to a particular experiment. Furthermore one can observe differences in Bragg spectroscopy between the various bands that we show is not due to chirality considerations. We do not propose an explicit experimental setup and simply assume that one can measure the dynamical structure factor directly. One such proposal to measure this precisely in an optical lattice is the so called "shelving method" [58]. When performing Bragg spectroscopy, the system is illuminated by two laser beams, described by wave vectors $\mathbf{p_1}, \mathbf{p_2}$ and frequencies $\omega_1 = p_1 c$, $\omega_2 = p_2 c$, respectively, and the differences in these quantities, $\mathbf{q} = \mathbf{p_1} - \mathbf{p_2}$ and $\omega = \omega_1 - \omega_2$, allows for transitions between different eigenstates of the original system. The Hamiltonian describing the interaction of the system with the laser beams is then given by

$$H_{\text{Bragg}} = \frac{\Gamma}{2} \int d^2 p \left(e^{-i\omega t} \Psi^\dagger(\mathbf{q} + \mathbf{p}) \Psi(\mathbf{p}) + \text{h.c.} \right), \tag{6.32}$$

where $\Psi^\dagger(\mathbf{p})$ is a field operator, creating a particle with real momentum $\mathbf{p}$ and Γ is the coupling strength of the lasers [171, 175, 174]. The dynamical structure factor in linear response theory for an infinite homogeneous system is directly connected to the density-density correlation function $\chi_{q,q}(\omega)$

$$S(q, \omega) = -\frac{1}{\pi} \text{Im} \chi_{q,q}(\omega) \tag{6.33}$$

via the fluctuation dissipation theorem [142]. For our case, we have to evaluate $S(q, \omega)$ for the inhomogeneous system, where the quasi-momentum is no longer a good quantum number. Within the linear response approximation, and accounting for the finite size of the system and finite time of the measurement process, we find:

$$S(q, \omega) = |\Gamma|^2 \Delta \sum_{\mu, \lambda} \frac{n_\lambda (1 - n_\mu) |A_{\lambda, \mu}(q)|^2}{(\omega - \omega_\mu + \omega_\lambda)^2 + \Delta^2}. \tag{6.34}$$

Here, λ, μ label the single-particle eigenstates of the system, n_ν and ω_ν are the occupation number and energy, respectively, of the state ν. We introduce a Lorentzian broadening factor Δ, to allow evaluation in a system of finite size. The scattering amplitude $A_{\lambda, \mu}(q)$ is the probability of a particle in state μ to scatter into the state λ by gaining momentum q and is given by the integral

$$A_{\lambda, \mu}(q) = \int d^3 r e^{-iqr} \psi_\mu^*(r) \psi_\lambda(r). \tag{6.35}$$

After determining the single particle eigenstates of the system, we can directly calculate the dynamical structure factor. Because we are focusing on the detection of edge states, we investigate a system with a Fermi energy located in a bulk gap at $\epsilon_F = -2t$ (see Fig. 6.4), where an edge state is located. There are now four general scattering processes possible, edge→edge, edge→bulk, bulk→edge and bulk→bulk. Edge→edge scattering is clearly distinguishable by analyzing the dynamical structure factor. Given a frequency ω, the set of possible momentum transfers allowed to another edge state is very limited because the edge states are well localized in momentum space. For the case of edge→bulk scattering, many different momenta are accessible and therefore we see a signal regardless of the value of q. This means for a fixed momentum transfer $\mathbf{q}$, $S(\mathbf{q}, \omega)$ as a function of ω consists of a δ-peak approximately around $\omega = q v_F$ [8] and a smeared out region, where the bulk bands are located. This can be seen in Fig. 6.11 (left), where the first peak indicates edge→edge scattering and the second and third peaks correspond to edge→bulk and bulk→bulk scattering. On the other hand, for a fixed frequency ω, the response in momentum space describing edge→edge scattering looks quite different from that obtained from edge→bulk scattering, as one can see from Fig. 6.11 a) and b), respectively. For the quartic confinement, the edge states form squircles in real space (Fig. 6.9), which means that low energy excitations are most favorable in x- or y-direction, resulting in the square-like structure of $S(q, \omega)$ in Fig. 6.11, which is approximately described

---

[8]In this case we used the Fermi velocity $v_F \equiv \partial_{k_y} \epsilon_F(k_y)$ of the edge states of the cylindrical geometry, where k_y is a good quantum number, to approximate the frequency ω, which is reasonable when looking at Fig. 6.9.
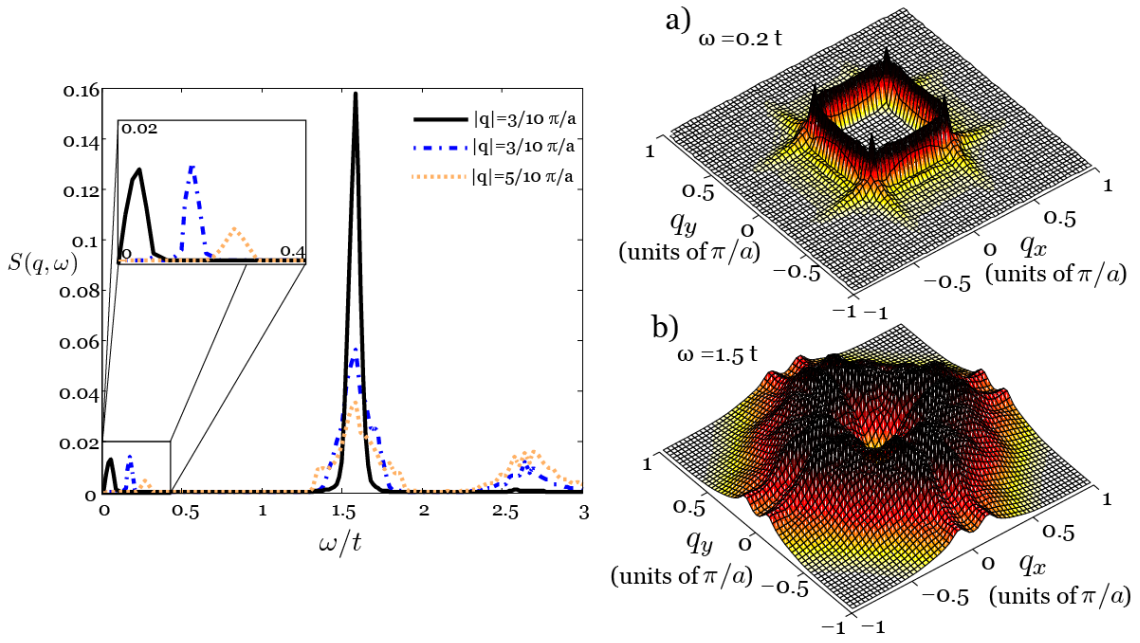
Figure 6.11: Dynamical structure factor for a system with quartic confinement and Fermi energy in the first bulk gap ($\epsilon_F = -2t$). Left: $S(q, \omega)$ for fixed momentum q as a function of ω. The first peak belongs to edge→edge scattering and its position is sensitive to q and can be written, for small ω, as $\omega_q = v_{F,\text{edge}}q$. The second and third peak belong to edge→bulk scattering from edge states into the third and fourth bulk bands, located around $\epsilon = 0$ and to bulk→bulk scattering from the first to second bulk bands, where the frequency is independent of q. No signal appears of scattering from edge states to the second bulk band, located at $\omega = 0.5t$, indicating a disconnection between these states, i.e. these states have vanishing matrix elements of the Bragg operator. Right: $S(q, \omega)$ for fixed frequency as a function of momentum transfer q for a) edge→edge scattering at $\omega = 0.2t$, b) bulk→bulk scattering processes at $\omega = 1.5t$.

by $\{q_{\text{allowed}}\} = \{(q_x, q_y) \mid \max\{|q_x|, |q_y|\} \approx q_0 = v_F/\omega\}$. In contrast, the dynamical structure factor of bulk→bulk scattering from the first to the second band is smeared out and depends on the Fermi surface of the occupied level at ϵ_F and the Fermi surface of the unoccupied band $\tilde{\epsilon}_F = \epsilon_F + \omega$. The allowed momenta are approximately described by $\{q_{\text{allowed}}\} = \{(q_x, q_y) \mid |q_x| + |q_y| \approx \tilde{\epsilon}_F/\tilde{v}_F\}$ and form a rough square which is rotated by $\varphi = \pi/4$ compared to the edge→edge scattering. Note that as a result of the structure of $A_{\mu,\lambda}(q)$, where a minimal spatial overlap of the two spatial wave functions is needed for obtaining a finite scattering amplitude, high frequency edge→edge scattering is exponentially suppressed because the presence of the trap causes energetically separated edge states to be localized to different distances from the center of the trap. This does not occur in the equivalent hard-wall system.

For the harmonically confined system, $S(q, \omega)$ as a function of ω for fixed q is qualitatively the same as in the quartic system. In contrast, $S(q, \omega)$ as a function of q for fixed ω for edge→edge scattering looks quite different than for quartic confinement. As seen in Fig. 6.10, the edge states have a circular symmetry and therefore no momentum transfer direction is preferred, which leads to the set of allowed states forming a circle $\{q_{\text{allowed}}\} = \{(q_x, q_y) \mid \sqrt{q_x^2 + q_y^2} \approx \omega/v_F\}$, shown in Fig. 6.12.

An important discovery of our calculations is that there is an obvious absence of spectral weight at frequencies where we expect signals of edge→bulk scattering. To highlight this, we calculate an artificial Bragg response where we allow only initial states in the energy range $-2.5t < \epsilon < -2t$ for transitions to states of higher energy. This means any signal due to possible bulk→edge or bulk→bulk transitions is suppressed. The spectra shown in Fig. 6.13 demonstrate edge→edge signal for the first bulk gap, edge→bulk signal to the third and fourth bulk bands, but conspicuously absent signal for the edge→2nd bulk band transitions, which would be expected for Bragg frequencies $0.5 < \omega < 1.5$. This implies that the first edge and second edge/bulk are disconnected, i.e. have a vanishing matrix element of the Bragg
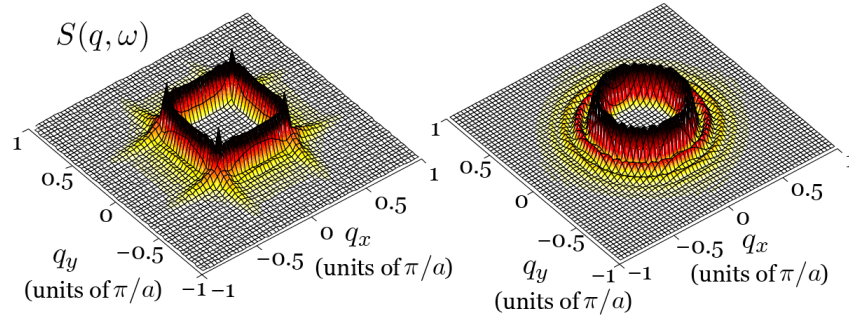
Figure 6.12: $S(q,\omega)$ for a fixed frequency $\omega = 0.2t$ as a function of momentum transfer q, for a Fermi energy $\epsilon_F = -2t$. Left: $S(q,\omega)$ for the quartic confined system. The system shows a strong response when one component of $q = (q_x, q_y)$ has an absolute value $|q_{x,y}| = q_0 = \omega/v_F$ because excitations along the x-axis, y-axis are most favorable (see Fig. 6.9). Right: $S(q,\omega)$ for the harmonically confined system. Here, the response is close to circularly symmetric in q-space, reflecting the shape of the eigenstates. No particular direction is anymore favorable, as long as the absolute value of $|q| = q_0$ is fixed.
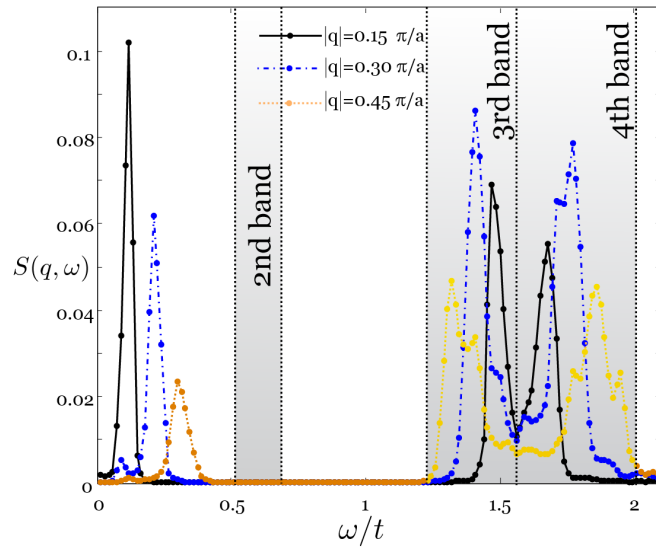
Figure 6.13: Dynamical structure factor $S(q,\omega)$ for fixed momentum q as a function of frequency, for a Fermi energy $\epsilon_F = -2t$, as seen in Fig. 6.11 but with artificially suppressed bulk→bulk scattering processes. The first peak belongs to edge to edge scattering processes and is sensitive to the momentum transfer q with approximate frequency $\omega_q = v_{F,\text{edge}}q$. The broadened peaks around $\omega = 1.5t$ belong to edge→bulk scattering to the third and fourth bulk bands. It is clearly visible that there is no scattering from the edge states to the second bulk band, which is located at $\omega = 0.5t$.

operator. It is possible to predict this behavior from the dispersion of the edge states (see Fig. 6.6), as one can see that the lowest edge mode, colored in red, passes unimpeded through the second bulk band, and never displays an avoided crossing with the blue edge mode of the second band or the second band itself, while it always merges with the 3rd or 4th band (with which we find non-vanishing matrix elements of the Bragg operator). For higher energies, and strong confinements, we see the opposite behavior of avoided crossings between red (a) edge modes and yellow (c) edge modes, indicating that one can expect a finite Bragg response from transitions between these states. Note that the lack of edge→bulk scattering is not a result of the soft-boundaries inhibiting real-space overlap. We have performed equivalent hard-wall boundary calculations where real-space overlap is guaranteed but we again observe an absence of signal for disconnected edge→bulk transitions. Note also, that we do not expect to observe a clear signal for large frequency edge→edge transitions regardless of the type of trap, as there is larger range of states

beneath the Fermi-edge that can be accessed with the Bragg laser. Hence, many different values of k_y will contribute, leading to a blurred signal.

In this section, we analyzed the properties of 2D topological edge states in softly confined systems with a confinement in one direction of the form $V(x) = V_0(x/L)^\delta$. By varying the confining potential from a hard-wall to a quartic or harmonic potential, we showed that the topological properties of the edge states in specific bulk gaps do not depend on the steepness of the confining potential, while a confinement sharper than harmonic is required to achieve an appreciable bulk region of the lattice. We suggest that quartic confinement is suitable to observe both edge state and bulk properties, which may be realized by superimposing attractive and repulsive Gaussian beams. Furthermore, we observed the emergence of robust auxiliary edge states, which provide additional structure to edge modes but do not influence the topological quantum numbers. The main feature of these auxiliary states is that they connect edge states which are spatially separated to bulk bands of the system. This provides a mechanism to preserve topological invariance, as soon as the edge states and bulk bands become spatially separated. In these cases the band-structure exhibits a series of avoided crossings that act to preserve the topological invariant. An analysis of the spectral density of softly confined systems in real space revealed the splitting and merging of edge states from different bulk bands, which is also indicative of their topological nature.

We also determined the wave functions of eigenstates in a completely trapped system and showed how these depend on the confining potential. With these, we calculated the dynamical structure factor which can, for instance, be measured by Bragg spectroscopy. We found that the dynamical structure factor can reveal the edge and bulk states of the system and their overlap.

In summary, we demonstrated that topological properties in ultracold atomic systems with artificial gauge fields are not sensitive to the trapping potentials available in optical lattice experiments and that the edge states of these systems can be clearly detected via Bragg spectroscopy. We believe that soft boundaries provide more detailed insight into the behavior of edge states, which cannot be observed in hard-wall systems, and are therefore worth investigation in their own right.

7. $\mathbb{Z}_2$-Topological Insulators with Interacting Ultracold Fermions

7.1 Time-Reversal Invariant Topological Insulators

In the previous chapter, we have discussed quantum Hall systems as prototypes for a $\mathbb{Z}$ topological classification. The topological invariant corresponding to these systems is the $\mathbb{Z}$ number C, which is the Chern number of the occupied bulk bands. It can equivalently be obtained from to the bulk-boundary correspondence of the edge states in a finite system. This topological invariant determines the Hall conductance σ_{xy}. By applying the time-reversal operator $\mathcal{T}$ to a Hamiltonian with a magnetic field, one effectively changes the sign of the magnetic field. This also changes the sign of the Hall conductance, i.e. the sign of the topological invariant is changed. This means that systems, which are time-reversal invariant, can only have a $\mathbb{Z}$ topological quantum number of zero, i.e. are topologically trivial [78]. However, Kane and Mele in their seminal paper [101] have found a different class of topologically non-trivial insulators for the case when time-reversal symmetry is unbroken, but the non-trivial topology is caused by spin-orbit interactions. Crucial for this new $\mathbb{Z}_2$ classification is the presence of two electronic flavors, which we call spin-up and spin-down. While the quantum Hall effect could be explained by a single fermionic flavor, this is not possible for a $\mathbb{Z}_2$ topological phase. The key idea is, that time-reversal symmetry is broken for each spin alone, but not for the combination of both spins. For spin-$1/2$ particles, the $\mathcal{T}$ operator is antiunitary, i.e. $\mathcal{T}^2 = -1$, since a rotation of the spin-state $|\uparrow\rangle$ around the angle $\phi = 2\pi$ recovers the state $-|\uparrow\rangle$. This directly leads to Kramer's theorem, which states that all eigenstates of a time-reversal invariant Hamiltonian H are at least two fold degenerate. Kramer's theorem can be proven by contradiction: Suppose $|\Psi\rangle$ is a non-degenerate eigenstate of the time-reversal invariant Hamiltonian H, then $\mathcal{T}|\Psi\rangle$ must also be an eigenstate corresponding to the same eigenenergy. Since $|\Psi\rangle$ is non-degenerate, $\mathcal{T}|\Psi\rangle = e^{i\varphi}|\Psi\rangle$ for some complex phase factor $e^{i\varphi}$. This would mean $\mathcal{T}^2|\Psi\rangle = |e^{i\varphi}|^2|\Psi\rangle = |\Psi\rangle$, which is not allowed because $1 \neq -1$. Therefore no non-degenerate states exist in a time-reversally invariant system [78].

The TKNN invariant for a $\mathcal{T}$ invariant system is always $C = 0$, but there must be an additional topological invariant for theses systems, since one can distinguish at least two fundamentally different classes of time-reversal invariant Hamiltonians, as we see in the following. We can understand this in a very simple picture by looking at a quantum Hall system: consider a quantum Hall system with non-zero topological quantum number. The spectrum of this system has edge states traversing the bulk gap, with opposite velocities on opposite edges. The $\mathcal{T}$ operator maps $-\mathbf{k} \to \mathbf{k}$, such that

$$\mathcal{T}H\mathcal{T} = \int_{\mathcal{B}} d\mathbf{k}\, \mathcal{T}|\mathbf{k}\rangle h(\mathbf{k})\langle\mathbf{k}|\mathcal{T} = \int_{\mathcal{B}} d\mathbf{k}\, |-\mathbf{k}\rangle h(\mathbf{k})\langle-\mathbf{k}| \neq H, \qquad (7.1)$$

where $h(\mathbf{k})$ is the subblock of H corresponding to the quasi-momentum $\mathbf{k}$ and the integral runs over the first Brillouin zone $\mathcal{B}$. Since H describes a topologically non-trivial system, there must exist at least one

pair of subblocks $h(\mathbf{k})$ and $h(-\mathbf{k})$, such that $h(\mathbf{k}) \neq h(-\mathbf{k})$. In contrast to the spinless system, for the spinful system the $\mathcal{T}$ operator maps $(-\sigma, -\mathbf{k}) \rightarrow (\sigma, \mathbf{k})$. Consider now a system, which is described by the Hamiltonian

$$H = H_\uparrow + H_\downarrow = \int_\mathcal{B} (|\uparrow, \mathbf{k}\rangle h(\mathbf{k}) \langle \uparrow, \mathbf{k}| + |\downarrow, \mathbf{k}\rangle h(-\mathbf{k}) \langle \downarrow, \mathbf{k}|) \, d\mathbf{k}. \tag{7.2}$$

Applying the $\mathcal{T}$ operator to this Hamiltonian then leads to

$$\mathcal{T} H \mathcal{T} = \int_\mathcal{B} (\mathcal{T}|\uparrow, \mathbf{k}\rangle h(\mathbf{k}) \langle \uparrow, \mathbf{k}|\mathcal{T} + \mathcal{T}|\downarrow, \mathbf{k}\rangle h(-\mathbf{k}) \langle \downarrow, \mathbf{k}|\mathcal{T}) \, d\mathbf{k} = H, \tag{7.3}$$

such that the system is trivial with respect to the $\mathbb{Z}$ classification. We realize two important consequences from equations (7.2) and (7.3). First, the system described by the Hamiltonian H is time-reversally invariant, which means that the Hamiltonian possibly relies only on intrinsic effects of the system, but not on external perturbations, such as magnetic fields in the quantum Hall effect. Second, although the Hall conductance of this system is always zero for filled bands, the spin Hall conductance $\sigma_{xy}^S \propto \sigma_{xy}^\uparrow - \sigma_{xy}^\downarrow$ is strictly quantized and therefore there must exist another topological quantum number, which indicates this quantization but is different from the $\mathbb{Z}$ quantum number for the QH effect.

The fact that this new classification is $\mathbb{Z}_2$ rather than $\mathbb{Z}$, i.e. that there are only two possible topological classes of time-reversal invariant Hamiltonians was rigorously proven by Kane and Mele [101, 100]. Here, we will focus on an explanation involving edge states and Kramer's theorem. Consider a Hamiltonian H, which is time-reversally invariant and describes a finite system. Either this Hamiltonian has no edge states in the spectrum, then H is topologically trivial. Alternatively, there are edge states in the spectrum, such that H is possibly topologically non-trivial. Again we only focus on the left edge of the system and apply Kramer's theorem, which tells us that for any state $|\mathbf{x}, \mathbf{k}\rangle$ in the spectrum, there exists an energetically degenerate state $|\mathbf{x}', -\mathbf{k}\rangle$. This can be seen, since $\mathcal{T}$ maps $|\mathbf{x}, \mathbf{k}\rangle \rightarrow |\mathbf{x}', -\mathbf{k}\rangle$, where $\mathbf{x}$ is a combination of the residual quantum number characterizing the eigenstates of H and may be changed by application of $\mathcal{T}$. Therefore, it is sufficient to analyze the spectrum on the left edge of the system and for the right half of the first Brillouin zone $k_y \in [0, \pi/a]$. If there is one edge state present in this part of the spectrum, it must be robust against perturbations that respect time-reversal symmetry and therefore respect Kramer's theorem. If there are two edge states present in this part of the spectrum, an external perturbation (in form of disorder or interactions) can easily lead to a hybridization of these states and to the formation of a gap in the spectrum, which would make the system topologically trivial. The hybridization of edge states is always possible when there is an even number of edge states present in this part of the spectrum, while for an odd number of states there is always one edge state protected by Kramer's theorem. From this argument, we can deduce that there indeed exist only two distinct topological classifications for time-reversally invariant systems: namely topologically trivial ($\nu = 0$) and topologically non-trivial ($\nu = 1$), whereas all topologically non-trivial systems are equivalent. The topological quantum number can then be defined in terms of edge states located at a single edge of the system. For a given Fermi energy E_F, one simply has to count the number $\tilde{N}$ of edge states in the interval $k_y \in [0, \pi/a]$ which cross the Fermi energy, such that

$$\nu = \tilde{N} \mathrm{mod} 2, \tag{7.4}$$

is the topological invariant for this system. In some literature, it is sometimes conventional to consider $k_y \in [-\pi/a, \pi/a]$, such that

$$\nu = N \mathrm{mod} 4 \tag{7.5}$$

is the correct formula that determines the topological invariant, where N is the number of edge states crossing E_F in the mentioned interval.

The topological invariant for time-reversal invariant systems can also be determined from the eigenstates of the infinite system, where no edge states are present in the spectrum [100, 50, 52, 51]. This approach is completely equivalent to the counting of edge states, since there exists a bulk-boundary correspondence for $\mathbb{Z}_2$ topological insulators as well[1] [44]. In two dimensions, the $\mathbb{Z}_2$ topological insulator is known as a quantum spin Hall insulator[2], which was originally predicted to exist in graphene and in two dimensional

---

[1]The argumentation is the same as for the QH system. When there exists an interface at which the system changes its topology, there must be states which close the bulk gap located at this interface.

[2]Although theoretically possible, quantum spin Hall insulators do generally not have a quantized spin Hall conductivity [101].

semiconductor system with a uniform strain gradient. However, the quantum spin Hall insulator so far has only been experimentally observed in HgCdTe quantum well structures [110, 9]. In the following section, we will discuss a certain model system for quantum spin Hall insulators, that can be engineered in cold-atom experiments [57], and investigate the effect of Hubbard interaction on this system.

7.2 Time-Reversal Invariant Hofstadter-Hubbard Model with Ultracold Fermions

D. Cocks, P. P. Orth, S. Rachel, **M. Buchhold**, K. Le Hur, and W. Hofstetter
arXiv:1204.4171, preprint

The following section discusses the effect of interactions on a $\mathbb{Z}_2$ topological insulator, namely the time-reversal invariant Hofstadter model with Rashba spin-orbit coupling, which can be implemented in cold atom experiments [57]. This paper was written in collaboration with Daniel Cocks, Peter Orth, Stephan Rachel, Karyn Le Hur and Walter Hofstetter and is available as a preprint with the title "Time-Reversal Invariant Hofstadter-Hubbard Model with Ultracold Fermions". My contribution to this work was the implementation of the spin-mixing CT-AUX solver for the RDMFT procedure and the performance of certain numerical calculations.

Ultracold quantum gases trapped in optical lattice potentials provide insight into strongly correlated condensed matter systems. Examples are the Mott-superfluid transition, the dynamics of the Hubbard model after a quench of parameters and simulation of quantum magnetism [7, 160, 165]. The precise experimental control over almost all system parameters, including the particle-particle interaction strength, is remarkable. Simulating more traditional electronic condensed matter systems is, however, complicated by the fact that cold atoms are charge neutral, such that the presence of a static magnetic field does not lead to a Lorentz force, i.e. to the emergence of orbital magnetism, for these atoms. An experimental breakthrough was thus the engineering of so-called "artificial" gauge-fields, which give rise to effective magnetic or electric fields for the neutral particles [34, 96, 124, 2, 97, 28], exemplary described in Sec. 5.4. Remarkably, they may even be generalized to simulate spin-orbit coupling or coupling to non-Abelian fields [143, 125, 177, 81, 24]. The effective electro-magnetic fields and couplings can be large, i.e. the flux per plaquette is of the same order as the density per lattice site, which allows for the realization of the quantum spin Hall effect (QSH) in a completely new experimental context [57, 54, 78].

The underlying idea of realizing time-reversal invariant two-dimensional (2D) topological phases with cold atoms is as simple as it is fundamental. Consider the (integer) quantum Hall effect (QHE) on a 2D square lattice where an external magnetic field along the z-direction breaks time-reversal and translational symmetry. This system is described by the Hofstadter Hamiltonian (6.21), which we described in the previous chapter. The single particle spectrum for arbitrary magnetic field strength – having the shape of a butterfly, see Fig. 6.3 – was first computed by Douglas Hofstadter [87] and is commonly referred to as the *Hofstadter butterfly*. If the flux per plaquette is a rational number $\alpha = p/q$, in units of the Dirac flux quantum $\Phi_0 = h/e$, the system remains translational invariant with an enlarged unit cell that contains q lattice sites, instead of a single one for the fluxless system. The spectrum consists of q bulk bands and in all bulk gaps one finds a finite Chern number C and, correspondingly, at least $|C|$ chiral edge modes at a single edge of the system[3]. Interestingly, for even values of q, the system is a semi-metal at half-filling and exhibits q Dirac cones. Fig. 7.1 displays the spectrum for the Hofstadter Hamiltonian in the first magnetic Brillouin zone for the case $\alpha = 1/2$, clearly showing the $q = 2$ Dirac cones where the bands touch.

To restore time-reversal symmetry, we can imagine applying a magnetic field in the z-direction that only couples to the up-spins and a second field of the same strength, but opposite direction, that only couples to the down-spins. We thus end up with a spinful and time-reversally (TR) invariant version of the

---

[3]A more detailed discussion can be found in chapter 6, here we just briefly review the essential results.
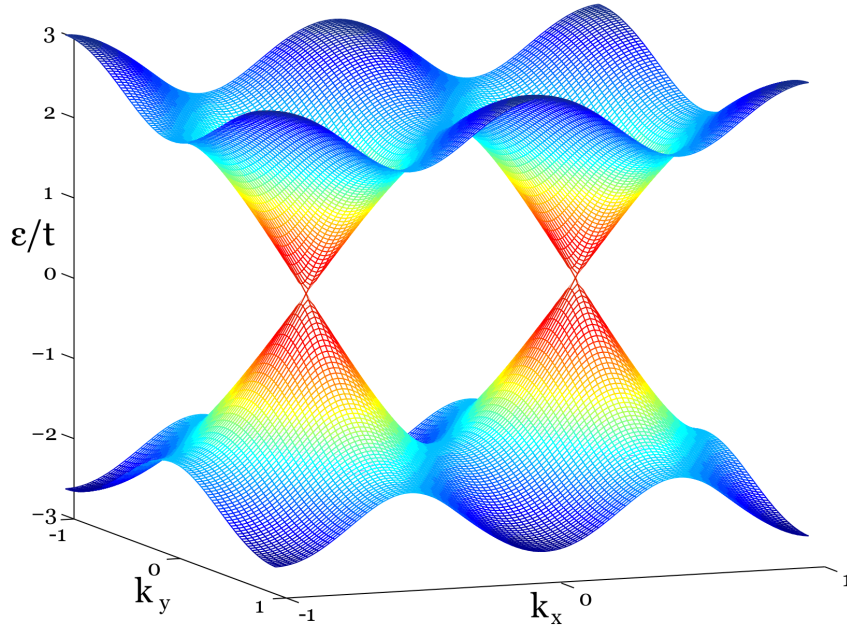
Figure 7.1: Single-particle spectrum of the Hofstadter Hamiltonian (7.6) for $\alpha = 1/2$, $\gamma = 0$ in the first magnetic Brillouin zone $\mathbf{k} \in [-\pi, \pi] \times [-pi/q, \pi/q]$ with $q = 2$. At zero energy, the two magnetic bands are touching each other via Dirac cones, making the system a semi-metal for a Fermi energy $\epsilon_F = 0$. The quasi-momenta are shown in units $\mathbf{k}_G = (\pi, \pi/2)$.

fundamental Hofstadter problem. Remarkably, such a scenario is feasible using cold-atoms in artificial gauge fields [57, 54]. Thus, the semi-metallic Dirac dispersion for even q becomes a generalization of graphene with a tunable number of Dirac cones. Energy gaps which were crossed by a single chiral edge mode in the QHE setup, are now traversed by a helical Kramer's pair of edge states, corresponding to a $\mathbb{Z}_2$ topological insulator phase, as discussed in Sec.7.1. Note that one can use the same Gedankenexperiment to construct the Kane-Mele model [101] from two time-reversed copies of Haldane's honeycomb model [76]. The Kane-Mele model with additional Hubbard interaction has recently been intensively studied [169, 89, 152, 197, 117, 201], in contrast to the Hofstadter problem, for which the effect of interactions has up to now not been considered.

In this section, we study the effect of interactions in the time-reversal invariant *Hofstadter-Hubbard model* using real-space dynamical mean-field theory (RDMFT, see chapter 1). We explain our numerical results using analytical arguments obtained from perturbation theory and renormalization group approaches. We consider interaction effects on both (semi-)metallic and gapped topological phases. Although $\mathbb{Z}_2$ topological insulators are known to be robust against disorder [138, 161, 148], rigorous and general results on the fate of topological insulators in the presence of Coulomb or Hubbard interactions are limited [198, 118, 71]. Some three-dimensional materials of the iridate family are possible candidates for systems where strong spin-orbit coupling and Coulomb interactions compete [145, 102]. In two spatial dimensions, however, topological insulator phases have so far only been found in HgTe/CdTe quantum wells [9, 110], where Coulomb interactions seem to be negligible.

7.2.1 Hofstadter-Hubbard Model

The non-interacting part of the Hamiltonian consists of two independent copies of the Hofstadter model (6.21), where the two distinct fermionic flavors (which we refer to as spins) feel an opposite effective magnetic field, i.e. a field $\mathbf{B} = B\sigma_z\mathbf{e}_z$, where $\mathbf{e}_z$ is the unit vector in z-direction and σ_z is the Pauli matrix. These distinct copies are then coupled by a Rashba-type spin-orbit coupling in the x-direction, which

gives the possibility to flip the spin of a particle that propagates in the x-direction. This Hamiltonian can be realized in cold-atom experiments (see Sec. 5.5) and states

$$H_0 = -t \sum_{x,y} \mathbf{c}^\dagger_{x+1,y} e^{i2\pi\gamma\sigma_x} \mathbf{c}_{x,y} + \mathbf{c}^\dagger_{x,y+1} e^{i2\pi\alpha\sigma_z x} \mathbf{c}_{x,y} + \text{h.c.}. \tag{7.6}$$

Here, $\mathbf{c}^\dagger_{x,y} = (c^\dagger_{\uparrow,x,y}, c^\dagger_{\downarrow,x,y})$ at lattice site (x,y), σ_x, σ_z are Pauli matrices and $\gamma \in [0, 0.25]$, $\alpha = p/q$ are the spin-orbit coupling strength, the magnetic flux per unit cell in units of the Dirac flux quanta, respectively. In the following, we express all energies in units of $t \equiv 1$. The realization of the non-interacting Hamiltonian (7.6) in cold-atom experiments, was proposed by Goldman *et al.* [57], where also the realizable topological phases of this model have been analyzed in terms of edge states for $\alpha = 1/6$. According to the $\mathbb{Z}_2$ classification of TR-invariant systems, one finds non-topological (semi-) metallic and normal insulator phases and topological non-trivial QSH phases, depending on the parameter γ and the Fermi energy of the system.
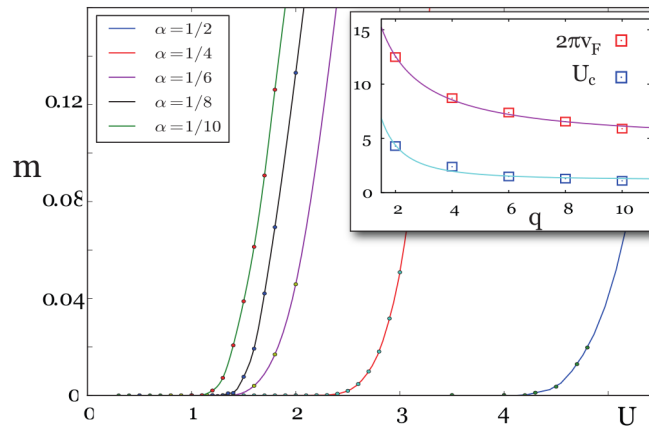
Figure 7.2: Magnetization $m = n_\uparrow - n_\downarrow$ in the Néel state is plotted versus interaction strength U. Shown are lines corresponding to the values $\alpha = 1/2$ (blue), $1/4$ (red), $1/6$ (magenta), $1/8$ (black), and $1/10$ (green). Inset: Fermi velocity $2\pi v_F$ (red symbols) for different $\alpha = 1/q$ is shown versus q. Also U_c (blue symbols) obtained within RDMFT versus q is shown. The magenta line is a fit of v_F to $\propto 1/q$ and the cyan line of U_c to $\propto 1/q^2$. Please note that the inset only holds for $\alpha = 1/q$ with even q and the fit is not to be understood as an interpolation for arbitrary q.

To include the effect of interactions, we add a Hubbard-type local interaction to the non-interacting Hamiltonian (7.6), such that the total Hamiltonian reads

$$H = H_0 + U \sum_{x,y} n_{\uparrow,x,y} n_{\downarrow,x,y}, \tag{7.7}$$

where the on-site interaction strength $U > 0$ can be tuned experimentally using Feshbach resonances and by adjusting the lattice depth.

We first consider the Hubbard-Hofstadter problem for general $\alpha = p/q$ at half-filling. For q odd the system is metallic with a nested Fermi surface, and antiferromagnetic Néel order occurs for infinitesimally small interaction $U = 0^+$ as for the ordinary square lattice[4]. For q even the situation is very different because the system is a semi-metal (SM) at half-filling. The non-interacting band structure exhibits q Dirac cones (with a multiplicity of 2 due to the spin), which are separated by momentum $2\pi/q$ in momentum space[5]. The $\alpha = 1/2$ case is thus very similar to graphene (but note that the coordination number for the square lattice is $z = 4$ rather than $z = 3$ for the case of graphene). For smaller α on the other hand, the

---

[4]This is in contrast to three dimensions, where a critical interaction strength $U_c > 0$ is required for antiferromagnetic ordering.
[5]The lattice constant a of the square lattice is set to unity $a \equiv 1$.

system embodies a generalization of graphene with a tunable number of valleys.

We investigate the SM-insulator transition for various $\alpha = 1/q$ (q even) within RDMFT. In Fig. 7.2, the magnetization is shown as a function of interaction strength U. The insulating phase for $U > U_c$ is antiferromagnetically (AF) ordered with a magnetization pointing in the z-direction and an ordering wave-vector $\mathbf{Q} = (\pi, \pi)$, which is the common Néel vector. We find that the critical value of U_c to enter the insulating and magnetically ordered phases decreases with increasing q. This is expected from the increasing scattering that can take place between the cones. At U_c we also observe a simultaneous opening of a single particle gap. Within our approach we thus find no sign of an intermediate non-magnetic gapped phase, which would indicate a possible spin-liquid phase [130, 8]. To understand the behavior of $U_c(q)$, we make use of Herbut's argument [85] (see Sec. 7.3). Herbut considered graphene and studied the SM-insulator transition within a large-N approach, and found that U_c depends on $2N$, the number of Dirac cones (N refers to the spin degeneracy), and the Fermi velocity v_F as $U_c \propto v_F/2N$. As shown in detail in Sec. 7.3, we are able to match our results with Herbut's analysis by replacing the Fermi velocities and $2N = qN$, where q is again the number of Dirac cones in the single-particle spectrum. In fact, from the band structure at $U = 0$, we find $v_F \propto 1/q$. Consequently, setting $N = 2$ for spin-1/2 particles, U_c should exhibit a $1/q^2$ behavior, which agrees very well with the RDMFT data, shown in the inset of Fig. 7.2. We further note that $\alpha = 3/8$, which exhibits a different v_F than $\alpha = 1/8$, is in agreement with our findings.

7.2.2 Tunable Magnetic Order

In this part, we consider the effect of finite γ in the Hamiltonian (7.6), i.e. the presence of Rashba-type spin-orbit coupling that breaks the axial spin symmetry, on the interaction induced magnetic ordering. Finite γ does change the type of magnetic order in general. To demonstrate this, we consider fixed $U = 5$ at $\alpha = 1/6$ and calculate the magnetization pattern for $\gamma = 0.125$ and $\gamma = 0.25$ in Fig. 7.3 obtained within RDMFT. We obtain similar results for other values of α and γ. For $\gamma = 0.125$, the magnetization lies in the $S^y - S^z$ plane and the spatially dependent magnetization reads

$$\mathbf{m}(\mathbf{r}) = s_{\text{tot}} \left(0, -\cos\frac{\pi x}{3}\cos\pi y, \sin\frac{\pi x}{3}\cos\pi y\right), \tag{7.8}$$

where s_{tot} is the modulus of the magnetization and is a function of the interaction strength U and the spatial coordinate $\mathbf{r}$. For $\gamma = 0.25$, the magnetic order is given by

$$\mathbf{m}(\mathbf{r}) = s_{\text{tot}}\,(0, 0, \cos\pi y). \tag{7.9}$$

Tuning the parameter γ, we thus pass from Néel order ($\gamma = 0$) to spiral order ($\gamma = 0.125$, shown in Fig. 7.3 and Eq. (7.8)) to collinear order ($\gamma = 0.25$, shown in Fig. 7.3 and Eq. (7.9)), thereby crossing two magnetic quantum phase transitions. Finally, we note that the modulus of the magnetization s_{tot} is staggered for the intermediate value of U shown in Fig. 7.3. The staggering decreases for larger values of U, reducing its spatial dependence in the limit $U \longrightarrow \infty$.

We can qualitatively understand this type of magnetic order by rigorously deriving a quantum spin Hamiltonian for even stronger interactions when charge fluctuations freeze out completely at half-filling. For the derivation, we consider a Hubbard model with a finite number of N lattice sites at half-filling, which reads

$$H = H_U + H_t = U\sum_{i=1}^{N} n_{\uparrow,i} n_{\downarrow,i} - t\sum_{\langle i,j\rangle} \mathbf{c}_i^\dagger e^{i\hat{\varphi}_{ij}}\mathbf{c}_j, \tag{7.10}$$

where the phase $\hat{\varphi}_{ij}$ is a lattice site dependent 2×2 matrix, according to Eq. (7.6). In the strong coupling limit, i.e. $U \gg t$, the hopping Hamiltonian H_t is considered as the perturbation and the ground state of the unperturbed system is the 2^N times degenerate[6]. To obtain a low-energy effective Hamiltonian, we apply a unitary transformation to the Hamiltonian (7.10), which is known as the Schrieffer-Wolff transformation. Consider therefore the hermitian operator S, such that

$$\tilde{H} = e^{-iS} H e^{iS} \tag{7.11}$$

---

[6]The ground state at half-filling consists of N singly occupied sites, where two spin degrees of freedom are possible at every lattice site.
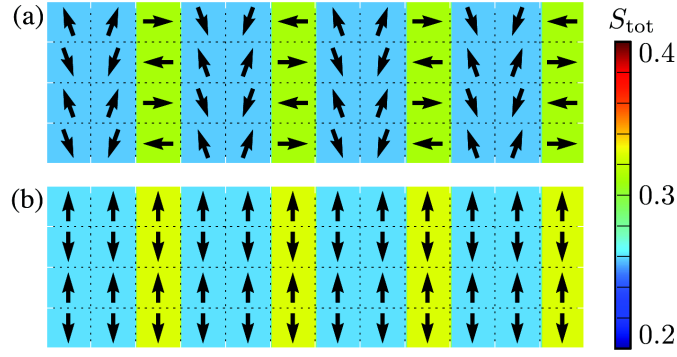
Figure 7.3: Real space magnetization profile $\mathbf{m}(\mathbf{r})$ in $S^y - S^z$ plane for $\alpha = 1/6$, $U = 5$ and $\gamma = 0.125$ (a) and $\gamma = 0.25$, respectively. The spiral order in (a) and collinear order in (b) can be explained by the effective spin model (7.22). The color scheme indicates the modulus of the magnetization, which is staggered for intermediate U.

is a unitary transformation of the original Hamiltonian. Expanding this transformation up to second order in the operator S leads to

$$\tilde{H} = H + i\,[H, S] - \frac{1}{2}\,[[H, S]\,, S] + \mathcal{O}(S^3). \tag{7.12}$$

Choosing the operator S such that

$$i[H_U, S] = -H_t \tag{7.13}$$

results for the Hamiltonian in

$$\tilde{H} = H_U + \frac{i}{2}\,[H_t, S] + \mathcal{O}(S^3). \tag{7.14}$$

By making use of (7.13), the matrix elements of the operator S can be expressed in the eigenbasis of H_U, which we call $\mathcal{B}$, leading to

$$\langle m|S|n \rangle = i\frac{\langle m|H_t|n \rangle}{E_m - E_n}, \tag{7.15}$$

where $|m\rangle, |n\rangle \in \mathcal{B}$ and E_m, E_n are the eigenenergies of H_U for the corresponding eigenstates. The diagonal elements of S can be chosen equal to zero, since H_t has vanishing diagonal elements in the eigenbasis of H_U. The matrix representation of S can be exploited, leading to

$$H_t S = \sum_{m,n} H_t |m\rangle\langle m|S|n\rangle\langle n| = i\sum_{m,n} H_t |m\rangle\frac{\langle m|H_t|n\rangle}{E_m - E_n}\langle n|. \tag{7.16}$$

After inserting (7.16) and its hermitian conjugate, the Hamiltonian (7.14) transforms to

$$\tilde{H} = H_U - \frac{1}{2}\sum_{m,n}\left(H_t|m\rangle\frac{\langle m|H_t|n\rangle}{E_m - E_n}\langle n| + |n\rangle\frac{\langle n|H_t|m\rangle}{E_m - E_n}\langle m|H_t\right). \tag{7.17}$$

Projecting the Hamiltonian (7.17) to the manifold of degenerate ground states, where the low energy physics takes place, leads to the states $|n\rangle$ belonging to the ground state manifold, with $E_n = 0$. On the other hand, the application of H_t always takes states out of the ground state manifold, such that $|m\rangle$ must always be an excited eigenstate with eigenenergy $E_m = U$. We can therefore drop both sums in (7.17) and write

$$\tilde{H} = H_U - \frac{1}{U}PH_t^2 P, \tag{7.18}$$

where P is the projector onto the ground state manifold. Since the first operator on the right of Eq. (7.18) is equal to zero in the ground state manifold, only contributions from the second operator have to be taken into account. The only non-zero contributions to the Hamiltonian can be expressed as

$$\tilde{H} = -\frac{t^2}{U}\sum_{\langle i,j \rangle} \mathbf{c}_i^\dagger e^{i\hat{\varphi}_{ij}}\mathbf{c}_j\mathbf{c}_j^\dagger e^{i\hat{\varphi}_{ji}}\mathbf{c}_i. \tag{7.19}$$

This operator can now be transformed into a sum of spin-1/2 operators, resulting in a Heisenberg-type model and recovering the antiferromagnetic Heisenberg Hamiltonian for $e^{i\hat{\varphi}_{ij}} = \mathbb{1}$. For the Hamiltonian (7.6), the matrix elements for coupling in the x-direction and y-direction have to be treated separately. The coupling in the y-direction is described by the matrices $e^{i\hat{\varphi}_{ij}} = e^{i2\pi x_i \sigma_z}$, such that for a specific summand of (7.19)

$$
\begin{aligned}
\mathbf{c}_i^\dagger e^{i\hat{\varphi}_{ij}} \mathbf{c}_j \mathbf{c}_j^\dagger e^{i\hat{\varphi}_{ji}} \mathbf{c}_i &= \mathbf{c}_i^\dagger e^{i2\pi\alpha x_i \sigma_z} \begin{pmatrix} (1 - n_{\uparrow,j}) & c_{\uparrow,j} c_{\downarrow,j}^\dagger \\ c_{\downarrow,j} c_{\uparrow,j}^\dagger & (1 - n_{\downarrow,j}) \end{pmatrix} e^{-i2\pi\alpha x_i \sigma_z} \mathbf{c}_i \\
&= \mathbf{c}_i^\dagger e^{i2\pi\alpha x_i \sigma_z} \begin{pmatrix} -S_z^j & -S_-^j \\ -S_+^j & S_z^j \end{pmatrix} e^{-i2\pi\alpha x_i \sigma_z} \mathbf{c}_i \\
&= \mathbf{c}_i^\dagger \begin{pmatrix} -S_z^j & -S_-^j e^{i4\pi\alpha x_i} \\ -S_+^j e^{-i4\pi\alpha x_i} & S_z^j \end{pmatrix} \mathbf{c}_i \\
&= -2 S_z^j S_z^i - \cos(4\pi\alpha x_i) \left(S_+^j S_-^i + S_-^j S_+^i \right) - i \sin(4\pi\alpha x_i) \left(S_+^j S_-^i - S_-^j S_+^i \right), \quad (7.20)
\end{aligned}
$$

where we have defined the spin operators

$$
S_z^i = \frac{n_{\uparrow,i} - n_{\downarrow,i}}{2}, \qquad S_+^i = S_x^i + i S_y^i = c_{\uparrow,i}^\dagger c_{\downarrow,i}. \tag{7.21}
$$

For the coupling in the x-direction, we find a similar expression, which in combination with (7.20) leads to the Heisenberg-type effective spin Hamiltonian

$$
\begin{aligned}
\tilde{H} &= J \sum_{x,y} \left\{ S_x^{x,y} S_x^{x+1,y} + \cos(4\pi\gamma) \left[S_y^{x,y} S_y^{x+1,y} + S_z^{x,y} S_z^{x+1,y} \right] \right. \\
&+ \left. \sin(4\pi\gamma) \left[S_z^{x,y} S_y^{x+1,y} - S_y^{x,y} S_z^{x+1,y} \right] \right\} \\
&+ J \sum_{x,y} \left\{ S_z^{x,y} S_z^{x,y+1} + \cos(4\pi\alpha x) \left[S_x^{x,y} S_x^{x,y+1} + S_y^{x,y} S_y^{x,y+1} \right] \right. \\
&+ \left. \sin(4\pi\alpha x) \left[S_y^{x,y} S_x^{x,y+1} - S_x^{x,y} S_y^{x,y+1} \right] \right\}, \tag{7.22}
\end{aligned}
$$

where we have introduced the coupling constant $J \equiv 4t^2/U$.

The first part of Eq. (7.22) describes a spin exchange in x-direction. For $\gamma = \frac{n}{2}$ with $n \in \mathbb{Z}$, we obtain a simple antiferromagnetic Heisenberg term. Other values of γ, however, break the $SU(2)$ symmetry and cause anisotropy of XXZ-type with S_x as the anisotropy direction in spin space. For $\gamma \neq \frac{n}{4}$, there is an additional Dzyaloshinskii-Moriya (DM) interaction term in the YZ-plane [43, 139], which is responsible for the spiral spin order in Fig. 7.3(a). Spin exchange in the y-direction is periodic with an extended unit cell in the x-direction depending on the flux $\alpha = p/q$: for odd q the unit cell contains q lattice sites, but for even q it only contains $q/2$ lattice sites, reflecting second order perturbation theory. For instance, one finds for the π-flux lattice ($\alpha = 1/2$) an ordinary Heisenberg exchange term. For other values of α, the XY-term exhibits a modulation of its amplitude depending on α, while the Z-term always favors AF Ising order. This rich magnetic order predicted by the spin Hamiltonian is in agreement with our RDMFT findings.

7.2.3   Topological Phases in the Hofstadter-Hubbard Model

In this section, we study the effects of interactions on systems that have a bulk gap, but possible gapless edge excitations, i.e. the effect of interactions on the $\mathbb{Z}_2$ classification. For $U = 0$, we distinguish the normal (NI) and topological (TI) insulating phases by calculating the $\mathbb{Z}_2$ invariant ν using Hatsugai's method [52].

For $U > 0$, we identify the phases by computing the spectral function in a cylindrical geometry using RDMFT and counting the number of gapless helical edge states crossing the bulk gap. The TI phase exhibits an odd number of helical Kramer's pairs per edge while the NI phase has an even number,
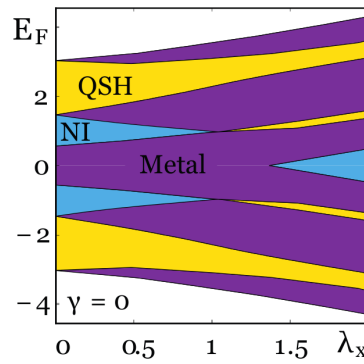
Figure 7.4: E_F-λ-phase diagram for $\alpha = 1/6$ at $\gamma = U = 0$. We find insulating phases for fillings $n_F = l/6$, with $l \in \{0, 1, 2, 4, 5, 6\}$ and (semi-)metallic phases otherwise. The insulating phases are either normal (NI) or quantum spin Hall (QSH) insulators. The staggering potential induces a phase transition from NI to QSH for $l = 2, 4$ and also from semi-metal to NI at half-filling $l = 3$.

including zero. Edge states are also crucial for detecting topological phases in cold-atom experiments, and we numerically study how robust they are with respect to interactions. In the following, we focus on fixed $\alpha = 1/6$, which qualitatively captures all phenomena that occur in this system for general $\alpha = p/q$. We also consider an additional term in the Hamiltonian, that is available in cold-atom setups [57, 54]: a staggering of the optical lattice potential along the x-direction

$$H_\lambda = \lambda \sum_j (-1)^x c_j^\dagger c_j, \tag{7.23}$$

which is added to the Hofstadter-Hubbard Hamiltonian (7.7).

In the axial symmetric case of $\gamma = 0$, there exist TI phases only away from half-filling, since the system is a (semi-)metal for $n_F = 1$ (and not too large λ, U). This is shown in Fig. 7.4, and is expected as the spinless Hofstadter problem at $\alpha = 1/6$ exhibits a QHE with Chern number $C = \pm 2$ if ϵ_F lies within the two energy gaps closest to zero and a QHE with $C = \pm 1$ for ϵ_F in the other gaps[7] (see Fig. 7.5). The Chern number corresponds to the number of chiral edge modes in an open geometry. In the time-reversal invariant system at hand, we thus find an according number of helical Kramer's pairs within the gaps. For a filling of $n_F = 1/6, 5/6$ the system is thus a TI. We observe this topological phase to be stable even for large interactions up to $U = 10$. A NI-TI phase transition can be induced in the other gap for $n_F = 2/6, 4/6$ by applying a sufficiently large staggered lattice potential $\lambda \leq 1$ (see Fig. 7.4). Fixing $n_F = 2/6$, we now turn on interactions, and observe that this phase is quite stable as shown in Fig. 7.6. Eventually, large enough interactions reverse the effect of the staggering potential and drive the system into the NI phase. Note that a static Hartree-like approximation (red dashed line) yields comparable results for small U but overestimates the effect of staggering for larger values of U.

A topological phase at half-filling occurs only if we break the axial symmetry in the system by considering $\gamma > 0$. We present both the non-interacting λ-γ phase diagram[8], shown in Fig. 7.7(a), and the interacting $\lambda - U$ phase diagram for different values of γ, which is shown in Fig. 7.7(b). Both semi-metal and QSH phases are robust up to interaction strengths of order $U \approx 3 - 5$, at which point larger interactions drive the system into a magnetically ordered state. A qualitative understanding of the interacting phase diagram follows from the observation that interactions mainly reverse the effect of staggering. Prominently, we observe an interaction-driven NI to QSH transition for $\gamma = 0.25$ and $\lambda \geq 1.5$, and a metal-QSH transition for $0.22 \leq \gamma < 0.25$ and $\lambda \geq 1$. Using RDMFT for a cylinder geometry, we are able to directly observe the behavior of the edge states in the interacting system. Gapless edge states are key ingredients to different detection schemes of topological phases in cold-atom systems [173, 172, 200, 3]. Since topological (QSH) phases are uniquely characterized by their helical edge states [196], a probe of

---

[7]The plus, minus sign for the Chern number C here refers to spin-up, spin-down fermions, which feel opposite magnetic fields and therefore the bulk gaps belong a Chern number with opposite sign.

[8]The non-interacting λ-γ phase diagram has also been obtained in [57], however, they have made a small mistake in their calculations, such that their result differs from the one that is presented here.
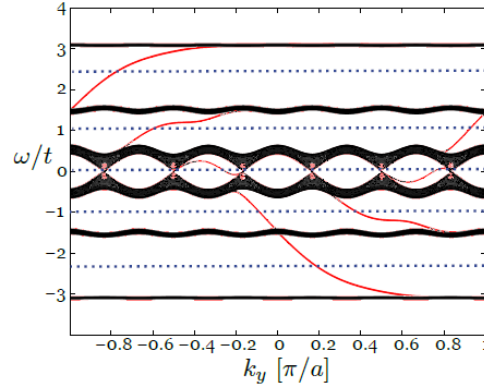
Figure 7.5: Spectrum of the spin-up fermions for the case $\alpha = 1/6$, showing QH phases for the first and second bulk gap with Chern numbers $C = -1, -2$, respectively. The corresponding topological phase for a system described by the time-reversal invariant Hofstadter-Hubbard model has the topological invariant $\nu = C \mod 2 = 1, 0$, i.e. a QSH phase for the first bulk gap and a NI phase in the second bulk gap.
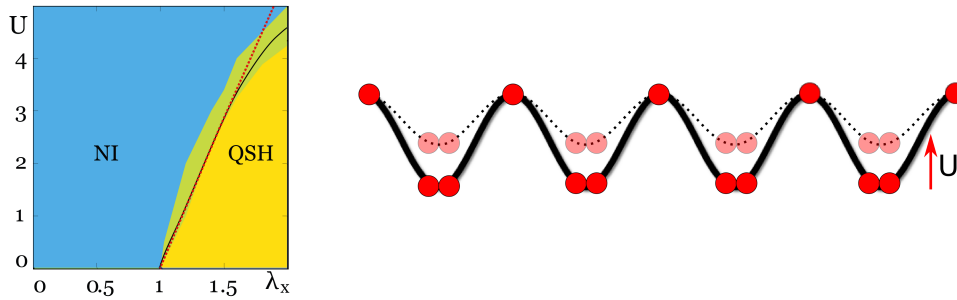

Figure 7.6: Left: U-λ-phase diagram at $n_F = 2/6$ and $\gamma = 0$ obtained within RDMFT, the red line indicates the phase boundary obtained by a Hartree-Fock-type static mean-field theory, which coincides with RDMFT for small interactions. Interactions reverse the staggering induced phase transition from a NI to a TI. This can be understood within a simple mean-field picture, as the interactions prefer a uniform density distribution, while the staggering prefers a staggered density distribution. Right: Mean-field picture of compensation of the staggering potential by interactions.

these states is the most direct measurement [57, 58, 21]. In Fig. 7.8, we give an example of the spectral function $A(k_y, \omega)$ for the interaction driven NI-QSH transition at $\gamma = 0.25, \lambda = 1.5$. For $U = 0.5$, we find no gapless edge modes that connect the two bulk bands, which correspond to the NI. On the other hand, at $U = 2$, we clearly find a single pair of helical edge modes traversing the bulk gap, which corresponds to the QSH phase.

In this section, we investigated the Hofstadter-Hubbard model using RDMFT complemented by analytical arguments. We quantitatively determined the interacting phase diagram including two additional terms relevant in cold-atom experiments, a lattice staggering and Rashba-type spin-orbit coupling. Interactions drive various phase transitions. Similar to graphene, we find that a semi-metal at half-filling turns into a magnetic insulator at a critical finite interaction strength. Rashba-type spin-orbit interactions lead to tunable magnetic order with collinear and spiral phases. We explicitly demonstrate the stability of the topological phases with respect to interactions, and verify the existence of robust helical edge states in the strongly correlated TI phase, which is crucial for experimental detection schemes.

7.3   Herbut's Argument

In Fig. 7.2 in Sec. 7.2.1, we presented numerical RDMFT results for the critical on-site interaction strength U_c as a function of $1/q$, which marks a zero temperature quantum phase transition between a semi-metallic phase and a magnetically ordered phase. The system develops a single-particle gap inside the
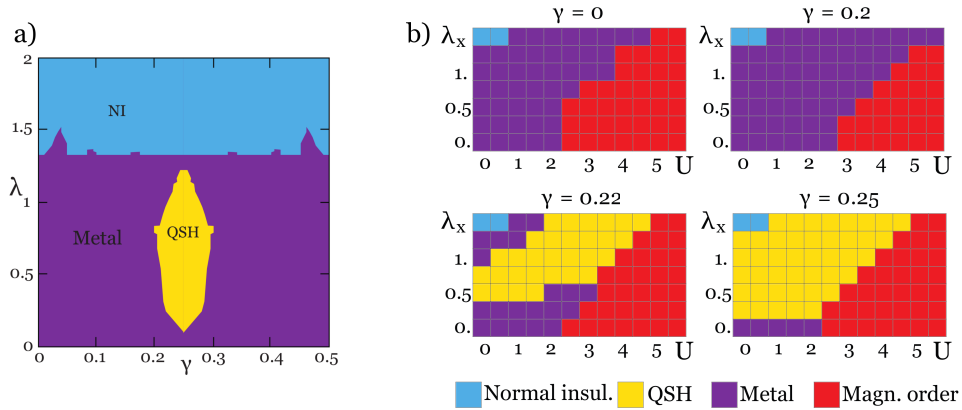
Figure 7.7: (a) λ-γ-phase diagram at half-filling $n_F = 1/2$ and $U = 0$. (b) U-λ-phase diagram at $E_F = 0$ for various values of γ and inverse temperature $\beta = 20$. Remarkably, interactions can drive a phase transition from NI to QSH and also from QSH to semi-metal. Lower interactions, where no magnetic ordering occurs, the main effect of the interactions is to reverse the effect of the staggering potential.
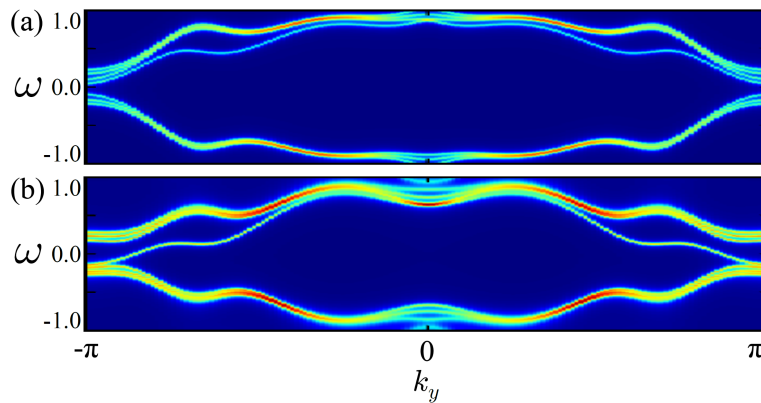

Figure 7.8: The spectral function $A(k_y, \omega)$ of the interacting system clearly distinguishes between (a) a NI phase with no edge states traversing the bulk gap at $U = 0.5$ and (b) a QSH phase at $U = 2$ with a single pair of edge modes (per edge) connecting the two bulk bands. Both plots are for $\alpha = 1/6, \gamma = 0.25$ and $\lambda = 1.5$.

magnetic phase. The magnetic order is antiferromagnetic and of Néel type.

In this section, we briefly sketch the slight modification of Herbut's argument [85] such that it applies to the Hofstadter-Hubbard model. In his letter, Herbut considers the low energy field theory of graphene in the presence of general Coulomb interactions, but also in the limit where only an on-site interaction U is present. Specifically, graphene exhibits four Dirac cones at low energies, a factor of two from the two valleys $\pm K(1, 1/\sqrt{3})$ and another factor of two originating from the fermionic flavors, i.e. the electronic spin. In his renormalization group analysis, Herbut extends the electronic spin from two to N_s flavors and determines the β-function of the Hubbard interaction up to leading order in a large-N_s expansion. The sign of the β-function indicates the stability of the system, which changes for the case when β becomes zero. When starting with a low energy theory that explicitly contains Dirac cones in the spectrum, the β-function therefore indicates the stability of the semi-metal phase towards interactions and, as soon as

β vanishes, the system undergoes a phase transition. From our numerical calculations, we know this is the SM-AF transition. In the notation of [85], the β-function reads[9]

$$\beta_a = -\tilde{g}_a - C_a \tilde{g}_a^2 + \mathcal{O}(\frac{1}{N_s}), \tag{7.24}$$

where $\tilde{g}_a = g_a \frac{2}{N_s}$ and

$$g_a = -\frac{U}{8\pi \tilde{v}_F t}, \tag{7.25}$$

with hopping amplitude t and dimensionless Fermi velocity $\tilde{v}_F = v_F/at$. In Herbut's notation, a is the short distance cutoff of the theory, which is formulated in the continuum and chosen such that $v_F = \tilde{v}_F at \equiv 1$. However, in our notation, a is the lattice spacing, which is always set $a = 1$, as well as the hopping t, such that $v_F = \tilde{v}_F \neq 1$. The constant in the β-function reads $C_a = 2N_v$, where N_v is the number of different valleys. For graphene, one finds that $N_v = 2$ but in the spinful Hofstadter system one rather finds that $N_v = q$ and so depends on the magnetic flux per unit cell $\alpha = p/q$. The critical value of the interaction U_c is obtained from the condition that the β-function changes sign, which yields

$$0 = \beta_a = -(\tilde{g}_a)_c - C_a (\tilde{g}_a)_c^2 \Leftrightarrow (g_a)_c = -\frac{2}{C_a N_s} = -\frac{1}{2q}, \tag{7.26}$$

where we have inserted the physical value of $N_s = 2$, in our Hofstadter model. In terms of the microscopic parameters this reads

$$\left(\frac{U}{t}\right)_c = \frac{8\pi \tilde{v}_F}{2q} = \frac{4\pi v_F}{q}. \tag{7.27}$$

The Fermi velocity $v_F(q)$ is exactly known from the non-interacting band structure of the Hofstadter model, and we find that it scales as $v_F(q) \sim 1/q$ for $\alpha = 1/q$ in the considered range $2 \leq q \leq 10$ (see inset Fig. 7.2). As a result, we predict that

$$\left(\frac{U}{t}\right)_c \sim \frac{1}{q^2} \tag{7.28}$$

which agrees very well with the RDMFT results, as we show in the inset of Fig. 7.2.

---

[9]In Herbut's continuum quantum field theory, the lattice spacing a is set as a cutoff for the Fourier transformation, leading to a discretized momentum space, which is why the renormalized coupling g_a has an index a.

8. Conclusion

In this thesis, we have investigated the effect of interactions and the trapping geometry of optical lattice experiments on topological phases in two dimensions, namely the time-reversal symmetry breaking quantum Hall phase, which is categorized by a $\mathbb{Z}$ topological invariant and the time-reversal symmetric quantum spin Hall effect, categorized by a $\mathbb{Z}_2$ invariant. For this purpose, we used a combination of numerical and analytical methods with a focus on the well-established real-space dynamical mean-field theory (RDMFT) in combination with highly accurate continuous-time Monte-Carlo (CT-QMC) impurity solvers. We implemented the continuous-time auxiliary field (CT-AUX) algorithm in its original form, developed by Emanuel Gull *et al.* [66], which relies on an expansion of the impurity action in the interaction, as well as the continuous-time hybridization expansion (CT-HYB) algorithm, developed by Philipp Werner *et al.* [189]. For the CT-HYB algorithm, we implemented several improvements to the standard solver. These include performing the Monte-Carlo measurements in a orthogonal polynomial basis and using improved estimators for the self-energy, as proposed by Hartmut Hafermann *et al.* [74, 16]. To take into account for Rashba-type spin-orbit coupling and non-zero magnetic flux through the system, the CT-QMC algorithms as well as the RDMFT procedure have successfully been extended to the case when the Green's function is not diagonal in spin-space, such that all local diagrams, involving both normal and anomalous Green's functions, are incorporated exactly.

We investigated the Hofstadter-Hubbard model, a theoretical model which has been proposed for cold-atom experiments [57] that covers both interaction effects and topological non-trivial phases, using RDMFT complemented by analytical arguments. We quantitatively determined the interacting and non-interacting phase diagram of this model numerically and found that, similar to graphene, a semi-metal at half-filling turns into a magnetic insulator at a finite critical interaction strength, while the metal-insulator transition occurs for an arbitrary small interaction $U = 0^+$. Adding a Rashba-type spin-orbit coupling leads to tunable magnetic order with collinear and spiral phases, which could qualitatively be understood by deriving an extended Heisenberg model from the Hofstadter-Hubbard model in the limit of large interactions $U \to \infty$. Furthermore, we investigated the effects of interactions on the topology of the Hofstadter-Hubbard model and found that strong interactions can not only destroy some topological phases but also that interactions can, remarkably, drive a transition from a topologically trivial phase into a topological non-trivial phase, which has up to now not been considered in the literature for moderate local interactions. Thereby we verified that helical edge states, indicating non-trivial topological phases in finite systems, are very robust, even in the strongly correlated regime. This last result is crucial for cold-atom experiments, since a large class of proposed detection schemes for topological phases in ultra-cold atoms relies on the detection of edge states in these systems.

Further essential questions concerning the realization of topological phases in optical lattice experiments addressed in this thesis are how topological phases can be detected in optical lattice experiments and how the geometry of an optical lattice experiment, i.e. the smooth confining potential, can affect its topology. We analyzed the properties of edge states in two-dimensional softly confined systems with a confinement

of the form $V(x) = V_0(x/L)^\delta$ and showed that the topological properties of the edge states in specific bulk gaps do not depend on the steepness of the confining potential. We observed the emergence of robust auxiliary states, which connect edge states to spatially separated bulk bands, thereby preserving the topological invariance of the system. As a possible detection method for topological edge states, we investigated Bragg spectroscopy of ultracold atoms and found that the dynamical structure factor can reveal the edge and bulk states of the system and their specific overlap.

With these results, we further verified that the realization of topological phases within ultracold atom experiments is particular interesting, since these phases allow for a huge number of interesting physical effects. On the other hand, we validated that optical lattice experiments, while possessing a further geometry due to the smooth trapping potential, are perfectly suited for the investigation of topological phases and that this geometry even can reveal new insights into the field of topological insulators, which are undetectable in systems with sharp interfaces between topologically distinct regions.

Although we have discussed many interesting physical effects in optical lattice systems with artificial gauge fields, there are many questions to investigate in the future. With the extension of RDMFT+CT-QMC to system with spin-orbit coupling and non-zero magnetic flux, we have developed a powerful tool to quantitatively investigate systems like the Hofstadter-Hubbard model. For instance, it is unclear what happens to a system where the Fermi energy is non-zero and away from a bulk gap, say the lowest magnetic band is half-filled. From the structure of the magnetic bands, one could expect a similar effect to block spin magnetism, which has been observed in multi-orbital systems, i.e. the formation of antiferromagnetic order on plaquettes larger than the unit cell. On the other hand, the Hubbard interaction induces a strong mixing of the distinct magnetic bands, which favors ferromagnetic ordering.

A further question is what happens to the topological edge states of a system at the phase transition to the antiferromagnetic phase. While for some transitions edge states could be observed in the spectrum even in the antiferromagnetic phase, the system is no longer time-reversal symmetric in the magnetic phase, such that these states are no longer protected by time-reversal invariance and could therefore be topologically trivial. A similar phenomenon has very recently been observed for the Bernevig-Hughes-Zhang model, where the correlations in the magnetic phase were shown to even stabilize non-trivial topology [199].

Another possibility for future investigations is to extend the RDMFT algorithm to lattice structures, other than the square lattice to find indications for a possible spin-liquid phase. The spin-liquid has been proposed to exist [130], or to not exist [168] as a strongly correlated phase on the honeycomb lattice. While we did not find any indications of a spin-liquid in our calculations, an analysis of different lattice geometries could possibly clarify for which geometries the spin-liquid phase can be expected. Therefore, the numerical procedure that we implemented for this thesis are very powerful and promise to be able to address some of the huge number of open questions in the context of topological phases and the implementation of topological systems within cold-atom experiments.

Acknowledgements

After studying five years at the Goethe university and being part of the group of Walter Hofstetter for three years, this thesis marks the end of the fantastic period of time that I have spent here in Frankfurt. For this great time, I am deeply grateful to all my fellows which accompanied me in the last five years and influenced my character and my way of thinking. When I look back to the beginning of my studies in Frankfurt and remember myself as a freshman, it becomes very clear to me how big your (mostly positive) influence on my personal development actually was and that it can not be overestimated. Therefore I really thank you.

During the period of my studies, many situations arose that I could not have handled without my friends Carlo, Henry and Lenka and my parents Horst and Gudrun Buchhold. Thank you very much for your care, help and support.

---

[1]To be precise, Ulf has made a contribution here too, thanks Ulf.

Bibliography

[1] M. Aguiar, V. Dobrosavljević, E. Abrahams, and G. Kotliar. Effects of disorder on the non-zero temperature Mott transition. Physical Review B, 71(20), May 2005.

[2] M. Aidelsburger, M. Atala, S. Nascimbène, S. Trotzky, Y.-A. Chen, and I. Bloch. Experimental Realization of Strong Effective Magnetic Fields in an Optical Lattice. Physical Review Letters, 107(25), December 2011.

[3] E. Alba, X. Fernandez-Gonzalvo, J. Mur-Petit, J. Pachos, and J. Garcia-Ripoll. Seeing Topological Order in Time-of-Flight Measurements. Physical Review Letters, 107(23), November 2011.

[4] Vinay Ambegaokar and Matthias Troyer. Estimating errors reliably in Monte Carlo simulations of the Ehrenfest model. American Journal of Physics, 78(2):150, February 2010.

[5] M H Anderson, J R Ensher, M R Matthews, C E Wieman, and E A Cornell. Observation of bose-einstein condensation in a dilute atomic vapor. Science (New York, N.Y.), 269(5221):198–201, July 1995.

[6] M. R. Andrews. Observation of Interference Between Two Bose Condensates. Science, 275(5300):637–641, January 1997.

[7] W S Bakr, A Peng, M E Tai, R Ma, J Simon, J I Gillen, S Fölling, L Pollet, and M Greiner. Probing the superfluid-to-Mott insulator transition at the single-atom level. Science (New York, N.Y.), 329(5991):547–50, July 2010.

[8] Leon Balents. Spin liquids in frustrated magnets. Nature, 464(7286):199–208, March 2010.

[9] B. A. Bernevig, T. L. Hughes, and S.-C. Zhang. Quantum Spin Hall Effect and Topological Phase Transition in HgTe Quantum Wells. Science, 314(5806):1757–1761, December 2006.

[10] B. Andrei Bernevig and Shou-Cheng Zhang. Quantum Spin Hall Effect. Physical Review Letters, 96(10), March 2006.

[11] M. V. Berry. Quantal Phase Factors Accompanying Adiabatic Changes. Proceedings of the Royal Society A: Mathematical, Physical and Engineering Sciences, 392(1802):45–57, March 1984.

[12] Juliette Billy, Vincent Josse, Zhanchun Zuo, Alain Bernard, Ben Hambrecht, Pierre Lugan, David Clément, Laurent Sanchez-Palencia, Philippe Bouyer, and Alain Aspect. Direct observation of Anderson localization of matter waves in a controlled disorder. Nature, 453(7197):891–4, June 2008.

[13] U. Bissbort, F. Deuretzbacher, and W. Hofstetter. Effective multi-body induced tunneling and interactions in the Bose-Hubbard model of the lowest dressed band of an optical lattice. page 12, August 2011.

[14] Immanuel Bloch. Ultracold quantum gases in optical lattices. Nature Physics, 1(1):23–30, October 2005.

[15] Immanuel Bloch and Wilhelm Zwerger. Many-body physics with ultracold gases. Reviews of Modern Physics, 80(3):885–964, July 2008.

[16] Lewin Boehnke, Hartmut Hafermann, Michel Ferrero, Frank Lechermann, and Olivier Parcollet. Orthogonal polynomial representation of imaginary-time GreenâĂŹs functions. Physical Review B, 84(7), August 2011.

[17] C. Bradley, C. Sackett, J. Tollett, and R. Hulet. Evidence of Bose-Einstein Condensation in an Atomic Gas with Attractive Interactions. Physical Review Letters, 75(9):1687–1690, August 1995.

[18] Uwe Brandt and Andreas Giesekus. Hubbard and Anderson models on perovskitelike lattices: Exactly solvable cases. Physical Review Letters, 68(17):2648–2651, April 1992.

[19] Vincent Bretin, Sabine Stock, Yannick Seurin, and Jean Dalibard. Fast Rotation of a Bose-Einstein Condensate. Physical Review Letters, 92(5), February 2004.

[20] E Brion, L H Pedersen, and K Mø lmer. Adiabatic elimination in a lambda system. Journal of Physics A: Mathematical and Theoretical, 40(5):1033–1043, February 2007.

[21] Michael Buchhold, Daniel Cocks, and Walter Hofstetter. Effects of smooth boundaries on topological edge modes in optical lattices. Physical Review A, 85(6), June 2012.

[22] R Bulla, A C Hewson, and Th Pruschke. Numerical renormalization group calculations for the self-energy of the impurity Anderson model. Journal of Physics: Condensed Matter, 10(37):8365–8380, September 1998.

[23] Ching-Kit Chan, Philipp Werner, and Andrew J. Millis. Magnetism and orbital ordering in an interacting three-band model: A dynamical mean-field study. Physical Review B, 80(23), December 2009.

[24] Lawrence W. Cheuk, Ariel T. Sommer, Zoran Hadzibabic, Tarik Yefsah, Waseem S. Bakr, and Martin W. Zwierlein. Spin-Injection Spectroscopy of a Spin-Orbit Coupled Fermi Gas. May 2012.

[25] Grzegorz Chimczak and Ryszard Tanaś. Fine tuning of quantum operations performed via Raman transitions. Physical Review A, 77(3), March 2008.

[26] C Chin, M Bartenstein, A Altmeyer, S Riedl, S Jochim, J Hecker Denschlag, and R Grimm. Observation of the pairing gap in a strongly interacting Fermi gas. Science (New York, N.Y.), 305(5687):1128–30, August 2004.

[27] Claude Cohen-Tannoudji, Bernard Diu, and Franck Laloe. Quantenmechanik: Teil 1 : 2 Durchgesehene Und Verbesserte Auflage (German Edition). Walter De Gruyter Inc, 1999.

[28] N. Cooper. Optical Flux Lattices for Ultracold Atomic Gases. Physical Review Letters, 106(17), April 2011.

[29] N.R. Cooper. Rapidly rotating atomic gases. Advances in Physics, 57(6):539–616, November 2008.

[30] Ph. Courteille, R. S. Freeland, and D. J. Heinzen. Observation of a Feshbach Resonance in Cold Atom Scattering. Physical Review Letters, 81(1):69–72, July 1998.

[31] Hans L. Cycon, Richard G. Froese, Werner Kirsch, and Barry Simon. Schrödinger Operators: With Applications to Quantum Mechanics and Global Geometry (Theoretical and Mathematica Springer, 1987.

[32] Gerd Czycholl. Theoretische Festkörperphysik: Von den klassischen Modellen zu modernen Forschungsthemen (Spring Springer, 2007.

[33] T. Dahm and L. Tewordt. Quasiparticle and Spin Excitation Spectra in the Normal and d-Wave Superconducting State of the Two-Dimensional Hubbard Model. Physical Review Letters, 74(5):793–796, January 1995.

[34] Jean Dalibard, Fabrice Gerbier, Gediminas JuzeliÅńnas, and Patrik Öhberg. Colloquium: Artificial gauge potentials for neutral atoms. Reviews of Modern Physics, 83(4):1523–1543, November 2011.

[35] Tung-Lam Dao, Antoine Georges, Jean Dalibard, Christophe Salomon, and Iacopo Carusotto. Measuring the One-Particle Excitations of Ultracold Fermionic Atoms by Stimulated Raman Spectroscopy. Physical Review Letters, 98(24), June 2007.

[36] K. Davis, M. Mewes, M. Andrews, N. van Druten, D. Durfee, D. Kurn, and W. Ketterle. Bose-Einstein Condensation in a Gas of Sodium Atoms. Physical Review Letters, 75(22):3969–3973, November 1995.

[37] B. DeMarco. Onset of Fermi Degeneracy in a Trapped Atomic Gas. Science, 285(5434):1703–1706, September 1999.

[38] D. Deutsch. Quantum Theory, the Church-Turing Principle and the Universal Quantum Computer. Proceedings of the Royal Society A: Mathematical, Physical and Engineering Sciences, 400(1818):97–117, July 1985.

[39] V. Dobrosavljević and G. Kotliar. Mean Field Theory of the Mott-Anderson Transition. Physical Review Letters, 78(20):3943–3946, May 1997.

[40] V. Dobrosavljevic and G. Kotliar. Dynamical mean-field studies of metal-insulator transitions. Philosophical Transactions of the Royal Society A: Mathematical, Physical and Engineering Sciences, 356(1735):57–74, January 1998.

[41] Richard Durrett. Essentials of Stochastic Processes (Springer Texts in Statistics). Springer, 1999.

[42] Sudipta Dutta, S. Lakshmi, and Swapan Pati. Electron-electron interactions on the edge states of graphene: A many-body configuration interaction study. Physical Review B, 77(7), February 2008.

[43] I. Dzyaloshinsky. A thermodynamic theory of âĂIJweakâĂİ ferromagnetism of antiferromagnetics. Journal of Physics and Chemistry of Solids, 4(4):241–255, January 1958.

[44] Andrew M. Essin and Victor Gurarie. Bulk-boundary correspondence of topological insulators from their respective GreenâĂŹs functions. Physical Review B, 84(12), September 2011.

[45] Tilman Esslinger. Fermi-Hubbard Physics with Atoms in an Optical Lattice. Annual Review of Condensed Matter Physics, 1(1):129–152, August 2010.

[46] L. Fallani, J. Lye, V. Guarrera, C. Fort, and M. Inguscio. Ultracold Atoms in a Disordered Crystal of Light: Towards a Bose Glass. Physical Review Letters, 98(13), March 2007.

[47] Richard P. Feynman. Simulating physics with computers. International Journal of Theoretical Physics, 21(6-7):467–488, June 1982.

[48] Simon Fölling, Fabrice Gerbier, Artur Widera, Olaf Mandel, Tatjana Gericke, and Immanuel Bloch. Spatial quantum noise interferometry in expanding ultracold atom clouds. Nature, 434(7032):481–4, March 2005.

[49] J. Freericks and Mark Jarrell. Magnetic Phase Diagram of the Hubbard Model. Physical Review Letters, 74(1):186–189, January 1995.

[50] Liang Fu and C. Kane. Time reversal polarization and a Z2 adiabatic spin pump. Physical Review B, 74(19), November 2006.

[51] Takahiro Fukui, Takanori Fujiwara, and Yasuhiro Hatsugai. Topological Meaning of Z 2 Numbers in Time Reversal Invariant Systems. Journal of the Physical Society of Japan, 77(12):123705, November 2008.

[52] Takahiro Fukui and Yasuhiro Hatsugai. Topological aspects of the quantum spin-Hall effect in graphene: Z2 topological order and spin Chern number. Physical Review B, 75(12), March 2007.

[53] Antoine Georges, Werner Krauth, and Marcelo J. Rozenberg. Dynamical mean-field theory of strongly correlated fermion systems and the limit of infinite dimensions. Reviews of Modern Physics, 68(1):13–125, January 1996.

[54] Fabrice Gerbier and Jean Dalibard. Gauge fields for ultracold atoms in optical superlattices. New Journal of Physics, 12(3):033007, March 2010.

[55] Stefano Giorgini and Sandro Stringari. Theory of ultracold atomic Fermi gases. Reviews of Modern Physics, 80(4):1215–1274, October 2008.

[56] N. Goldman, W. Beugeling, and C. Morais Smith. Topological phase transitions between chiral and helical spin textures in a lattice with spin-orbit coupling and a magnetic field. EPL (Europhysics Letters), 97(2):23003, January 2012.

[57] N Goldman, I Satija, P Nikolic, A Bermudez, MA Martin-Delgado, M Lewenstein, and IB Spielman. Realistic time-reversal invariant topological insulators with neutral atoms. Physical review letters, 105(25):255302, 2010.

[58] Nathan Goldman, Jérôme Beugnon, and Fabrice Gerbier. Detecting Chiral Edge States in the Hofstadter Optical Lattice. Physical Review Letters, 108(25), June 2012.

[59] E. Gorelik, I. Titvinidze, W. Hofstetter, M. Snoek, and N. Blümer. Néel Transition of Lattice Fermions in a Harmonic Trap: A Real-Space Dynamic Mean-Field Study. Physical Review Letters, 105(6), August 2010.

[60] Markus Greiner, Olaf Mandel, Tilman Esslinger, Theodor W Hänsch, and Immanuel Bloch. Quantum phase transition from a superfluid to a Mott insulator in a gas of ultracold atoms. Nature, 415(6867):39–44, January 2002.

[61] Axel Griesmaier, Jörg Werner, Sven Hensler, Jürgen Stuhler, and Tilman Pfau. Bose-Einstein Condensation of Chromium. Physical Review Letters, 94(16), April 2005.

[62] Rudolf Grimm and Matthias Weidemüller. Advances In Atomic, Molecular, and Optical Physics Volume 42, volume 42 of Advances In Atomic, Molecular, and Optical Physics. Elsevier, 2000.

[63] Y. Guldner, J. Vieren, M. Voos, F. Delahaye, D. Dominguez, J. Hirtz, and M. Razeghi. Quantum Hall effect in In_{0.53}Ga_{0.47}As-InP heterojunctions with two populated electric subbands. Physical Review B, 33(6):3990–3993, March 1986.

[64] E. Gull, M. Ferrero, O. Parcollet, A. Georges, and A. Millis. Momentum-space anisotropy and pseudogaps: A comparative cluster dynamical mean-field analysis of the doping-driven metal-insulator transition in the two-dimensional Hubbard model. Physical Review B, 82(15), October 2010.

[65] E. Gull, P. Werner, O. Parcollet, and M. Troyer. Continuous-time auxiliary-field Monte Carlo for quantum impurity models. EPL (Europhysics Letters), 82(5):57003, June 2008.

[66] E. Gull, P. Werner, X. Wang, M. Troyer, and A. J. Millis. Local order and the gapped phase of the Hubbard model: A plaquette dynamical mean-field investigation. EPL (Europhysics Letters), 84(3):37009, November 2008.

[67] Emanuel Gull, Andrew Millis, Alexander Lichtenstein, Alexey Rubtsov, Matthias Troyer, and Philipp Werner. Continuous-time MonteÂǎCarlo methods for quantum impurity models. Reviews of Modern Physics, 83(2):349–404, May 2011.

[68] Emanuel Gull, Olivier Parcollet, Philipp Werner, and Andrew J. Millis. Momentum-sector-selective metal-insulator transition in the eight-site dynamical mean-field approximation to the Hubbard model in two dimensions. Physical Review B, 80(24), December 2009.

[69] Emanuel Gull, Peter Staar, Sebastian Fuchs, Phani Nukala, Michael Summers, Thomas Pruschke, Thomas Schulthess, and Thomas Maier. Submatrix updates for the continuous-time auxiliary-field algorithm. Physical Review B, 83(7), February 2011.

[70] Emanuel Gull, Philipp Werner, Andrew Millis, and Matthias Troyer. Performance analysis of continuous-time solvers for quantum impurity models. Physical Review B, 76(23), December 2007.

[71] V. Gurarie. Single-particle GreenâĂŹs functions and interacting topological insulators. Physical Review B, 83(8):1–15, February 2011.

[72] Olivier Gygi, Helmut Katzgraber, Matthias Troyer, Stefan Wessel, and G. Batrouni. Simulations of ultracold bosonic atoms in optical lattices with anharmonic traps. Physical Review A, 73(6), June 2006.

[73] Lucia Hackermüller, Ulrich Schneider, Maria Moreno-Cardoner, Takuya Kitagawa, Thorsten Best, Sebastian Will, Eugene Demler, Ehud Altman, Immanuel Bloch, and Belén Paredes. Anomalous expansion of attractively interacting fermionic atoms in an optical lattice. Science (New York, N.Y.), 327(5973):1621–4, March 2010.

[74] Hartmut Hafermann, Kelly Patton, and Philipp Werner. Improved estimators for the self-energy and vertex function in hybridization-expansion continuous-time quantum Monte Carlo simulations. Physical Review B, 85(20), May 2012.

[75] Olle Häggström. Finite Markov Chains and Algorithmic Applications (London Mathematical Society Student Texts). Cambridge University Press, 2002.

[76] F. D. M. Haldane. Model for a Quantum Hall Effect without Landau Levels: Condensed-Matter Realization of the "Parity Anomaly". Physical Review Letters, 61(18):2015–2018, October 1988.

[77] B. Halperin. Quantized Hall conductance, current-carrying edge states, and the existence of extended states in a two-dimensional disordered potential. Physical Review B, 25(4):2185–2190, February 1982.

[78] M. Hasan and C. Kane. Colloquium: Topological insulators. Reviews of Modern Physics, 82(4):3045–3067, November 2010.

[79] Y. Hatsugai. Topological aspects of the quantum Hall effect. Journal of Physics: Condensed Matter, 9:2507, 1997.

[80] Yasuhiro Hatsugai. Edge states in the integer quantum Hall effect and the Riemann surface of the Bloch function. Physical Review B, 48(16):11851–11862, October 1993.

[81] Philipp Hauke, Olivier Tieleman, Alessio Celi, Christoph Ölschläger, Juliette Simonet, Julian Struck, Malte Weinberg, Patrick Windpassinger, Klaus Sengstock, Maciej Lewenstein, and André Eckardt. Non-Abelian gauge fields and topological insulators in shaken optical lattices. page 7, May 2012.

[82] Kristjan Haule. Quantum Monte Carlo impurity solver for cluster dynamical mean-field theory and electronic structure calculations with adjustable cluster base. Physical Review B, 75(15), April 2007.

[83] Kristjan Haule and Gabriel Kotliar. Strongly correlated superconductivity: A plaquette dynamical mean-field theory study. Physical Review B, 76(10), September 2007.

[84] R. Helmes, T. Costi, and A. Rosch. Mott Transition of Fermionic Atoms in a Three-Dimensional Optical Trap. Physical Review Letters, 100(5), February 2008.

[85] Igor F. Herbut. Interactions and Phase Transitions on GrapheneâĂŹs Honeycomb Lattice. Physical Review Letters, 97(14), October 2006.

[86] J. Hirsch and R. Fye. Monte Carlo Method for Magnetic Impurities in Metals. Physical Review Letters, 56(23):2521–2524, June 1986.

[87] Douglas Hofstadter. Energy levels and wave functions of Bloch electrons in rational and irrational magnetic fields. Physical Review B, 14(6):2239–2249, September 1976.

[88] W. Hofstetter, J. Cirac, P. Zoller, E. Demler, and M. Lukin. High-Temperature Superfluidity of Fermionic Atoms in Optical Lattices. Physical Review Letters, 89(22), November 2002.

[89] M. Hohenadler, T. Lang, and F. Assaad. Correlation Effects in Quantum Spin-Hall Insulators: A Quantum Monte Carlo Study. Physical Review Letters, 106(10), March 2011.

[90] Carsten Honerkamp and Walter Hofstetter. Ultracold Fermions and the SU(N) Hubbard Model. Physical Review Letters, 92(17), April 2004.

[91] J. Hubbard. Electron Correlations in Narrow Energy Bands. Proceedings of the Royal Society A: Mathematical, Physical and Engineering Sciences, 276(1365):238–257, November 1963.

[92] J. Hubbard. Electron Correlations in Narrow Energy Bands. II. The Degenerate Band Case. Proceedings of the Royal Society A: Mathematical, Physical and Engineering Sciences, 277(1369):237–259, January 1964.

[93] J. Hubbard. Electron Correlations in Narrow Energy Bands. III. An Improved Solution. Proceedings of the Royal Society A: Mathematical, Physical and Engineering Sciences, 281(1386):401–419, September 1964.

[94] A. ImamogÂŕlu, D. D. Awschalom, G. Burkard, D. P. DiVincenzo, D. Loss, M. Sherwin, and A. Small. Quantum Information Processing Using Quantum Dot Spins and Cavity QED. Physical Review Letters, 83(20):4204–4207, November 1999.

[95] D. Jaksch, C. Bruder, J. Cirac, C. Gardiner, and P. Zoller. Cold Bosonic Atoms in Optical Lattices. Physical Review Letters, 81(15):3108–3111, October 1998.

[96] D Jaksch and P Zoller. Creation of effective magnetic fields in optical lattices: the Hofstadter butterfly for cold neutral atoms. New Journal of Physics, 5(1):56–56, May 2003.

[97] K. Jiménez-García, L. LeBlanc, R. Williams, M. Beeler, A. Perry, and I. Spielman. Peierls Substitution in an Engineered Lattice Potential. Physical Review Letters, 108(22), May 2012.

[98] Robert Jördens, Niels Strohmaier, Kenneth Günter, Henning Moritz, and Tilman Esslinger. A Mott insulator of fermionic atoms in an optical lattice. Nature, 455(7210):204–7, September 2008.

[99] C. L. Kane and E. J. Mele. Size, Shape, and Low Energy Electronic Structure of Carbon Nanotubes. Physical Review Letters, 78(10):1932–1935, March 1997.

[100] C. L. Kane and E. J. Mele. Quantum Spin Hall Effect in Graphene. Physical Review Letters, 95(22), November 2005.

[101] C. L. Kane and E. J. Mele. Z_{2} Topological Order and the Quantum Spin Hall Effect. Physical Review Letters, 95(14), September 2005.

[102] Mehdi Kargarian, Jun Wen, and Gregory Fiete. Competing exotic topological insulator phases in transition-metal oxides on the pyrochlore lattice with distortion. Physical Review B, 83(16), April 2011.

[103] Toshiya Kinoshita, Trevor Wenger, and David S Weiss. Observation of a one-dimensional Tonks-Girardeau gas. Science (New York, N.Y.), 305(5687):1125–8, August 2004.

[104] K. Klitzing, G. Dorda, and M. Pepper. New Method for High-Accuracy Determination of the Fine-Structure Constant Based on Quantized Hall Resistance. Physical Review Letters, 45(6):494–497, August 1980.

[105] Akihisa Koga and Philipp Werner. Polarized Superfluidity in the Imbalanced Attractive Hubbard Model. Journal of the Physical Society of Japan, 79(6):064401, May 2010.

[106] Akihisa Koga and Philipp Werner. Superfluid State in the Periodic Anderson Model with Attractive Interactions. Journal of the Physical Society of Japan, 79(11):114401, October 2010.

[107] Michael Köhl, Henning Moritz, Thilo Stöferle, Kenneth Günter, and Tilman Esslinger. Fermionic Atoms in a Three Dimensional Optical Lattice: Observing Fermi Surfaces, Dynamics, and Interactions. Physical Review Letters, 94(8), March 2005.

[108] Mahito Kohmoto. Zero modes and the quantized Hall conductance of the two-dimensional lattice in a magnetic field. Physical Review B, 39(16):11943–11949, June 1989.

[109] Tohru Koma and Hal Tasaki. Decay of superconducting and magnetic correlations in one- and two-dimensional Hubbard models. Physical Review Letters, 68(21):3248–3251, May 1992.

[110] M. Konig, S. Wiedmann, C. Brune, A. Roth, H. Buhmann, L. W. Molenkamp, X.-L. Qi, and S.-C. Zhang. Quantum Spin Hall Insulator State in HgTe Quantum Wells. Science, 318(5851):766–770, November 2007.

[111] E. Kozik, K. Van Houcke, E. Gull, L. Pollet, N. Prokof'ev, B. Svistunov, and M. Troyer. Diagrammatic Monte Carlo for correlated fermions. EPL (Europhysics Letters), 90(1):10004, April 2010.

[112] Thierry Lahaye, Tobias Koch, Bernd Fröhlich, Marco Fattori, Jonas Metz, Axel Griesmaier, Stefano Giovanazzi, and Tilman Pfau. Strong dipolar effects in a quantum ferrofluid. Nature, 448(7154):672–5, August 2007.

[113] L. D. Landau and L. M. Lifshitz. Quantum Mechanics Non-Relativistic Theory, Third Edition: Volume 3. Butterworth-Heinemann, 1981.

[114] Andreas M. Läuchli and Philipp Werner. Krylov implementation of the hybridization expansion impurity solver and application to 5-orbital models. Physical Review B, 80(23), December 2009.

[115] R. Laughlin. Quantized Hall conductivity in two dimensions. Physical Review B, 23(10):5632–5633, May 1981.

[116] R. B. Laughlin. Anomalous Quantum Hall Effect: An Incompressible Quantum Fluid with Fractionally Charged Excitations. Physical Review Letters, 50(18):1395–1398, May 1983.

[117] Dung-Hai Lee. Effects of Interaction on Quantum Spin Hall Insulators. Physical Review Letters, 107(16), October 2011.

[118] Michael Levin and Ady Stern. Fractional Topological Insulators. Physical Review Letters, 103(19), November 2009.

[119] Maciej Lewenstein, Anna Sanpera, Veronica Ahufinger, Bogdan Damski, Aditi Sen(De), and Ujjwal Sen. Ultracold atomic gases in optical lattices: mimicking condensed matter physics and beyond. Advances in Physics, 56(2):243–379, March 2007.

[120] Lih-King Lim, Andreas Hemmerich, and C. Morais Smith. Artificial staggered magnetic field for ultracold atoms in optical lattices. Physical Review A, 81(2), February 2010.

[121] Nan Lin, Emanuel Gull, and A. Millis. Optical conductivity from cluster dynamical mean-field theory: Formalism and application to high-temperature superconductors. Physical Review B, 80(16), October 2009.

[122] Nan Lin, Emanuel Gull, and Andrew Millis. Physics of the pseudogap in eight-site cluster dynamical mean-field theory: Photoemission, Raman scattering, and in-plane and c-axis conductivity. Physical Review B, 82(4), July 2010.

[123] Y.-J. Lin, R. Compton, A. Perry, W. Phillips, J. Porto, and I. Spielman. Bose-Einstein Condensate in a Uniform Light-Induced Vector Potential. Physical Review Letters, 102(13), March 2009.

[124] Y-J Lin, R L Compton, K Jiménez-García, J V Porto, and I B Spielman. Synthetic magnetic fields for ultracold neutral atoms. Nature, 462(7273):628–32, December 2009.

[125] Y-J Lin, K Jiménez-García, and I B Spielman. Spin-orbit-coupled Bose-Einstein condensates. Nature, 471(7336):83–6, March 2011.

[126] Xiong-Jun Liu, Xin Liu, Congjun Wu, and Jairo Sinova. Quantum anomalous Hall effect with cold atoms trapped in a square lattice. Physical Review A, 81(3), March 2010.

[127] Dirk-Sören Lühmann, Ole Jürgensen, and Klaus Sengstock. Multi-orbital and density-induced tunneling of bosons in optical lattices. New Journal of Physics, 14(3):033021, March 2012.

[128] D. Makogon, I. B. Spielman, and C. Morais Smith. Spin-charge-density wave in a rounded-square Fermi surface for ultracold atoms. EPL (Europhysics Letters), 97(3):33002, February 2012.

[129] Leonardo Mazza, Alejandro Bermudez, Nathan Goldman, Matteo Rizzi, Miguel Angel Martin-Delgado, and Maciej Lewenstein. An optical-lattice-based quantum simulator for relativistic field theories and topological insulators. New Journal of Physics, 14(1):015007, January 2012.

[130] Z Y Meng, T C Lang, S Wessel, F F Assaad, and A Muramatsu. Quantum spin liquid emerging in two-dimensional correlated Dirac fermions. Nature, 464(7290):847–51, April 2010.

[131] Albert Messiah. Quantum Mechanics (2 Volumes in 1). Dover Publications, 1999.

[132] Nicholas Metropolis, Arianna W. Rosenbluth, Marshall N. Rosenbluth, Augusta H. Teller, and Edward Teller. Equation of State Calculations by Fast Computing Machines. The Journal of Chemical Physics, 21(6):1087, June 1953.

[133] Walter Metzner and Dieter Vollhardt. Correlated Lattice Fermions in d=âĹđ Dimensions. Physical Review Letters, 62(3):324–327, January 1989.

[134] K. Michielsen, H. De Raedt, and T. Schneider. Metal-insulator transition in a generalized Hubbard model. Physical Review Letters, 68(9):1410–1413, March 1992.

[135] E. Miranda and V. Dobrosavljevic. Dynamical mean-field theories of correlation and disorder. page 78, December 2011.

[136] Goetz Moeller, Qimiao Si, Gabriel Kotliar, Marcelo Rozenberg, and Daniel Fisher. Critical Behavior near the Mott Transition in the Hubbard Model. Physical Review Letters, 74(11):2082–2085, March 1995.

[137] A. J. Moerdijk, B. J. Verhaar, and A. Axelsson. Resonances in ultracold collisions of ˆ{6}Li, ˆ{7}Li, and ˆ{23}Na. Physical Review A, 51(6):4852–4861, June 1995.

[138] J. Moore and L. Balents. Topological invariants of time-reversal-invariant band structures. Physical Review B, 75(12), March 2007.

[139] Tôru Moriya. Anisotropic Superexchange Interaction and Weak Ferromagnetism. Physical Review, 120(1):91–98, October 1960.

[140] Erich Mueller. Artificial electromagnetism for neutral atoms: Escher staircase and Laughlin liquids. Physical Review A, 70(4), October 2004.

[141] Mikio Nakahara. Geometry, Topology and Physics (Graduate Student Series in Physics). Adam Hilger, 1990.

[142] J. W. Negele and Henri Orland. Quantum Many-Particle Systems (Frontiers in Physics). Perseus Books (Sd), 1988.

[143] K. Osterloh, M. Baig, L. Santos, P. Zoller, and M. Lewenstein. Cold Atoms in Non-Abelian Gauge Potentials: From the Hofstadter "Moth" to Lattice Gauge Theory. Physical Review Letters, 95(1), June 2005.

[144] R. Peierls. Zur Theorie des Diamagnetismus von Leitungselektronen. Zeitschrift fi£¡r Physik, 80(11-12):763–791, November 1933.

[145] Dmytro Pesin and Leon Balents. Mott physics and band topology in materials with strong spinâĂŞorbit interaction. Nature Physics, 6(5):376–381, March 2010.

[146] Lode Pollet, Nikolay ProkofâĂŹev, and Boris Svistunov. Incorporating dynamic mean-field theory into diagrammatic Monte Carlo. Physical Review B, 83(16), April 2011.

[147] M. Potthoff and W. Nolting. Metallic surface of a Mott insulatorâĂŞMott insulating surface of a metal. Physical Review B, 60(11):7834–7849, September 1999.

[148] Emil Prodan, Taylor Hughes, and B. Bernevig. Entanglement Spectrum of a Disordered Topological Chern Insulator. Physical Review Letters, 105(11), September 2010.

[149] Nikolay ProkofâĂŹev and Boris Svistunov. Bold Diagrammatic Monte Carlo Technique: When the Sign Problem Is Welcome. Physical Review Letters, 99(25), December 2007.

[150] Nikolay ProkofâĂŹev and Boris Svistunov. Fermi-polaron problem: Diagrammatic Monte Carlo method for divergent sign-alternating series. Physical Review B, 77(2), January 2008.

[151] I. Rabi, N. Ramsey, and J. Schwinger. Use of Rotating Coordinates in Magnetic Resonance Problems. Reviews of Modern Physics, 26(2):167–171, April 1954.

[152] Stephan Rachel and Karyn Le Hur. Topological insulators and Mott physics from the Hubbard interaction. Physical Review B, 82(7), August 2010.

[153] Giacomo Roati, Chiara D'Errico, Leonardo Fallani, Marco Fattori, Chiara Fort, Matteo Zaccanti, Giovanni Modugno, Michele Modugno, and Massimo Inguscio. Anderson localization of a non-interacting Bose-Einstein condensate. Nature, 453(7197):895–8, June 2008.

[154] S. Rombouts, K. Heyde, and N. Jachowicz. A discrete Hubbard-Stratonovich decomposition for general, fermionic two-body interactions. Physics Letters A, 242(4-5):271–276, June 1998.

[155] S. Rombouts, K. Heyde, and N. Jachowicz. Quantum Monte Carlo Method for Fermions, Free of Discretization Errors. Physical Review Letters, 82(21):4155–4159, May 1999.

[156] J. Ruseckas, G. JuzeliÅńnas, P. Öhberg, and M. Fleischhauer. Non-Abelian Gauge Potentials for Ultracold Atoms with Degenerate Dark States. Physical Review Letters, 95(1), June 2005.

[157] Laurent Sanchez-Palencia and Maciej Lewenstein. Disordered quantum gases under control. Nature Physics, 6(2):87–95, February 2010.

[158] V. Scarola and S. Das Sarma. Edge Transport in 2D Cold Atom Optical Lattices. Physical Review Letters, 98(21), May 2007.

[159] U Schneider, L Hackermüller, S Will, Th Best, I Bloch, T A Costi, R W Helmes, D Rasch, and A Rosch. Metallic and insulating phases of repulsively interacting fermions in a 3D optical lattice. Science (New York, N.Y.), 322(5907):1520–5, December 2008.

[160] Ulrich Schneider, Lucia Hackermüller, Jens Philipp Ronzheimer, Sebastian Will, Simon Braun, Thorsten Best, Immanuel Bloch, Eugene Demler, Stephan Mandt, David Rasch, and Achim Rosch. Fermionic transport and out-of-equilibrium dynamics in a homogeneous Hubbard model with ultracold atoms. Nature Physics, 8(3):213–218, January 2012.

[161] Andreas Schnyder, Shinsei Ryu, Akira Furusaki, and Andreas Ludwig. Classification of topological insulators and superconductors in three spatial dimensions. Physical Review B, 78(19), November 2008.

[162] F. Schreck, L. Khaykovich, K. L. Corwin, G. Ferrari, T. Bourdel, J. Cubizolles, and C. Salomon. Quasipure Bose-Einstein Condensate Immersed in a Fermi Sea. Physical Review Letters, 87(8), August 2001.

[163] D. Semmler, K. Byczuk, and W. Hofstetter. Mott-Hubbard and Anderson metal-insulator transitions in correlated lattice fermions with binary disorder. Physical Review B, 81(11):10, March 2010.

[164] D. Semmler, K. Byczuk, and W. Hofstetter. Anderson-Hubbard model with box disorder: Statistical dynamical mean-field theory investigation. Physical Review B, 84(11), September 2011.

[165] Jonathan Simon, Waseem S Bakr, Ruichao Ma, M Eric Tai, Philipp M Preiss, and Markus Greiner. Quantum simulation of antiferromagnetic spin chains in an optical lattice. Nature, 472(7343):307–12, April 2011.

[166] M Snoek, I Titvinidze, C TÅŚke, K Byczuk, and W Hofstetter. Antiferromagnetic order of strongly interacting fermions in a trap: real-space dynamical mean-field analysis. New Journal of Physics, 10(9):093008, September 2008.

[167] Anders Sø rensen, Eugene Demler, and Mikhail Lukin. Fractional Quantum Hall States of Atoms in Optical Lattices. Physical Review Letters, 94(8), March 2005.

[168] Sandro Sorella, Yuichi Otsuka, and Seiji Yunoki. Absence of a Spin Liquid Phase in the Hubbard Model on the Honeycomb Lattice. page 5, July 2012.

[169] D. Soriano and J. Fernández-Rossier. Spontaneous persistent currents in a quantum spin Hall insulator. Physical Review B, 82(16), October 2010.

[170] I. Spielman. Raman processes and effective gauge potentials. Physical Review A, 79(6), June 2009.

[171] D. Stamper-Kurn, A. Chikkatur, A. Görlitz, S. Inouye, S. Gupta, D. Pritchard, and W. Ketterle. Excitation of Phonons in a Bose-Einstein Condensate by Light Scattering. Physical Review Letters, 83(15):2876–2879, October 1999.

[172] T.D. Stanescu, Victor Galitski, and S.D. Sarma. Topological states in two-dimensional optical lattices. Physical Review A, 82(1):013608, 2010.

[173] T.D. Stanescu, Victor Galitski, JY Vaishnav, C.W. Clark, and S.D. Sarma. Topological insulators and metals in atomic optical lattices. Physical Review A, 79(5):053639, 2009.

[174] J. Steinhauer, R. Ozeri, N. Katz, and N. Davidson. Excitation Spectrum of a Bose-Einstein Condensate. Physical Review Letters, 88(12), March 2002.

[175] J. Stenger, S. Inouye, A. Chikkatur, D. Stamper-Kurn, D. Pritchard, and W. Ketterle. Bragg Spectroscopy of a Bose-Einstein Condensate. Physical Review Letters, 82(23):4569–4573, June 1999.

[176] Henk T. C. Stoof, Dennis B. M. Dickerscheid, and Koos Gubbels. Ultracold Quantum Fields (Theoretical and Mathematical Physics). Springer, 2009.

[177] J. Struck, C. Ölschläger, M. Weinberg, P. Hauke, J. Simonet, A. Eckardt, M. Lewenstein, K. Sengstock, and P. Windpassinger. Tunable Gauge Potential for Neutral and Spinless Particles in Driven Optical Lattices. Physical Review Letters, 108(22), May 2012.

[178] Yolande Szczech, Michael Tusch, and David Logan. Finite-Temperature Magnetism in the Hubbard Model. Physical Review Letters, 74(14):2804–2807, April 1995.

[179] D. Tanasković, V. Dobrosavljević, E. Abrahams, and G. Kotliar. Disorder Screening in Strongly Correlated Systems. Physical Review Letters, 91(6), August 2003.

[180] Hal Tasaki. Ferromagnetism in the Hubbard models with degenerate single-electron ground states. Physical Review Letters, 69(10):1608–1611, September 1992.

[181] M. Theis, G. Thalhammer, K. Winkler, M. Hellwig, G. Ruff, R. Grimm, and J. Hecker Denschlag. Tuning the Scattering Length with an Optically Induced Feshbach Resonance. Physical Review Letters, 93(12), September 2004.

[182] D. Thouless, M. Kohmoto, M. Nightingale, and M. den Nijs. Quantized Hall Conductance in a Two-Dimensional Periodic Potential. Physical Review Letters, 49(6):405–408, August 1982.

[183] E. Tiesinga, B. J. Verhaar, and H. T. C. Stoof. Threshold and resonance phenomena in ultracold ground-state collisions. Physical Review A, 47(5):4114–4122, May 1993.

[184] A G Truscott, K E Strecker, W I McAlexander, G B Partridge, and R G Hulet. Observation of Fermi pressure in a gas of trapped atoms. Science (New York, N.Y.), 291(5513):2570–2, March 2001.

[185] D. C. Tsui, H. L. Stormer, and A. C. Gossard. Two-Dimensional Magnetotransport in the Extreme Quantum Limit. Physical Review Letters, 48(22):1559–1562, May 1982.

[186] RO Umucal\ilar, Hui Zhai, and MÖ Oktel. Trapped Fermi gases in rotating optical lattices: Realization and detection of the topological Hofstadter insulator. Physical review letters, 100(7):70402, 2008.

[187] P. van Dongen. Extended Hubbard model at strong coupling. Physical Review B, 49(12):7904–7915, March 1994.

[188] Martin Weigel. Error estimation and reduction with cross correlations. Physical Review E, 81(6), June 2010.

[189] Philipp Werner, Armin Comanac, Luca deâĂŹ Medici, Matthias Troyer, and Andrew Millis. Continuous-Time Solver for Quantum Impurity Models. Physical Review Letters, 97(7), August 2006.

[190] Philipp Werner, Emanuel Gull, Olivier Parcollet, and Andrew Millis. Momentum-selective metal-insulator transition in the two-dimensional Hubbard model: An 8-site dynamical cluster approximation study. Physical Review B, 80(4), July 2009.

[191] Philipp Werner and Andrew Millis. Hybridization expansion impurity solver: General formulation and application to Kondo lattice and two-orbital models. Physical Review B, 74(15), October 2006.

[192] Philipp Werner and Andrew Millis. Doping-driven Mott transition in the one-band Hubbard model. Physical Review B, 75(8), February 2007.

[193] Philipp Werner and Andrew J. Millis. High-Spin to Low-Spin and Orbital Polarization Transitions in Multiorbital Mott Systems. Physical Review Letters, 99(12), September 2007.

[194] Sebastian Will, Thorsten Best, Simon Braun, Ulrich Schneider, and Immanuel Bloch. Coherent Interaction of a Single Fermion with a Small Bosonic Field. Physical Review Letters, 106(11), March 2011.

[195] Sebastian Will, Thorsten Best, Ulrich Schneider, Lucia Hackermüller, Dirk-Sören Lühmann, and Immanuel Bloch. Time-resolved observation of coherent multi-body interactions in quantum phase revivals. Nature, 465(7295):197–201, May 2010.

[196] Congjun Wu, B. Andrei Bernevig, and Shou-Cheng Zhang. Helical Liquid and the Edge of Quantum Spin Hall Systems. Physical Review Letters, 96(10), March 2006.

[197] Wei Wu, Stephan Rachel, Wu-Ming Liu, and Karyn Le Hur. Quantum spin Hall insulators with interactions and lattice anisotropy. Physical Review B, 85(20), May 2012.

[198] Cenke Xu and J. Moore. Stability of the quantum spin Hall effect: Effects of interactions, disorder, and Z2 topology. Physical Review B, 73(4), January 2006.

[199] Tsuneya Yoshida, Robert Peters, Satoshi Fujimoto, and Norio Kawakami. Topological antiferromagnetic phase in a correlated Bernevig-Hughes-Zhang model. page 5, July 2012.

[200] Erhai Zhao, Noah Bray-Ali, Carl Williams, I. Spielman, and Indubala Satija. Chern numbers hiding in time-of-flight images. Physical Review A, 84(6), December 2011.

[201] Dong Zheng, Guang-Ming Zhang, and Congjun Wu. Particle-hole symmetry and interaction effects in the Kane-Mele-Hubbard model. Physical Review B, 84(20), November 2011.

[202] M W Zwierlein, J R Abo-Shaeer, A Schirotzek, C H Schunck, and W Ketterle. Vortices and superfluidity in a strongly interacting Fermi gas. Nature, 435(7045):1047–51, June 2005.